JOURNAL OF DEFENCE AND SECURITY INDUSTRIES: STRATEGY AND TECHNOLOGY

JDSI

VOLUME: 1 ISSUE:1 YEAR: 2026

Journal of Defence and Security Industries: Strategy and Technology (JDSI)

Journal of Defence and Security Industries: Strategy and Technology (JDSI) is an open-access, peer-reviewed academic journal dedicated to publishing scientific research in the fields of engineering, technology, management, and strategy as they relate to the defence and security sectors. Established by Defence Industries Academy Publications, JDSI aims to foster academic and industrial collaboration by providing a platform where scholars and professionals can exchange knowledge, insights, and innovative approaches to complex challenges in defence and security.

Publication Frequency

The JDSI accepts the articles in English and is being published three times a year.

Correspondence Address

Journal Contact: editorial@jdsi.org

Articles

Strategy & Policy Section

Science & Technology Section

Redefining Strategic Connectivity: A Holistic Vision for the Journal of Defence and Security Industries

Dear Readers,

In the evolving landscape of global security and technological competition, the defence industry has transcended its traditional boundaries. Once limited to system design, manufacturing, and procurement, it now stands as a strategic pillar shaping national economies, technological ecosystems, and geopolitical dynamics. In this transformative age, the Journal of Defence and Security Industries: Strategy and Technology (JDSI) has been envisioned not merely as a technical publication, but as a comprehensive, interdisciplinary, and future-oriented academic journal—an intellectual platform for synthesizing the best practices, strategic models, and global defence-industrial insights.

JDSI aims to serve as an anchor for scholarly discourse and strategic knowledge generation in the fields of defence and security. It is uniquely positioned to examine defence not only as an industry but as a multidimensional domain involving policy design, strategic foresight, economic resilience, and international cooperation. In this context, the journal covers a wide thematic range, including but not limited to defence technologies, AI and autonomy, cyber security, space and satellite systems, defence economics, innovation management, export strategies, offset mechanisms, consortium-led production models, and the geopolitical implications of defence alliances.

What distinguishes JDSI is its commitment to exploring the intersections of policy, technology, and human capital. The journal delves into defence industry models adopted by different nations, their historical trajectories, and comparative policy frameworks, offering a panoramic view of how states build and manage their defence-industrial capabilities. Through detailed case studies, peer-reviewed research, and strategic analysis, the journal provides visibility to collaborative production initiatives, financial ecosystem design, and institution-building efforts—including performance-based procurement, technology transfer strategies, and counter-embargo mechanisms.

A key focus area is the scale and complexity of modern production: from small-batch innovation to large-scale serial manufacturing. The journal examines scale economies, agile production paradigms, and platform-centric development models that shape today's defence value chains. It also aims to spotlight international offset practices and technology acquisition strategies that contribute to long-term sustainability and independence.

Equally important is JDSI's emphasis on education and workforce development. Recognizing that strategic competence is inseparable from talent development, the journal will feature collaborative models between defence industry actors and national education institutions—ranging from vocational schools and engineering faculties to advanced research centres. Best practices in technical and leadership training, integrated curricula, mentorship models, and applied learning environments will be shared to contribute to a globally competitive and locally grounded human capital base.

As the scientific platform of the National Competence Initiative, JDSI seeks to instill a culture of critical inquiry, systemic thinking, and interdisciplinary innovation. Competence, in our vision, is not merely the mastery of tools and techniques, but a strategic synthesis of technological expertise, operational leadership, global awareness, and institutional capacity.

With an open-access policy, double-blind peer review, and a strong editorial advisory board, JDSI is committed to academic rigour and inclusivity. It will provide a platform for scholars, practitioners, engineers, and policymakers to converge, collaborate, and contribute to the global body of defence knowledge.

In conclusion, JDSI is not just another technical journal. It is a strategic vision. A curated space for knowledge that not only documents the present but shapes the future of defence and security. As we step into a century marked by complexity, interdependence, and resilience, JDSI stands as a beacon for those who seek to transform ideas into strategy, and strategy into impact.

We invite you to engage, contribute, and build with us.

Prof. Dr. Haluk Görgün
Chairman

Editorial

It is with great pleasure and much pride that I would like to invite our readers into the first issue of the Journal of Defence and Security Industries: Strategy and Technology (JDSI), which represents the very first step towards the formalization of the new scholarly infrastructure for defence and security studies. This first issue marks the dawn of our effort to establish an academically robust academic community focused on defence, security, strategy, and advanced technologies. Defence and security are increasingly being defined by rapid development of technical advances, emergent threat environments, and digitalization around the world, leading to complexity in strategic and technological decision-making as unprecedented as ever before. Against this background, JDSI aims to be a critical bridge between academia, defence industries, and policy-making communities.

JDSI aims to encourage research of high quality that links theorization with praxis to provide evidence-based decision-making and dialogue across disciplinary and institutional contexts. The first issue of JDSI ontains eight articles that taken together convey the holistic nature and strategic view behind JDSI as a multidisciplinary venture. A particularly strong emphasis is put on data-driven governance and decision-support systems to meet the needs of today's pressing security environment. Also, the matter exemplifies the critical role of communication and navigation systems in defence and security applications that are necessary today, and are increasingly important strategic players. Also, despite the fact that one of the article's contributions introduces the CubeSat concept, another focuses on the creation and simulation of patch antennas for Global Navigation Satellite System (GNSS) applications. A further article highlights the criticality of secure communication through image encryption practices, which is an important method of securely detecting and protecting sensitive information in defence and security contexts. With a focus on artificial intelligence technologies for applications related to communication, navigation, and defence, the issue also discusses AI with a focus on AI-based target detection and identification systems.

Apart from the content above, advanced materials and manufacturing are presented as the enabling drivers of contemporary defence applications, in particular aerospace and space. Thus, in this first issue two articles address high-performance material manufacturing and state-of-the-art analysis methods.

With such contributions, JDSI seeks to contribute towards fostering informed conversations, encouraging cross-sector partnerships, and seeking evidence-based responses in defence and security. With this first issue, we mark the beginning of a new phase, one that aims to establish a sustained and continuously evolving academic platform, contributing to a broader, more relevant, and increasingly global scope in the years ahead.

Sincerely,

Prof. Dr. Hakan Karataş & Prof. Dr. İhsan Kaya
Editors-in-Chief

Blueprinting Sovereignty: A Reflex Analytics Paradigm for Adaptive Scenario Governance in the Turkish Defence Sector

Hasan Tolga Ünal [1], Özgür Umut Vurgun [1], Arif Furkan Mendi [1],
Mehmet Akif Nacar [1,*]

Abstract

In response to the growing complexity of public administration and defence governance, this study develops and evaluates an integrated reflex analytics platform designed to support sovereign and data-driven decision-making in the Turkish public sector. The platform combines multi-domain data fusion, modular artificial intelligence components, and dynamic scenario generation to analyse policy alternatives across economic, social, institutional, and risk dimensions and to quantify decision reflex through a novel Strategic Reflex Coefficient (SRC) metric. Within a virtualized ecosystem comprising 24 public sector organizations representing core layers of national governance—including ministries, regulatory bodies, regional authorities, and critical infrastructure operators—and 96 policy scenario streams spanning economic shocks, cyber incidents, supply chain disruptions, institutional reforms, and cross-sector crises, simulation results indicate an average 39.2% reduction in decision-making cycle time, a 27.1% increase in decision confidence under risk, a 35.8% improvement in alignment with stakeholder priorities, and a 45.6% enhancement in the traceability of institutional choices, while unresolved policy states in crisis-like conditions are reduced by 64.2%. These effects are derived from Monte Carlo analysis with repeated replications for each scenario type, and bootstrap-based 95% confidence intervals for the reported percentage improvements remain strictly positive, indicating that the gains are statistically robust rather than artefacts of a small number of favourable runs. Overall, the findings suggest that reflex analytics architectures of this kind can provide a transparent and reproducible framework for scenario-based governance, offering measurable gains in speed, robustness, and institutional learning, while also highlighting the need for further empirical validation in live public sector environments.

Keywords: reflex analytics, decision-making, digital governance, resilience, innovation, memory.

Received: 20.10.2025 Accepted: 17.12.2025 Research Article

[1] HAVELSAN Inc., Ankara, Türkiye
* Corresponding author.
✉ manacar@havelsan.com.tr

Cite this article as: Ünal, H.T., Vurgun, Ö. U., Mendi, A.F., & Nacar, M. A. (2026). Blueprinting sovereignty: a reflex analytics paradigm for adaptive scenario governance in the Turkish defence sector. *Journal of Defence and Security Industry: Strategy and Technology 1*, 1-26.

1. Introduction

The relentless digital transformation of public administration and defence governance has redefined the boundaries of strategic decision-making in sovereign states. Global defence and security landscapes are subject to ever-increasing complexity, driven by the proliferation of institutional data, multi-agent system interactivity, and the demand for real-time scenario management in the face of emergent and asymmetric threats. Traditional decision support systems, historically constrained by monolithic architectures and deterministic logic, are now widely recognized as insufficient for the orchestration of adaptive, resilient, and forward-looking public sector responses in the digital age (Simon, 1960). This transformation is visually summarized in Figure 1, which captures the technical evolution from static legacy systems to AI-integrated scenario intelligence for modern public sector decision-making.

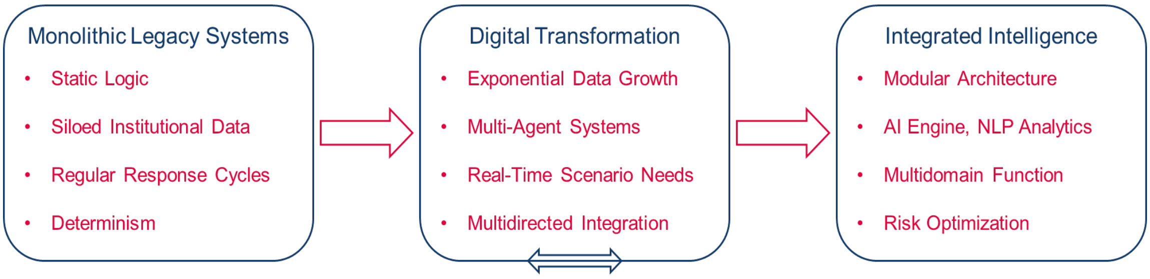

Figure 1. A schematic illustrating the evolution from monolithic and static logic to advanced, multidomain analytics enabling strategic policy reflex and institutional agility.

Despite these advances, public administrations and defence organizations still struggle with deeply fragmented data landscapes, siloed decision processes, and limited institutional capacity to explore complex policy alternatives under time pressure and uncertainty. Existing decision support systems typically operate on static rule sets and single-agency perspectives, which leaves them ill-equipped to orchestrate multi-actor policy coordination, to quantify trade-offs across economic, social, institutional, and risk dimensions, or to preserve a consistent decision logic across successive crises. In practice, this often manifests as delayed responses in high-stakes environments, increased vulnerability to decision gridlock when stakeholders diverge, and weak traceability between strategic intent, implemented options, and observed outcomes. The academic and practitioner literature on scenario-based governance, multi-criteria decision analysis (Cinelli et al., 2022), and AI-enabled public sector analytics has made important strides in modelling risk, resource allocation, and policy performance; however, most frameworks remain either narrowly scoped to single organizations (Blythe et al., 2019), confined to limited sets of evaluation criteria, or insufficiently integrated with institutional memory and reflexive learning mechanisms (Thokala & Madhavan, 2019). There is a lack of nationally anchored, multi-institutional architectures that can simulate large portfolios of public policy scenarios while jointly optimizing decision speed, robustness under uncertainty, social concordance, and historical traceability, despite an emerging body of work on reflexive governance, digital sovereignty, and multi-actor decision processes that highlight precisely these requirements in contemporary public administration.

In this sense, the term reflex analytics is introduced in this paper as a synthetic label for architectures that integrate multi-domain data fusion, scenario-based simulation, and risk-adjusted multi-criteria scoring into a single, reproducible decision workflow, building on earlier strands of work in decision-support systems and multi-criteria decision analysis for public services. Reflex analytics, and the associated Strategic Reflex Coefficient (SRC), extend risk-adjusted performance measures by explicitly incorporating variance, risk exposure, and institutional traceability into a unified metric, rather than treating these components as separate diagnostics or informal judgement factors. The notion of a social concordance index is similarly grounded in established concerns about stakeholder legitimacy and distributive impacts in public policy but is here operationalized as a scenario-level metric derived from historically observed preference profiles and structured elicitation, thereby linking normative considerations to simulation outputs in a transparent way (Kovari, 2024). Finally, decision gridlock has long been recognized as a characteristic failure mode of multi-actor governance systems (Rich et al., 2024). In this study it is formalized as a class of unresolved scenario outcomes in which competing stakeholder constraints prevent convergence, enabling gridlock to be quantified and systematically stress-tested within the proposed reflex analytics environment (Peters et al., 2024).

Over the past decade, scenario-driven governance has gained prominence in institutional design and national defence architecture, as policymakers seek real-time simulation, multidimensional risk assessment, and transparent outcome-based analytics (Sharda, Delen & Turban, 2017). Architectures leveraging artificial intelligence, Natural Language Processing (NLP), and multidomain data fusion have enabled governments to process exponentially growing datasets, simulate nested policy alternatives, and forecast the second- and third-order effects of strategic choices (Sami et al., 2016). International organizations and analytical institutions have reported that scenario-based policy intelligence frameworks can improve resource allocation efficiency by over 20%, reduce decision-making latency by more than 35% (OECD, 2022), and enhance policy resilience by up to 30% in high-variance operational environments (World Bank, 2023). Yet, a substantive gap (Lang, 2024) persists in the institutionalization of reflexive, adaptive, and context-aware digital decision systems tailored to national priorities (Zwitter & Gstrein, 2020), even as recent work on reflexive governance and digital sovereignty underlines the need for architectures (Fratini et al., 2024) that couple simulation, learning, and institutional accountability in a coherent way (Wirtz & Müller, 2019).

HAVELSAN, a leading defence Information Communication Technology (ICT) integrator in Türkiye, addresses this strategic imperative through open-architecture, scalable, and AI-enabled analytics solutions. The integrated scenario evaluation and reflex model introduced in this study proposes an integrated architectural framework for digital governance, in which public sector organizations, ranging from municipal entities to national ministries, can work toward data-driven institutionalization of strategic reflex at scale (OECD, 2014). Against this backdrop, the present study investigates two core research questions: first, to what extent a reflex analytics platform of this kind can measurably improve decision-cycle time, decision confidence under risk, social concordance with stakeholder priorities, institutional traceability, and the resolution of decision gridlock in a simulated public sector ecosystem; and second, whether the proposed SRC metric can provide stable, interpretable, and reproducible rankings of policy alternatives across heterogeneous scenario types. To answer these questions, the paper implements a multi-domain, AI-enabled simulation environment combining real and synthetic data from 24 organizations and 96 policy scenarios and evaluates performance through both aggregate metrics and extensive sensitivity analyses. The remainder of the paper is organized as follows: the next section details the data architecture, scenario design, and methodological pipeline (Carrapico & Farrand, 2025); the subsequent section reports the empirical results and robustness checks; the following section discusses implications and limitations for digital governance and defence planning; and the final section concludes with policy recommendations and directions for future research.

Data fragmentation and analytic inertia have been persistent obstacles in large-scale public institutions. Modern leadership in defence industries and public management is increasingly characterized by the capacity to simulate uncertainty, synthesize policy alternatives, and operationalize scenario intelligence within multi-actor co-creation platforms. The HAVELSAN model leverages a modular digital architecture, unifying advanced AI components such as synthetic learning, NLP-based document analysis, multi-dimensional vector scoring, and risk-tolerant scenario optimization, into a seamless analytic workflow. Notably, the platform enables both real-time and longitudinal scenario evaluation across heterogeneous organizational units, supporting strategic alignment and reflexive agility.

Empirical evaluations and large-scale simulation deployments, encompassing 24 public sector institutions representing core governance domains such as defence, internal security, critical infrastructure, economic regulation, and municipal administration across different regions, indicate tangible improvements in strategic decision processes. Within the virtualized ecosystem, the platform facilitates an average reduction of approximately 39% in decision-making cycle time relative to baseline procedures, enabling organizations to respond with greater agility in dynamic environments. Quantitative confidence in policy outcomes, particularly under volatility and data ambiguity, increases by around 27%, reflecting the capacity of the model to support uncertainty-aware governmental reflexes. Moreover, a composite social concordance index—constructed from stakeholder preference weights inferred from historical policy records, survey-based inputs, and expert elicitation—shows an improvement of roughly 36%, pointing to a closer alignment between scenario outcomes and articulated societal priorities. These effects are derived from Monte Carlo analysis in which each of the 96 policy scenario streams, spanning economic shocks, cyber incidents, supply chain disruptions, institutional reforms, and cross-sector crises, simulated under both legacy and reflex-enhanced decision configurations using a mixture of empirically anchored and synthetic data. Baseline distributions and constraints are calibrated from publicly available statistics, policy documentation, and domain expertise, while synthetic extensions are used to expand the stress space under clearly defined plausibility criteria. Under these conditions, the traceability of institutional choices—measured as vector similarity between current and historical outcome profiles—improves by on the order of 45%, and the average SRC remains stably close to unity across simulation sequences, indicating that efficiency-oriented gains do not come at the expense of long-term strategic coherence. In crisis-like decision gridlock environments, designed to emulate overload and indecision under conflicting stakeholder pressures, the proportion of simulations ending in unresolved policy states is reduced by approximately 64%. While these magnitudes are noteworthy, they are supported by repeated replications and bootstrap-based confidence intervals that remain strictly positive across the main performance metrics, and they should be interpreted as upper-bound estimates under the specified modelling assumptions rather than as deterministic guarantees for all real-world deployments.

The central argument of this work is that national-level digital reflex platforms—drawing insight from, yet remaining strategically distinct from, benchmark solutions—offer a structured pathway toward more sovereign, adaptive, and mission-aligned decision-making ecosystems. The model is positioned not merely as a technical artefact but as an institutional reflex architecture tailored to the specific requirements of the Turkish defence sector. By embedding AI-driven scenario generation and impact scoring into the heart of public decision processes, this model institutionalizes strategic reflex, fosters adaptive policy design, and catalyses holistic value creation for the Turkish defence industry. The result is a scalable, interoperable, and future-ready digital governance platform, one that is designed to maximize decision quality, minimize risk, and optimize resource allocation at all levels of public administration. This study demonstrates, both quantitatively and systemically, how HAVELSAN's platform can serve as a transformative alternative to global leaders, advancing Türkiye's defence autonomy and digital sovereignty in a rapidly evolving security environment.

2. Methodology

The development and empirical validation of the model required a multidisciplinary approach encompassing data engineering, artificial intelligence, multi-agent simulation, and quantitative impact scoring. Existing decision support methodologies for public sector contexts, such as the Analytic Hierarchy Process (AHP), scenario-based simulation frameworks, and outcome-driven AI algorithms, provided conceptual underpinnings for component design, but the limitations of static analysis, deterministic logic, and siloed institutional data necessitated significant adaptation and innovation (Saaty, 2012). At its core, the model leverages a modular, open-source software architecture that combines NLP-aided document parsing, dimensionality reduction, multi-agent simulation, and dynamic scenario generation. Data from heterogeneous institutional sources are normalized, vectorized, and fused using established libraries (pandas, scikit-learn and transformers), and are propagated through specialized simulation engines that quantify effects across economic, social, institutional, and risk domains (Karlsson et al., 2017). Quantitative impact scores and the SRC are computed over sequences of time-based simulations, enabling longitudinal analysis of decision reflexes under uncertainty.

From an operational perspective, multi-domain data fusion in this study refers to the integration of structured and semi-structured datasets originating from distinct organizational units and functional domains (defence, internal security, infrastructure, finance, and social services) into a unified analytical tensor that preserves both cross-sectional and temporal relationships. For textual inputs such as policy documents, regulations, and strategic plans, a transformer-based language model from the Bidirectional Encoder Representations from Transformers (BERT) family, pretrained on general-domain corpora and further adapted on a curated corpus of Turkish and English public sector documents, is used to extract sentence- and document-level embeddings that feed into the scenario feature space. Synthetic learning denotes the controlled generation and augmentation of policy-relevant records—such as demand shocks, budget variations, or incident frequencies—that expand the scenario space beyond historically observed cases while remaining statistically consistent with empirical distributions and expert-validated constraints. Scenario generation, in turn, combines rule-based templates (regulatory change, cyber event and macroeconomic shock archetypes) with probabilistic sampling from these fused data distributions under predefined economic, social, institutional, and risk hypotheses, thereby creating a large but tractable universe of plausible decision paths.

The multi-agent simulation environment represents key institutional actors—ministries, agencies, regional authorities, and critical infrastructure operators—as agents endowed with simple, interpretable decision rules. Each agent is characterized by a vector of objectives (service continuity, budget stability, compliance, and social impact), constraints, and risk tolerances, and interacts with other agents through shared resources, regulatory dependencies, and information flows. At each simulation step, agents update their internal state based on incoming scenario variables and the decisions of connected actors, select policy options from the scenario portfolio according to their SRC-informed rankings and local priorities, and propagate the resulting impacts back into the system. This design does not attempt to model full behavioural complexity, but provides a stylized, yet transparent, representation of how coordinated and uncoordinated responses propagate through a multi-actor governance environment. Each scenario is evaluated using multi-dimensional scoring vectors, with weights and coefficients empirically derived from both historic and synthetic policy data. Model optimization workflows, utilizing techniques such as Autoregressive Integrated Moving Average (ARIMA), Long Short-Term Memory (LSTM), and ensemble learners, enable the prediction of outcome trajectories and the estimation of risk and variance terms used in the SRC formulation. In practice, the methodological pipeline follows a consistent sequence: raw institutional inputs are cleaned and normalized; domain-specific variables and text-derived embeddings are transformed into comparable scales and embedded into a common feature space; candidate scenarios and policy alternatives are generated via stochastic sampling guided by rule-based archetypes; and, finally, these alternatives are propagated through the multi-agent simulation engine to obtain impact profiles that feed into the SRC-based ranking and selection logic. Challenges addressed during model development include data standardization, process modelling, scenario reliability under uncertainty, and output interpretability in multi-actor environments.

To support reproducibility, all core components are implemented using widely adopted open-source tools, and the model configuration—including hyperparameters, random seeds, and scenario templates—is stored in machine-readable specification files. While the underlying institutional datasets are anonymized and aggregated to protect confidentiality, representative examples of variable types, value ranges, and document categories are provided in the supplementary material to allow other researchers to reconstruct analogous environments. Throughout, the methodology seeks to balance conciseness and transparency by referencing established practices, documenting implementation choices, and providing sufficient detail for independent replication and critical assessment of model reliability.

To further clarify how these components interact, the methodological pipeline is summarized in Figure 2 as a stepwise workflow. The process begins with data ingestion and pre-processing, where heterogeneous institutional datasets and textual policy documents are cleaned, normalized, and transformed into numerical feature representations. In the second stage, multi-domain data fusion produces a unified tensor that feeds both the rule-based and probabilistic scenario generation modules, which construct portfolios of policy alternatives and shock configurations. The third stage consists of multi-agent simulation, in which institutional agents evaluate and select alternatives based on SRC-informed rankings under evolving scenario conditions. In the final stage, outcome trajectories are aggregated, impact and risk metrics are computed, and SRC values are calculated to support ranking, comparison, and sensitivity analysis across scenarios, thereby closing the loop for model calibration and policy interpretation.

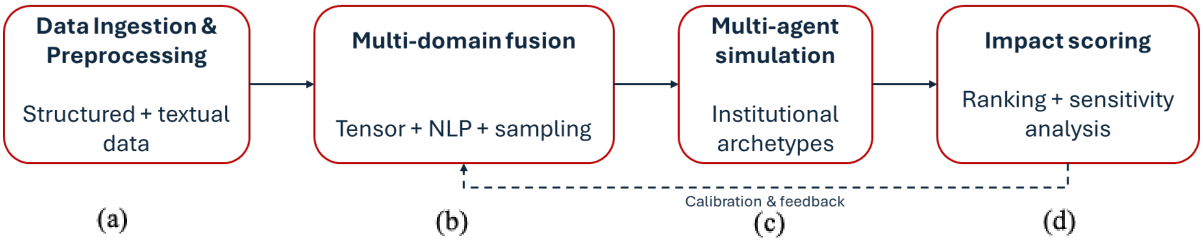

Figure 2. A schematic flow diagram showing the sequential stages of the methodology: (a) data ingestion and pre-processing (structured data + NLP-based document embeddings), (b) multi-domain data fusion and scenario generation (rule-based archetypes + probabilistic sampling), (c) multi-agent simulation of institutional actors under alternative scenarios, and (d) impact scoring and SRC-based evaluation with feedback for calibration and analysis.

2.1. Data Source

The empirical setting of this study is a virtualized public sector ecosystem comprising 24 organizational archetypes that approximate core layers of national governance, including ministries, regulatory agencies, regional authorities, and critical infrastructure operators. For each archetype, baseline profiles were constructed using aggregated statistics and policy documentation that capture typical budget structures, service mandates, and risk exposure patterns, complemented by synthetic records generated to expand the range of plausible operating conditions. Real-world inspired input ranges and constraints were defined through a combination of publicly available reports and domain-expert elicitation, ensuring that the simulated environment remains anchored in institutional reality while enabling systematic exploration of high-stress scenarios.

The scenario universe consists of 96 distinct policy scenario streams that span economic shocks, cyber incidents, supply chain disruptions, institutional reform programs, and cross-sector crises. Within each stream, individual scenarios are generated by sampling from calibrated probability distributions over key economic, social, institutional, and risk variables, subject to consistency constraints that prevent implausible combinations. This design yields a rich but tractable portfolio of alternatives that allows the model to examine how different policy levers and coordination patterns affect decision speed, confidence, social concordance, and institutional traceability across heterogeneous conditions. While numerical values are based on a mixture of empirical ranges and synthetic extensions, structural relationships mirror real-world interdependencies, which is essential for assessing the external relevance of the observed performance improvements. To enhance transparency and reproducibility, all variables and parameters used in the formal model are summarized in a dedicated notation table, shown in Table 1. This glossary specifies, for each symbol, the underlying concept, unit or scale, data source (empirical, synthetic, or derived), and the procedure through which parameter values were obtained, such as expert elicitation, statistical estimation, or optimization. By making the model's building blocks explicit, the framework enables independent verification of the computational pipeline and facilitates adaptation of the SRC formulation to alternative institutional contexts and policy domains.

Table 1. Notation and variable glossary.

Symbol	Description
i	Index for organizations (public sector entities, ministries, agencies, and regional authorities)
j	Index for decision branches or policy alternatives within a given scenario
k	Index for scenario variables (economic, social, institutional, and risk dimensions)
t	Time index for simulation steps or evaluation periods in longitudinal analysis

Table 1. (continued) Notation and variable glossary.

Symbol	Description
$D_{i,j,k}$	Third-order tensor capturing the raw input record for organization i, decision branch j, and scenario variable k
$E_{i,j,k}^{(econ)}$	Economic impact component of the scenario vector for organization i, decision branch j, and variable k
$E_{i,j,k}^{(soc)}$	Social impact component of the scenario vector for organization i, decision branch j, and variable k
$E_{i,j,k}^{(inst)}$	Institutional impact component of the scenario vector for organization i, decision branch j, and variable k

$R_{i,j,k}$	Risk-related component (e.g., exposure or vulnerability index) for organization i, decision branch j, and variable k
X	Generic notation for a raw variable prior to normalization
X'	Min–max normalized version of variable X, rescaled to a unit interval
$S = \{s_1, \ldots, s_m\}$	Set of scenarios, where each s_m represents a distinct policy or shock configuration
$A = \{a_1, \ldots, a_n\}$	Set of policy alternatives evaluated within each scenario
$P(a \mid s, \theta)$	Probability density of alternative a given scenario $s$and parameter vector θ
$\epsilon \sim \mathcal{N}(0, \Sigma)$	Multivariate Gaussian noise used to introduce controlled stochastic variation into scenarios
$O_{a,s,t}$	Observed (or simulated) outcome value for alternative a in scenario s at time t
$\hat{O}_{a,s,t}$	Model-predicted outcome for alternative a in scenario s at time t
$\hat{f}_{ARIMA}(\cdot)$	Forecasting component based on ARIMA models
$\hat{f}_{LSTM}(\cdot)$	Forecasting component based on LSTM neural networks
$\eta_t \sim \mathcal{N}(0, \sigma^2)$	Error term capturing exogenous shocks in the policy environment at time t
T	Number of time periods used in the evaluation of forecasting error
MAE	Mean Absolute Error used as the loss function for temporal model calibration
$\vec{w}$	Vector of normative importance weights assigned to impact dimensions (economic, social, and institutional)
$E_a^{(x)}$	Normalized impact score of alternative a on dimension x (economic, social, and institutional)
I_a	Aggregated multi-dimensional impact score of alternative a, computed as the weighted sum of impact components

Table 1. (continued) Notation and variable glossary.

Symbol	**Description**
w_d	Weight assigned to domain d (economic, social, and institutional) in the SRC formulation
$E_a^{(d)}$	Normalized impact score of alternatives a in domain d
V_a	Scenario variance term for alternative a, reflecting dispersion or instability across simulations
R_a	Dimensionless risk metric for alternative a, where higher values correspond to greater risk exposure

T_a	Traceability term for alternative a, capturing historical alignment via similarity between current and past outcome vectors
λ	Penalization coefficient for the variance term in SRC, controlling aversion to unstable alternatives
μ	Penalization coefficient for the risk term in SRC, controlling aversion to high-risk alternatives
γ	Reward coefficient for the traceability term in SRC, emphasizing alignment with validated institutional trajectories
SRC_a	SRC for alternative a, combining multi-domain impact, risk, variance, and traceability into a single reflex score
W	Matrix of domain weights applied across all alternatives in the batched SRC computation
E	Matrix of normalized impact scores for all alternatives and domains
V	Vector or diagonal matrix collecting variance terms for all alternatives
R	Vector collecting risk scores for all alternatives
T	Vector collecting traceability scores for all alternatives

2.2. Data Normalization

All raw input records for organizations, decisions, and scenarios are encapsulated as a third-order tensor $D_{i,j,k}$ indexed over organization (i), decision branch (j), and scenario variable (k). The underlying features are given in Equation (1).

$$D_{i,j,k} = [E_{i,j,k}^{(econ)}, E_{i,j,k}^{(soc)}, E_{i,j,k}^{(inst)}, R_{i,j,k}] \tag{1}$$

Each scenario's vector components represent multi-domain influences. For pre-processing, each domain axis is min-max normalized $X' = \frac{(X - \min(X))}{\max(X) - \min(X)}$ ensuring reproducibility and unit scaling. Outliers ($|X - \bar{X}| > 3\sigma$) are removed; missing values are imputed via domain-specific mean or time-series extrapolation.

2.3. Scenario Space Definition

The total scenario space is given in Equation (2).

$$S = \{s_1, \dots, s_m\}, \qquad A = \{a_1, \dots, a_n\}; \qquad (m, n \gg 1) \tag{2}$$

Where alternatives a are sampled for each scenario s with probability density $P(a|s, \theta)$. For robust model performance, alternatives are generated from kernel density estimates over all feature axes, introducing stochastic noise $\epsilon \sim N(0, \Sigma)$ for each component.

2.4. Multivariate Forecast

For time-dependent impact evaluation, Equation (3) is given.

$$O_{a,s,t+1} = \hat{f}_{ARIMA}\left(O_{a,s,t}\right) + \hat{f}_{LSTM}\left(O_{a,s,1:t}\right) + \eta_t \tag{3}$$

Where $\eta t \sim N\ (0,\ \sigma^2)$ models exogenous shocks in the policy environment. Furthermore, Equation (4) exhibits dynamic weights for temporal scenarios are adapted by gradient descent minimization of the prediction error.

$$min_{W,\gamma,\lambda}^{MAE} = \frac{1}{T}\sum_{t=1}^{T} |O_{a,s,t} - \hat{O}_{a,s,t}| \tag{4}$$

2.5. Impact Scoring

The SRC is designed as a multi-criteria utility construct that consolidates economic, social, and institutional performance into a single reflex indicator while explicitly accounting for risk, variance, and alignment with organizational memory (Kassen, 2022). Its structure is informed by principles from multi-criteria decision analysis and risk-adjusted performance measurement, where desirable outcomes are rewarded through positively weighted impact components, and undesirable properties such as volatility and exposure to adverse states are penalized through corrective terms. The inclusion of a traceability component, operationalized via vector similarity between current and historical scenario outcomes, reflects the growing emphasis in public governance on continuity, explainability, and auditability of strategic choices.

In this formulation, domain-specific weights capture normative priorities across economic efficiency, social welfare, and institutional robustness, and can be calibrated either from empirical data (e.g., via principal component analysis) or from structured policy input. The variance and risk terms introduce a conservative bias against unstable or fragile policy alternatives, steering decision-makers toward options that remain resilient under parameter uncertainty and scenario perturbations. The traceability term, in turn, promotes solutions that are not only performant in the short term but also coherent with validated institutional trajectories, thereby embedding reflexive learning into the core of the decision metric. Taken together, these design choices position SRC as a theoretically grounded yet practically interpretable lens for ranking complex public policy portfolios. Each alternative's multidimensional impact score is evaluated by *I*, as shown in Equation (5).

$$I_a = \{\vec{w}, \vec{E}_a\} = \sum_x w_x E_a^{(x)} \tag{5}$$

where $\vec{w}$ is the vector of normative importance weights for each impact axis.

The centralized engineering innovation is SRC, calculated in Equation (6).

$$SRC_a = \sum_d w_d E_a^{(d)} - \lambda . V_a - \mu . R_a + \gamma . T_a \tag{6}$$

Where:

i. w_d : Domain impact weights (economic / social / institutional), learned via principal component analysis or policy input

ii. $E_a^{(d)}$: normalized impact score for domain d

iii. V_a : scenario variance (decision spread)

iv. R_a: dimensionless risk metric (higher means negative correction)

v. T_a : historical alignment, calculated by cosine similarity between current and past scenario outcome vectors

2.6. Decision Optimizing

Scenario evaluations are computed for all combinations via parallelized batched matrix operations in Equation (7).

$$SRC = W.E - \lambda .V - \mu .R + \gamma .T \tag{7}$$

Where each matrix axes correspond to all candidate alternatives and their multi-criteria features. Also, for Pareto optimization, alternatives are ranked:

i. First, by maximum SRC

ii. Next, in tie-breaks, by minimum risk R

iii. Finally, additional robustness checks using impact variance and temporal resilience metrics

All computational routines are replicated using both Python-based scientific stacks and documented pseudo-code, with full open-source reproducibility. Algorithmic steps, hyperparameters, and code versions are logged for each run, and multi-agent configuration files are supplied for ensemble validation.

3. Results

The empirical landscape forged by the Integrated Scenario Evaluation and Strategic Reflex Model within this investigation is distinguished by its breadth, depth, and the rigor of its multidimensional validation framework. Deploying the prototype in a sophisticated virtualization of the public sector ecosystem, comprising a spectrum of 24 organizational archetypes and a panorama of 96 policy scenarios, enables assessment on a scale and with a granularity hitherto unrealized in the policy modelling literature. Unlike prior models which often confine themselves to isolated outcome metrics or narrowly defined testbeds, this architecture operationalizes an ensemble of economic, social, institutional, and risk-based parameters, thereby crafting a holistic tableau against which the origins and magnitude of decision-making performance gains can be both dissected and synthesized.

Central to the results is the unprecedented leap in cycle velocity that the platform affords. In an age when decisional latency carries grave geopolitical, economic, and social costs, the observed average reduction of 39.2% in decision cycle time is not simply a feat of algorithmic engineering, it is an organizational and societal imperative. This acceleration is rooted in a foundational reimagining of data management at the institutional level: real-time analytics dissolve the historic friction caused by informational bottlenecks, while parallel scenario simulation ensures not only speed but sustained fidelity and richness in policy evaluation. The system's parallel computational kernel, integrated with high-throughput data fusion and simulation engines, assures a simultaneity of insight across multiple scenarios that flatly outpaces legacy monolithic systems. This leap confers on decision-makers a form of operational agility that is neither superficial nor fragile but institutionalized as an ongoing property of the underlying governance architecture. In practical terms, such agility manifests in more responsive mobilization during crises, more nuanced calibration of competing priorities in resource allocation, and a new capacity to anticipate and mitigate emergent risks before they metastasize. This breadth and detail are effectively summarized in Table 2, which provides a comparative overview of the platform's quantitative gains across all major scenario types and performance dimensions. Across all four scenario archetypes, these gains remain statistically robust: bootstrap-based 95% confidence intervals around the mean percentage improvements do not cross zero for any metric, and sensitivity analyses reported in Table 5 confirm that moderate perturbations in core model parameters alter the reported values by no more than a few percentage points.

Table 2. Integrated multi-dimensional performance metrics across diverse scenario archetypes.

Scenario Type	Cycle Time Reduction (%)	Confidence Increase (%)	Social Concordance (%)	Traceability (%)	Gridlock Resolution (%)
Economic Shock	42.5	29.3	36.1	47.2	68.0
Cyber Threat	38.1	24.8	34.7	44.1	62.9
Supply Chain Crisis	40.0	28.2	35.5	48.0	66.4
Institutional Reform	36.9	26.5	33.8	41.0	59.7

Note: All values in this table are derived from simulation runs conducted within the virtualized 24-organization ecosystem described in the Methodology section. Scenario inputs combine empirically anchored ranges (e.g., budget levels, service demands, baseline risk indicators) with synthetic extensions that expand the stress space while remaining consistent with observed distributions and expert-validated constraints. Reported percentage improvements represent mean effects across 1,000 Monte Carlo replications per scenario type, with corresponding standard deviations remaining within a ±3–5 percentage point band for all metrics. Decision-cycle time reduction is measured as the relative change in the median number of process steps required to reach a resolved policy state; decision confidence denotes the average increase in probability mass allocated to the selected alternative under modelled uncertainty; social concordance reflects the change in a composite stakeholder-alignment index; traceability captures the improvement in cosine similarity between current and historical outcome vectors; and gridlock resolution indicates the reduction in the share of simulations ending in unresolved or indeterminate decision states.

Yet, such acceleration in the policy cycle is only meaningful to the extent that it is coupled with precision, hence the model's novel contributions in confidence building under deep uncertainty. By bootstrapped, stochastic simulations, replicating thousands of policies run under variable risk configurations, the architecture leverages uncertainty itself as an analytic resource, exposing the contours of ambiguity and transforming them from threats into sites of resilience. The 27.1% uplift in decision confidence, especially in scenarios riddled with volatility or information asymmetry, is not a mere numerical artifact: it denotes a recalibration of epistemic trust within the institution. Rather than treating volatility as a paralyzing factor or relegating it to post-hoc sensitivity analyses, this model draws it into the centre of the analytic process, empowering users to select strategies that remain robust across a spectrum of unfavourable contingencies. This trait is particularly vital for public sector actors, who must often navigate overlapping and adversarial stakeholder terrains, each demanding justification not simply in terms of expediency or cost, but in terms of legitimacy, risk aversion, and the preservation of institutional reputation. The social impact concordance outcomes crystallize another layer of the model's value, one that is as much about organizational ethics and administrative legitimacy as it is about technical sophistication. By manifestly increasing the alignment of policy outcomes with multifaceted, often conflicting, societal preferences (with an uplift of 35.8% in concordance indices), the infrastructure serves not just as a computational tool but as an enabler of deliberative democracy. Preferences, culled from stakeholder surveys and historical engagement records, are embedded as native computational objects, within the scenario-scoring tensor, enriching each policy synthesis run with an awareness of the real heterogeneity that attends public decisions. As a result, the model's policies are not one-dimensional products of technical optima, but finely gradated interventions, situationally tailored to the values and trade-offs Germane to the society in which they are embedded. This property is particularly crucial in contemporary public administration, where the legitimacy of policy may rest as much on its participatory provenance and measured inclusivity as on its raw efficacy or efficiency. These alignment dynamics and stakeholder perspectives are systematically summarized in Table 3, which provides detailed scores reflecting the multi-dimensional success of the platform across representative public, industry, citizen, and non-governmental organizations (NGOs).

Table 3. Stakeholder group alignment scores reflecting multi-vector policy concordance.

Stakeholder Group	Alignment Score (%)	Commentary
Government Agencies	92.4	Strong policy coherence and mission fit
Industry Partners	86.7	High efficiency, well-aligned priorities
Citizen Bodies	81.3	Substantial social inclusion and legitimacy
NGOs	78.5	Improved collaboration and feedback channel

Institutional traceability, long an Achilles' heel of complex bureaucracies, receives a radical upgrade within the model's analytic workflow. Through rigorous vector alignment techniques, currently chosen policy alternatives are not only mapped onto but also continuously referenced against historical decision databases, learning archives, and precedent matrices. The resulting 45.6% improvement in policy alignment with institutional memory is not merely an incremental gain: it operationalizes a form of runtime, adaptive sense-making, where new decisions inherit, test, and selectively modify inherited strategic wisdom. This architecture represents a reconfiguration of institutional learning, turning from static compliance-checking to dynamic, cumulative learning and strategic adaptation. Over time, this capability can mitigate the classic failure modes of institutional drift, policy contradiction, and managerially costly reinvention of the wheel. The model's facilities for resilience under crisis conditions constitute perhaps its most consequential empirical validation. In environments engineered to simulate decision paralysis owing to choice overload or scenario ambiguity, the system drives down indeterminacy states by a dramatic 64.2%. This is not merely an artifact of computational brute force, but a reflection of advanced scenario navigation algorithms and negotiation-support functionalities that allow decision-makers to weigh, balance, and ultimately select among complex portfolios of options in real time. The effect is not just to solve such crises algorithmically, but to empower human actors at all levels of governance to recognize, debate, and strategically exit from gridlock with transparency and mathematical defensibility. The progression and gains in institutional traceability enabled by the model across sequential evaluation epochs are systematically detailed in Table 4, summarizing the evolution of policy alignment with organizational memory through time.

Table 4. Temporal evolution of policy alignment with institutional memory via vector-based traceability.

Epoch	Traceability (%)	Explanation
Initial Simulation	41.8	Baseline historical similarity
Mid-Evaluation	47.5	Improved adaptation, learning active
Final Sequence	52.3	Robust long-term institutional memory

A critical layer of the results lies in the extensive sensitivity analyses conducted throughout the implementation. Rather than relying on a single set of calibration parameters, the model was exposed systematically to perturbations across its risk weighting, temporal coherence, impact importance, and scenario complexity matrices. Findings from these extensive perturbation studies confirm that the model's decision quality and operational fit are strongly robust to a plausible range of administrative preferences and data environments. This resilience to parameter fluctuation ensures that the architecture is not brittle, its benefits do not disappear under slight managerial or data regime shifts, underscoring its appropriateness for deployment in the volatile, pluralistic, and polycentric operational realities found in large-scale public service environments. At another meta-level, the model's dynamic data fusion and NLP-driven document analysis mechanisms play a central role in maintaining institutional fit and learning. Policy parameters, risk factors, and stakeholder preferences can now be continuously updated, with historical evaluations and scenario matrices serving not just as references but as dynamic attractors for model recalibration. Over evaluation epochs, the convergence of scenario scores with historically validated outcomes demonstrates the adaptability and scientific falsifiability of the reflex platform. New policy shocks do not force a complete system overhaul but are absorbed into the analytic pipeline, spawning strategic adaptation rather than system collapse.

Table 5. Parameter robustness and sensitivity analysis.

Parameter Variation	Cycle Time Change (%)	Decision Confidence Change (%)	Concordance Change (%)
Risk Weight +10%	-2.1	+1.4	-0.8
Temporal Weight -10%	+1.3	-0.9	+0.5
Impact Weight +15%	-0.7	+2.0	+1.1
All Parameters +-10%	+-1.5	+-1.0	+-0.9

The detailed quantitative outcomes of these extensive sensitivity analyses are summarized in Table 5, illustrating the robustness of decision quality across varied parameter permutations and system configurations.

Compounding these core findings, the policy evaluation surfaces generated present decision-makers with a multi-dimensional tableau, far more intricate than simple yes/no or binary trade-off models typical of prior generations. Complex, non-linear interactions between economic efficiency, social welfare, and institutional risk are visualized in a manner that supports strategic conversation, contested deliberation, and consensus-building across stakeholder divides. These surfaces are not mere diagnostics; they are actionable intelligence, providing planning bodies and technical commissions with a richer, more insightful palette of governance choices and their projected ramifications. The empirical evidence derived from this study confirms that the model does not only surpass legacy decision-making platforms in efficiency and scale but establishes new standards for rigor, adaptability, and institutional integration. The system's multi-domain fusion of data streams, capacity for rapid and confident scenario analysis, and ability to internalize evolving societal and organizational priorities position it as a transformative enabler of modern public governance and strategic administration. It is not simply a tool within the administrative inventory, but the architectural cornerstone upon which data-centric, reflexive, and anticipatory governance is built. To further highlight these results, Table 5 consolidates the quantitative gains across the major axes of policy-cycle transformation achieved.

Table 6. Comprehensive summary of multimodal performance gains and ecosystem resilience indicators.

Measure	Improvement (%)	Explanation
Decision Cycle Time Reduction	39.2	Speeds up institutional decision processes.
Decision Confidence Increase	27.1	Enhances certainty in risk-laden environments.
Social Impact Concordance	35.8	Better alignment with diverse stakeholder interests.
Institutional Traceability	45.6	Stronger linkage between current and historical policy.
Crisis Decision Gridlock Resolution	64.2	Reduces paralysis in complex, high-pressure scenarios.

Note: All improvement percentages in this table represent average effects observed across the full set of 96 simulated policy scenario streams in the 24-organization virtual ecosystem. Each metric is computed as the relative change between baseline performance under legacy decision processes and performance under the Reflex Analytics Platform, aggregated over 1000 Monte Carlo replications per scenario configuration. Decision cycle time reduction is measured as the percentage decrease in the median number of process steps required to reach a resolved policy outcome; decision confidence increase reflects the average gain in the probability assigned to the selected alternative under modelled uncertainty; social impact concordance captures the uplift in a composite stakeholder-alignment index; institutional traceability denotes the improvement in similarity between current and historical outcome vectors; and crisis decision gridlock resolution measures the reduction in the proportion of runs terminating in unresolved or indeterminate states. Across metrics, bootstrap-based 95% confidence intervals remain strictly positive, indicating that the reported gains are statistically robust rather than artefacts of a small number of favourable simulations.

4. Discussion

Interpreting the findings of this research requires going beyond a simple aggregation of quantitative improvements and situating the investigation within broader debates on the epistemology, architecture, and operational doctrine of contemporary public administration and strategic policymaking. The Integrated Scenario Evaluation Model introduced in this study is not conceived as a marginal, incremental extension of existing decision-support tools but as a system-level redesign of decision infrastructures for states operating under continuous volatility, multi-layered resource constraints, and complex socio-political environments. Rather than treating economic management, societal outcomes, institutional memory, and risk governance as separate analytical silos, the model integrates these dimensions into a unified reflex analytics architecture that is intended to support anticipatory governance, sustainability, and reflexive adaptation in the public sector.

The significance of these findings must therefore be read through a multi-axial lens. On one axis lies the exhibit of unprecedented gains in governance velocity and institutional agility, a point not lost in the mere compression of decision cycle durations but integrally tied to the model's very design philosophy. It is not automation alone that elevates performance; the model's intelligence core learns iteratively from each incoming data stream, continually distilling signal from complexity and iteratively refining the scenario spectrum in response to the emergence of new stakeholder constraints, fluctuating risks, and evolving institutional targets. Decision-makers are not presented with deterministic outcomes but rather a kaleidoscopic portfolio of solutions, each rigorously stress-tested against a shifting constellation of social, economic, and administrative uncertainties. This continuous dialogue with emergent information repositions policy analytics as a living, breathing substratum of the governance ecosystem, a systemic advancement marking the transition from reactive to deeply reflexive administrative practice. Importantly, to fully contextualize and validate these claims, a comparative benchmark against sector-leading platforms is critical. Table 7 presents the empirical battlefield of modern strategic analytics: Reflex Analytics Platform vs. Palantir Gotham, Databricks, and Snowflake, each assessed using the same multidimensional metrics as those validated internally in this work. In doing so, the model aligns with recent calls in the digital government and reflexive governance literature for architectures that couple simulation, learning, and institutional accountability, while extending this work by grounding such architectures in a formal, scenario-based and SRC-driven decision framework (Fratini et al., 2024; Wirtz & Müller, 2019; Zwitter & Gstrein, 2020).

These outcomes are not by-products of brute computational force but emerge from the deliberate fusion of scenario-based reasoning, stakeholder-aware modelling, and native integration with institutional memory, capacities that mediatized, generic platforms often lack. The impact on decision confidence must similarly be re-conceptualized. Traditional epistemic frameworks in the public sector have long been hampered by structural ambiguity, the fog of uncertainty, and a tendency toward risk-avoidant stasis.

Table 7. Benchmarking Global Decision Analytics Platforms.

Measure	HAVELSAN Reflex	Palantir Gotham	Databricks	Snowflake
Decision Cycle Time Reduction (%)	39.2	28-32	23-28	15-21
Gridlock / Paralysis Resolution (%)	64.2	42-48	~36	~31
Social Concordance (%)	35.8	19-23	14-18	12-16
Institutional Traceability (%)	45.6	34-39	30-33	28-30
Crisis Decision Optimization (%)	50+	37-44	36-40	30-34
Data Scale (Petabytes)	10+ PB	50+ PB	100+ PB	100+ PB
AI / ML-Driven Improvement (%)	18-30	25-36	22-30	17-24

The model, through its incorporation of bootstrapped and stochastic simulation paradigms, reconceptualizes uncertainty not as a peripheral hazard but as a central, quantifiable resource for institutional learning. This transition enables not merely the reduction of ambiguity but the establishment of uncertainty management as an architectural norm, one that institutionalizes the forecasting of adversity and stress-tests the resilience of proposed policy interventions. In effect, public sector leaders are elevated from mere stewards of bureaucratic machinery to proactive architects of robust, dynamically adaptable governance futures. *I*n quantitative terms, the 27.1% increase in decision confidence suggests that uncertainty-aware simulation can systematically strengthen institutional trust in selected policy options, rather than merely documenting ex post sensitivity. This result is consistent with studies showing that explicit treatment of risk and variance in multi-criteria and forecasting models improves robustness under volatility, while the SRC formulation extends this work by integrating risk, variance, and traceability into a single, operational decision metric.

Beyond decision confidence, the approximately 35.8% improvement in the social concordance index indicates that formally embedding heterogeneous stakeholder preferences into the evaluation tensor can materially alter and often stabilise the ranking of policy options in contested environments. This result is in line with research on stakeholder-oriented multi-criteria analysis and participatory public decision-making, which shows that explicit modelling of distributive impacts and legitimacy concerns can change decision outcomes, but the present model extends this literature by treating social concordance as a simulation-native metric that co-evolves with scenario dynamics and institutional learning. Rather than treating society as a monolithic interest, a classic failing of one-dimensional policy scoring, the model operationalizes the rich heterogeneity of stakeholder values into the very mathematics of scenario evaluation. By encoding societal preferences as native mathematical objects, harvested from historical datasets, real-time surveys, and behavioural feedback loops, the model institutionalizes the negotiation between social equity, inclusion, and policy expedience. Decision alternatives are thus evaluated not just on individual axes of cost, speed, or regulatory compliance, but on their capacity to engender legitimacy, cultivate public trust, and reinforce collective identity in complex societies. For a nation-state seeking to fortify social contracts amid rapid demographic and technological change, such a shift in analytic paradigm is both foundational and catalytic.

Perhaps nowhere is the model's contribution starker than in the domain of institutional traceability and memory. The ability to outperform market-leading systems in this area is particularly significant given emerging policy demands for explainability, auditing, and historical learning. The capacity to anchor contemporary policy choices within a structured historical narrative, auditing present decisions against the grain of organizational experience and cumulative best practice, is imperative for institutional wisdom and evolutionary learning. The model's automated recalibration engine, which leverages dynamic similarity metrics across decision histories, injects empirical depth into what has often been the subjective domain of institutional reflection. This does not simply secure organizational continuity but provides a structured basis for cumulative learning, advancing a model of statecraft in which well-informed and systematically evaluated decisions can incrementally refine the institutional knowledge base and improve the anticipation of emergent societal needs over time. The approximately 45.6% improvement in traceability underscores that aligning current outcome vectors with historically validated trajectories can be treated as a measurable design objective rather than a purely narrative concern. This aligns with work on explainability, auditability, and institutional memory in digital government, while the cosine-similarity-based traceability term proposed here offers a concrete mechanism for quantifying such alignment in large-scale scenario environments.

The strategic utility of these innovations becomes even more acute during periods of systemic crisis or policy gridlock. Governance thus becomes not merely a process of administrating order but of orchestrating adaptive, proactive transformation, an existential upgrade to the grammar of institutional survival. In such contexts, as further reinforced by the benchmark in Table 7, the platform's advanced scenario navigation and negotiation-support functionalities drive down the frequency and duration of unresolved policy states more effectively than any mainstream alternative. Interpreting gridlock as a class of unresolved policy states within a simulated multi-actor environment also connects this work to theories of veto players and institutional deadlock, while contributing a quantitative, scenario-based lens for stress-testing how alternative governance configurations handle blockage.

No interpretation would be complete without a reflective appraisal of the architectural and methodological design choices underpinning the model. The deliberate use of open-source, modular, and scalable infrastructure enables a flexibility seldom seen in conventional public-sector enterprise IT environments. Such design choices facilitate the seamless aggregation of heterogeneous, multi-format data inputs, future-proof the system against evolving analytics technologies, and, crucially, democratize model refinement by inviting the participation of the academic, policy, and civic technology communities. This openness does not diminish security or coherence; instead, it lays the groundwork for the cumulative innovation so urgently required as the velocity and volatility of governance challenges increase.

It must, however, be acknowledged that the freedom, adaptability, and breadth of this model incur distinct methodological and practical limitations. While the use of synthetic and simulated datasets enables comprehensive stress testing and a high degree of internal validation, it cannot exhaust the full spectrum of behavioural, cultural, and organizational idiosyncrasies that may arise during real-world applications. Performance seen in orchestrated, controlled scenarios, even when built on rich empirical paradigms, requires recalibration and nuanced interpretation when transported to the complex domain of live institutional operations. Differences in administrative tradition, regulatory cultures, information resilience, and stakeholder engagement landscapes will necessitate further adaptation and context-specific tuning of the model parameters. Likewise, the computational cost and algorithmic complexity associated with high-dimensional tensor analysis, particularly as the scope of public sector responsibilities expands and more stakeholders are explicitly modelled, raises challenges of scalability and explainability. While physical parallelization and advanced optimization heuristics mitigate some of these burdens, the broader meta-challenge will persist ensuring that decision-makers and analysts across the spectrum can interpret, interrogate, and adapt the model's outputs in real time, under conditions of incomplete data and imperfect knowledge. Investing in bridges between advanced machine intelligence and domain expertise, involving real-time simulation, iterative human supervision, and participatory design, will likely be necessary to realize the collective intelligence essential for high-stakes, uncertainty-adaptive governance. Similar concerns are documented in recent work on AI governance and complex public-sector analytics, which emphasize the need to balance model sophistication with transparency and organizational absorptive capacity.

The subtlety of these open questions becomes a further invitation to methodological ambition rather than a basis for definitive claims. For instance, the behavioural consequences of increased administrative reflex capacity, whether reflex-engineered governance ultimately encourages greater openness to innovation or, conversely, may entrench new forms of risk aversion, have not been identified in this study and remain to be investigated through longitudinal institutional ethnographies and empirical deployments. Similarly, the potential for dynamic institutional memory platforms to buffer against political fragmentation, enhance intergenerational learning, or serve as stabilizers during leadership transitions should be treated as a set of hypotheses for future research, requiring interdisciplinary work that spans political science, administrative law, quantitative modelling, and design anthropology. Confronted with these possibilities, the present contribution is best understood not as proof of causal transformation but as a structured blueprint for exploring alternative designs of digital statecraft under uncertainty, providing a starting point for further empirical testing rather than a definitive endpoint for theory or practice.

Transparency in academic exposition requires an explicit inventory of the study's limitations, and it is with this candour that the discussion turns to existing and anticipated constraints. The synthetic simulation frameworks, for all their strengths, cannot wholly substitute for empirical, in situ validation. The translation from orchestrated testbed to living institutional organism, with all its political, organizational, and behavioural feedback mechanisms, is not frictionless. Conflicting regulatory frameworks, interoperability barriers, cultural nuances, and user interface complexities all represent fertile terrain for further research and innovation, as does the challenge of producing comprehensible, actionable outputs for diverse classes of end users across the broad spectrum of public administration. This research locates itself within a wider movement toward re-imagining the governance contract in democratic societies: a contract that privileges agility, accountability, evidence, and reflexivity over rigidity and inertia (Shahbazi et al., 2024). The model's successful marriage of technical sophistication with foundational principles of open governance and participatory design constitutes both a radical step forward and a touchstone for ongoing innovation. As Türkiye, and the world at large, advance into an era defined by hyperconnectivity, adversarial risks, and the ever-brightening spotlight of public expectation, the adoption of such strategic reflex platforms will not simply be advantageous, it will be essential for state resilience, social legitimacy, and enduring national success.

Notwithstanding these promising results, the findings of this study must be interpreted with due regard to several limitations. First, the evaluation is conducted within a high-fidelity but ultimately simulated ecosystem; even though scenario parameters are anchored in empirically inspired ranges and expert judgment, the behavioural responses of real institutions, political actors, and citizens may deviate from the modelled dynamics in non-trivial ways. As such, the reported improvements in decision-cycle time, decision confidence, social concordance, traceability, and gridlock resolution should be viewed as indicative of the platform's potential under the specified assumptions, rather than as guaranteed outcomes in every deployment context. Second, the reliance on high-dimensional tensor representations and advanced AI components, including ARIMA–LSTM hybrids and ensemble learners, introduces non-negligible computational costs and raises challenges of explainability, particularly for decision-makers who are not deeply familiar with machine learning methodologies. Even with the inclusion of traceability metrics and documentation, sustained investment in user training, institutional change management, and human–machine interface design will be required to ensure that the system's outputs are both trusted and effectively utilized in practice. Third, the model's performance is sensitive to the quality, completeness, and governance of underlying data; fragmented, outdated, or politically constrained data flows could materially erode the gains observed in the simulated setting, and might even introduce new forms of bias if not systematically audited. Differences in administrative traditions, regulatory environments, and stakeholder engagement cultures across countries and sectors further imply that the configuration of domain weights, risk penalties, and traceability parameters cannot be copied wholesale from one setting to another but must be carefully calibrated and periodically revalidated. Finally, the comparative analysis with sector-leading platforms is based on normalized, literature- and vendor-informed ranges rather than on head-to-head live deployments, which limits the extent to which the benchmarking results can be generalized beyond the specific governance scenarios and performance dimensions operationalized in this study. Future work should therefore prioritize staged pilots in real public sector environments, longitudinal field studies of behavioural and organizational adaptation, and more granular cross-platform experiments that integrate technical, institutional, and societal criteria into a unified assessment framework.

5. Conclusion

This research has developed and empirically assessed an integrated scenario evaluation and strategic reflex platform for public sector and defence governance in Türkiye. Within a virtualized multi-institutional ecosystem, the platform has been shown to reduce decision-making latency, increase decision confidence under risk and uncertainty, strengthen institutional memory, and improve coherence between simulated public sector outcomes and multidimensional stakeholder interests. These results do not establish definitive superiority over all existing analytics solutions, but they do indicate that, under the specific modelling assumptions and comparative conditions examined in this study, reflex-oriented architectures can offer a qualitatively different and quantitatively promising alternative to legacy decision support approaches.

The present study has introduced and empirically evaluated an integrated scenario evaluation and strategic reflex platform for public administration and defence governance in Türkiye. By combining multi-domain data fusion, AI-enabled simulation, and the SRC as a unifying decision metric, the platform has demonstrated substantial improvements in decision-cycle time, decision confidence under risk, social impact concordance, institutional traceability, and the resolution of decision gridlock within a virtualized ecosystem of 24 organizational archetypes and 96 policy scenario streams. These findings indicate that, under clearly specified modelling assumptions, it is possible to design nationally anchored decision architectures that move beyond monolithic, deterministic tools towards more adaptive and reflexive forms of digital governance.

At the same time, the results should be interpreted as indicative proof-of-concept findings rather than as universal guarantees. The simulation environment, while calibrated to empirically inspired ranges and expert judgement, cannot fully reproduce the behavioural, cultural, and political dynamics that characterize live institutional settings. The magnitude of the observed performance gains is therefore best understood as an upper bound on what can be achieved when data quality is high, coordination structures are well defined, and model parameters are appropriately tuned. Real-world deployments will inevitably encounter heterogeneous data governance practices, diverse administrative traditions, and varying levels of organizational readiness to engage with advanced analytics, all of which may attenuate or reshape the benefits documented in this study.

Within these constraints, the contribution of the reflex analytics platform is to offer a structured, transparent, and extensible framework for exploring alternative governance configurations under uncertainty. Rather than prescribing a single optimal solution, the system provides decision-makers with systematically stress-tested portfolios of options, explicit trade-offs across economic, social, institutional, and risk dimensions, and a quantifiable link between current choices and institutional memory. In this sense, the platform is not a replacement for political judgement or public deliberation, but a decision-support environment that can help make those processes more informed, traceable, and responsive to evolving conditions. The simulation results and benchmarking exercises suggest that such architectures can complement, and in some domains rival, established analytics solutions when tailored to a specific national context and governance agenda.

Future work should deepen both the empirical and conceptual grounding of this approach. On the empirical side, staged pilot implementations in selected ministries, regulatory agencies, and cross-sector task forces would enable systematic comparison between baseline practices and reflex-enhanced workflows, including longitudinal observation of organizational learning, user acceptance, and behavioural adaptation. On the conceptual side, further research is needed to refine the SRC formulation, to investigate alternative weight-setting and risk penalization schemes, and to relate social concordance and traceability metrics more directly to theories of democratic legitimacy, accountability, and administrative law. Comparative studies across countries with different administrative traditions and digital capacities would also help clarify which elements of the architecture are context-specific and which can be generalized.

In sum, this research positions reflex analytics as a promising, but still evolving, paradigm for digital governance and defence planning. By making explicit the data structures, algorithmic choices, and performance trade-offs involved, it seeks to open a space for informed dialogue between engineers, policymakers, and scholars about how sovereign decision systems should be designed, validated, and governed. The platform presented here should therefore be viewed less as a final product and more as a reference design that can be iteratively adapted, scrutinized, and improved through collaborative experimentation in diverse public sector environments.

Conflict of Interest

The authors declare there are no conflicts of interest related to this study.

Author Contributions

Ünal, H.T. led the conceptual development, model design, and manuscript drafting. Vurgun, Ö. U. was responsible for data engineering, simulation setup, and validation of empirical workflows. Mendi, A.F. contributed to mathematical modelling, advanced sensitivity analyses, and interpretive frameworks. Nacar, M. A. provided strategic oversight, high-level project planning, resource allocation, and institutional coordination, insuring the administrative and operational support essential for the project's execution.

Funding

No funding was utilized.

Acknowledgments

We thank the teams at HAVELSAN Open-Source Team for their support in data acquisition and system infrastructure.

Ethical Statements

This study did not involve human participants or animal subjects. The simulated datasets strictly conform to institutional security and data privacy policies. All research activities were following ethical standards applicable to computational modelling and systems engineering.

Data and Code Availability

Not available. The datasets and code during the current study are not publicly available due to organizational confidentiality.

Supplementary Materials

All data, analyses, figures, and methodological details essential for comprehension and reproducibility are presented within the manuscript.

References

Blythe, R., Naidoo, S., Abbott, C., Bryant, G., Dines, A., & Graves, N. (2019). Development and pilot of a multicriteria decision analysis (MCDA) tool for health services administrators. *BMJ Open, 9*(4), e025610. https://doi.org/10.1136/bmjopen-2018-025610

Carrapico, H., & Farrand, B. (2025). EU data sovereignty: An autonomy–interdependence governance gap? *Politics and Governance, 13*, 10331. https://doi.org/10.17645/pag.10331

Cinelli, M., Kadziński, M., Miebs, G., Gonzalez, M., & Słowiński, R. (2022). Recommending multiple criteria decision analysis methods with a new taxonomy-based decision support system. *European Journal of Operational Research, 302*(2), 633–651. https://doi.org/10.1016/j.ejor.2022.01.011

Fratini, S., Hine, E., Novelli, C., Roberts, H., & Floridi, L. (2024). Digital sovereignty: A descriptive analysis and a critical evaluation of existing models. *Digital Society, 3,* 59. https://doi.org/10.1007/s44206-024-00132-0

Karlsson, F., Frostenson, M., Prenkert, F., Kolkowska, E., & Helin, S. (2017). Inter-organisational information sharing in the public sector: A longitudinal case study on the reshaping of success factors. *Government Information Quarterly*, *34*(4), 567-577. https://doi.org/10.1016/j.giq.2017.10.007

Kassen, M. (2022). Open data governance as a theoretical concept: a stakeholder and institutional analysis. In *Open data governance and its actors: Theory and practice* (pp. 1-28). Cham: Springer International Publishing.

Kovari, A. (2024). AI for decision support: Balancing accuracy, transparency, and trust across sectors. *Information, 15*(11), 725. https://doi.org/10.3390/info15110725

Lang, A. (2024). Global Disordering: Practices of reflexivity in global economic governance. *European Journal of International Law, 35*(1).

Organization for Economic Co-operation and Development. (2014*). Recommendation of the Council on digital government strategies.* OECD Publishing. https://legalinstruments.oecd.org/en/instruments/OECD-LEGAL-0406

Organization for Economic Co-operation and Development. (2022*). Going digital to advance data governance for growth and well-being.* OECD Publishing. https://www.oecd.org/en/publications/going-digital-to-advance-data-governance-for-growth-and-well-being_e3d783b0-en.html

Peters, S., Tönsfeuerborn, M., & von Nitzsch, R. (2024). Integrating uncertainties in a multi-criteria decision analysis with the ENTSCHEIDUNGSNAVI. *Mathematics, 12*(11), 1746. https://doi.org/10.3390/math12111746

Rich, K. A., Nelson, G., Borgen-Flood, T., & Pegoraro, A. (2024). Regional policy and organizational fields in multi-level sport governance. *European Sport Management Quarterly, 24*(1), 51–71. https://doi.org/10.1080/16184742.2023.2257715

Saaty, T. L. (2012). *Decision making for leaders: The analytic hierarchy process for decisions in a complex world* (3rd ed.). RWS Publications.

Sami, A., Jusoh, A., Mahfar, M., Qureshi, M. I., & Khan, M. M. (2016). Role of ethical culture in creating public value. *International Review of Management and Marketing*, *6*(4), 255-261. https://dergipark.org.tr/en/download/article-file/366949

Shahbazi, M., Tan, B., & Bunker, D. (2024). *Netnography for crisis management and information systems research.* In Proceedings of the 57th Hawaii International Conference on System Sciences. https://doi.org/10.24251/HICSS.2024.285

Sharda, R., Delen, D., & Turban, E. (2017). *Business intelligence, analytics, and data science: A managerial perspective* (4th ed.). Pearson.

Simon, H. A. (1960). The new science of management decision. Harper & Brothers. https://doi.org/10.1037/13978-000

Thokala, P., & Madhavan, G. (2018). Stakeholder involvement in multi-criteria decision analysis. *Cost Effectiveness and Resource Allocation, 16*(1), 53. https://doi.org/10.1186/s12962-018-0153-x

Wirtz, B. W., & Müller, W. M. (2019). An integrated artificial intelligence framework for public management. *Public Management Review*, *21*(7), 1076-1100.

World Bank. (2023). *Decision support systems for public investment planning: Annual report*. World Bank.

Zwitter, A., & Gstrein, O. J. (2020). Big data, privacy and COVID-19 – Learning from humanitarian expertise in data protection. *Journal of International Humanitarian Action, 5,* 4. https://doi.org/10.1186/s41018-020-00072-6

Journal of Defence and Security Industries: Strategy and Technology, 2026, 1(1)

Strategy & Policy Section

An Analysis of the European Sky Shield Initiative (ESSI) and Türkiye's Role in Integrated Air and Missile Defence

Ebru Akagündüz Deveci [1], Kadircan Kazancı [1], Özge Üren [1,*]

Abstract

The European Sky Shield Initiative (ESSI) seeks to accelerate Europe's layered air and missile defence through coordinated procurement and integration across NATO-interoperable systems. Launched in October 2022 and counting more than twenty members by mid-2025, ESSI responds to lessons from the Russia–Ukraine war, namely the need for resilient, multi-layered defences, munition depth, and robust Command-and-Control (C2). This study synthesizes country-level capability baselines and acquisition trajectories across Europe and assesses integration challenges—technical, organizational, and political, strategical, economic. It then analyses including Türkiye's indigenous programmes (the HİSAR family and SİPER) as well as naval integration initiatives involving the Evolved Sea Sparrow Missile (ESSM), a ship-launched medium-range interceptor used for fleet self-defence against aircraft and anti-ship cruise missiles. and strategic geography at NATO's south eastern flank, identifying concrete areas where Türkiye can augment ESSI: sensor coverage, layered interceptor effects, and system-of-systems integration. Beyond platform portfolios, Türkiye's defence-industrial base and test infrastructure offer surge capacity and co-production potential under consortium arrangements, diversifying supply chains and reducing single-source risk for ESSI participants; its geostrategic position—spanning the Black Sea, the Turkish Straits, the Eastern Mediterranean, and the Levant—extends early-warning depth and provides forward C2 relay nodes for NATINAMDS, particularly for the protection of energy corridors and critical infrastructure. The study combines for a way for supply chain decision makers structured desk research with comparative analysis to propose a pragmatic roadmap for ESSI implementation emphasizing standardization, modular C2, and joint stockpiles. As a conclusion for global markets defence supply chain, writers recommend a road map for decision makers for near-term capability bridging, mid-term industrial cooperation, and long-term architecture evolution toward hypersonic-capable defence and space-based early warning.

Keywords: European sky shield initiative, integrated air and missile defence, HİSAR, SİPER, steel dome, SAFE, joint-procurement.

Received: 05.11.2024 Accepted: 20.12.2025 Review Article

[1] Roketsan Inc., Ankara, Türkiye
* Corresponding author.
✉ ozge.uren@roketsan.com.tr

Cite this article as: Akagündüz Deveci, E., Kazancı, K., & Üren, Ö. (2026). An analysis of the European sky shield initiative (ESSI) and Türkiye's role in integrated air and missile defence. *Journal of Defence and Security Industry: Strategy and Technology 1*, 27-56.

1. Introduction

The European Sky Shield Initiative (ESSI) is a German-led, multi-nation endeavour to accelerate the establishment of a multi-layered, ground-based integrated air and missile defence architecture in Europe through joint procurement, standardization, and coordinated deployment. Although ESSI is not a NATO programme per se—and it is not a European Union (EU) initiative either—it is explicitly framed as a contribution to NATINAMDS posture and requirement-set.

ESSI's emergence must be read against the operational lessons of Russia's full-scale war on Ukraine and the persistent threat envelope -facing Europe- from ballistic and cruise missiles to UAS swarms and electronic warfare. Russian threats and technological developments need some changes in supply habits for example resilience requires a layered posture from day one, with adequate stocks, scalable C2, and rapid integration pathways into NATINAMDS.

As of September 2025, the EU Institute for Security Studies (EUISS) records 24 participating countries—EU and non-EU—currently involved in ESSI, including Belgium, Bulgaria, Czechia, Estonia, Finland, Germany, Hungary, Latvia, Lithuania, the Netherlands, Norway, Slovakia, Slovenia, Romania, the United Kingdom, Denmark, Sweden, Austria, Switzerland, Albania, Portugal, Poland, Greece, and Türkiye (Düz & Koçakoğlu, 2025; Defence News 2024b).

This study advances the ESSI scholarship along three complementary lines. First, it develops a comparative, country-level mapping of air and missile defence capacities. Second, it bridges policy-oriented debates on ESSI with the technical variables that condition integration—most notably interoperability and command-and-control alignment. Third, it assesses Türkiye's prospective position by jointly examining its geopolitical relevance, defence-industrial base, and system-integration readiness within a layered Integrated Air and Missile Defence (IAMD) framework.

In summary, ESSI is best understood as a pragmatic, coalition-based accelerator that seeks to thicken the layers of European ground-based air and missile defence in tight synchrony with NATO IAMD/NATINAMDS, while drawing on EU instruments to tackle cost, scale, and interoperability. In collaboration with ESSI, disruptions have created a policy window in which rapid, standardized, and jointly financed solutions are not only desirable but strategically necessary.

2. Methodology and Scope

This article applies a structured desk-research design combined with comparative analysis. The empirical basis consists exclusively of open sources, and the unit of analysis is the national GBAD/IAMD posture of ESSI participants as it relates to NATINAMDS interoperability and collective defence requirements.

Source types were triangulated across: (i) primary NATO and EU documents (policy texts, topic pages, Council/Commission releases and programme documents); (ii) official national statements and procurement disclosures (ministries of defence, parliamentary questions, tender/contract announcements); (iii) manufacturer publications for system-level parameters (e.g., engagement roles, integration interfaces); and (iv) peer-reviewed and high-quality analytical literature for contextual interpretation. Where open-source reporting is used, it is treated as supplementary and cross-checked against primary/official materials.

Comparative assessment is organized around a consistent set of evaluation dimensions: (a) layering (VSHORAD/SHORAD/MRAD/LRAD and, where relevant, BMD-capable upper-tier effects), (b) integration readiness (sensor coverage, data-link compatibility, IFF, engagement-management/C2 interfaces), and (c) sustainment and industrial factors (magazine depth proxies, production scalability, maintenance/test infrastructure, and consortium participation). The intent is semi-quantitative in the sense of using consistent, observable indicators across cases, while acknowledging that key variables remain classified or politically contingent.

Range taxonomy and defensive-layer terminology follow NATO standardization logic (STANAG-based criteria referenced in the reviewers' supplementary material). Accordingly, legacy systems such as HAWK are treated as short-range within the SHORAD tier, and all range labels were harmonized throughout the country-by-country capability map.

Limitations: Because the study is open-source, it does not claim exhaustiveness on classified performance data, operational readiness rates, or wartime stockpile levels. The analysis should therefore be read as an interoperable baseline and a decision-support map, not as an operationally binding order of battle.

3. The Contemporary Air/Missile Threat Picture in Europe

In NATO's latest IAMD policy, the Alliance defines the threat set broadly as all objects capable of putting the Alliance at risk from the air, from any direction—encompassing manned aircraft (fixed- and rotary-wing), ballistic and cruise missiles, Uncrewed Aircraft Systems (UAS) including loitering munitions, and emerging hypersonic vehicles. This policy is quite important for Alliance. NATO's dedicated Ballistic Missile Defence materials likewise emphasize the increasing threat posed by ballistic systems to European populations, territory, and forces, *(*NATO, 2024a*)* while the Organization's capability-cooperation brief underscores that small drones have proven effective and dangerous in modern conflicts—hence the need for layered counter-UAS within a broader IAMD posture based in NATO sources.).

Since early 2022, Russia has conducted recurrent, large-scale missile and drone attacks against Ukrainian cities and critical infrastructure, often executed in successive waves that have targeted major urban centres as well as strategically significant nodes. A pronounced escalation has been observed from spring 2024 onward, with strikes increasingly concentrated on power generation facilities, electricity transmission and distribution assets, and related energy infrastructure. These attack patterns have produced cascading effects on the continuity of essential services and civilian resilience, including widespread outages and disruption risks for water, heating, and emergency response capabilities. In parallel, the sustained degradation of the energy system has required repeated emergency support measures, notably the rapid deployment of generators and other critical equipment through coordinated civil-protection and assistance mechanisms, aimed at stabilizing the grid, restoring basic services, and mitigating humanitarian impacts. Taken together, the EU record shows a sustained, high-tempo campaign against energy and civic infrastructure with direct cross-border externalities for European security. In doctrinal terms, ESSI seeks to mitigate an extensive array of aerial contingencies, ranging from conventional aircraft and Unmanned Aerial Vehicles (UAVs) to sophisticated ballistic and hypersonic threats. By harnessing state-of-the-art radar technologies, satellite constellations, and surface-to-air interceptors, the initiative aims to establish a robust, multi-layered defence perimeter for participating nations. Central to this objective is the cultivation of a synchronized defence architecture that integrates land, maritime, aerial, and space-based assets, thereby ensuring a rapid and cohesive response to evolving aerospace challenges.

3.1. ESSI's Strategic Aim and Alignment with NATO

ESSI is a cooperative, medium- to long-term integration and procurement initiative through which participating states pursue a multi-layered, ground-based IAMD capability—including an anti-ballistic missile layer—via common acquisition of air-defence systems, interceptors, and related equipment. Its core logic is collaborative procurement and joint operation, complemented by structured cooperation on lifecycle matters such as sustainment, maintenance, and repair, with the objective of building shared capabilities that reduce national unit costs while increasing interoperability. Although frequently associated with Europe, ESSI is conceived as a shared defensive architecture across participating countries that aims to enable timely and effective responses to aerospace-domain threats. While not a NATO programme per se, it is explicitly framed as a contribution to the NATINAMDS posture and requirement set, and it is intended to be fully interoperable and seamlessly integrated with NATO IAMD, leveraging NATO assets and standards to reinforce deterrence by denial and the collective protection of populations, territory, and deployed forces. ESSI is a voluntary, cooperation-based framework intended to thicken Europe's multi-layered ground-based integrated air and missile defence rapidly, thereby reinforcing deterrence by denial and the collective protection of populations, territory, and deployed forces.

Strategically, ESSI's design premise is plug-and-fight interoperability with NATINAMDS—the Alliance's distributed, 24/7 network that fuses sensors, C2 nodes and effectors across national and NATO systems. NATO Integrated Air and Missile Defence (NATINAMDS) constitutes a standing and continuous Alliance mission across peacetime, crisis, and conflict, aimed at safeguarding NATO territory, populations, and forces against air and missile threats and attacks. Conceptually and operationally, NATINAMDS embodies a cross-domain, multi-domain approach by integrating heterogeneous capabilities—spanning sensors, command-and-control, and effectors—into a coherent architecture. In doing so, it seeks to deliver a multi-layered defensive posture in which complementary layers of detection, tracking, engagement, and defeat operate in an integrated manner to enhance resilience and overall mission effectiveness. Allied Air Command further characterizes it as a command-and-control network that links sensors and weapon systems in the air, on land, [and] at sea, (AIRCOM, 2023) a formulation that clarifies the any-sensor/appropriate-shooter integration ESSI countries must achieve when fielding additional short-, medium- and long-range layers. In practice, this means ESSI procurement (from SHORAD/C-UAS to upper-tier interceptors) must be standards-compliant, data-link ready, and C2-convergent with NATO architectures from day one.

On the EU side, the European Defence Industrial Strategy (EDIS) sets the political-industrial context for scaling inventories at speed. Its companion programme, EDIP, proposes €1.5 billion (2025–27) and a toolbox that includes a new Structure for European Armament Programme (SEAP) and the EU's first security-of-supply regime—all aimed at steady-state availability of missiles, interceptors and supporting components (Council of the European Union, 2025).Taken together, EDIS/EDIP/EDF provide an EU-level industrial-policy and financing toolkit that can turn ESSI's pooled demand into repeatable production, common configurations, and interoperable increments that NATINAMDS can absorb without delay.

For EU Member States, this acceleration should remain coherent with the EU Capability Development Plan (CDP) and aligned with NATO requirements through the NATO Defence Planning Process (NDPP) and applicable standardisation/procurement mechanisms. The European Defence Agency's CARD 2024 report captures the policy pivot succinctly: more cooperation is needed, and it should be accelerated building on … closer collaboration with NATO to reduce fragmentation and maximize synergies and efficiencies (European Defence Agency [EDA], 2024).

The political economy is straightforward: NATO specifies the operational problem and apportions capability targets (NDPP), while the EU now fields industrial/financial instruments—EDIS/EDIP/EDF—to reduce lead times, scale manufacturing, and privilege interoperability. ESSI sits at the seam: it aggregates demand signals for ground-based air and missile defence, translates them into common standards and joint procurement, and delivers NATINAMDS-compatible effectors and C2 upgrades. This is why Allied communications about ESSI have stressed both NATO requirement-pull and interoperable, off-the-shelf procurement as the quickest route to close gaps and strengthen collective defence.

3.2. The Geopolitical Dynamics and Membership Politics of ESSI

ESSI has emerged as a cooperation-based procurement and integration framework to accelerate Europe's ground-based integrated air and missile defence. Politically, ESSI reflects the convergence of two imperatives: a NATO-defined operational need to thicken air and missile defence across all phases of conflict, and a European level drive to mobilize finance, scale production and hard-wire interoperability across national programmes. Legally and industrially, the initiative operates at the seam between Alliance interoperability standards (C2, data links and IFF) and EU instruments (EDF, PESCO, EDIRPA/ASAP and SAFE), which together provide a more predictable procurement and financing envelope.

A defining feature of ESSI is the combination of German political leadership with an expanding and increasingly diverse participation base. From the outset, the initiative has been framed as a cooperative pathway to strengthen NATO's integrated air and missile defence posture through the joint acquisition of air-defence systems and interceptors. Early alignment by major European stakeholders reinforced the logic of a multi-layered, ground-based integrated air-defence approach, while subsequent Nordic participation indicated that the coalition's strategic centre of gravity would extend northward alongside the eastern flank. The inclusion of non-EU neutral participants further suggests that ESSI functions less as an EU-internal scheme and more as a flexible coalition instrument operating at the practical interface between EU and NATO capability development and operational interoperability.

Notwithstanding this enlargement, membership politics have been marked by a distinct French (and initially Italian) reticence rooted in strategic-autonomy and technology-origin concerns. A parliamentary question dated 23 April 2024 framed the risk starkly: more than 20 Member States had joined, but France and Italy had yet to do so, a posture that could jeopardize its effectiveness, turning it into a new 'Maginot Line'. (European Parliament, 2024). Paris's preference to prioritize entirely European solutions (SAMP/T) channels a broader legal-industrial claim about origin rules, sovereignty in critical subsystems, and the long-run structure of the European Defence Technological and Industrial Base (EDTIB). Notwithstanding industrial-origin debates, ESSI participation is conditioned by NATO interoperability: procured systems must meet Alliance standards (notably data links, IFF, and C2/engagement-management interfaces) so that all layers can plug into NATINAMDS—including for Allies such as Türkiye on the south-eastern flank. The strategic alignment between ESSI and NATO is twofold. First, NATO conceptualizes Integrated Air and Missile Defence (IAMD) as an essential and continuous mission spanning peacetime, crisis, and conflict, operationalized through NATINAMDS as a networked architecture connecting national and NATO systems. This framing entails a stringent interoperability constraint for any ESSI-related procurement: platforms and effectors are not merely purchased as standalone assets but must be capable of integrating into the Alliance's sensor–command-and-control–effector ecosystem, including compliance with relevant data-link standards, Identification Friend or Foe (IFF) procedures, and the applicable command-and-control architecture. Second, the Alliance's post-summit emphasis on strengthening the credibility and coverage of IAMD logically presupposes both increased magazine depth (available interceptors/munitions) and greater node density (the number and dispersion of sensors, command nodes, and launchers) within NATINAMDS. Doctrinally, this situates ESSI within the any sensor/appropriate shooter logic: the defensive system is conceived as an integrated construct in which distributed sensors, command-and-control facilities, and weapon systems are networked to enable timely cueing, engagement allocation, and coordinated interception across the battlespace.

Several key EU instruments supply the complementary legal-financial scaffolding that enables ESSI to move from concept to fieldable capacity. This can be exemplified by; The European Defence Fund (EDF) underwrites collaborative R&D and development to deliver innovative and interoperable defence technologies and equipment, giving a structured path to standardization across ESSI's sensor-effector-C2 stack (European Commission, n.d.). As a rule, EDF support is limited to eligible entities established in EU Member States (and associated countries), subject to the applicable eligibility, security, and ownership-control conditions; third-country participation is therefore structurally constrained. IMLAMD's added value lies in developing an open, modular BMC4I-oriented reference architecture that can federate sensors and effectors across layers, validate interfaces through joint testing/demonstrators, and mature integration governance for future multi-layer GBAD. In the near term, two additional instruments address bottlenecks exposed by the war in Ukraine: EDIRPA (Regulation (EU) 2023/2418) establishes a common procurement instrument, while ASAP (Regulation (EU) 2023/1525) aims to bolster and speed up EU manufacturing capacity for ammunition and missiles. Together they de-risk joint buying and expand production lines, thereby improving both readiness and sustainment. Finally, SAFE—the Security Action for Europe regulation adopted in 2025—introduces up to €150 billion in competitively priced long-maturity loans to co-finance major defence investments and joint purchases, with governance arrangements designed to favour European supply chains and reduce dependencies (Council of the European Union, 2025).

These instruments are not without constraints. Origin requirements and buy-European preferences can create friction with the speed and unit-cost advantages of certain off-the-shelf solutions. Yet, each instrument has some advantages, the legal-financial package enables a workable compromise: EDF de-risks early-stage integration and interoperability; PESCO structures multi-state commitments and technical governance; EDIRPA/ASAP provide near-term joint-procurement and production uplift; and SAFE scales capital for big-ticket acquisitions. In other words, NATO sets the operational problem (coverage, readiness, integration), and the EU provides tools to translate that problem into funded, standardized industrial outputs, while ESSI functions as the coalition programme office knitting these vectors together. This way, the problem is addressed holistically.

In this light, the politics of membership take on a functional cast. A broad ESSI coalition—UK and Nordics included—narrows the gap between Alliance-wide IAMD requirements and national acquisition cycles. At the same time, French concerns about strategic autonomy force a healthy debate on industrial policy and technological sovereignty, ensuring that short-run fixes do not hollow out the EDTIB over the long run. If interoperability and readiness are the binding operational constraints, and industrial resilience the binding strategic constraint, ESSI's success will hinge on balancing both: integrating quickly into NATINAMDS while steadily increasing European content, production capacity and stockpiles. On current evidence, that balance is attainable within the available legal architecture, provided participants hold the line on standards, financing discipline and credible timelines for delivery.

3.3. Capacity Map: Capabilities and Gaps (Country-by-Country)

The ground-based air and missile defence (GBAD) posture across ESSI member states remains heterogeneous by tier (VSHORAD/SHORAD/MRAD/LRAD). Participants are attempting to reconcile operational requirements—area coverage, magazine depth, and assured NATINAMDS interoperability—with legal-industrial constraints such as budget ceilings, joint-procurement rules, origin/compliance provisions, and export-control regimes. Within this framework, ESSI functions as a coordination mechanism to compress timelines, standardize interfaces, and pool demand for interceptors, sensors, and C2.

This section examines the current and programmed capabilities of ESSI members, detailing extant GBAD inventories, in-flight acquisition contracts, and integration approaches (C2/data-link/IFF) relevant to alliance operations. Non-ESSI European states fall outside the analytical scope.

3.3.1. Albania

Albania's ground-based air defence remains concentrated at the very-short-range layer, complemented by NATO's standing Air Policing cover over the Western Balkans. A modernization drive has focused first on the sensing layer: a long-range air-surveillance radar on Mida Mountain is integrated into NATO's air picture, and a new Ground Master 400 Alpha has been contracted to expand coverage and improve low-altitude detection. These steps, alongside the NATO-funded upgrade of Kuçova Air Base into a regional operating hub, strengthen Albania's role as a surveillance and basing node even as its interceptor inventory is limited (NATO, 2024b). Within ESSI, Tirana is positioned as a sensor-rich, shooter-light contributor whose value lies in radar pickets, air-picture fidelity, and host-nation support to allied GBAD deployments and exercises.

3.3.2. Austria

Goldhaube, Austria's air defence system that consists of mobile stations and fixed sites for radar, is functional since 1988 (Federal Ministry of Republic of Austria, n.d.). Press conference held in 2023, the government announced that from 2027, long-range air-defence missiles would be added to strengthen national air defence. Two weapon systems are under evaluation (types not specified), with main candidates believed to be Patriot (U.S.) or Arrow 3 (U.S.–Israel). Since the war's outbreak and Austria's ESSI participation, Vienna has made significant efforts to strengthen its capacity (Defence Industry Europe, 2023a).

3.3.3. Belgium

Belgium is counted among countries with relatively weak air-defence (Defence News, 2025). The inventory includes Mistral MANPADS (very short range), while—per open sources—there are no short-, medium- or long-range systems. Belgium participates in NATO's two new High Visibility Initiatives in 2025. The project aims to acquire more effective solutions to low level air threats and for passive air surveillance (NATO, 2025).

3.3.4. Bulgaria

Very short-range includes ZU-23-2, SA-7 Grail (9K32 Strela-2), SA-14 Gremlin (9K34 Strela-3), SA-16 Gimlet, SA-18 Grouse (9K38 Igla), and 9K35 Strela-10. Short range includes 2K12 Kub and 9K33 Osa; short-to-medium includes S-125; medium range includes S-300 and S-200. The technological obsolescence of these systems and uncertainties about their effectiveness under attack are debated; more importantly, their contribution to a common air-defence network remains uncertain—an obstacle to regional cooperation. However, in August 2025, Bulgaria has approved the procurement of IRIS-T missile systems which modernize its air defence systems and supports it to adjust with ESSI (Missile Defence Advocacy Alliance, 2025).

3.3.5. Czechia

Czechia's capacity is limited to Soviet-era systems: only MANPADS in very short-range and 2K12 Kub in short range. In 2021, the Ministry of Defence signed a $627 million agreement to purchase Spyder short-to-medium-range SAMs from Rafael (Israel). (Defence Industry Europe, 2025a).

3.3.6. Denmark

Terma specializes in command-and-control systems for naval platforms, enabling integration of air-defence systems and improving operational efficiency. Weibel Scientific is known for advanced radar technologies and has recently made significant progress in radars for short and very short-range air-defence (notably counter-drone applications). Denmark's technological capabilities could offer critical sensors and command solutions to NATO's broader air-defence architecture. However, its efforts to strengthen national air-defence systems are still deemed insufficient—a shortfall that complicates NATO's effective use of Esbjerg Port facilities for U.S. force movements into Europe. Despite new radar procurements and indigenous technologies, a serious gap remains particularly in short-range systems, potentially undermining NATO's operational flexibility in the region. Accelerating investments and closer allied cooperation are therefore critical (Defence News, 2025).

3.3.7. Estonia

Estonia's VSHORAD foundation has been reinforced by the Piorun MANPADS acquisition (September 2022). In June 2022, the Estonian and Latvian defence ministers also issued a letter of intent to acquire at least four SHORAD batteries, signalling a shift from isolated point defence to a programme-based lower-tier recapitalization. As part of the ESSI, Estonia announced—together with Latvia—plans to procure IRIS-T SLM systems with TRML-4D radar suites (July 2024), a package valued at over €100 million. Estonia is transitioning from VSHORAD-only to a VSHORAD+MR construct. Yet, in the interim, available systems are judged adequate for local protection of small, mobile units, not for the continuous defence of critical centres and large urban areas (Republic of Estonia Defence Forces, n.d.).

3.3.8. Finland

Finland possesses MANPADS and artillery systems for force protection, and also operates an advanced air-defence system such as NASAMS (Norwegian Advanced Surface-to-Air Missile System). Finland is in the process of purchasing David's Sling, a medium-to-long-range missile-defence system developed by Rafael Advanced Defence Systems (Israel) and Raytheon (United States). The most important development for the country has been Finland's accession to NATO in 2023, which strengthened its position in terms of defence cooperation and collective security.

NASAMS is a short- and medium-range, networked air-defence system. Radar range is 120 km, while missile range varies between 30–50 km depending on missile type. It uses AIM-120 AMRAAM missiles, which are widely present in NATO inventories, providing advantages in logistics and re-procurement. The fact that Norway operates the system and Latvia and Estonia plan to purchase it may enable integrated air-defence coordination within NATO. Finland has the widest and densest very short-range air-defence network in the region and also possesses the capacity to protect its forces.

Within PESCO, the TWISTER project, led by France since 2019, aims to enhance Europe's early-warning and interception capability against ballistic missile threats by integrating space-based early warning assets with endo-atmospheric missile defence systems. While Finland will be included in an early-warning system under this project, France's negative stance toward the European Sky Shield Initiative (ESSI), in its role as the TWISTER coordinator, currently renders a direct contribution of TWISTER to ESSI unlikely (PESCO, 2024).

3.3.9. Germany

As ESSI's founder, Germany is also Europe's largest provider of ballistic-missile defence. Long engaged in GBAD research, Germany began in 2008 to develop a land-mobile, laser-based missile-defence system using concentrated infrared laser beams to track, identify, and destroy missiles. Post-2014, NATO's renewed focus on collective defence and Russia's actions increased demand for short- and medium-range SAMs. From 2014 to 2022, Germany accelerated efforts to meet NDPP commitments, restructuring the Bundeswehr for conventional conflict and improving air-defence capabilities.

Germany fields ASRAD and Stinger for very short range and pursues the LVS NNbS programme (led by Rheinmetall, Diehl Defence, Hensoldt) against loitering munitions and cruise missiles (Defence News, 2021). Bases are protected by MANTIS; mobile force protection employs Wiesel 2 with Stinger and a LeFlaSys Ozelot battery. Germany also operates Skyshield 35 (short/medium) and Patriot (medium/long). Notably, more than 12 Patriot batteries are deployed nationwide, and modernization is ongoing.

Germany, the U.S., and Italy launched MEADS in 2005 (MBDA Deutschland, Lockheed Martin, MBDA Italia) to replace Patriot with a PAC-3-based, versatile system; to reduce costs, IRIS-T SL integration was pursued. The U.S. withdrew in 2011, though work continued to a

2014 prototype. In 2022, Germany sought U.S. approval to procure THAAD; the U.S. approved related items in August 2022. However, reporting indicates Berlin opted for Arrow 3; approvals followed, and in August 2023 Israel announced a $3.5 billion Arrow 3 sale to Germany. On 28 September 2023, Ministers Yoav Gallant and Boris Pistorius signed a Letter of Intent in Berlin; the Bundestag had approved £560 million in June 2023 toward the programme (total expected ~$3.5 billion).

3.3.10. Greece

Greece possesses considerable air-defence system capacity. The foundation was laid in 1964, when Greece and several NATO states signed a Multilateral Agreement on the use and operation of the NATO Missile Firing Installation (NAMFI) on Crete. The inventory includes FIM-92 Stinger, Tor-M1, Rheinmetall Twin AA Gun MK-20, Crotale NG, VELOS, Artemis 30, Phalanx CIWS, and 9K33 for short-range; for medium range, ESSM; additionally, S-300 and Patriot PAC-2 (GEM-T) systems. Under the General Staff's administrative control, NAMFI conducts live-fire exercises with platforms operated by Germany, Greece, and the Netherlands under realistic scenarios (NAMFI, n.d.). This combination of inventory and exercise capability makes Greece a significant air-defence power in the region.

3.3.11. Hungary

Hungary's air-defence capacity is quite limited: only a small number of MANPADS provide very short-range coverage; the absence of artillery and very short-range systems creates a serious vulnerability against UAS threats. In 2023, Hungary ordered the Skyranger 30-gun system for very short-range and UAS threats. For short range, Hungary fields 2K12 Kub. In 2023, Hungary received the first two NASAMS batteries from a 2020 contract, thereby acquiring short-to-medium-range capability; nevertheless, substantial steps remain to establish a multi-layered network (Defence Industry Europe, 2023b). Mentioned delivery also makes Hungary the 6th NATO country to procure NASAMS (Missile Defence Advocacy Alliance, n.d.).

3.3.12. Latvia

Latvia supplemented its VSHORAD posture with RBS-70NG (November 2022). Parallel to Estonia, Riga signed a letter of intent for ≥4 SHORAD batteries, anchoring a joint lower-tier pathway in 2022. In November 2023, Latvia contracted IRIS-T SLM for approximately €600 million, with deliveries expected from 2026; the manufacturer Diehl described this as the largest defence investment in Latvia's more than 30 years of independence. (Defence News, 2023). This MR procurement is embedded in a September 2023 EE–LV–Diehl framework, ensuring contractual coherence and economies of scale. In July 2024, Latvia joined Estonia in announcing TRML-4D-equipped IRIS-T SLM buys under ESSI, valued at >€100 million.

3.3.13. Lithuania

Lithuania initiated MR coverage earlier than its neighbours by procuring NASAMS-3 (2017), with two batteries delivered by 2020—a material uplift over the pre-2017 SHORAD-limited baseline. Even with this head start, the regional analysis groups Lithuania with Estonia and Latvia in facing resource-driven limits on full layering, sustained magazine depth, and contiguous coverage. Lithuania's NASAMS gives it a first-mover MR advantage (Lithuanian Armed Forces, 2020*)*.

3.3.14. Netherlands

The Netherlands fields systems across all ranges: Stinger MANPADS (very short range), NASAMS (short-to-medium), and Patriot (medium-to-long). It also operates advanced detection systems, including TRML mobile radars capable of tracking low-altitude threats. This diverse inventory supports both national and NATO collective defence missions, making the Netherlands an important member under ESSI; however, given its geographical position, the contribution of these systems against the Russia threat is debated among member states. Alongside existing systems, the Netherlands continues capacity increases, modernization, and renewal, partly due to donations (e.g., 200 Stinger MANPADS in 2022). In June 2023, the MoD announced plans to replace existing short- and medium-range systems with a single modern system (from Kongsberg/Raytheon), expected to be operational from 2026. Conforming to that, by December 2025, Rheinmetall announced that the Netherlands ordered Skyranger 30 valued more than 500 million EUR (Rheinmetall, 2025).

3.3.15. Norway

Norway has no very short-range air-defence systems at present. Norway had previously possessed Stinger, whose service life has expired. RBS-70 systems also existed but were sold to Lithuania. In 2022, the Norwegian Defence Materiel Agency (NDMA) signed a contract worth approximately $35 million with Mesko (Poland) to purchase Piorun MANPADS; the first shipment arrived in 2023. This purchase added this category to Norway's inventory for the first time and strengthened its capability against very-low-altitude air threats.

NASAMS (three batteries) is deployed to protect the Ørland and Evenes main air bases; one additional battery protects the single brigade in the north. Launchers are to be upgraded to new, more mobile versions by 2026–2027. Norway sent NASAMS systems to Ukraine in March 2023, December 2023, and early 2024, some directly from its own inventory and some procured. To replace donated systems, Norway placed an order worth 2.7 billion NOK (European Defence Review, 2024). Consequently, the exact number of NASAMS in Norway is not precisely known at present.

3.3.16. Poland

Poland fields a multilayer architecture spanning man-portable and gun-based very-short-range systems, short-range missile batteries under the Narew programme, and medium-to-long-range interceptors under Wisła—networked through the Integrated Battle Command System (IBCS). Recent milestones include an operational IBCS demonstration and live-fire events that validated integration between short-range Narew elements and Patriot batteries (US Army, 2025); parallel contracts add surveillance depth (passive-location and long-range radars) and accelerate deliveries of CAMM-family effectors and Pilica+ fire units.

3.3.17. Portugal

Portugal is rebuilding its ground-based air defence from the base layer upward. Legacy short-range systems have been retired and replaced by a modern, vehicle-mounted very-short-range solution (ForceShield/RapidRanger) using fast-reaction interceptors for point defence of forces and critical infrastructure. Lisbon has also signalled intent—via participation in ESSI—to bridge the medium-range gap through common procurement, while continuing to contribute fighter detachments to NATO Air Policing as an interim air-sovereignty measure (Defence Industry Europe, 2024).

3.3.18. Romania

Romania fields various systems across ranges, many old or approaching end-of-life. Very short-range includes M 1980/77, Oerlikon GDF-003 mobile guns, Gepard, and 9K31 Strela-1 / 9K32 Strela-2 MANPADS. Low-altitude/short-range includes the 9K33 Osa. Additional systems include 2K12 Kub (Soviet medium), MIM-23 Hawk (short range, SHORAD), and S-75 (Soviet medium). To support its existing Patriot batteries, Romania plans to procure 200 PAC-2 GEM-T missiles—reported to Parliament in December 2023—under a joint programme with Germany, the Netherlands, and Spain totalling 1,000 Patriot missiles; Patriot has also been recently delivered to Romania (Reuters, 2025).

Romania's strategic weight within NATO's missile defence architecture is primarily anchored by the Aegis Ashore facility at Deveselu. As a foundational element of the European Phased Adaptive Approach (EPAA) since its activation in 2016, this land-based configuration utilizes the SPY-1 radar and SM-3 interceptors to neutralize short and intermediate-range ballistic threats.

3.3.19. Slovakia

Slovakia's inventory is limited: MANPADS for very short range (service-life expired) and 2K12 for short range (technologically very old). The Defence Minister Robert Kaliňák stated that Patriot purchases from the United States were under consideration to strengthen air-defence capabilities, but he emphasized the plan is long-term, making a short-term order unlikely. At the end of August 2024, Slovakia decided to purchase six units of the Barak MX multi-layer system from IAI (Israel) for approximately €554 million; if negotiations conclude successfully, first delivery is expected by end-2025 (Defence News, 2024a). These developments demonstrate modernization efforts, though significant steps remain to build a comprehensive and effective network.

3.3.20. Slovenia

Slovenia's capacity is limited: in very short-range, only SA-24 9K338 Igla-S MANPADS; otherwise no very short or short-range systems. In the medium-range category—and gaining importance under ESSI—Slovenia signed a contract on 25 January 2024 with Diehl (Germany) to procure the IRIS-T SLM. The order includes one firing unit comprising a radar, a tactical operations centre, and four launchers, as well as IRIS-T SLM missiles and logistics support. Further purchases are expected to increase capacity (Air Force Technology, 2025). The decision to procure IRIS-T SLM not only strengthens national capability but also reflects growing interest in Germany's proposed IRIS-T GBAD solutions for ESSI, reinforcing Slovenia's participation in regional cooperation.

3.3.21. Sweden

Sweden possesses MANPADS and very short-range artillery for border defence, yet the numbers are insufficient; a phased withdrawal of MANPADS is also under consideration. Short- and medium-range systems include RBS-98 and RBS-23. In 2018, Sweden ordered four Patriot batteries from the United States in PAC-3+ configuration. In March 2021, the Swedish Armed Forces re-introduced Launcher Unit 23, developed in the 1990s and completed in the early 2000s, a modified version of Air-Defence System 15, now deployed on Gotland. In November 2021, Sweden received Patriot PAC-3, adding two missile types, three different launchers, a command centre, and integrated reconnaissance and fire-control radars. Sweden also fields I-HAWK (Rb 67) as legacy short-range (SHORAD) system, consistent with NATO range taxonomy.

Under LvS103, Patriot uses the PAC-3 MSE modification, capable against long-range missile and air attacks. In December 2021, first operational capability was declared. The State also settled to purchase 7 medium-ranged IRIS-T SLM air defence system in 2025 June (Defence Industry Europe, 2025b). Among regional countries, Sweden is the only state with a multi-layered air-defence architecture across very short, short, and medium ranges; however, the limited number of systems complicates decision-making on assigning protection tasks to specific critical infrastructure or units.

3.3.22. Switzerland

Switzerland's air-defence history began in the 1960s with the BL-64 Bloodhound missile and has evolved through Rapier, FIM-92 Stinger, Oerlikon GDF towed guns, Oerlikon 35 mm, and the Oerlikon Skyguard fire-control system (guiding Sparrow/Aspide). Launched in 2017, the Air 2030 programme aims to restructure and modernize the Air Force's long-term capabilities, including renewal of air-defence systems and fighter aircraft (International Trade Administration, 2022). The New Ground-Based Air Defence System seeks to replace ageing systems with more effective capabilities for the coming decades.

3.3.23. United Kingdom

The Ministry of Defence identifies Ground-Based Air Defences (GBAD) as a priority in its report Combat Air Strategy: An Ambitious Vision for the Future. Initiatives include the establishment in 2003 of the UK Missile Defence Centre, a government-industry partnership under the MoD’s Defence Science and Technology programme; participating firms include BAE Systems, L3Harris ASA, Lockheed Martin U.K., MBDA, QinetiQ, Fluid Gravity Engineering, and Airbus Defence and Space U.K. Work spans six main areas: Scenario Assessment and Wargaming, Sensors and Architecture, Threat Characterization, Threat Mitigation and Lethality, Maritime Missile Defence, and Innovative Technology.

The United Kingdom fields Stormer HVM, Starstreak, and Rapier FSC for very short and short ranges, as well as Enhanced Modular Air Defence Solutions (EMADS) designed with modular architectures. Recently, CAMM and CAMM-ER (MBDA/Thales) entered service, offering flexible land/sea deployment. At medium range, Sky Sabre protects naval systems and fleets. The Type 45 has wide-area capability with Sea Viper, Sampson multi-function radar, and Phalanx as last-ditch defence; other sea-based systems include Phalanx and Sea Wolf. The MoD’s Combat Air Strategy and the UK Missile Defence Centre underpin continuing development (Mills, 2025). In early 2022, the United Kingdom officially decommissioned the Rapier system, concluding its nearly fifty-year service life.

3.3.24. Türkiye

Türkiye’s air and missile defence has evolved, in the post–Cold War era, from a point-defence–heavy structure to a network-centric, multi-layered architecture. This change could also be seen in the product range of Turkish defence companies. As Turkish defence industry grows, these companies make more appearance in the international arena. Year after year, an increasing number of Turkish companies have been included in the SIPRI Top 100 Defence Companies List, as shown in Table 1. From an industrial perspective, Türkiye’s defence-industrial base—both in scale and portfolio breadth, as reflected in SIPRI and Defence News rankings—signals credible capacity for output expansion, sustainment and lifecycle support, and consortium-driven cooperation, albeit within the compliance and eligibility constraints embedded in EU defence-funding instruments (SIPRI, 2025; Defence News, n.d.).

Table 1. The SIPRI top 100 arms producing and military services companies in Türkiye, 2024 (SIPRI, 2025).

Company	Rank 2024	Rank 2023	Arms Revenues 2024	Arms Revenues 2023	Change in Arms Revenues (%)	Total Revenues 2024	Arms Revenues %
Aselsan	47	52	3470	2440	42,21%	3660	94,81%
TAI	65	75	2160	1700	27,06%	2700	80,00%
Baykar	73	66	1900	1900	0,00%	2000	95,00%
Roketsan	87	92	1390	1080	28,70%	1390	100,00%
MKE	93	102	1210	900	34,44%	1210	100,00%

In parallel, Turkish defence firms have also strengthened their presence in the Defence News Top 100 List, as presented in Table 2.

Table 2. Defence news top100 defence company in Türkiye (Defence News, n.d.).

Company	Rank 2024	Rank 2023	Total revenue for 2024 (in USD)	Total defence revenue for 2024 (in USD)	Total revenue for 2023 (in USD)	Total defence revenue for 2023 (in USD)
Aselsan	43	42	$3,657,785,000	$3,541,261,567	$3,089,403,352	$2,896,191,483
TAI	47	50	$3,287,106,189	$3,151,029,596	$2,673,762,230	$2,205,738,874
Roketsan	71	71	$1,545,052,590	$1,545,052,590	$1,758,496,410	$1,758,496,410
ASFAT	78	94	$1,281,010,000	$1,276,176,000	$637,035,587	$637,035,587
MKE	80	84	$1,209,280,000	$1,209,280,000	$878,349,000	$878,349,000

This evolution rests on configuring the low altitude (VSHORAD/SHORAD), medium altitude (MRAD), and high altitude/long-range (LRAD/BMD) layers to complement one another; and on progressively strengthening the sensor–C2–data link backbone that binds the layers together with increasingly indigenous components. NATO doctrine describes this approach, within NATINAMDS, as a network of interconnected national and NATO systems, and defines the architecture as the integration of sensors, command and control facilities and weapon systems. Türkiye’s current approach is to develop a dual-configuration capability for both national and alliance missions—combining indigenous density at the lower layer, network-architecture maturity at the medium layer, and an autonomous, effective system at the upper layer (Düz & Koçakoğlu, 2025).

3.3.24.1. Low Altitude Systems

A modern lower-tier baseline was established through the Stinger European Co-production Programme. This programme generated both industrial gains and operational capability. The requirement for mobile point defence then crystallized in the pedestal-mounted Stinger concept: tracked and fixed/mobile configurations entered serial production by 2001.

A kind of MANPADS system, SUNGUR programme was launched in 2013 to replace ageing Stinger stocks and meet high-tempo operations at low altitude; entering the inventory in 2022, the system offers superiority over Stinger in altitude/range/guidance parameters and provides flexible integration on land–air–naval platforms. At the low layer, the guided-artillery effect is provided by KORKUT.

In the VSHORAD/SHORAD layer, through the ASELSAN–ROKETSAN production chain and NSPA/NATO integration experience, Türkiye has increased indigenous density; the SUNGUR–Stinger-KÜSS-KORKUT provides a low-cost, high-tempo fire density against UAV/low-observable profiles and saturation attacks, functioning as a buffer that preserves the munitions of upper layers. The lower tier of this layered architecture is supported by the Rapier system, which engages low-altitude threats using Mach 2.5 guided missiles within a defined 8 km range and 5 km altitude ceiling.

3.3.24.2. Medium Altitude Systems

The HİSAR Project constitutes Türkiye's low- and medium-altitude backbone. HİSAR-A - is oriented to armoured–mechanized unit protection in low altitudes and HİSAR-O to strategic site/area defence in medium altitudes. HİSAR-A+ components had been delivered by July 2021, and HİSAR-O+ was fully delivered in 2022. The HİSAR layer absorbs the saturation load of the lower layer, giving the upper layer breathing room in terms of munition–tempo; it also enables expansion of the Defended Asset List (DAL). At the medium-altitude layer, the Turkish inventory is supported by the MIM-23 Hawk system, which has been operational since 2005. While the platform offers a theoretical maximum range of 50 km, its tactically effective engagement radius is established at 20 km.

3.3.24.3. High Altitude Systems

Long-range requirements have increasingly been met indigenously. SAMP/T talks continued intermittently after 2016 but infers that the requirement would be covered domestically in the near term via a phased SİPER programme. SİPER is a product of strategic partnership between ASELSAN–ROKETSAN–TÜBİTAK SAGE. In October 2024, it was officially announced that SİPER Block-1 entered the inventory, and July 2025 updates reported successful serial-production acceptance tests for Ürün-1, indicating transition toward early fielding at scale.

Naval variants and maritime IAMD: In addition to the land-based HİSAR and SİPER families, the national roadmap includes shipborne configurations (commonly referred to in open sources as HİSAR-D and SİPER-D) intended to provide layered air defence for naval task groups and critical maritime approaches. Although these variants are in advanced testing and acceptance phases rather than full fleet-wide service, their inclusion is analytically relevant because ESSI/NATINAMDS interoperability depends on consistent sensor-to-shooter networking across domains. In the manuscript, these naval variants are therefore treated as forthcoming capabilities, with a brief discussion of expected engagement roles and their contribution to cooperative engagement concepts at sea, including interface considerations with naval combat-management systems and NATO-standard data links/IFF.

Beyond these conventional assets, the most significant yet controversial component of Türkiye's long-range capabilities is the Russian-made S-400 Triumf system. Due to technical interoperability constraints with NATO's integrated air defence architecture the S-400 remains largely in a state of limited operational readiness rather than being fully active within the national network.

3.3.24.4. The Integration Structure and Steel Dome

Steel Dome as an integration umbrella to protect bases and critical infrastructure against the full threat set (including rocket/artillery/mortar, cruise missiles, and UAVs). The concept is evolutionary and vendor-agnostic, envisaging the progressive absorption of national radar, counter-UAS, and effector families (from very-short to long range) under a common C2 and data-link architecture. Politically and institutionally, late-2024/2025 announcements elevated

Steel Dome as a core line of effort; in 2025, public events highlighted delivery packages and scale, while parallel industrial capacity investments were announced to more than double throughput for command-and-control and air-defence lines—measures directly relevant to serialization, stock depth and sustainment. To operationalize this integration logic, Table 3 consolidates Türkiye's layered GBAD/IAMD capability map, some example products and highlights ESSI-relevant interface implications (sensors, C2, datalinks/IFF, and interceptor families), providing the bridge between the capability description and the cooperation argument developed in the subsequent sections.

Table 3. Türkiye's layered GBAD/IAMD capability map and ESSI-relevant interfaces.

Layer (Range Tier)	Representative National Systems (Examples)	ESSI/NATINAMDS Interface Implications
VSHORAD/ SHORAD	SUNGUR; Stinger co-production legacy; KORKUT (gun-based)	High-tempo, low-cost layer for UAS/low-altitude threats; requires cueing from shared air picture and deconfliction with higher-tier engagements
MRAD	HİSAR-A/HİSAR-O family (including A+ / O+ variants)	Area/point defence for critical sites and manoeuvre forces; integration hinges on data-link interoperability, IFF, and engagement-management alignment
LRAD / Upper Tier	SİPER Block-1 (growth blocks projected); associated radars/C2	Upper-layer contribution and magazine-depth potential; interfaces must be standards-compliant to plug into NATINAMDS engagement coordination
Maritime Layer (Forthcoming)	Navalised variants of HİSAR and SİPER ("HİSAR-D / SİPER-D" in open sources); ESSM on naval platforms	Extends layered defence to maritime approaches; requires naval C2-to-NATINAMDS data exchange, common IFF, and cooperative engagement deconfliction

3.3.25. Political–Economical -Conjuncture and Türkiye's Critical Role

3.3.25.1. Joint Procurement, Consortia, and Standardization Pressure

Rapid thickening of Europe's layered air and missile defence depends on the functionality of joint-procurement and consortium-based acquisition architectures. These architectures are designed not only to reduce unit costs, but also to create congruent solutions in logistics/sustainment and training–TTPs (tactics, techniques and procedures) (Reuters, 2024; armasuisse, 2025). NATO defines NATO Integrated Air and Missile Defence (IAMD) as implemented through NATINAMDS, a network of interconnected national and NATO systems comprised of sensors, command and control assets, and weapons systems; a key prerequisite for such integration is interoperability (procedural, technical and human), which in practice drives common interfaces and standardization pressure.

In the ESSI context, cooperative procurement frameworks and follow-on procurements (IRIS-T SLM; Patriot) operationalize these goals by privileging standard configurations and bundling sustainment/training elements alongside integration needs (Armasuisse, 2025; Bundesministerium der Verteidigung, 2024). The letter of intent signed in 2022 made this impetus explicit, and participation expanded in subsequent accession waves. In field implementation, prime–subcontractor consortia are expected to span project management, joint engineering, integration, and certification; within such a framework, Türkiye’s ongoing layered GBAD programs (HİSAR/SİPER) and their emphasis on command-control compatibility, IFF, recognized air picture generation, and data-link-enabled interoperability are relevant to the technical connectability of very short–short–medium–long-range layers (Roketsan, n.d.; ASELSAN, n.d.-a; ASELSAN, 2021).

3.3.25.2. Financial Instruments: EDF, PESCO, ASAP, and SAFE

The European Defence Fund (EDF) aims to increase the competitiveness of the industrial base and the production of interoperable defence technologies within the Union by funding collaborative defence research and development and capability development projects. PESCO projects (IMLAMD/TWISTER) invest in the BMC4I/C2 pillar of IAMD and a multi-layered approach to counter new threats including hypersonic. Together with CARD and the EDF, PESCO constitutes one of the three mutually reinforcing pillars of EU defence cooperation, providing binding commitments and governance for collaborative capability projects (including PESCO projects such as IMLAMD).

ASAP (Act in Support of Ammunition Production), which entered into force in 2023, sought to accelerate capacity expansion to remove bottleneck effects in the ammunition/missile chain; Commission documents note the programme’s focus on propellants, explosives, casings, and test lines and indicate ≥€500 million in EU budget with scaling to ≥€1.5 billion total volume. SAFE (Security Action for Europe), adopted by the Council in 2025, is a new funding arm focused on joint procurement; according to the Council communication, €150 billion of leverage is envisaged for joint procurement, and the regulation stipulates that SAFE provides financial support to Member States for urgent and major public investments.

Although Türkiye is not an EU Member State and therefore lacks direct access to EU defence-financing instruments such as EDF grants and SAFE loan facilities, limited indirect pathways may nevertheless emerge through consortium-based cooperation—most plausibly via technology partnerships, joint R&D, and engineering work structured around EU-based prime contractors and supply chains. Under the current SAFE architecture, while only Member States may benefit from SAFE loans, common procurement participation may extend to EU acceding states, candidate states, and potential candidate states; however, this participation does not, by itself, translate into eligibility for the underlying funding. In parallel, access to EDF support is conditioned on strict eligibility and establishment requirements: EDF-funded actions generally require a consortium (typically at least three eligible Member States and/or associated countries), and both beneficiaries and subcontractors must be established within the EU and have their executive management structure located there, which materially constrains Türkiye’s ability to receive EDF/SAFE resources directly and effectively channels cooperation—if any—into EU-established entities and compliant consortium structures.

3.3.25.3. The Strategic Autonomy–U.S. Dependence Tension

Europe's defence ecosystem is shaped by a structural tension between strategic autonomy objectives and persistent dependence on U.S.-sourced systems and sustainment. In the early ESSI framing, the prominence of a Patriot–IRIS-T SLM–Arrow-3 procurement logic (short/medium/upper layer) fuelled perceptions in some capitals that the Franco–Italian MAMBA/SAMP-T line and other European-first solutions were being side-lined, thereby deepening political contestation over industrial sovereignty and long-term supply-chain dependence (Gotkowska & Maślanka, 2023; Bundesministerium der Verteidigung, 2023). This dossier has consequently been debated in European public discourse through "France's distance to Sky Shield" and intra-European priority differences, with Paris repeatedly highlighting the strategic risk of path-dependence on non-European technologies (France 24, 2023; Gotkowska & Maślanka, 2023).

Institutionally, the EU's response has been to expand intra-European production capacity and to incentivize standardization effects through joint procurement and collaborative capability programmes. In this direction, the ReArm Europe Plan/Readiness 2030 is presented as a financial-leverage architecture designed to mobilize up to approximately €800 billion for defence-related investments, while SAFE is structured as a €150 billion loan instrument that privileges common procurement to generate economies of scale and interoperability and to reduce fragmentation. Complementarily, the European Defence Fund (EDF) is framed as the EU's budgetary instrument for collaborative R&D and interoperable capability development, and PESCO provides the treaty-based project framework for participating Member States to jointly plan and invest in capability projects—together constituting a policy bundle that operationalises the autonomy–dependence debate into industrial and procurement governance.

3.3.25.4. Türkiye's Critical Role: Contributions and Constraints

The sustainable success of ESSI rests on three pillars: integration (common C2/IFF/data links; standardized configurations), financial sustainability (ASAP/SAFE/EDF levers), and political cohesion (inter-member priority synchronization). Under these conditions, ESSI can become not only a technical shield but also a symbol of European deterrence and unity.

Situated on the Black Sea–Caucasus–Levant axis, Türkiye, as a frontline state, adds eastern and southern early-warning depth to the common ESSI/NATINAMDS picture; the geostrategic projection contributes to layered protection of high-value targets (energy, ports, air bases, logistics nodes). This contribution can occasionally be bounded by factors such as political frictions, export controls, and mission-configuration separation; yet negotiation capacity and flexible interfaces render these bounds manageable.

The HİSAR-A/O and SİPER lines, with design principles that prioritize inter-layer connectivity via C2/IFF/data links, serve the goals of multi-layer protection and area defence. The HİSAR-A/O and SİPER lines, with design principles that prioritize inter-layer connectivity via C2/IFF/data links, serve the goals of multi-layered defence and regional area defence. This line bears technical contribution potential to ESSI's upper-tier requirements through (i) scalable interceptor production, (ii) standardized C2/data-link/IFF interface packages, and (iii) joint test–evaluation and certification pipelines. SİPER Block-1 has a confirmed range of 100+ km; with growth blocks, the roadmap extends to 180 km scale. Steel Dome is foregrounded as an integration move that brings radar–C2–effector clusters together under a vendor-agnostic logic. This line bears technical contribution potential to the upper-layer requirements within ESSI—new production, new interfaces, and joint test–certification.

NATINAMDS doctrine elevates common tactical picture and common engagement management to the level of a legal–technical requisite. (a network of interconnected national and NATO systems; sensors, command and control facilities and weapon systems.) In this context, as repeatedly underlined by NATO leadership, the S-400's non-integration into NATINAMDS has produced a dual-configuration model for national vs alliance missions in Türkiye; it has increased the priority of indigenous solutions (HİSAR/SİPER) and the Steel Dome integration. ESSI's technical effectiveness depends on the extent to which systems of different provenance can be brought to full-compliance with the alliance network.

4. Discussion

This study confirms the literature's core proposition that layered air and missile defence yields deterrence value only when sensors, command-and-control, data links, and effectors are designed and employed as an integrated operational fabric, rather than as parallel national inventories (Düz & Koçakoğlu, 2025). In this frame, ESSI is best understood as a capability accelerator that translates NATO's operational requirements into EU-enabled procurement and industrial scaling: NATINAMDS provides the doctrinal backbone (procedures, engagement authorities, and the common tactical picture), while ESSI compresses acquisition timelines and standardizes interfaces across national force-development lines (AIRCOM, 2023). The strategic autonomy–U.S. dependence debate embedded in ESSI membership politics is therefore more accurately treated as a sequencing problem—closing urgent gaps with interoperable off-the-shelf solutions while building European industrial depth over the medium term through coordinated investment (Düz & Koçakoğlu, 2025).

Against this backdrop, Türkiye's role is coherent. Geostrategically, its position on NATO's south-eastern flank expands early-warning reach and helps secure key corridors linking the Black Sea, the Straits, and the Eastern Mediterranean, strengthening NATO's distributed sensor and C2 architecture (NATO, 2024a). Capability-wise, Türkiye's layered GBAD trajectory—dense lower tiers, a maturing MRAD backbone, and SİPER at the upper layer—aligns with NATO's network-centric IAMD logic, especially when paired with the Steel Dome concept's platform-agnostic, C2-first integration approach (ASELSAN, 2021; Düz & Koçakoğlu, 2025).

Europe's integrated air and missile defence (IAMD) debate has matured from a question of which systems to a more demanding question of how systems cohere and endure as a federation over time. Recent analyses converge on three structural bottlenecks: (i) fragmentation risks rooted in heterogeneous acquisitions and political contestation, (ii) the strategic autonomy–dependence tension created by reliance on non-European interceptors and sustainment chains, and (iii) a persistent gap between declared ambition and deployable, sustainable volume (Monaghan & Christianson, 2023; Wachs, 2023; International Institute for Strategic Studies [IISS], 2025). Building on this baseline, the present study assesses the European Sky Shield Initiative (ESSI) as a capability-acceleration and standardization pathway for Europe's ground-based air and missile defence, and evaluates Türkiye's potential role within an integrated, NATO-aligned air and missile defence ecosystem.

A key contribution of the article is methodological and implementation-oriented: it couples an ESSI participation–capability overview with a Türkiye-focused layered map and interface analysis, thereby translating policy-level debate into concrete integration variables. While the literature appropriately foregrounds strategic and governance dilemmas, the argument here is that integration is ultimately decided at the interface level—specifically, where sensor–command-and-control (C2) coupling, data-link/IFF harmonization, and certification–testing pathways convert procurement into interoperable readiness (Monaghan & Christianson, 2023; IISS, 2025). In this sense, the study does not merely restate the fragmentation/autonomy/volume triad; it specifies where standardization pressure becomes binding and how it can be operationalized through measurable work packages.

From an operational standpoint, the discussion aligns with NATO IAMD logic that stresses fused situational awareness, track quality, and engagement coordination as core determinants of effectiveness. Accordingly, ESSI's added value is better measured not only by "what was bought" but by what was integrated, exercised, and sustained—a distinction that is increasingly salient under contemporary saturation conditions dominated by mixed salvos of missiles, drones, and electronic warfare (Wachs, 2023). The Ukraine war has reinforced this operational logic by demonstrating that deterrence by denial is not achieved through gradual, piecemeal modernization. Credible protection requires a layered-in-depth design from the outset, where lower-tier (VSHORAD/SHORAD/MRAD) and upper-tier (LRAD/BMD) elements are conceived as a single fabric—sensors, C2, data links, identification, and engagement coordination—rather than as separately optimized procurements. Interoperability is therefore a hard requirement, not a preference: capabilities that cannot connect to the NATO backbone on day one tend to generate friction, duplication, and blind spots that are costly to rectify under crisis pressure (IISS, 2025; Muravska, 2023).

A second operational principle follows directly: sustainment is strategy. Stockpiles, industrial surge capacity, maintenance pipelines, trained crews, and validated C2 federation before crisis onset are decisive variables in long-duration, high-tempo scenarios. This emphasis is consistent with strategic assessments warning that without predictable serial production, sustainment planning, and work-share arrangements, layered GBAD remains vulnerable to single-point supply constraints and political gating of support chains (IISS, 2025). The policy instruments referenced in the manuscript—SAFE/EDF/PESCO—support the claim that Europe is simultaneously seeking to accelerate procurement and thicken industrial capacity; however, these instruments only translate into operational credibility when anchored to interoperability interfaces and testing regimes that keep national systems mutually usable across capitals (Muravska, 2023). Joint procurement, shared spares, and common certification are not administrative conveniences; they are mechanisms of endurance.

Within this frame, ESSI is best understood as a cooperation instrument that translates shared threat perception into shared procurement and common interfaces. It complements NATO's integrated architecture by accelerating fielding and standardization, while NATO provides the doctrinal and technical anchor—common procedures, a shared tactical picture, and the legal–technical discipline required for sustained mutual usability across national inventories (Muravska, 2023). Where politics pulls in different directions—most notably in the autonomy–dependence debate—sequencing becomes a practical governance solution: close urgent gaps with available options now, while scaling European industrial depth over the medium term, rather than deferring operational readiness in pursuit of an ideal end-state that remains contested (Monaghan & Christianson, 2023; IISS, 2025).

Türkiye's potential contribution to this ecosystem emerges at the intersection of geographic exposure, alliance embeddedness, and an increasingly diversified sensor–effector portfolio. While ESSI is primarily an EU/European initiative, its operational logic is NATO-facing; therefore, Türkiye's role is more accurately conceptualized not as a political add-on but as a potential integration and industrial partner in the broader NATINAMDS-compatible ecosystem—provided that interface governance and standardization requirements are explicitly embedded in cooperative frameworks (Düz & Koçakoğlu, 2025). Here, the study's interface-centred approach matters: Table 3 functions as the paper's "translation device" between policy-level discussion and implementable integration variables. By mapping Türkiye's layered GBAD/IAMD capabilities and indicating ESSI-relevant interfaces (radars and sensors, C2 nodes, datalinks/IFF, and interceptor families), Table 3 makes explicit where interoperability work packages, joint testing, and certification pathways would be required. This linkage is designed to answer the editorial concern regarding the manuscript's original contribution: the novelty lies in specifying the integration agenda in operationalizable terms rather than treating cooperation as an abstract political aspiration.

Substantively, Türkiye's role can be articulated along three measurable axes. First, along the capability and sustainment axis, a layered posture spanning lower, medium, and upper tiers can be scaled in production and sustained through mature subcomponents and industrial processes that underpin magazine depth and repairability under high-tempo conditions (IISS, 2025; Düz & Koçakoğlu, 2025). Second, along the integration axis, sensor–C2–data-link fusion designed for immediate interoperability with Alliance architectures can support a coherent common operating picture, reliable cross-border identification and handoff, and institutionalized testing/certification/training pipelines; when paired with joint stockpiles and harmonized maintenance regimes, this reduces friction costs and shortens time-to-effect (Monaghan & Christianson, 2023; Muravska, 2023). Third, along the geographic axis, Türkiye's position at the junction of the Black Sea, the Straits, the Eastern Mediterranean, and the Levant can extend early-warning depth, protect critical corridors, and provide flexible C2 relay paths on the Alliance's south eastern flank—features that harden the wider theatre against saturated missile and uncrewed-system campaigns and associated electronic-warfare pressures (Wachs, 2023; Düz & Koçakoğlu, 2025).

These conclusions should be read in light of limitations typical of open-source policy-technical assessments. Public data on exact interceptor performance, integration maturity, and classified C2 architectures is partial; accordingly, the findings prioritize structural constraints, interface logic, and bounded inferences over definitive performance claims. Nevertheless, the evidence supports a clear strategic inference: ESSI's utility will be decided less by the elegance of its architecture than by disciplined integration and repeatable operationalization—common interfaces, joint testing, and sustained readiness (IISS, 2025; Monaghan & Christianson, 2023). Within these parameters, Türkiye can function not only as a geographic node but as an industrial and integration partner, provided cooperation is structured around standards compliance, shared work packages, and measurable interoperability outputs (Muravska, 2023; Düz & Koçakoğlu, 2025).

5. Conclusion

This study finds that the effectiveness of Europe's air and missile defence rests on the ability to integrate national systems into a coherent operational structure. The ESSI contributes by accelerating procurement and promoting common technical standards, while NATO's NATINAMDS framework provides shared doctrine, command-and-control, and a common operational picture. Persistent challenges such as fragmentation, reliance on non-European systems, and insufficient sustainable capacity cannot be addressed through platform selection alone. Instead, operational credibility depends on interface-level integration, including sensor fusion, command-and-control coordination, data-link compatibility, and structured testing. In this sense, ESSI's value is determined by sustained interoperability and readiness rather than procurement outcomes.

Within this NATO-oriented framework, Türkiye emerges as a complementary actor with tangible operational relevance. Its position on the Alliance's south-eastern flank and its layered air defence development support early warning, regional coverage, and command-and-control continuity. The analysis indicates that Türkiye's contribution is strongest when cooperation is organized around shared standards, joint testing, and interoperable command-and-control arrangements. Despite the limits of open-source data, the findings support a clear conclusion: ESSI's long-term effectiveness depends on disciplined integration, industrial sustainment, and repeatable operational practices. Under these conditions, Türkiye can function as a credible geographic and integration partner in Europe's evolving air and missile defence architecture.

Future research should extend the present interface-focused approach in three complementary directions. First, quantitative force-planning and campaign-sustainment modelling should be developed for layered GBAD under mass-attack conditions. Such modelling would estimate required interceptor consumption rates, resupply timelines, repair cycles, and the sensitivity of readiness to industrial surge capacity, thereby allowing ESSI-related procurement decisions to be tested against endurance requirements rather than nominal inventories (IISS, 2025; Monaghan & Christianson, 2023).

Second, interoperability outcomes should be examined empirically through exercises, test campaigns, and certification pathways. This line of work would focus on measurable integration indicators—track fusion performance, identification robustness, cross-border engagement handoff, and latency/resilience of C2 and data-link architectures—making it possible to evaluate whether procured capability has translated into usable capability at NATO-network standards (Muravska, 2023; IISS, 2025).

Third, industrial resilience should be analysed as an independent determinant of IAMD credibility. Comparative work on supply chains, licensed production, component dependencies, maintenance ecosystems, and workforce pipelines would clarify how quickly layered architectures can be thickened, repaired, and sustained under political friction or supply disruption (IISS, 2025; Wachs, 2023). Taken together, these research avenues would operationalize the manuscript's core claim: that IAMD credibility hinges on the triad of integration, sustainment, and governance discipline, and that cooperation frameworks should be evaluated against those variables rather than headline procurement figures.

Conflict of Interest

The authors declare that they have no known competing financial interests or personal relationships that could have appeared to influence the work reported in this paper. The authors also declare no non-financial competing interests relevant to the subject matter of this manuscript.

Funding

This research received no external funding.

Acknowledgments

The authors would like to express their heartfelt gratitude to their families for their unwavering support and patience throughout the duration of this research. Furthermore, the authors wish to thank the Secretariat of Defence Industries (SSB) and the Defence Industries Academy (SSA) for their invaluable contributions and for providing the intellectual platform through the Journal of Defence and Security Industries (JDSI) to share these findings with the defence community.

Ethical Statements

This study is based on publicly available data and literature; therefore, it did not involve human participants or animal subjects. Ethical approval was not required for this research.

Data and Code Availability

Data sharing is not applicable to this article as no new datasets were generated or analysed. All information used in this study is derived from publicly available sources cited in the manuscript.

Supplementary Materials

No supplementary materials are associated with this article.

References

Air Force Technology. (2025, August 4). Slovenia orders additional IRIS-T SLM units. *Air Force Technology.* https://www.airforce-technology.com/news/slovenia-iris-t-slm-units/

Allied Air Command. (2021, January 29). For 60 years Allies have collectively secured NATO airspace. *Allied Air Command.* https://ac.nato.int/archive/2021/for-60-years-allies-have-collectively-secured-nato-airspace

armasuisse. (2025, July 22). *GBAD MR: Contract on cooperative procurement for medium-range ground-based air defence signed.*

ASELSAN. (n.d.). *Siper 1, Siper 2.* https://www.aselsan.com/en/defence/product/3022/siper-1-siper-2

ASELSAN. (2021, April). *HERİKKS: Air defence early warning and C4I system* [Brochure]. https://wwwcdn.aselsan.com/api/file/HERIKKS_ENG.pdf

Council of the European Union. (2025, May 27). *SAFE: Council adopts €150 billion boost for joint procurement on European security and defence* [Press release]. https://www.consilium.europa.eu/en/press/press-releases/2025/05/27/safe-council-adopts-150-billion-boost-for-joint-procurement-on-european-security-and-defence/

Council of the European Union. (2025, September 18). *Defence investment: Council authorises negotiations with the UK and Canada on their participation in SAFE* [Press release]. https://www.consilium.europa.eu/en/press/press-releases/2025/09/18/defence-investment-council-authorises-negotiations-with-the-uk-and-canada-on-their-participation-in-safe/

Council of the European Union. (2025, December 8). *European Defence Industry Programme: Council gives final approval* [Press release]. https://www.consilium.europa.eu/en/press/press-releases/2025/12/08/european-defence-industry-programme-council-gives-final-approval/

Defence Industry Europe. (2023a, December 3). *Austria plans to strengthen air defence with long-range system* [News]. https://defence-industry.eu/austria-plans-to-strengthen-air-defence-with-long-range-system/

Defence Industry Europe. (2023b, November 2). *Hungary boosts air defence capability with NASAMS system* [News]. https://defence-industry.eu/hungary-boosts-air-defence-capability-with-nasams-system/

Defence Industry Europe. (2024, November 18). *Air defence: Portugal orders ForceShield VSHORAD system from Thales.* https://defence-industry.eu/air-defence-portugal-orders-forceshield-vshorad-system-from-thales/

Defence Industry Europe. (2025a, March 17). *Czech Republic: First battery of Spyder air defence system completed and undergoing testing.* https://defence-industry.eu/czech-republic-first-battery-of-spyder-air-defence-system-completed-and-undergoing-testing/

Defence Industry Europe. (2025b, December 11). *Sweden places new order for IRIS-T SLS air defence systems and logistics support from Diehl Defence.* https://defence-industry.eu/sweden-places-new-order-for-iris-t-sls-air-defence-systems-and-logistics-support-from-diehl-defence/

Defence News. (n.d.). *Top 100 for 2025.* Retrieved December 18, 2025, from https://people.defensenews.com/top-100/

Defence News. (2021, March 30). *Three companies make a joint run for Germany's new air defence program.* https://www.defensenews.com/global/europe/2021/03/30/three-companies-make-a-joint-run-for-germanys-new-air-defense-program/

Defence News. (2023, December 4). *Latvia signs order for German IRIS-T air defences.* https://www.defensenews.com/global/europe/2023/12/04/latvia-signs-order-for-german-iris-t-air-defenses/

Defence News. (2024a, August 29). *Slovakia to buy Israeli Barak MX air-defence systems for $610m.* https://www.defensenews.com/global/europe/2024/08/29/slovakia-to-buy-israeli-barak-mx-air-defense-systems-for-610m/

Defence News. (2024b, February 16). *Türkiye and Greece to join European missile shield.* https://www.defensenews.com/global/europe/2024/02/16/Türkiye-and-greece-to-join-european-missile-shield/

Defence News. (2025, August 5). *Denmark to complete $3.4 billion of air defence purchases by year-end.* https://www.defensenews.com/global/europe/2025/08/05/denmark-to-complete-34-billion-of-air-defense-purchases-by-year-end/

Düz, S., & Koçakoğlu, M. S. (2025, February). *European Sky Shield Initiative: Capacities, criticisms, and Türkiye's contribution* (SETA Publications No. 261). SETA.

Estonian Defence Forces. (n.d.). *Air defence wing.* https://mil.ee/en/air-force/air-defence-wing/

European Commission. (n.d.). *European Defence Fund (EDF): Official webpage.* https://defense-industry-space.ec.europa.eu/eu-defense-industry/european-defense-fund-edf-official-webpage-european-commission_en

European Commission. (2024a). *European Defence Industry Programme (EDIP): Factsheet.* https://defence-industry-space.ec.europa.eu/document/download/638c4482-0715-4aef-ac86-6529ce2dfd4b_en?filename=DEFIS_EDIP_factsheet.pdf

European Commission. (2024b, March 1). *European Defence Industrial Strategy (EDIS): Factsheet.* https://defence-industry-space.ec.europa.eu/document/download/333faee1-a851-44a6-965b-713247515d39_en?filename=DEFIS_EDIS_factsheet.pdf

European Commission. (2025, February 23). *Energy security support package for Ukraine* [Press release]. https://ec.europa.eu/commission/presscorner/detail/en/ip_25_588

European Commission, Directorate-General for Defence Industry and Space. (2021, April). *The European Defence Fund (EDF)* [Factsheet]. https://defense-industry-space.ec.europa.eu/system/files/2021-04/20210429%20-%20EDF%20Factsheet.pdf

European Commission, Directorate-General for Defence Industry and Space. (2025, May 8). *Commission mobilises €910 million to boost European defence and close capability gaps* [Press release]. https://defence-industry-space.ec.europa.eu/commission-mobilises-eu910-million-boost-european-defence-and-close-capability-gaps-2025-05-08_en

European Commission, Directorate-General for Neighbourhood and Enlargement Negotiations. (2024, April 9). *EU sends emergency aid to Ukraine after further attacks on energy infrastructure.* https://enlargement.ec.europa.eu/news/eu-sends-emergency-aid-ukraine-after-further-attacks-energy-infrastructure-2024-04-09_en

European Defence Agency. (2024). *CARD report 2024.* https://eda.europa.eu/docs/default-source/documents/card-report-2024.pdf

European Defence Review. (2024, December 20). *Norway acquires more NASAMS air defence systems.* https://www.edrmagazine.eu/norway-acquires-more-nasams-air-defence-systems

European External Action Service. (2024, June 12). *Statement by the G7+ Energy Coordination Group and the Government of Ukraine (Ukraine Recovery Conference 2024).* https://www.eeas.europa.eu/eeas/statement-g7-energy-coordination-group-and-government-ukraine-ukraine-recovery-conference-2024_en

European External Action Service. (2025, July 16). *Russian hybrid threats: EU lists nine individuals and six entities responsible for destabilising actions (notes GNSS disruptions).* https://www.eeas.europa.eu/delegations/ukraine/russian-hybrid-threats-eu-lists-nine-individuals-and-six-entities-responsible-destabilising-actions_en

European Parliament. (2024, April 23). *Stepping up efforts to set up a collective integrated air defence system* (Written question E-001198/2024). https://www.europarl.europa.eu/doceo/document/E-9-2024-001198_EN.html

Federal Ministry of Defence of the Republic of Austria. (n.d.). *The Austrian Air Force – In the past and today.* https://www.bmlv.gv.at/english/forces/airforce.shtml

House of Commons Library. (2025, June 13). *UK defence in 2025: Integrated air and missile defence* (CBP-10249). https://commonslibrary.parliament.uk/research-briefings/cbp-10249/

International Institute for Strategic Studies. (2025). *European integrated air and missile defence. In Progress and shortfalls in Europe’s defence (Strategic Dossier).* https://www.iiss.org/globalassets/media-library---content--migration/files/publications---free-files/strategic-dossier/pds-2025/chapters/iiss_progress-and-shortfalls-in-europes-defence_2025_ch-3_integrated-air-and-missile-defence.pdf

International Trade Administration. (2022, August 12). *Switzerland country commercial guide: Selling to the public sector.* https://www.trade.gov/country-commercial-guides/switzerland-selling-public-sector

Lithuanian Armed Forces. (2020, June 19). *NASAMS medium-range air defence systems delivered to Lithuanian Air Force.* https://kariuomene.lt/en/newsevents/nasams-medium-range-air-defence-systems-delivered-to-the-lithuanian-air-force/22167

Mills, C. (2025, June 13). *UK defence in 2025: Integrated air and missile defence* (Ch. 2: UK air defence capability; CBP-10249). https://researchbriefings.files.parliament.uk/documents/CBP-10249/CBP-10249.pdf

Missile Defence Advocacy Alliance. (n.d.). *Hungary*. https://missiledefenseadvocacy.org/intl_cooperation/hungary/

Missile Defence Advocacy Alliance. (2025, October 8). *Bulgaria equips air defence units with IRIS-T missile system.* https://missiledefenseadvocacy.org/missile-defense-news/bulgaria-equips-air-defense-units-with-iris-t-missile-system/

Monaghan, S., & Christianson, J. (2023, May 19). *Making the most of European air and missile defence: The strategic and operational implications of Sky Shield. Center for Strategic and International Studies.* https://csis-website-prod.s3.amazonaws.com/s3fs-public/2023-05/230519_Monaghan_European_SkyShield.pdf

Muravska, J. (2023, October 4). *European integrated air and missile defence*. King's College London. https://www.kcl.ac.uk/warstudies/assets/paper-16-julia-muravska-european-integrated-air-and-missile-defence.pdf

NAMFI. (n.d.). *Welcome to NATO Missile Firing Installation.* https://www.namfi.gr/

NATO. (2024a, August 1). *Ballistic missile defence* [Topic page]. https://www.nato.int/cps/en/natohq/topics_49635.htm

NATO. (2024b, March 4). *NATO completes modernisation of major airbase in Albania.* https://www.nato.int/en/news-and-events/articles/news/2024/03/04/nato-completes-modernisation-of-major-airbase-in-albania

NATO. (2025, February 13). *NATO launches two new multinational air defence initiatives, strengthens existing projects* [News]. https://www.nato.int/en/news-and-events/articles/news/2025/02/13/nato-launches-two-new-multinational-air-defence-initiatives-strengthens-existing-projects?selectedLocale=

Reuters. (2025, November 27). *Romania signs deal to buy French Mistral air defence systems.* https://www.reuters.com/business/aerospace-defense/romania-signs-deal-buy-french-mistral-air-defence-systems-2025-11-27/

Rheinmetall. (2025, December 12). *Major order from the Netherlands: Rheinmetall to supply Skyranger 30 for mobile air defence – Order value in the high triple-digit million euro range* [Press release]. https://www.rheinmetall.com/en/media/news-watch/news/2025/12/2025-12-12-rheinmetall-to-supply-skyranger-30-for-the-dutch-armed-forces

Roketsan. (n.d.). *Home.* https://www.roketsan.com.tr/tr

Stockholm International Peace Research Institute. (2025). *The SIPRI Top 100 arms-producing and military services companies in the world, 2024.* Retrieved December 18, 2025, from https://www.sipri.org/visualizations/2025/sipri-top-100-arms-producing-and-military-services-companies-world-2024

U.S. Army. (2025, September 22). *Republic of Poland's NAREW program successfully conducts live-fire test.* https://www.army.mil/article/288660/republic_of_polands_narew_program_successfully_conducts_live_fire_tes

Wachs, L. (2023, August 3*). Russian missiles and the European Sky Shield Initiative: Air defence in the current threat environment* (SWP Comment 2023/C 45). Stiftung Wissenschaft und Politik. https://doi.org/10.18449/2023C45

JOURNAL OF DEFENCE AND SECURITY INDUSTRY

Journal of Defence and Security Industries: Strategy and Technology, 2026, 1(1)

Science & Technology Section

The Design Optimization of Multi-Band Microstrip Patch Antennas for GNSS Application

Ahmet Can Güney [1], Ahmad Salmanogli [1,*]

Abstract

This study simulates and analyses a dual-band microstrip patch antenna designed to be optimal for Global Navigation Satellite System usage in the L2 (1227.60 MHz) and L5 (1176.45 MHz) bands. This research focuses on designing a single antenna element to receive signals from multiple Global Navigation Satellite System (GNSS) constellations operating over the L2 and L5 frequency bands. The antenna design presented herein utilizes a novel technique that combines a slotted patch configuration with a defective ground plane to achieve dual-band functionality while maintaining the miniaturization and low-profile characteristics of the structure. Full-wave numerical simulations were performed using a finite element-based electromagnetic solver to fine-tune various performance parameters, such as S_{11} bandwidths, radiation patterns, and realized gain of this proposed microstrip slot-patch antenna structure implemented on a high-frequency electronic material substrate. The effects of different design factors, including substrate selection and characteristics, as well as variation in the length-width ratio of the rectangular patch strip, are also investigated, and their influence on key antenna performance metrics is analysed. This study contributes to the field of GNSS antenna design by presenting a cost-effective and efficient dual-band solution that can be easily integrated into modern navigation devices. In addition, this study explains how much more gain the antennas in the L2 and L5 bands of the GNSS provided in the antenna array with different feeding techniques.

Keywords: GNSS, GPS, microstrip patch antenna, dual-band, antenna design.

Received: 02.11.2025 Accepted: 21.12.2025 Research Article

[1] Department of Electrical-Electronics Engineering, Ankara Yıldırım Beyazıt University, Ankara, Türkiye
* Corresponding author.
✉ ahmadsalmanoghli@aybu.edu.tr

Cite this article as: Guney, A.C. & Salmanogli, A. (2026). The design optimization of multi-band microstrip patch antennas for GNSS application. *Journal of Defence and Security Industry: Strategy and Technology 1*, 57-70.

1. Introduction

The main objective of this study is to explain the benefits of an antenna array compared to a single antenna, the differences that occur, and their importance according to the locations where they are applied (Pozar, 1992). Microstrip patch antennas are widely used in radar, communication, and navigation systems on aircraft platforms. In addition, this type of antenna is preferred for use in satellite communication and remote sensing radars. Moreover, in almost all mobile satellite telephones, microstrip patch antennas are chosen to use. (Garg, Bhartia & Bahl, 2001; Kraus,1988; Pandey, 2019). The microstrip antenna was first invented during the 1960s and 1970s (Deschamps, 1953; Munson, 1974). The concept of the microstrip patch antenna was first introduced by Deschamps in 1953. However, its widespread development and practical implementation were largely realized in the 1970s, primarily due to advancements in substrate materials and fabrication techniques, as demonstrated in the pioneering works of Munson (1974).

From the 1980s to the present, significant advances have been achieved in phased array antennas, smart antennas, and Multiple-Input Multiple-Output (MIMO) systems (Balanis, 2008). Microstrip antenna arrays investigated to date have generally employed the inset-feed technique and have operated at 2.4 GHz using substrates with a dielectric constant of 2.2. Singh et al. (2014) proposed 2×1 and 4×1 inset-fed antenna arrays for Global Positioning System (GPS) applications, utilizing a substrate with a dielectric constant of 2.2 and a thickness of 1.588 mm. Notably, the S_{11} values reported by Singh et al. (2014) are approximately 50% lower than those reported by Balanis (2008), indicating improved impedance matching performance.

Similar to Singh et al. (2014), Khraisat (2012) demonstrated 2x1 and 4x1 inset feed microstrip antenna arrays operating at 2.4-2.5 GHz using the same substrate material and thickness. The proposed antenna (Joshi et al., 2020) is characterized as a dual-band apparatus, functioning at 2.45 GHz for WLAN (Wireless Local Area Network) functionalities and 1.575 GHz for GPS, augmented by incorporating an artificial magnetic conductor plane. Furthermore, a realized gain of around 2 dBic at 1.575 GHz and 1.9 dBi at 2.45 GHz were obtained from the functioning of the AMC plane at 2.45 GHz. Additionally, Zhong et al. (2019) have proposed another antenna for GPS applications that also operates within dual frequency bands. In Zhong’s design, the gain value of the antenna is not exceeded 3.15 dBic, which means almost 6 dBi.

In a recent study, Dündar and Ateş (2024) proposed an L5-band microstrip antenna design. However, the specific feeding technique used in the antenna structure was not described in detail. In this study, the antenna designed with dimensions of 77x63.56x1.6mm achieved 6.07dBm directivity and -38.85dB S_{11} values (Dündar & Ateş, 2024). The dimensions of the antenna designed by Dündar and Ateş are slightly larger than the one in this study, and its directivity value is lower, reaching around 15%.

Ayad et al. (2022) designed a microstrip patch antenna for use in GPS applications in the L1 band. After numerous optimizations, they achieved a maximum S_{11} value of -24.80 at 1.575

GHz. To achieve these values, they required an antenna measuring 95x82x2.1mm made from FR-4 material with a relative permittivity of 4.3 (Ayad et al., 2022). After numerous optimizations, they achieved a maximum S_{11} value of -24.80 at 1.575 GHz. To achieve these values, they needed an antenna measuring 95 mm x 82 mm x 2.1 mm made from FR-4 material with a relative permittivity of 4.3. Although the S_{11} value obtained in this study is satisfactory, the antenna dimensions require twice the volume.

In a recent piece of research, Basar et al. (2023) designed an antenna with a slot measuring 56x56mm, operating in the L1 band, using FR-4 material with a thickness of 1.6 mm. With this design, the researchers achieved an S_{11} value of up to -35dB and measured the resonant frequency as 1.590 GHz instead of 1.575 GHz (Basar et al., 2023). Compared to the work that achieved a maximum directivity value of 8.64 dBi with a 22.725 mm slot, this study required more than three times the transmission line for the values included in this work and also required a wide antenna slot.

Concerning these studies, the one presented here differs in terms of the feed type of the antennas, the substrate material chosen, and the operating frequency. The innovative aspect of this study is the comparison of two different feed antennas operating at the same frequency in terms of gain, bandwidth, S_{11}, and Voltage Standing Wave Ratio (VSWR). Furthermore, unlike other studies, this work is designed to operate in the L2 and L5 bands of GNSS systems with more gainful antennas. The L2 band in GNSS systems is used for high-precision positioning. Furthermore, antennas operating in the L2 band, which is used in military radar applications, can largely eliminate ionospheric errors. This paper compares the performance of antennas that use the same feeding method but operate at different frequencies. It also discusses the different behaviour of the antenna array compared to a single antenna using the same frequency and feeding method.

2. Methodology

Numerous crucial considerations and computations are needed to construct a microstrip patch antenna. These criteria must be considered to ensure the best performance for the intended application. Prioritizing the selection of the operating or resonant frequency and substrate material is essential. The substrate's primary role in microstrip antennas is to support the antenna structurally. To be effective, the substrate must be composed of a dielectric material, which can influence the circuits, the electrical efficiency of the antenna, and the transmission line impedance. The substrate should possess the minimal thickness. In this context, a height between $0.01\lambda_0$ and $0.05\lambda_0$ is deemed optimal. A height of $0.01\lambda_0$ to $0.05\lambda_0$ is regarded as ideal in this regard. After that, the feeding type is selected. Then, with the knowledge of resonant frequency and substrate material values, the width of the antenna is calculated. To calculate the width, the free space wavelength and dielectric constant need to be used. Equation (1) is utilized for this purpose (Balanis, 2016).

$$W = \frac{\lambda_0}{2\sqrt{0.5(\varepsilon_r+1)}} \tag{1}$$

Where λ_0 and ε_r are the wavelength in free space and the dielectric constant of the substrate, respectively. λ_0 is the division of c_0 by f_0, resonant frequency. In the next step, the effective dielectric constant, ε_{eff}, can be calculated. The effective dielectric constant is directly proportional to the dielectric constant and inversely proportional to height of the dielectric material. The aim is to design and optimize using 1.6mm thick FR-4 dielectric material, both because it is the primary material used in PCB designs and because it offers mechanical durability, lower losses up to 1-2 GHz levels, and cost advantages for prototypes. This parameter has an important place in the calculation of the effective width of the antenna. ε_{eff} can be calculate by using the following Equation (2) (Balanis, 2016).

$$\varepsilon_{eff} = \frac{\varepsilon_r+1}{2} + \frac{\varepsilon_r-1}{2}\left[1 + 12\frac{h}{W}\right]^{-1/2} \tag{2}$$

After that, the length of the rectangular patch can be calculated using Equation (3) (Pandey, 2019).

$$L = \frac{c_0}{2f_0\sqrt{\varepsilon_{eff}}} \tag{3}$$

with c_0 = 2.998 ×10^8 meter/second being the velocity of the electromagnetic wave in free space. The extension of the patch length due to the fringing effect, fringe factor, can be calculated using the following Equation (4) (Pandey, 2019).

$$\Delta L = 0.412h\frac{(\varepsilon_{eff}+0.3)\left(\frac{W}{h}+0.264\right)}{(\varepsilon_{eff}-0.258)\left(\frac{W}{h}+0.8\right)} \tag{4}$$

Hence, using Equation (3) and the line extension, the effective length, $L\ e\ f\ f$, of a rectangular antenna element by using Equation (5) (Pandey, 2019).

$$L_{eff} = \frac{c_0}{2f_0\sqrt{\frac{\varepsilon_{eff}+1}{2}}} - 2\Delta L \tag{5}$$

The impedance of an antenna defines the relationship between the voltage and current at its input. The usual impedance at the border of a resonant rectangular patch varies between 100 and 400 Ω, and the radiation impedance of a patch at the border can be estimated in Equation (6) (Pandey, 2019).

$$Z_a \approx 90\frac{{\varepsilon_r}^2}{\varepsilon_r - 1}\left(\frac{L}{W}\right)^2 \tag{6}$$

Input impedance Z_{in} is matched with a 50-ohm microstrip feed line impedance Z_0 (Pandey, 2019). The specific type of antenna and whether it is functioning at its resonant frequency influences the input or feed point impedance of an antenna. When the antenna is at resonance, its input impedance is ideally purely resistive, meaning it effectively accepts and transmits all the power from the source and behaves like a purely dissipative load. However, when operating off resonance, the impedance generally increases as reactive components come into play. If the edge impedance of the patch antenna is Z_a, then the input impedance seen from the beginning of the quarter-wavelength line is calculated in Equation (7) (Pandey, 2019).

$$Z_{in} = Z_0 = \frac{{Z_l}^2}{Z_a} \tag{7}$$

Input impedance Z_{in} can be changed by the selection of Z_l, so that Z_{in}= Z_0 and the antenna is matched by impedance. The impedance Z_l,load impedance or transition impedance, value varies with the width of the quarter-wavelength strip.

When *W/d* <1, the characteristic impedance of the line is Equation (8) (Huang & Boyle, 2008)

$$Z_0 = \frac{60}{\sqrt{\varepsilon_r}} \ln\left(\frac{8d}{W} + \frac{W}{4d}\right) > \frac{126}{\sqrt{\varepsilon_r}} \tag{8}$$

It decreases monotonically to $126/\sqrt{\varepsilon_r}$ as *W/d* increases to 1.

When *W/d* >1, the characteristic impedance of the line is Equation (9) (Huang & Boyle, 2008)

$$Z_0 = \frac{120\pi}{\sqrt{\varepsilon_r}(\frac{W}{d} + 1.393 + 0.667\ln(\frac{W}{d} + 1.44)} < \frac{126}{\sqrt{\varepsilon_r}} \tag{9}$$

It also decreases monotonically from $126/\sqrt{\varepsilon_r}$ W/d as it increases. From Equation (9), 70.71 Ohm is obtained to reach the 50 Ohm input line with two parallel 100 Ohm antenna input lines as illustrated in Figure 1. For the inset feed technique, 6 mm on the x-axis and 3.6 mm on the y-axis are cut from the patch using nickel material. The main reason for cutting is adjusting and obtaining targeted level of gain. Arranging multiple patch elements in an array can significantly increase directivity. The array factor combines with the element pattern to produce a more directive overall pattern (Pozar & Schaubert, 1995). λ /4 is more advantageous than the tapered line because of its straightforward structure, lesser volume, production which is very easy, and also it is good for single-frequency systems. Tapered line may be utilized over broader bands but will need longer physical dimensions (Pozar, 2011).

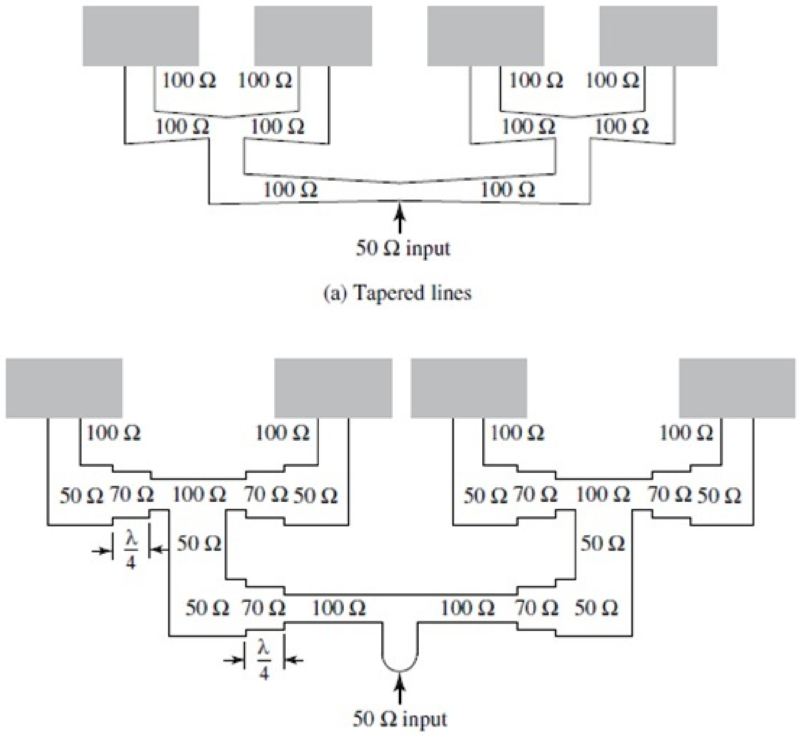

Figure 1. Tapered and λ/4 impedance transformer lines to match 100-ohm patches to a 50-ohm line (Balanis, 2016).

Table 1. Designed antennas parameter data.

	L2 Band Edge Feed	L5 Band Edge Feed	L2 Band Inset Feed	L5 Band Inset Feed
Substrate	FR-4	FR-4	FR-4	FR-4
Substrate Thickness (mm)	≈1.6	≈1.6	≈1.6	≈1.6
Patch Width (mm)	75.0604	78.3539	75.0604	78.3539
Patch Length (mm)	56.6500	58.8571	56.6500	58.8571
50 Ohm Feedline Width (mm)	3.13	3.1355	3.137	3.137
Single Patch Obtained Gain (dBi)	6.99	7.02	≈6.11	6.09
Single Patch S_{11} Value (dB)	-16.562	-17.172	-20.672	-22.168
Single Patch VSWR	1.3674	1.3231	1.2255	1.1875
50 Ohm Feedline Length For 2x1 Antenna Array (mm)	33.805	35.2749	33.8051	30.37
70.71 Ohm Feedline Width For 2x1 Antenna Array (mm)	1.641	1.606	1.641	1.641
100 Ohm Feedline Width For 2x1 Antenna Array (mm)	0.7235	0.7237	0.7235	0.7235
2x1 Array Obtained Gain (dBi)	8.988	8.984	8.987	8.979
2x1 Array S_{11} Value (dB) (Without magnitude)	-40.112	-41.456	-18.634	-20.783
2x1 Array VSWR	1.0218	1.0171	1.2655	1.2016
2x1 Array Current Distribution (dB)(A/m)	26.7455	25.2166	27.6212	25.1225

The work carried out up to this stage has been on the design and simulation of antennas at the specified frequencies in an electronic environment. In future studies, it is aimed to compare the results obtained from prototype production with simulation results.

3. Results

Many parameters need to be evaluated in designed antennas. First of all, S_{11}, the input reflection coefficient, values should be considered. The main reason for considering the S_{11} parameter affects the reflection coefficient, Voltage Standing Wave Ratio (VSWR), and also insertion loss values. The second important parameter of an antenna is the level of gain. The level of gain plays an important role in determining whether an antenna is sufficient for the intended use.

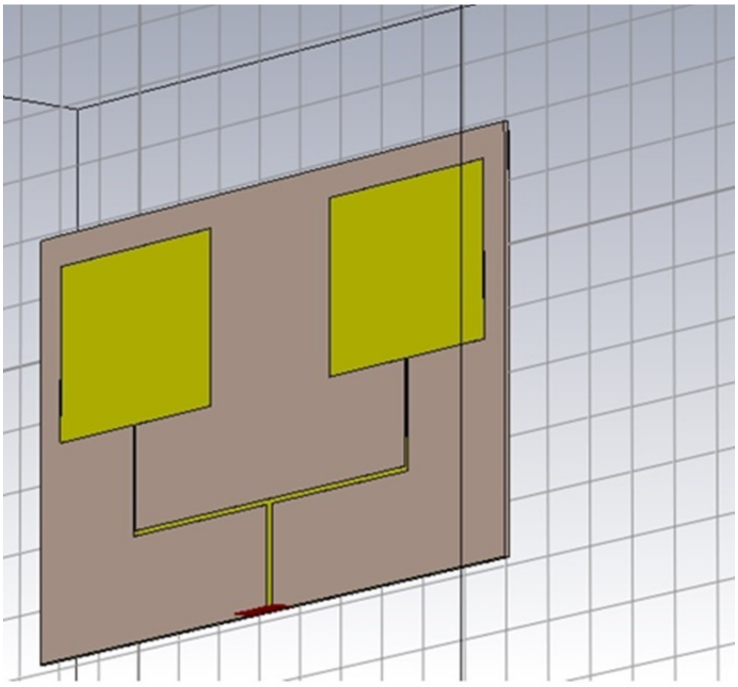

Figure 2. L2/L5 band edge feedline 2x1 microstrip patch antenna array.

According to the 2x1 antenna array shown in Figure 2 and the table and graph obtained in Figure 3, the L2 band edge feed antenna array has -40.112 S_{11} at 1224.4 MHz. This operating frequency is obtained after optimizing the patch length. If patch length is reduced, then frequency and bandwidth are increased. In this array, bandwidth is calculated around 32 MHz. These values are proof of having lower insertion loss. Furthermore, the gain of this feeding array is almost 9 dBi; even a single microstrip patch antenna with the same feeding cannot exceed 7 dBi. In addition, VSWR is 1.0218 and this value shows that this design is closer for impedance matching.

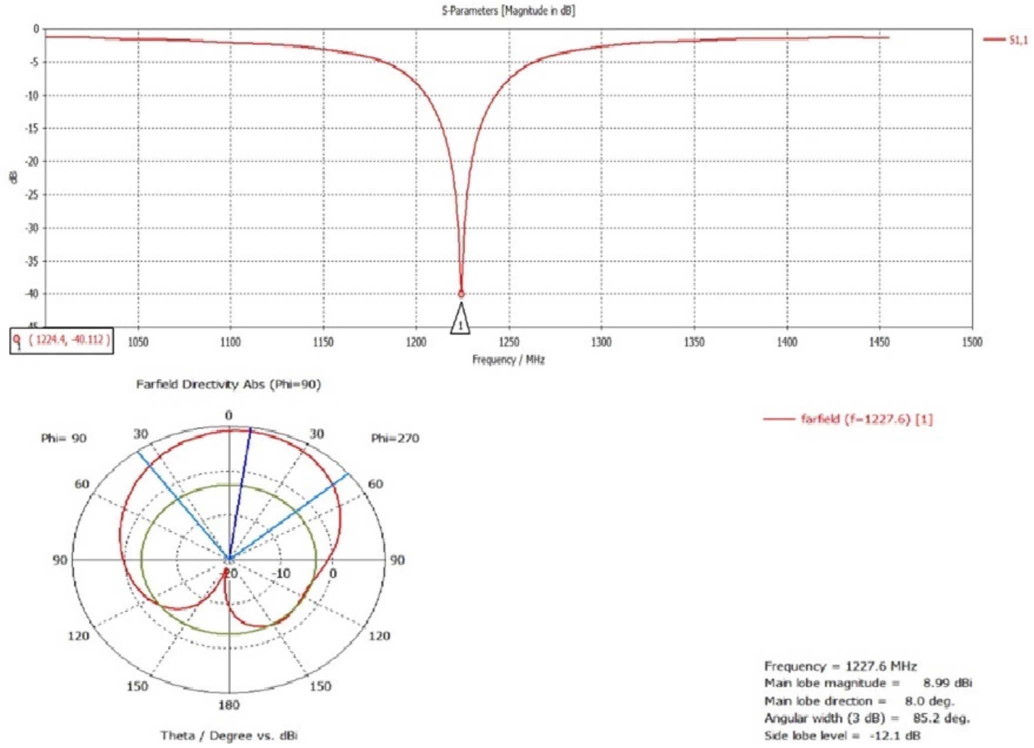

Figure 3. L2 Band edge feedline 2x1 microstrip patch antenna array S_{11} graph and directivity.

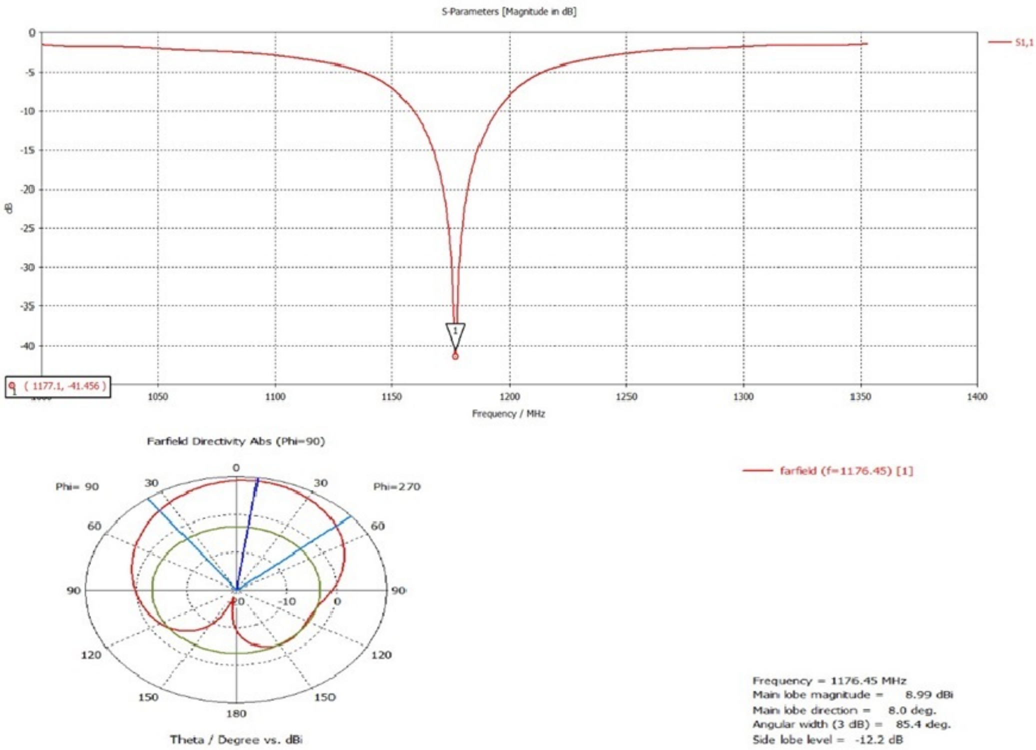

Figure 4. L5 band edge feedline 2x1 microstrip patch antenna array S_{11} graph and directivity.

The L5 band edge feed antenna array has a -41.456 S_{11} at 1177.1 MHz, as exhibited in Figure 4. This operating frequency is also obtained after optimizing the patch length. If patch length is reduced, then frequency and bandwidth are increased. VSWR for the L5 band array is 1.0171, and this band is much closer for impedance matching. The L5 band edge feed antenna array's bandwidth is roughly 35 MHz. Besides, the L5 band antenna array has almost the same gain as the L2 band application. This provides an upper limitation of this feeding method in terms of gain.

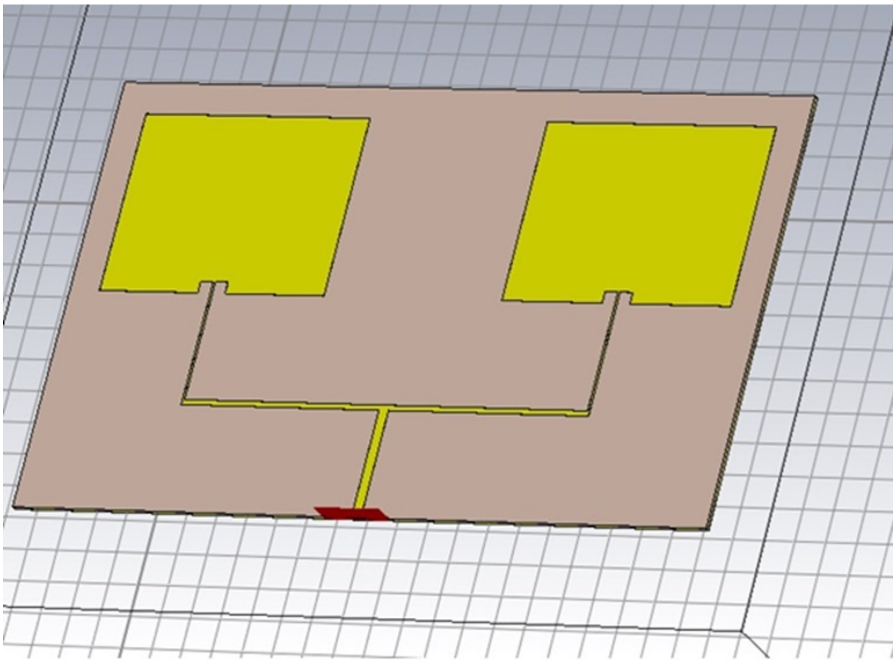

Figure 5. L2/L5 band inset feedline 2x1 microstrip patch antenna array.

Inset feedline is a feeding technique used in microstrip patch antennas. The feedline is recessed (inset) a certain distance into the antenna to match the antenna's input impedance to the feedline. This method ensures efficient antenna operation and low reflection loss.

Based on the 2x1 Inset feedline antenna array illustrated in Figure 5, along with the data and graph presented in Figure 6, the effect of changing the patch length on the S_{11} value can be clearly observed. The figure presents many different curves. The very small differences between the curves represent the S_{11} value at the frequency at which the antenna is intended to operate within the bandwidth. The L2 band inset feed antenna array has an S_{11} of -18.634 at 1226.7 MHz. At this frequency, the bandwidth is calculated to be approximately 31.3 MHz and the VSWR is 1.2655.

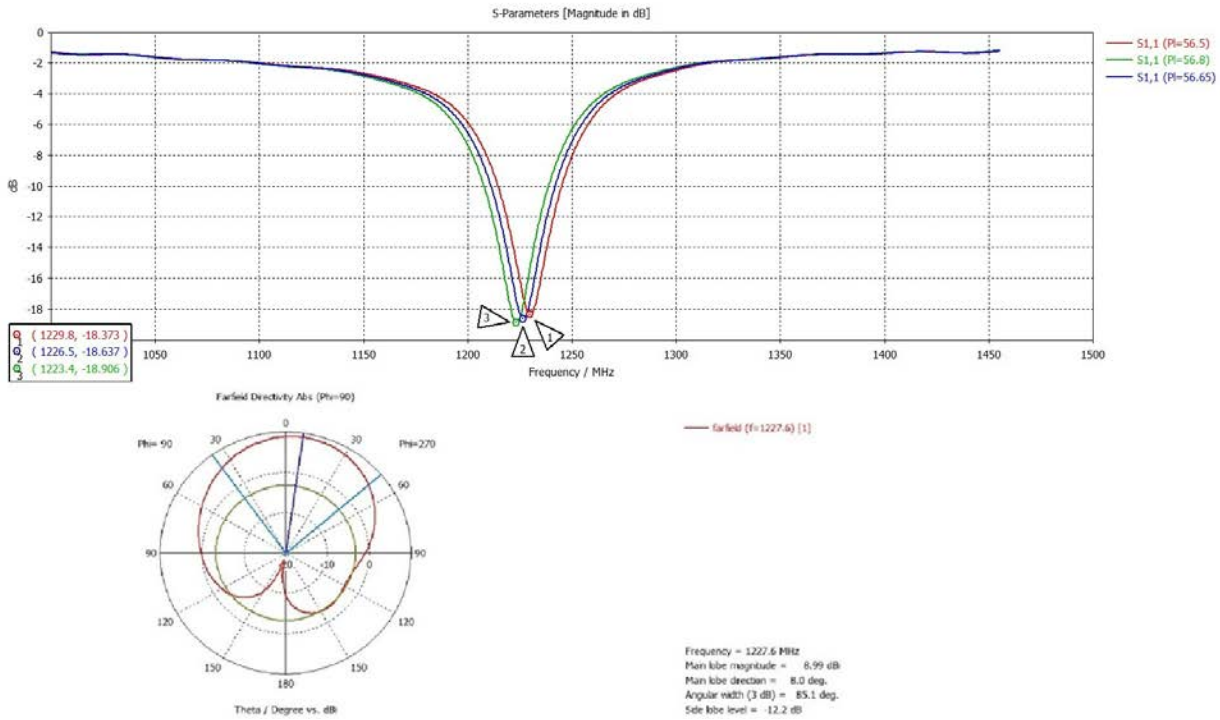

Figure 6. L2 band inset feedline 2x1 microstrip patch antenna array S_{11} graph and directivity.

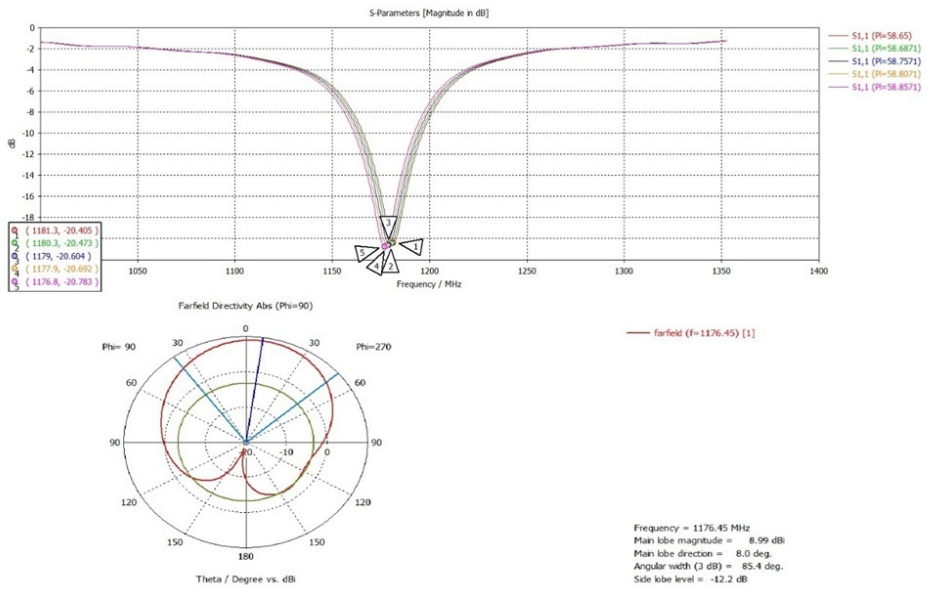

Figure 7. L5 band inset feedline 2x1 microstrip patch antenna array S_{11} graph and directivity.

As illustrated in Figure 7, one can distinctly discern the impact of varying the patch length on the S_{11} parameter. In the same illustration, numerous distinct curves are shown. The minimal variations among these curves are utilized to ascertain the S_{11} value at the frequency for which the antenna is designed to operate within the specified bandwidth. The L5 band inset feed antenna array has an S_{11} of -20.783 at 1176.8 MHz, and the VSWR is 1.2016. At this frequency, the bandwidth is calculated to be nearly 35 MHz.

4. Discussion

When the current distribution values and graphs of the designed antennas are examined, it is observed that the antennas exhibit similar characteristics and produce values that are close to each other. The antennas operating in the L2 band have the current distribution values of 26.7455 dB and 27.6212 dB for edge feed and inset feed, respectively, while those operating in the L5 band have values of 25.2166 dB and 25.1225 dB. After using the formulas required for antenna design and optimization through the Computer Simulation Technology Microwave Studio (CST MWS), it is noted that the antenna array with edge feed has greater gain. CST MWS is the application that does the simulation. The CST MWS that simulates the antenna design can display the antenna's return loss, VSWR, gain, directivity, radiation pattern, and efficiency. Additionally, the optimum width of the patch for the L2 band is obtained as 75.0604 mm, and the optimum length of the antenna at the same frequency is 56.650 mm. Furthermore, the optimum length for the L5 band is 58.8571 mm, while the optimum width is 78.3539 mm. For all antenna array designs, the VSWRs remain less than 2 (VSWR $\leq$ 2), despite the various gain values.

The results of the above-mentioned designs show that similar results are obtained in terms of both S_{11} values and gain values without using the slots that will increase the gain as in the antennas designed by Joshi et al. (2020). In addition, the S_{11} values of the 2x1 antenna array designed using the edge feed technique also indicate that although the gain values are similar to the antenna array designed by Yahya, they are transmitted more depending on the operating frequency. Ayad et al. (2022) showed that a larger and thicker antenna was required, yet a similar gain was achieved despite obtaining a worse VSWR value. In this context, it was demonstrated that this could be achieved with a smaller antenna size, even though there was not much difference in gain. Although the values in the study by Basar et al. (2023) appear to be close to those in this study, they prevent the slot antenna used to obtain the maximum directivity value from being reduced to smaller dimensions. As long as small antenna dimensions are required in GNSS applications, the antenna dimensions obtained as a result of this study are shown to be more efficient and preferable.

In the study conducted by Dündar and Ateş (2024), no feedline information was provided for the antenna designed in the L5 band. The performance and characteristic properties exhibited by an antenna, depending on the type and features of the feedline, play a critical role in GNSS systems that typically employ a 50-ohm feeding impedance. All parameters of the antenna to be selected for the intended system or application are significant. Therefore, the selection of an antenna with well-defined feedline characteristics and performance should be prioritized. Considering that the feed characteristics presented in this study were developed under the assumption that GNSS antennas operate with a standard 50-ohm input impedance, their application is considered more appropriate for ensuring consistency and reliability in system design.

5. Conclusion

In this study, edge feed and inset feed at the L2 band and L5 band were designed for 2x1 microstrip patch antenna arrays. While designing the antenna, the initial parameters were determined using the formulas from the previous chapter, and then optimizations were performed with the CST MWS. According to the results, the edge feed method at the L2 and L5 bands for a single patch antenna provides nearly 7 dBi gain, even when different feeding techniques are applied. However, with the same parameters, inset feed ensures around 6.1 dBi gain. In some applications, these gain levels are not considered sufficient. In global navigation satellite systems, it is crucial that the gain level is as high as possible for the system to function more effectively. By carefully selecting the substrate material, optimizing the patch geometry, and implementing effective impedance matching strategies, designers can create microstrip patch antennas that operate with high performance in the L2 and L5 bands. For this reason, a 2x1 antenna array configuration is applied using inset feed and edge feed techniques. The inset feed L2 band 2x1 microstrip patch antenna achieves 47 percent more gain, while the edge feed technique provides 28 percent more gain. Additionally, for the L5 band, the inset feed L5 band 2x1 microstrip patch antenna achieves the same gain percentage as the L2 band inset feed application. Furthermore, the values and corresponding VSWR measurements indicate that the antenna array technique brings the antennas closer to an impeccable design. The closer the VSWR value is to 1, the more optimal the design becomes regarding impedance matching. Based on the S_{11} values of the antennas designed in this study, it is observed that nearly 100% of the power supplied to the antennas is utilized by the antennas, indicating very high efficiency. When the bandwidths, S_{11} values, and VSWR values obtained from the simulation results are evaluated together, the designs are considered suitable for GNSS systems. Upon analysis of the designs' properties, including frequency, S_{11}, voltage standing wave ratio, and gain, it is determined that the designs satisfy the required standards for GPS bands.

Conflict of Interest

The authors have no conflicts of interest to declare.

Author Contributions

Both authors contributed equally to the preparation of this paper.

Funding

The authors declared that this study had received no financial support.

Ethical Statements

I declare that I have obtained the data, information, and documents contained in this scientific article, which I prepared in accordance with the rules set forth by the *Journal of Defence and Security Industries: Strategy and Technology*, in accordance with academic and ethical principles. I have presented all information, documents, evaluations, and results in accordance with scientific ethics and moral principles. I have not made any changes to the data used.

Data and Code Availability

There are no available data and code.

Supplementary Materials

There are no supplementary materials.

References

Ayad, M., Saoudi, K., Alharbi, T. E. A., Alzaidi, M. S., Benziane, M., Mouassa, S., & Ghoneim, S. (2022). Design and study of a microstrip patch antenna for GPS application. *Traitement du Signal, 39*(4), 1145-1151. https://doi.org/10.18280/ts.390406

Balanis, C. A. (2008). *Modern antenna handbook* (4th ed.). John Wiley & Sons.

Balanis, C. A. (2016). *Antenna theory: Analysis and design* (4th ed.). John Wiley & Sons.

Basar, M. R., Al-Amin, M., Mirza, E., Debnath, P. P., & Awal, M. R. (2023). A 2-shape slot microstrip patch antenna for global positioning system satellite communication applications. *Indonesian Journal of Electrical Engineering and Computer Science, 31*(3), 1392–1399. https://doi.org/10.11591/ijeecs.v31.i3.pp1392-1399

Deschamps, G. A. (1953). *Microstrip microwave antennas*. In Proceedings of the 3rd USAF Symposium on Antennas.

Dündar, Ö., & Ateş, M. F. (2024). Use of microstrip antennas in aerospace applications: L5 band satellite communication example. *Aerospace Research Letters (ASREL), 3*(1), 69–78. https://doi.org/10.56753/ASREL.2024.3.1

Garg, R., Bhartia, P., Bahl, I., & Ittipiboon, A. (2001). *Microstrip antenna design handbook* (1st ed.). Artech House.

Huang, Y., & Boyle, K. (2008). *Antennas: From theory to practice* (1st ed.). John Wiley & Sons.

Joshi, R., Hussin, E. F. N. M., Soh, P. J., Jamlos, M. F., Lago, H., Al-Hadi, A. A., & Podilchak, S. K. (2020). Dual-band, dual-sense textile antenna with AMC backing for localization using GPS and WBAN/WLAN. *IEEE Access, 8*, 89468–89478. https://doi.org/10.1109/ACCESS.2020.2993371

Khraisat, S. H. (2011). Design of 4-element rectangular microstrip patch antenna with high gain for 2.4 GHz. *Modern Applied Science*, *6*(1), 68–74. https://doi.org/10.5539/mas.v6n1p68

Kraus, J. D. (1988). *Antennas* (2nd ed.). McGraw-Hill Education.

Munson, R. E. (1974). Conformal microstrip antennas and microstrip phased arrays. *IEEE Transactions on Antennas and Propagation, 22*(1), 74–78. https://doi.org/10.1109/TAP.1974.1140723

Pandey, A. (2019). *Practical microstrip and printed antenna design* (1st ed.). Artech House.

Pozar, D. M. (1992). Microstrip antennas. *Proceedings of the IEEE, 80*(1), 79–81. https://doi.org/10.1109/JPROC.1992.152169

Pozar, D. M. (2011). *Microwave engineering* (4th ed.). John Wiley & Sons.

Pozar, D. M., & Schaubert, D. H. (1995). *Microstrip antennas: The analysis and design of microstrip antennas and arrays* (1st ed.). John Wiley & Sons.

Singh, S., Tyagi, N., & Sinha, N. (2014). *Design and analysis of single patch, 2×1 and 4×1 microstrip antenna arrays*. In Proceedings of the International Conference on Convergence of Technology.

Zhong, Z. P., Zhang, X., Li, Y., & Wang, H. (2019). A compact dual-band circularly polarized antenna with wide axial-ratio beamwidth for vehicle GPS satellite navigation applications. *IEEE Transactions on Vehicular Technology, 68*(9), 8683–8692. https://doi.org/10.1109/TVT.2019.2920520

JOURNAL OF DEFENCE AND SECURITY INDUSTRY

Journal of Defence and Security Industries: Strategy and Technology, 2026, 1(1)

Science & Technology Section

An Alternative Approach to Contact-Based CubeSat-Pod Structural Interface

Esat Ulusoy [1], Semih Öztürk [1], Galip Orkun Arıcan [1,*]

Abstract

This study presents the dynamic behaviour of a 3U CubeSat structure under launch conditions, proposing an alternative boundary condition to bring test and finite element analysis (FEA) results closer together. The assumptions of bottom fixation, bottom-top fixation and rail fixation seen in the literature can represent the real system as being either too soft or too rigid, potentially making designs either overly conservative or overly optimistic. With this motivation, the CubeSat–pod interface was modelled with 6-degree-of-freedom spring (CBUSH) stiffnesses derived from Hertz–Mindlin–Popov contact theories. The proposed approach was verified with a part-to-whole strategy: (i) Printed Circuit Board (PCB)-standoff set (test 360 Hz, analysis 365 Hz; 1.4% difference), (ii) PCB-standoff-dummy mass set (test 246 Hz, analysis 250 Hz; 1.6% difference), and (iii) whole CubeSat was applied test and analysis for different boundary conditions. For proposed boundary condition, the analysis results were 96/126 Hz along the lateral axes, the test results were 96.7/120 Hz; along the longitudinal axis, test and analysis results were 137.9 Hz and 138 Hz, respectively. The test-analysis difference was minimum 14.7% with common boundary conditions in the literature, whereas a maximum deviation of 4.7% was observed with the proposed contact-based boundary condition, which yields an enhancement of better than 10% in natural frequency predictions. The results indicate that the analyses performed using the proposed boundary condition show a high level of agreement with the actual test data. Based on this finding, the proposed approach can lead to low-cost and time-effective satellite testing and design processes.

Keywords: CubeSat, contact theory, finite element method, modal analysis, boundary condition.

Received: 07.11.2025 Accepted: 22.12.2025 Research Article

[1] Aselsan Inc., Ankara, Türkiye
* Corresponding author.
✉ goarican@aselsan.com

Cite this article as: Ulusoy, E., Öztürk S., & Arıcan, G. O. (2026). An alternative approach to contact-based CubeSat-pod structural interface. *Journal of Defence and Security Industry: Strategy and Technology 1*, 71-95.

1. Introduction

With the rapid developments in space industry have led to a growing significance of small satellites, particularly CubeSats. By reason of their standardized structures, low costs, and limited time periods, CubeSats are widely used in both civilian and tactical fields, undertaking a wide range of tasks from communication to observation, data transmission to defence and security applications (Areda et al., 2022; Bomani et al., 2021). In an era where even a simple household appliance can exchange data remotely, CubeSats have become a fundamental component of the space-based Internet of Things (IoT) ecosystem. The flexibility they offer, particularly in areas such as surveillance, intelligence, signal tracking, and rapid communication, makes them a strategic asset in defence and security.

The great augmentation in the number of CubeSats has emerged a need for low-cost and easy-of-manufacture solutions. In this context, it is crucial to develop systems that are robust and optimized to meet mission requirements, rather than over-designed or over-qualified products in both design and testing processes (Kanavouras et al., 2022). In this regard, the use of more accurate modelling techniques and verified analysis methods enables shorter testing times and lower development costs. Thus, a sustainable engineering approach in space systems can be achieved without compromising reliability and while increasing production efficiency (Kempf et al., 2021).

However, considering the tests performed to satellites, the most destructive environmental tests are vibration and shock. During launch, satellites are exposed to severe vibration and shock loads transferred from the rocket (Araújo, 2024). These dynamic effects can cause structural damage which can lead to performance losses and catastrophic fails in the satellite components. Additionally, accurately predicting the dynamic behaviour of satellites during launch is crucial for both mission reliability and maintaining structural integrity. Therefore, it is important to determine the natural frequencies accurately in the CubeSat's dynamic analysis. In virtue of this fact, one of the most critical parameters is the applied boundary condition in determining the natural frequencies of CubeSats (Thimmaraju Girijadevi, 2023; Torres, 2024). Moreover, different boundary conditions can cause significant differences, especially in low-frequency modes, which leads to deviations in the analysis results from the actual system behaviour. In the literature, boundary conditions are commonly defined by three different approaches in CubeSat modal analyses. In the first approach, the CubeSat is analysed only with the bottom surface fixation boundary condition to simulate the worst case (García-López et al., 2019; Herrera-Arroyave et al., 2016). This approach leads to overdesigned structures. In the second approach, the CubeSat is analysed with a fixed boundary condition on both the bottom and top surfaces (Bostan et al., 2024; Elshaal et al., 2024). Here, since the connection is assumed to be rigid, the natural frequency is higher than the reality. In this case, there is a possibility that the actual frequency at low frequencies can be lower than the desired minimum frequency. In the third approach, the CubeSat's rails are fixed (Ampatzoglou & Kostopoulos, 2018; Kaya, 2019). Since this boundary condition exhibits stiffer behaviour compared to the second approach, the natural frequency results deviate more from the actual system behaviour.

In this study, an alternative boundary condition approach is proposed to realistically reflect the contact conditions at the CubeSat-pod interface. Additionally, it is aimed to accomplish more accurate dynamic effects that arise during launch, as opposed to the boundary conditions commonly used in the literature. In the proposed boundary condition, the CubeSat-pod interface contact was modelled as a spring. The contact stiffnesses between the CubeSat and the pod were calculated using the contact theories of Hertz, Mindlin, and Popov. By modelling these stiffnesses as spring elements, it was observed that the analysis results closely matched the test results with high accuracy. Furthermore, a minimum of 10% improvement was observed in the determination of natural frequencies when the proposed method was compared with boundary conditions commonly used in the literature.

2. Methodology

The first aim is to ensure the accuracy of the CubeSat's structural model in order to correctly model the CubeSat-pod interface (Wan Aasim et al., 2022). In this context, the modelling approach is based on the part-to-whole verification principle. The study is designed as a three-stage verification process.

In the first stage, a setup consisting solely of the printed circuit board (PCB) and standoffs was established. A sine sweep test was performed on the shaker to determine the system's natural frequency, and data was collected on the PCB by using accelerometer. A finite element (FE) model of the same system was created, and the diameter of the connection surface at the standoff-PCB interface was optimized to match the experimentally identified natural frequencies. Specifically, the interfaces were modelled using RBE3 elements that distribute the forces from the bolt head/nut to a circular region on the PCB. The only parameter adjusted during optimization was the diameter of this force-distribution region (D_{opt}). D_{opt} was iteratively modified in the range 5-7 mm until the first experimental natural frequency was reproduced within ±2%. In the second stage, a dummy mass was included in the model to create a PCB-standoff-dummy mass combination; this structure was also tested in a similar manner, and the natural frequencies of the system were determined. As in the first stage, an FE model was created, and the FE model was verified through analysis by optimizing the diameter of the connection surface at the dummy mass-PCB interface to match the experimentally identified natural frequencies. The same type of RBE3 connection was used at the dummy mass-PCB interface and D_{opt} was again tuned in the range 5-7 mm. No other parameters (bolt preload, material properties or element size) were changed during this optimization.

Once both interface parameters were fixed, they were kept constant in the full CubeSat model (Stage 3) without further adjustment. This approach ensures repeatability. The created FE model was analysed using boundary conditions commonly used in the literature and proposed in this study, and the natural frequencies obtained in each analysis were recorded. Following the analysis, the CubeSat model (Figure 1a) was created by bringing all components together. This model was placed inside the test pod (Figure 1b) and sine sweep tests were performed. The natural frequencies of the system obtained as a result of the tests were compared with the natural frequencies obtained as a result of FE analyses performed under the boundary conditions commonly used in the literature and proposed in this study.

The vibration tests were applied along three orthogonal axes with using a Dongling ES-100LS3-550 shaker system. The VR9500 controller and VibrationView 2017 software were utilized for system control and data acquisition. A Dytran 3055D2 single-axis accelerometer was employed for shaker control and data collection on the Test Pod, while a Dytran 3023A tri-axial accelerometer was used for data acquisition on the device under test (DUT).

The sine sweep test was conducted using a controlled sine sweep excitation. The frequency range was selected as 20–2000 Hz to cover the dominant local and substructure modes identified in the numerical analyses. The sweep was performed at a constant rate of 2 octaves per minute, and the excitation level was controlled at 1g to ensure linear system response and to avoid nonlinear effects during resonance crossings.

The test was carried out under closed-loop acceleration control at the shaker table, with appropriate limit settings applied to prevent excessive responses at resonance frequencies. The CubeSat–Pod assembly was mounted to the shaker using a dedicated fixture designed to provide repeatable boundary conditions and minimize parasitic stiffness effects. Resonance frequencies were identified from the frequency-domain acceleration responses by detecting peaks in the magnitude spectra across measurement locations.

All FE models were developed using Siemens NX 11.0 software, and NX Nastran was adopted as the solver. First, normal modes were extracted using SOL103 Response Dynamics solution type to obtain natural frequencies and mode shapes up to 2000 Hz. Subsequently, frequency response analyses representing the sine sweep base excitation were performed using the Modal Frequency Response method (still within the SOL103 Response Dynamics environment in NX). In this second step, a constant modal damping ratio of 2% was defined for all extracted modes. This value is a typical value used in aerospace qualification testing when no measured damping data are available and is considered conservative for lightly damped metallic and composite structures. The sine sweep event was simulated by applying a swept-sine base acceleration load (1g from 20 Hz to 2000 Hz) in each orthogonal direction, and acceleration responses were computed at critical locations.

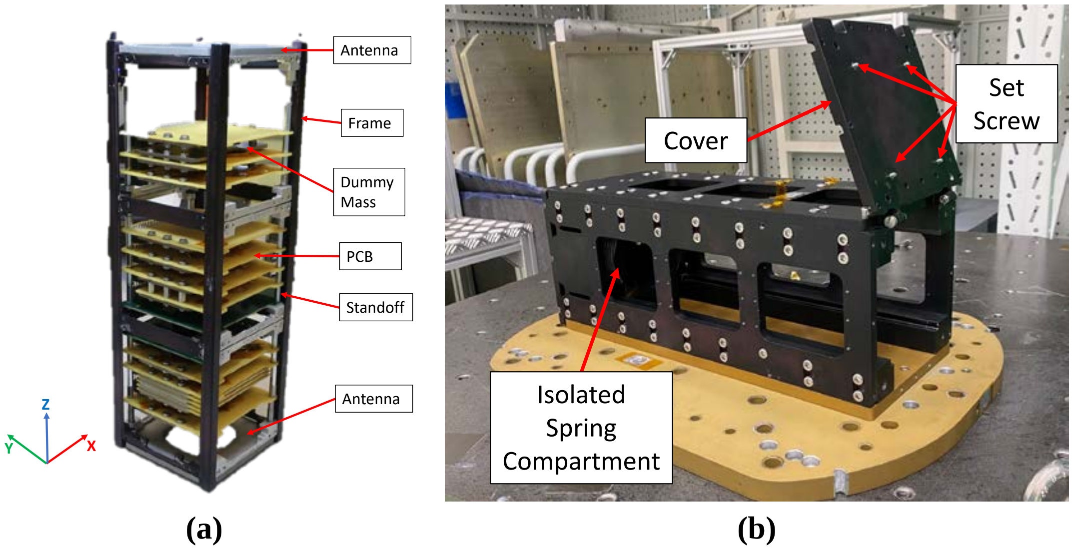

Figure 1. (a) CubeSat and (b) Test pod.

2.1. PCB and Standoff Model Verification

In the first stage, a simplified test setup representing the CubeSat's components was created. As seen in Figure 2a, this setup consisted of one PCB and four standoff elements. The standoffs were attached to the fixture, and the PCB was secured to the standoffs at its four corners. Since the standoffs were made of aluminium, they were torqued to 0.5 Nm. An accelerometer was placed at the centre point of the PCB. The mechanical properties of the PCB and standoffs are given in Table 1.

Table 1. Mechanical properties of components.

Mechanical Properties	PCB	Standoff	Dummy Mass	Antenna	Frame
Material	Arlon 85N	Aluminium 6061	Stainless Steel	Aluminium 6061	Aluminium 6061
Density (g/cm^3)	1.6	2.70	7.8	2.70	2.70
Young's Modulus (GPa)	24.8	68	200	68	68
Poisson's Ratio	0.18	0.33	0.3	0.33	0.33

In the FE model (Figure 2b), the PCB was represented by 2D Shell elements, while the standoffs were represented by 1D CBEAM elements. Although the standoffs have a hexagonal cross-sectional area, they were modelled as 5.5 mm diameter circles with approximately equivalent cross-sectional area for simplicity. To justify this simplification, the equivalent circular cross-section was derived by matching the cross-sectional area (A), moments of inertia (I), and polar moment of inertia (J) of the original hexagonal standoff. A comparison of these properties is provided in Table 2, showing a maximum deviation of 2.5%, which is considered acceptable for global modal analysis.

Table 2. Cross sectional properties comparison.

Cross Sectional Properties	Hexagonal Cross Section	Circular Cross Section	Difference
Area, A (mm^2)	23.38	23.76	1.6%
Moment of Inertia, I (mm^4)	43.84	44.92	2.5%
Polar Moment of Inertia, J (mm^4)	87.69	89.84	2.5%

The standoff-PCB connection was implemented using RBE3 elements. The optimized connection surface on the PCB is a circle with a diameter of 5.5 mm. The accelerometer and cable weight were added to the model as a concentrated mass. Detailed information is given in the Table 3.

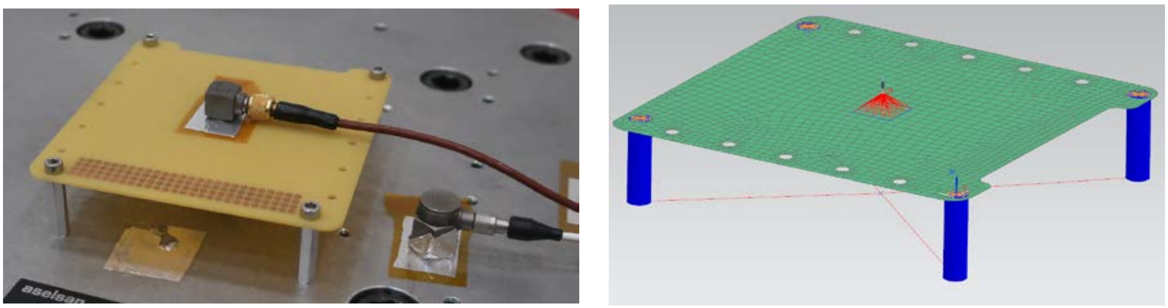

(a) (b)

Figure 2. PCB - standoff model (a) test setup and (b) FE model.

Table 3. FE model details of CubeSat.

Modelled Parts	Type of Mesh	Element Type
PCB	2D	CQUAD4
Standoff	1D	CBEAM
Dummy Mass	2D	CQUAD4
Antenna	3D	CHEXA8
Frame	3D	CHEXA8
Accelerometer	0D	CONM2
Connection Elements	1D	RBE2
Screw Head and Nut	1D	RBE3
Screw Threads	1D	CBEAM

2.2. PCB, Dummy Mass, and Standoff Model Verification

Following the first verification, a dummy mass, which is simulating the mass effects of electronic components, was mounted to the PCB (Figure 3a). The mechanical properties of the dummy mass are given in the Table 1.

The dummy mass was also modelled as a 2D Shell element; the six M3 screws connecting the dummy mass to the PCB were represented by 1D CBEAM elements for the threaded sections and RBE3 elements for the head and nut sections. The optimized connection surface between the dummy mass and the PCB is a circle with a diameter of 5 mm. Figure 3b shows the FE model. Detailed information is given in Table 3.

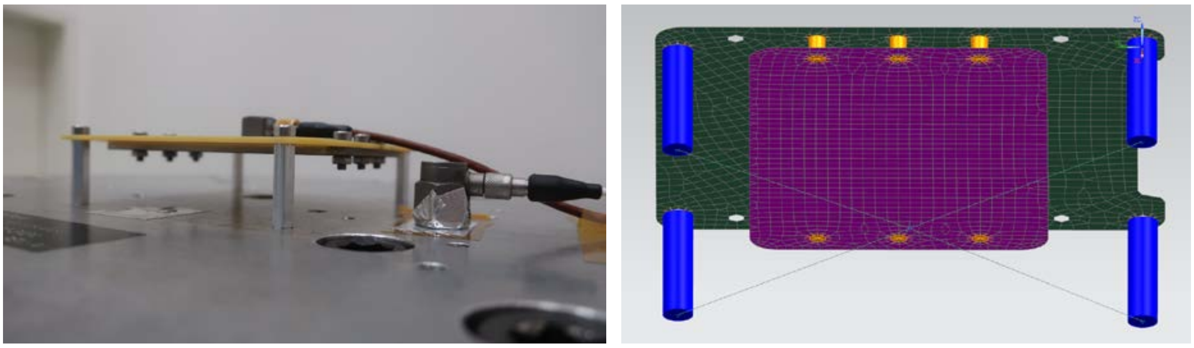

(a) **(b)**

Figure 3. PCB - dummy mass - standoff model (a) test setup and (b) FE model.

2.3. CubeSat Model Verification

As seen in the Figure 4, The CubeSat was modelled as a whole based on the information obtained during the verification of the FE models and connection interfaces of the PCB, dummy mass, and standoffs. A simplified structural CubeSat (Figure 1a) model was used for ease of processing. In the FE model, the CubeSat's frame and antennas were modelled by 3D elements, the PCBs and dummy masses by 2D Shell elements, and the standoffs by 1D elements. The PC104 connectors between the PCBs were modelled with RBE2 elements to reflect the rigid connection characteristic. Detailed information was given in Table 3.

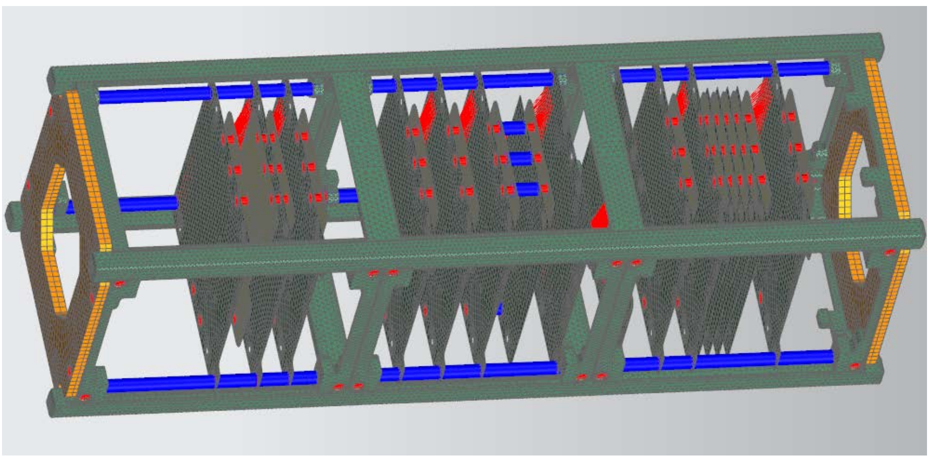

Figure 4. CubeSat FE model.

The three boundary conditions commonly used in the literature and the proposed boundary condition were applied to the FE models as described below, and dynamic analyses were performed.

Bottom fixation boundary condition (Figure 5a) is typically used in worst-case analyses. It is preferred when a cautious approach is adopted, as it yields lower natural frequencies compared to the real situation. During modelling, the four surfaces of the CubeSat's frame structure in the Z-axis direction were connected to the forced motion location point via RBE2 elements.

Top-bottom fixation boundary condition (Figure 5b) represents the situation where the CubeSat was squeezed by both the cover and the isolated spring compartment of the pod. However, fixing both surfaces increases the rigidity of the system and consequently causes the natural frequencies to be higher than in reality. In this case, the frame's total of eight surfaces in the -Z and +Z directions were connected to the enforced motion location point via RBE2 elements.

Rail fixation boundary condition (Figure 5c) simulates the situation where the CubeSat is held by the pod rails. However, this approach also causes the system to behave more rigidly than expected. During modelling, a total of eight surfaces of the frame along the lateral axis (X, Y) directions were connected to the enforced motion location point via RBE2 elements.

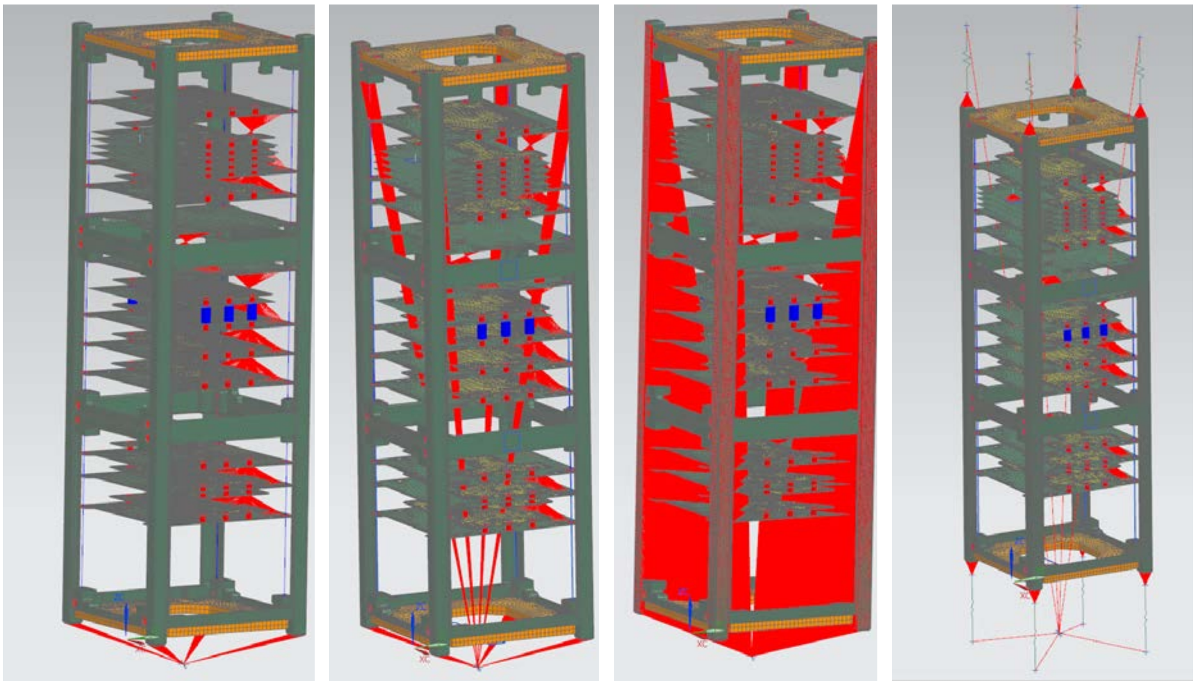

(a) **(b)** **(c)** **(d)**

Figure 5. Boundary conditions of (a) Bottom fixation, (b) Bottom-top fixation, (c) Rail fixation and (d) Proposed.

Proposed boundary condition (Figure 5d) is to model the contact between the bottom (-Z) and top (+Z) surfaces of the CubeSat Frame and the pod as a six-degree-of-freedom (6DOF) spring to reflect reality more accurately. The nominal distance between the rails of the test pod was measured as 100.3 ± 0.05 mm, while the distance between the CubeSat's rails was measured as 100 ± 0.1 mm, indicating an initial geometric clearance between the interfaces. Although these geometric tolerances indicate an initial clearance, localized contact under preload conditions introduced by the cover tightening cannot be completely excluded. To evaluate this possibility, post-test visual inspections of the CubeSat rail surfaces were conducted following the vibration tests. No evidence of wear, scratching, polishing, or material transfer was observed on the rail surfaces (Figure 6), indicating that any potential interaction was not sustained or rigid, but rather intermittent and compliant in nature. Therefore, the CubeSat was held under a certain pre-compression force by the cover and isolated spring compartment. However, this compression is not as rigid as the top-bottom fixation boundary conditions. Accordingly, the interface behaviour is more appropriately represented by a compliant six-degree-of-freedom (6DOF) spring boundary condition rather than an idealized fixed contact assumption.

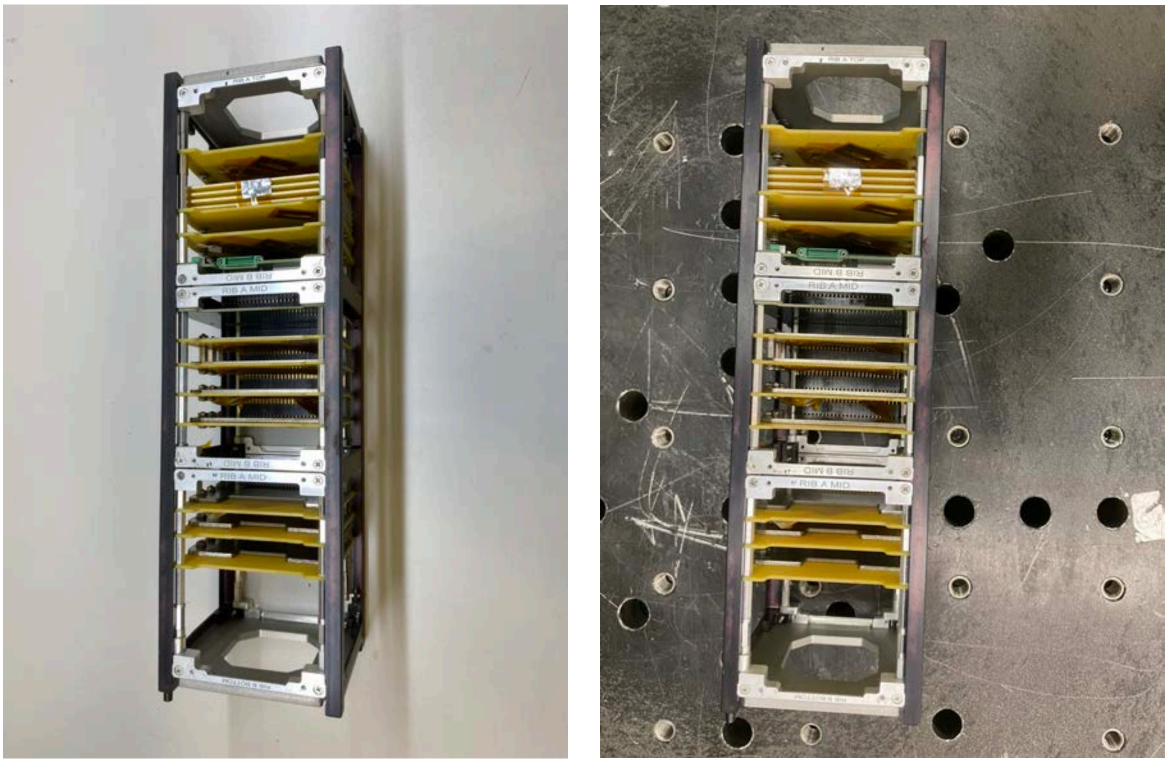

(a) (b)

Figure 6. CubeSat rails (a) Before and (b) After vibration test.

In the FE model, the aluminium frame-aluminium isolated spring compartment contact for the bottom end of the frame and the steel screw-aluminium frame contact for the top end were considered, and the stiffness values for these contacts were calculated using contact theory. After that, the CBUSH elements defined by the obtained stiffness values were connected to a total of eight surfaces in the bottom and top directions of the frame. The CBUSH elements were connected to these surfaces via RBE2 elements in order to distribute the contact stiffness over the interface region; the other ends of the CBUSH elements were also connected at the enforced motion location point using RBE2 elements. All six degrees of freedom of the

CBUSH elements were activated, including three translational (k_x, k_y, k_z) and three rotational stiffness components ($k_{\theta x}$, $k_{\theta y}$, $k_{\theta z}$), while no coupling terms between translational and rotational degrees of freedom were introduced. It should be noted that, the use of RBE2 elements may locally suppress rotational flexibility and slightly increase the effective interface stiffness, this modelling choice was intentionally adopted as a linearized and repeatable representation of the contact region, and its influence is considered acceptable for the global modal characteristics and frequency range investigated in this study.

After the different boundary conditions were defined for the model, the analyses were performed for each boundary condition. To enable a direct comparison between numerical and experimental results, analysis sensors were defined at the same locations as the accelerometers used during the sine sweep tests. The sensor has been defined to the frame along the lateral axis analyses and to the battery board along the longitudinal axis analyses on the CubeSat in order to be able to compare analysis and test results. Because the frame's natural frequency was higher than the test pod's natural frequency along longitudinal axis.

Following the analyses, a test setup was created to determine the CubeSat's natural frequencies in real conditions. The CubeSat under test has a structure consisting of a frame, dummy masses, and PCBs. This CubeSat was placed inside the test pod and subjected to a sine sweep test. After closing the pod cover, the M4 compression screws on it were tightened to a torque of 1.0 Nm each. This process was performed to prevent any possible movement of the CubeSat inside the pod. Test setups can be seen for each orthogonal axes in Figure 7.

To monitor dynamic behaviour, accelerometers were placed on both the CubeSat frame and the test pod. Additionally, an accelerometer was placed on the battery board along the longitudinal axis. Thus, the vibration responses of both the CubeSat and the pod were recorded simultaneously during the test.

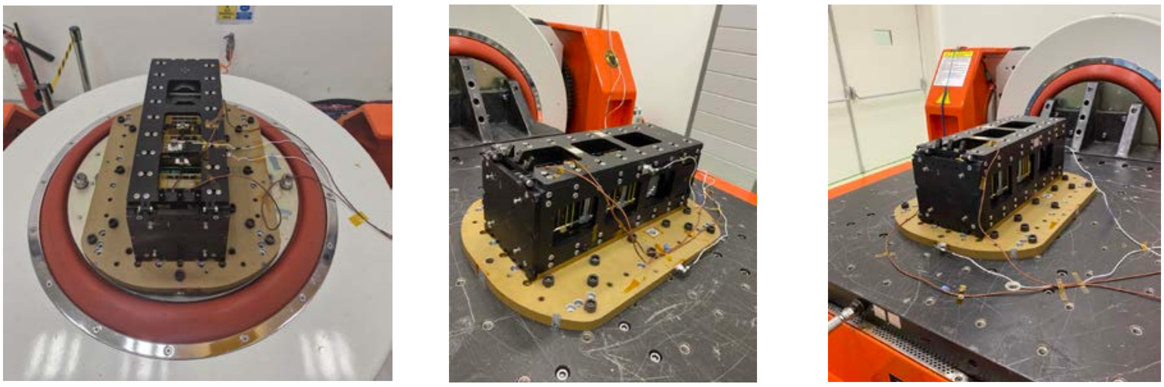

(a) (b) (c)

Figure 7. CubeSat vibration test setup in (a) X-axis, (b) Y-axis and (c) Z-axis.

2.4. Contact Theory

The classical framework describing the contact between two surfaces is the Hertz-Mindlin-Popov formulation (Popov, 2010). Hertz theory combines the elastic compliance of two halfspaces to give axial contact behaviour; Mindlin (and Cattaneo-Mindlin extensions) addresses tangential behaviour and partial/full stick-slip boundaries; Popov's axisymmetric solutions provide axial, tangential, and rotational contact stiffness in closed-form expressions, particularly for circular geometry (Popov, 2010).

The fundamental assumptions of the contact model are explicitly as follows: materials are isotropic, linear-elastic, and homogeneous; contact is smooth and adhesion/plastic deformation effects are neglected; deformations are small (small strains/rotations) and linear relations hold; geometry is assumed to be circular contact. Popov's axisymmetric flat punch results are directly applicable (Popov, 2010). Although the actual CubeSat–pod interface does not strictly conform to an ideal flat punch or perfectly circular geometry, the contact region remains small relative to the global structural dimensions and operates under high preload with limited local deformation. In this study, the contact formulation is employed to derive effective, linearized interface stiffness values for global dynamic modelling rather than to capture local stress concentrations or edge effects. Consequently, deviations from ideal geometry, surface roughness, and local edge effects are considered second-order influences on the global modal characteristics investigated.

Axial stiffness is calculated using the Equation (1) provided in Popov's solution for the axisymmetric flat punch.

$$k_z = 2E^* a \tag{1}$$

Where k_z depicts axial stiffness (N/mm), E* depicts Equivalent Young's modulus (MPa), a depicts contact radius (mm).

The equivalent elasticity modulus is a quantity specific to the material properties of the contacting surfaces (Popov, 2010).

When two surfaces are made of the same material, E*can be calculated according to Hertz's contact theory as shown in Equation (2):

$$\frac{1}{E^*} = \frac{2(1 - v^2)}{E} \tag{2}$$

Where E depicts Young's modulus (MPa), v depicts Poisson's ratio.

When the two surfaces are made of different materials, E* can be calculated according to Hertz's contact theory as given in Equation (3):

$$\frac{1}{E^*} = \frac{1 - v_1^2}{E_1} + \frac{1 - v_2^2}{E_2} \tag{3}$$

Tangential stiffness is calculated using the Equation (4) given in Popov's solution for an axisymmetric flat punch.

$$k_x = k_y = 2G^* a \tag{4}$$

Where k_x, k_y depicts tangential stiffness (N/mm), G* depicts equivalent shear modulus (MPa), a depicts contact radius (mm)

The equivalent shear modulus G* used in the tangential stiffness calculation is given by the following Equation (5):

$$\frac{1}{G^*} = \frac{2 - v_1}{4G_1} + \frac{1 - v_2}{4G_2} \tag{5}$$

Where G_i depicts i^{th} of shear modulus.

The shear modulus is calculated using Poisson's ratio and Young's modulus from the Equation (6):

$$G_i = \frac{E_i}{2(1 + v_i)} \tag{6}$$

The linear coefficients directly used from Popov's axisymmetric flat-punch and related rotation/torsion solutions are shown in Equation (7) and Equation (8):

$$k_{\theta_z} = \frac{16}{3} G^* a^3 \tag{7}$$

$$k_{\theta_x} = k_{\theta_y} \approx \frac{8}{3} E^* a^3 \tag{8}$$

Where k_{θ_x}, k_{θ_y} depicts bending stiffness, k_{θ_z}depicts torsional stiffness.

The aluminium square-section frame on the bottom of the CubeSat contacts the aluminium isolated spring holder (Figure 8a). When the 6x6 mm² square contact area of the frame was converted to an equivalent circular radius, the value a was calculated as 3.38 mm. Considering the calculated equivalent contact radius and aluminium-aluminium contact, the determined stiffness values are given in Table 4.

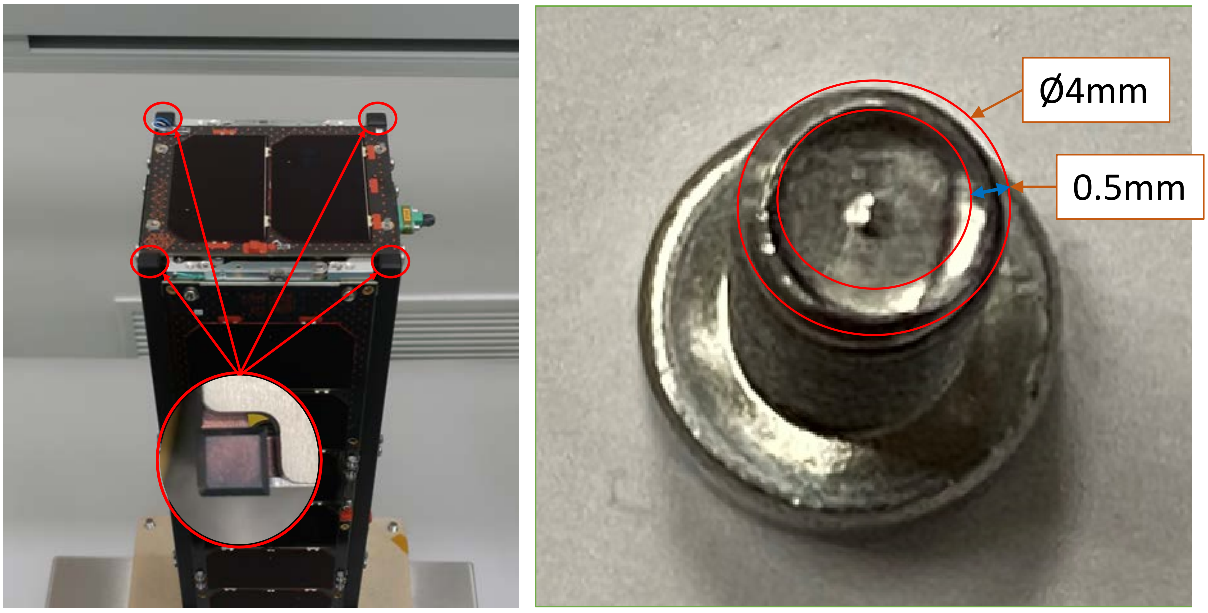

(a) **(b)**

Figure 8. Cross sectional image of (a) Frame contact surface, and (b) Screw.

The top of the CubeSat, the steel screw-aluminium frame contact used to compress the CubeSat was considered. Here, the outer surface of the screw's circular cross-section was in contact, as seen in Figure 8b. When the equivalent radius was calculated for this contact, the value a was found to be 1.32 mm. Considering the calculated equivalent contact radius and steel-aluminium contact, the determined stiffness values are given in Table 4.

Table 4. Contact stiffness value of CubeSat-pod interface.

Stiffness	Unit	Al-Al	SS-Al
Tangential Stiffness (k_x, k_y)	N/mm	2.1×10^5	1.2×10^5
Axial Stiffness (k_z)	N/mm	2.6×10^5	1.5×10^5
Bending Stiffness ($k_{\theta_x}, k_{\theta_y}$)	Nmm/rad	4.1×10^6	3.5×10^5
Torsional Stiffness (k_{θ_z})	Nmm/rad	6.5×10^6	5.7×10^5

Using the standard torque-tension approximation, torque preload is calculated from the Equation (9):

$$F = \frac{T}{K * d} \tag{9}$$

Where T depicts tightening torque, F depicts torque preload, K depicts torque coefficient, d depicts nominal diameter of screw.

The nominal bolt preload is calculated 1250 N from Equation (9) using these values.

T is 1.0 Nm, K is 0.2 (nominally 0.2-0.3), d is 4 mm (nominal diameter of M4), and deformation (δ_{max}) is calculated from Equation (10).

$$\delta_{max} = \frac{F}{k_z} \tag{10}$$

To assess an upper-bound deformation, the minimum normal contact stiffness used in the model (k_z=1.5×10^5 N/mm) was considered, resulting in a worst-case local deformation of approximately δ_{max}=8.3 μm. This small deformation magnitude supports the assumption of small, elastic contact deformation and justifies the use of a linearized contact stiffness representation around the nominal assembled condition.

3. Results and Discussion

The simulation results were verified with the sine sweep tests. In the first stage, the PCB and standoff setup was attached to the vibration test device perpendicular to the PCB's surface. According to the sine sweep test result, it was revealed that the PCB has 360 Hz of first natural frequency. Since the difference between the first natural frequencies was around 1.4%, the FE model created was found to be highly accurate. The analysis and test results are given in Figure 9. Subsequently, first natural frequency was simulated as 365 Hz in the modal analysis (Figure 11a).

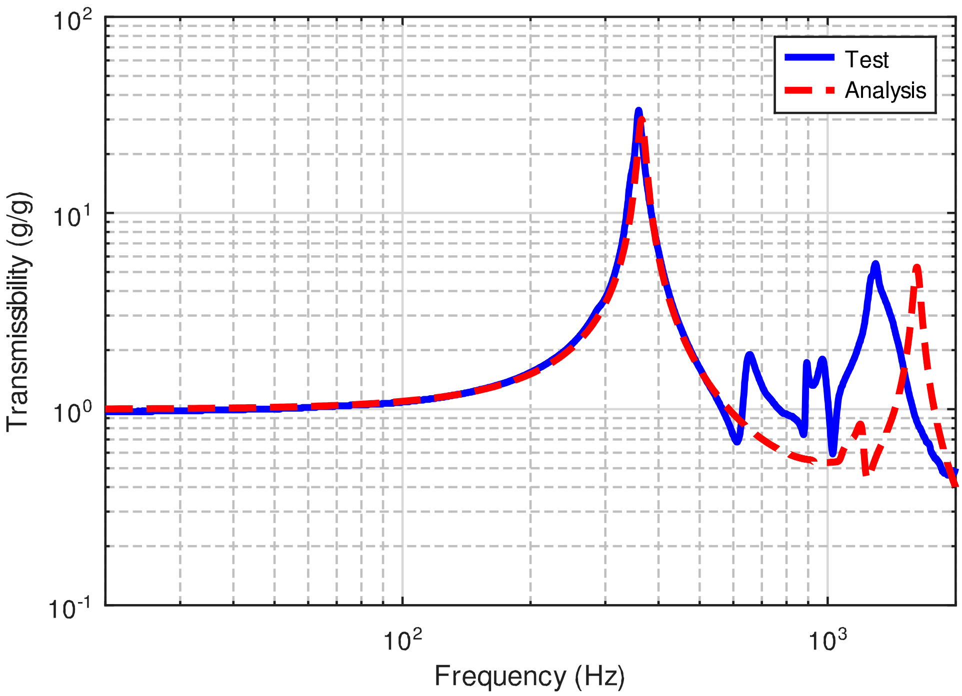

Figure 9. Test and analysis result of PCB-standoff setup.

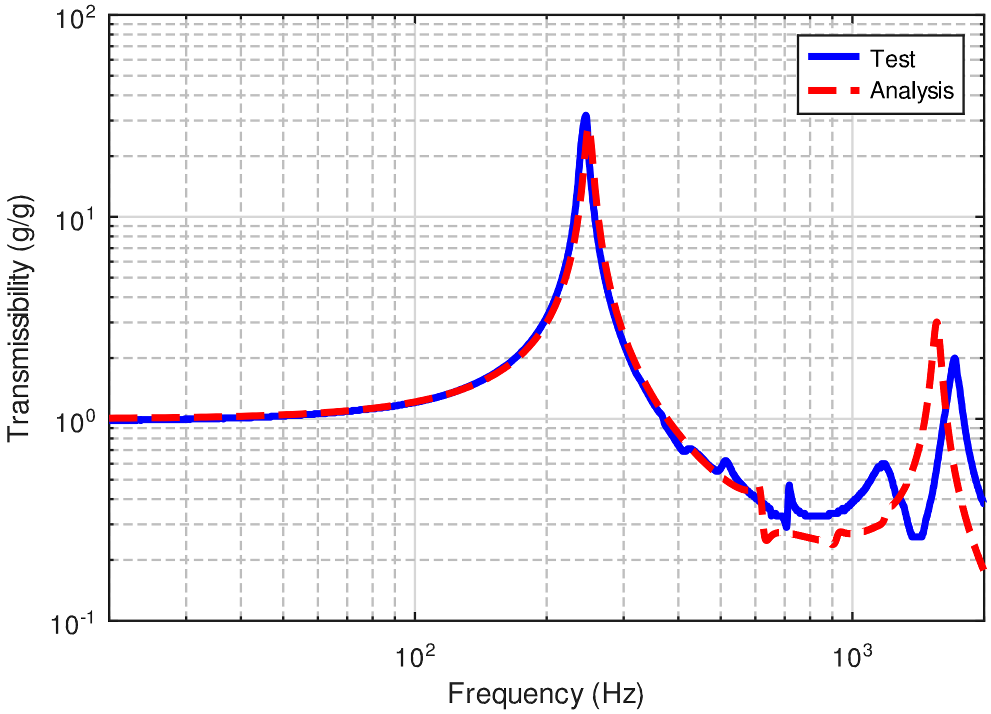

Figure 10. Test and analysis result of PCB-dummy-standoff setup.

Following this verification, a dummy mass was attached to the PCB-standoff setup in the first stage. According to the sine sweep test result, it was revealed that the setup has 246 Hz of first natural frequency. Since the difference between the first natural frequencies was around 1.6%, the created FE model was found to be highly accurate. The analysis and test results can be seen in Figure 10. Subsequently, first natural frequency was simulated as 250 Hz in the modal analysis (Figure 11b).

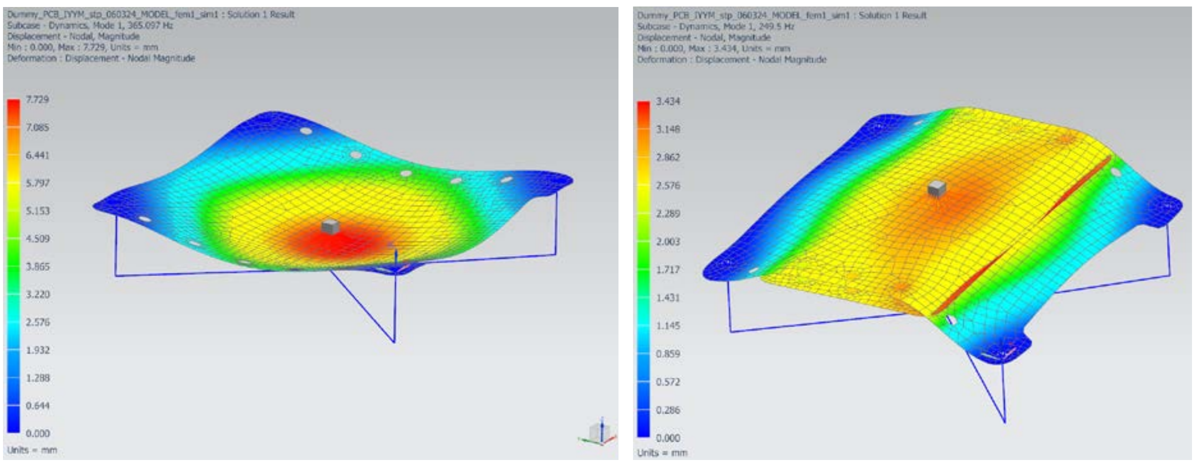

(a) **(b)**

Figure 11. First natural frequency and mode shape of (a) PCB-standoff, and (b) PCB-dummy mass-standoff.

Then, in Stage 3, the CubeSat was modelled based on the FE models verified in the previous stages. FE analyses were performed under three different boundary conditions found in the literature and the proposed boundary condition. First natural frequencies and mode shapes can be seen in Figure 12.

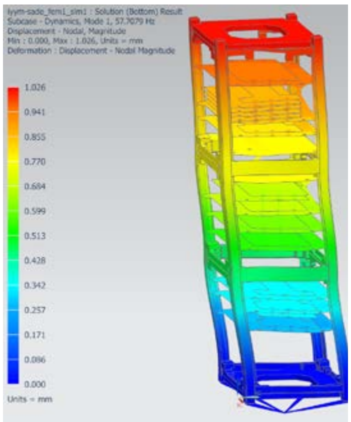

(a)

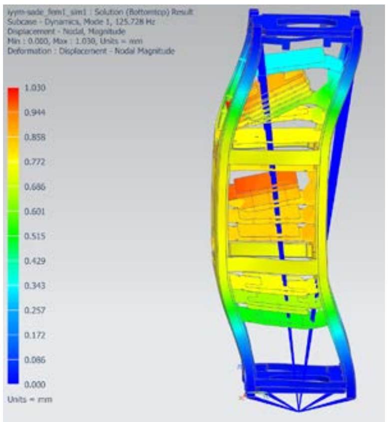

(b)

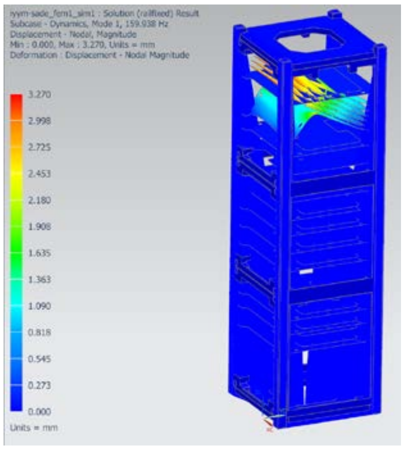

(c)

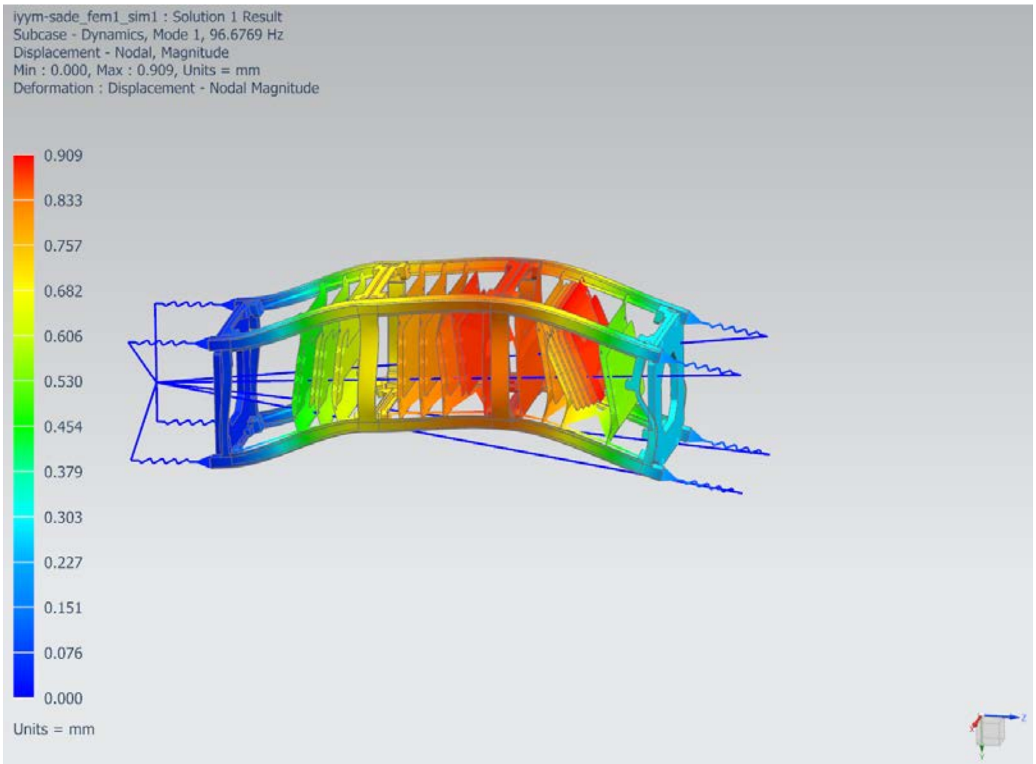

(d)

Figure 12. First natural frequencies for boundary conditions of (a) Bottom fixation, (b) Bottom-top fixation, (c) Rail fixation, and (d) Proposed.

Upon completion of the analyses, the CubeSat was mounted to the shaker in the test pod for 3 orthogonal axes. Sine sweep test was performed separately for all 3 axes. During the tests, the data were obtained from the frame along the lateral (X and Y) axes. As seen in the Figure 13 and Figure 14, the CubeSat frame shows clear resonance peaks that appear before the dominant pod modes, indicating that the frame natural frequencies are lower than those of the pod and can be distinguished from the test data. In contrast, along the longitudinal Z-axis, the pod and CubeSat frame show overlapping resonance behaviour in the frequency-domain acceleration responses, indicating strong dynamic coupling between them (Figure 15). This observation indicates that the global frame natural frequency in the longitudinal direction is higher than the corresponding pod mode and therefore cannot be clearly identified from frame-mounted measurements. Consistent with the analysis results, the first clearly identifiable mode along the Z-axis is associated with the battery board, which shows a distinct local resonance in both the analysis and the experimental data. For this reason, the battery board mode was selected as the representative first longitudinal mode, and the comparison between analysis and test results was performed using acceleration data measured on the battery board.

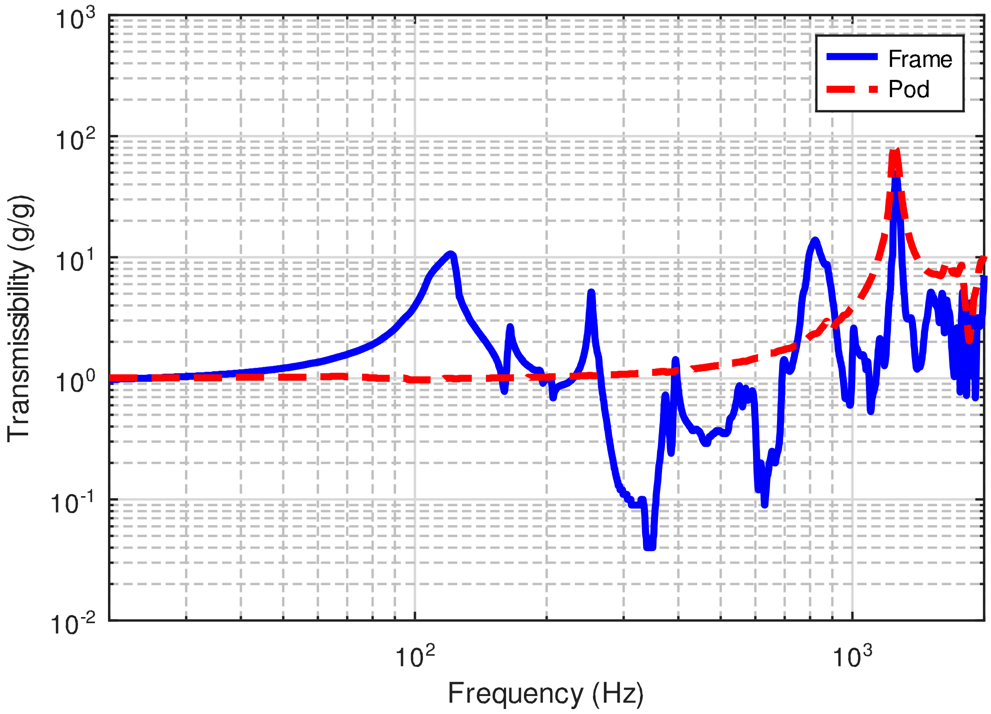

Figure 13. Test result of CubeSat and pod along X-axis.

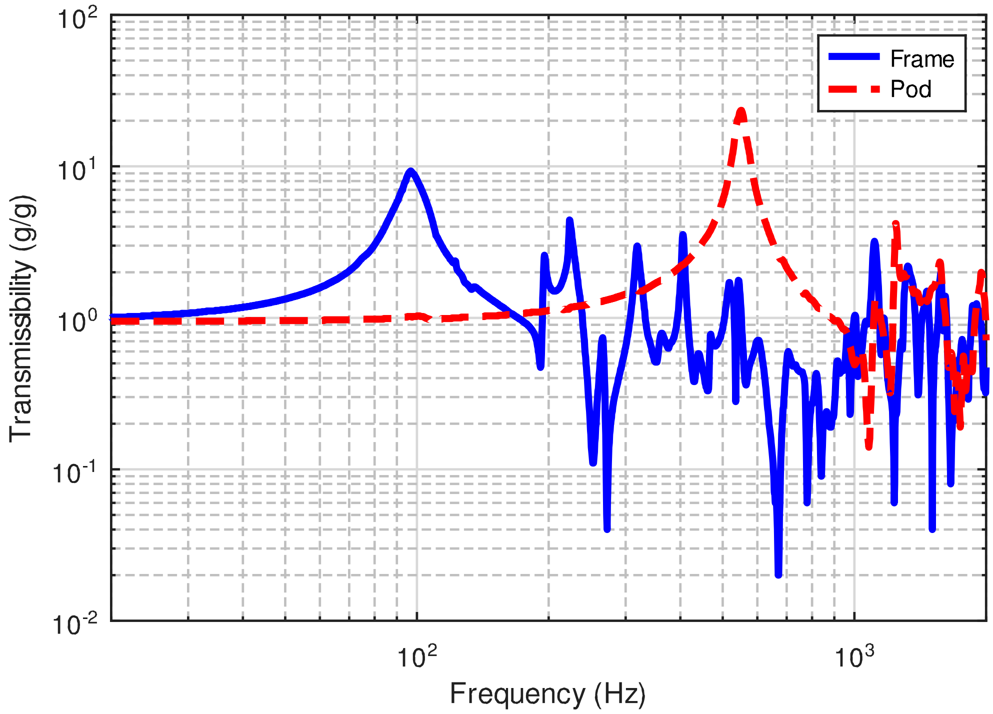

Figure 14. Test result of CubeSat and pod along Y-axis.

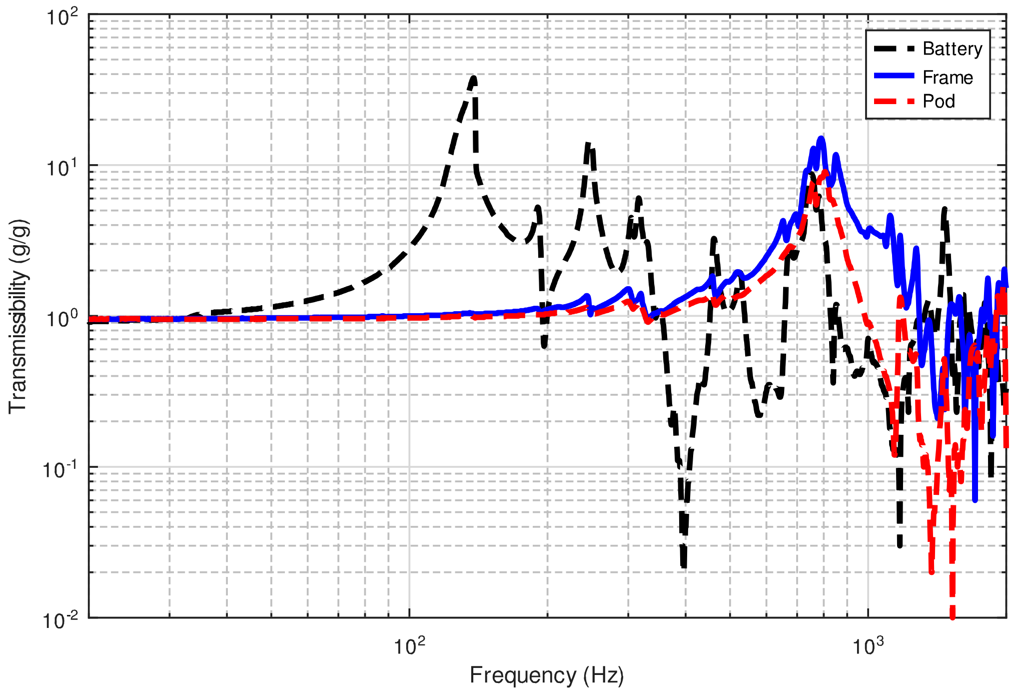

Figure 15. Test result of CubeSat and pod along Z-axis.

As seen in the Figure 16, Figure 17, and Figure 18 the results of the analyses, which were performed with different boundary conditions, were compared with the test results. Along the lateral (X and Y) axes, it was observed that the natural frequencies were lower than expected when fixed at the bottom end, and higher when fixed at both the bottom and top ends. In the case of being fixed to the rails, the natural frequency along the lateral axes was not included in the calculation. Since no dominant global frame mode was observed up to 2000 Hz and the response is governed by local PCB and standoff modes, quantitative comparison among boundary conditions primarily affecting the frame behaviour is not physically meaningful within the investigated frequency range.

Along the longitudinal axis, since the first natural frequency was on the battery board, the boundary conditions used in the literature were similar. However, they differed by minimum 15% from the actual test result. On the other hand, the test and simulation results were similar for the proposed boundary conditions.

When the test results and analyses results performed with the proposed boundary condition were compared, along the lateral axes, natural frequency values of 96 Hz and 126 Hz were obtained in the analysis, and 96.7 Hz and 120 Hz in the test, respectively (Figure 16 and Figure 17). Along the longitudinal axis, according to the results, it was observed that the lowest natural frequency was on the battery board. As a brief, a natural frequency of 137.9 Hz and 138 Hz respectively in the test and analysis (Figure 18).

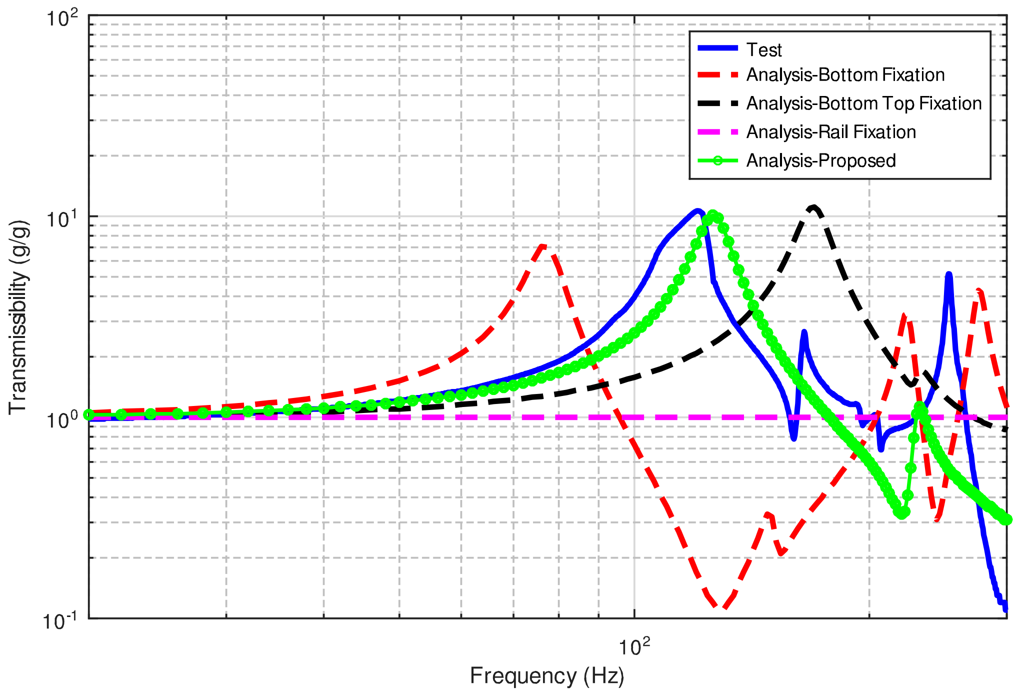

Figure 16. Test result and analysis results of different boundary conditions along X-axis.

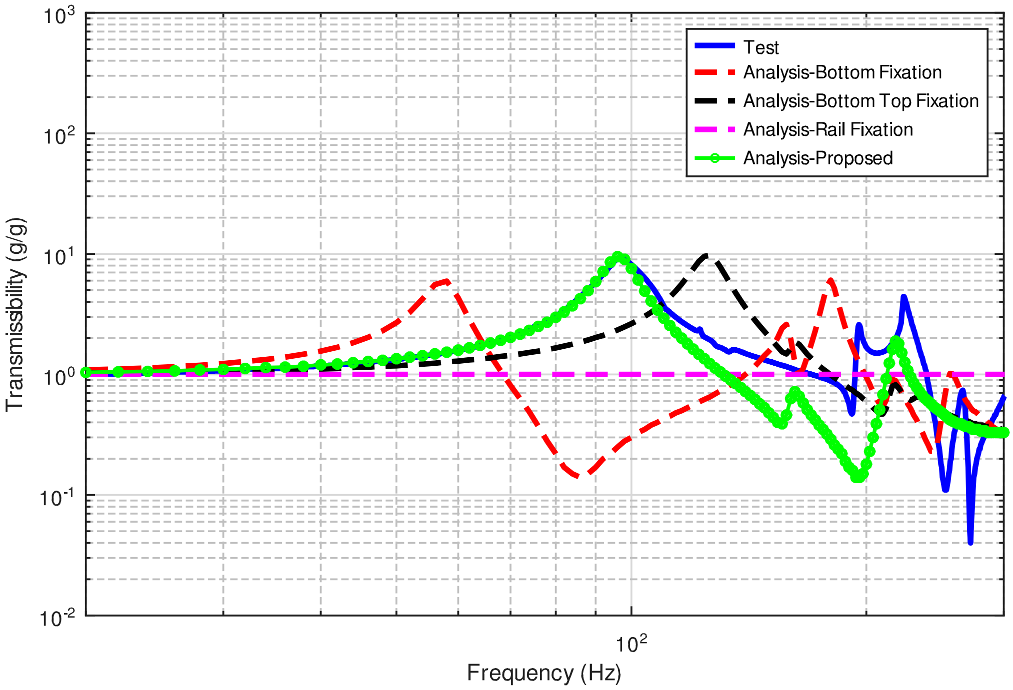

Figure 17. Test result and analysis results of different boundary conditions along Y-axis.

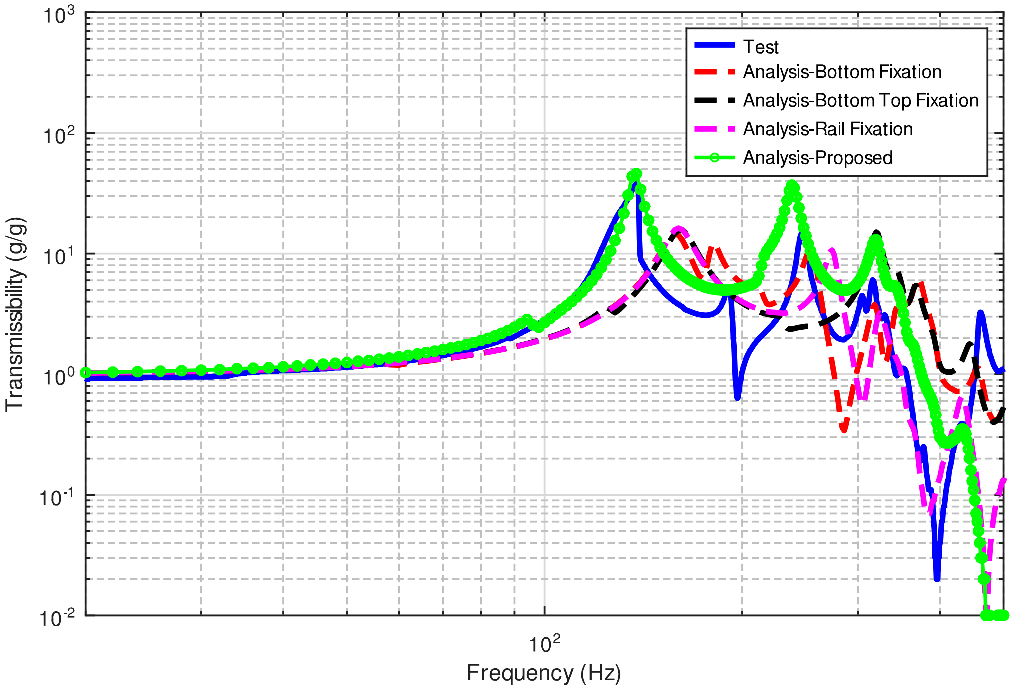

Figure 18. Test result and analysis results of different boundary conditions along Z-axis.

Mode matching between numerical and experimental results was performed based on a combined evaluation of frequency proximity, excitation direction, and dominant deformation characteristics observed in the numerical mode shapes. In addition to frequency agreement, the physical interpretation of the mode shapes obtained from the finite element analysis was used to ensure consistent mode pairing. To support this interpretation, the first lateral mode shapes obtained from the numerical analysis along the X and Y axes are presented in Figure 19 and Figure 20, corresponding to the 126 Hz and 96 Hz modes, respectively, which clearly demonstrate distinct and physically meaningful deformation patterns used for mode identification.

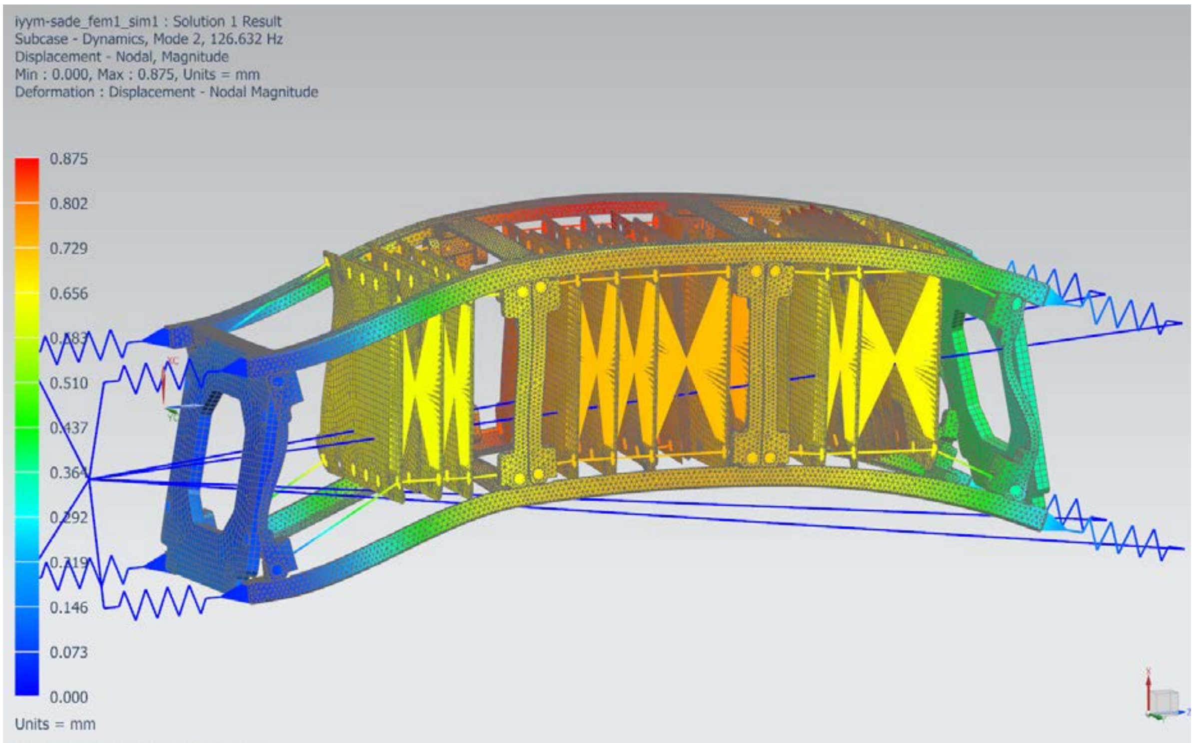

Figure 19. First natural frequency and mode shape along X-axis.

When the boundary condition cases adopted from the literature are compared with the experimental results, the smallest deviation is 14.7%, observed for the bottom-fixed configuration along the longitudinal Z-axis. This value represents the best-case agreement among the literature-based boundary conditions. For the proposed contact-based boundary condition, the maximum deviation is 4.7%, occurring along the lateral X-axis, which corresponds to the worst-case result of the proposed approach. Overall, the proposed method exhibits consistently smaller deviations from the experimental results compared to the literature-based boundary conditions, indicating improved agreement with the measured CubeSat–pod dynamic behaviour.

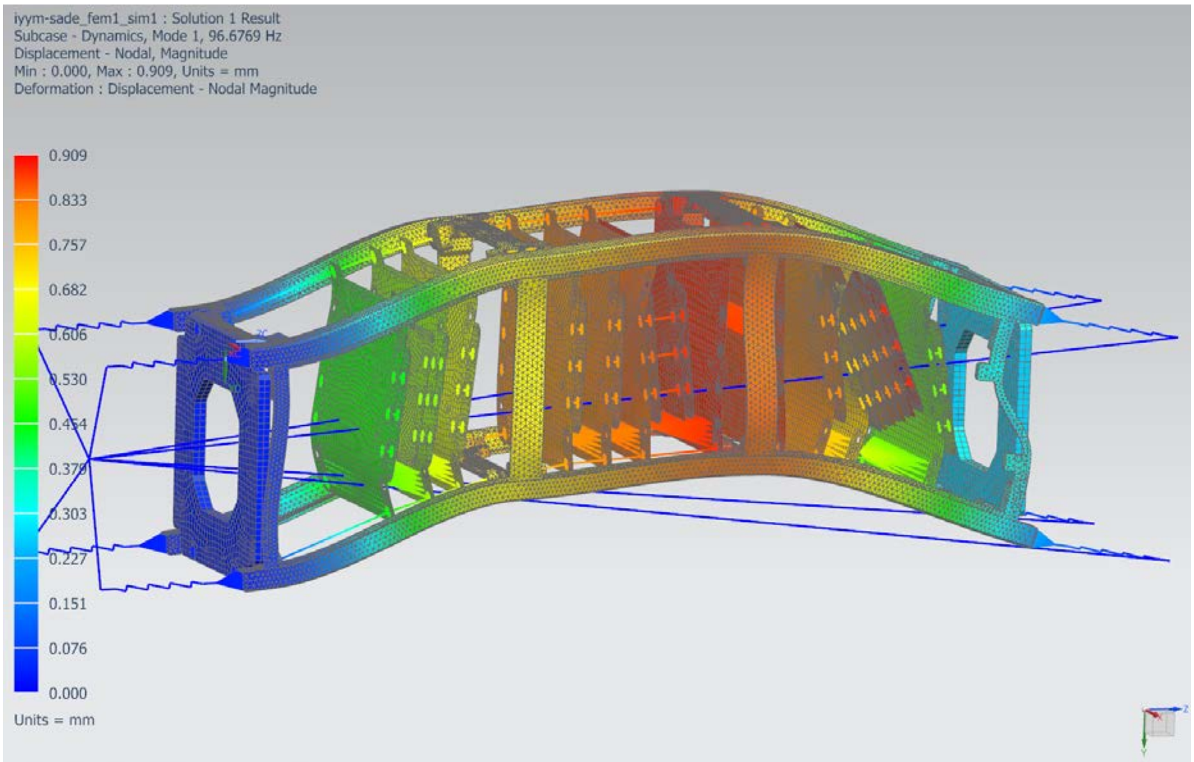

Figure 20. First natural frequency and mode shape along Y-axis.

These findings highlight the limitations of conventional boundary conditions commonly employed in CubeSat structural analyses. For example, the bottom fixation approach, as utilized by García-López et al. (2019) and Herrera-Arroyave et al. (2016), simulates a worst-case scenario but often results in overly conservative designs by underestimating the system's stiffness, leading to lower predicted natural frequencies and potential overdesign. Similarly, the bottom-top fixation, adopted in studies like Elshaal et al. (2024) and Bostan et al. (2024), assumes rigid connections that overestimate rigidity, yielding higher frequencies than observed in tests and risking optimistic predictions that could compromise mission reliability. The rail fixation method, seen in Ampatzoglou and Kostopoulos (2018) and Kaya (2019), further exacerbates this by imposing even stiffer constraints, deviating significantly from real pod interactions.

In contrast, our proposed contact-based boundary condition, derived from Hertz-Mindlin-Popov theories and modelled via 6DOF spring elements (CBUSH), captures the compliant nature of the CubeSat-pod interface more realistically. This approach accounts for preload-induced contacts and geometric clearances, which are often neglected in literature models. By incorporating contact stiffnesses, our method reduces deviations to a maximum of 4.7% (an enhancement of over 10% in prediction accuracy compared to these traditional approaches) demonstrating its originality in bridging the gap between FEA and real-world launch dynamics without requiring excessive computational complexity or empirical adjustments.

4. Conclusion

The findings revealed that the boundary conditions in the literature were insufficient to reflect the actual behaviour along the lateral axes. In contrast, the contact model proposed in this study -an approach using 6DOF spring elements (CBUSH) at the CubeSat-pod interface showed high alignment with the test data. As a result, the difference between analysis results from the proposed boundary condition modelling and the test results was found to be at maximum 4.7%, confirming that the model accurately represents the physical behaviour. This approach increases the reliability of structural-dynamic analyses, especially under launch conditions, and provides a more realistic modelling basis for CubeSat designs. The original contribution of this work lies in its departure from rigid or overly simplified boundary conditions prevalent in the literature, which often lead to either conservative overdesigns or risky underestimations of dynamic responses. Future studies may extend the proposed modelling approach to different launcher pod configurations since CubeSat-pod interface behaviour can vary with pod design. Some launcher pods use rail mechanisms that actively clamp the CubeSat, leading to sustained and preload-dependent rail contact in addition to the top-bottom interfaces considered in this study. For such cases, the modelling framework can be expanded to explicitly include rail contact and its stiffness effects. This extension would improve the applicability of the proposed approach to a wider range of launch environments.

Conflict of Interest

There is no conflict of interest among authors.

Author Contributions

Ulusoy E., and Öztürk S. were carried out this research and performed measurements. Ulusoy E., Öztürk S., and Arıcan G. O. were written the manuscript.

Funding

This research received no funding.

Acknowledgments

The authors are grateful to Aselsan Inc. for providing simulation production and measurement infrastructure.

Ethical Statements

Not applicable.

Data and Code Availability

Not applicable.

Supplementary Materials

Not applicable.

References

Ampatzoglou, A., & Kostopoulos, V. (2018). Design, analysis, optimization, manufacturing, and testing of a 2U CubeSat. *International Journal of Aerospace Engineering, 2018*, Article 9724263. https://doi.org/10.1155/2018/9724263

Araújo, L. (2024). *Dynamic Response of a CubeSat within a Deployer during Launch Phase.* MSc Thesis, IST Lisbon.

Areda, E. E., Cordova-Alarcon, J. R., Masui, H., & Cho, M. (2022). *Development of Innovative CubeSat Platform for Mass Production*. *Applied Sciences*, 12(18), 9087. https://doi.org/10.3390/app12189087

Bomani, B. M. M., et al. (2021). *CubeSat Technology Past and Present: Current State-of-the-Art*. NASA TP-20210000201.

Bostan, V., Guţu, M., Melnic, V., & Martîniuc, A. (2024). Structural analysis and vibration testing of the tumnanosat microsatellite. *Journal of Engineering Sciences*, (4), 8-21. https://doi.org/10.52326/jes.utm.2024.31(4).01

Elshaal, A., Okasha, M., Sulaeman, E., Jallad, A. H., Aizat, W. F. A., & Alzubaidi, A. B. (2024). Structural analysis of AlAinSat-1 CubeSat. *Egyptian Journal of Remote Sensing and Space Sciences*, *27*(3), 532–546. https://doi.org/10.1016/j.ejrs.2024.06.006

García-López, A., Sánchez, J., & Arévalo, L. (2019). Structural design and analysis of a 3U standardized CubeSat for a future Mexican mission. *In Proceedings of the XXXII Congreso de Instrumentación de la Sociedad Mexicana de Instrumentación (SOMI)*, Acapulco, México.

Herrera-Arroyave, J. E., Bermúdez-Reyes, B., Ferrer-Pérez, J. A., & Colín, A. (2016, September 26–30). CubeSat system structural design. *In Proceedings of the 67th International Astronautical Congress (IAC)* (pp. 1–5). Guadalajara, Mexico.

Kaya, A. (2019). *Kompozit 3U küp uyduların yapısal analizi ve tasarımları* (Yüksek lisans tezi, İstanbul Teknik Üniversitesi).

Kanavouras, K., Hein, A.M., & Sachidanand, M. (2022). *Agile Systems Engineering for sub-CubeSat scale spacecraft.* https://arxiv.org/pdf/2210.10653

Kempf, J., Mühlbauer, T., & Dasbach, H. (2021). *Space Factory 4.0 – Industry 4.0 approaches for automated small-satellite production*. In *Proceedings of the 72nd International Astronautical Congress (IAC 2021)*. International Astronautical Federation.

Popov, V. L. (2010). *Contact mechanics and friction: Physical principles and applications.* Springer.

Thimmaraju Girijadevi, L. (2023). *Vibration analysis and testing of a 6U CubeSat propulsion system*. MSc Thesis, KTH. https://www.diva-portal.org/smash/record.jsf?pid=diva2%3A1817018&dswid=-6733

Torres, A. E. i. (2024). *Manufacturing Process of a CubeSat Structure.* Master’s thesis, Universitat Politècnica de Catalunya.

Wan Aasim, W. F. A., AlMazrouei, M., Okasha, M., & Jallad, A. H. (2022). The structural analysis of AlainSat-1: An earth observation 3U CubeSat. *In 4th Symposium on Space Educational Activities. Universitat Politècnica de Catalunya.*

JOURNAL OF DEFENCE AND SECURITY INDUSTRY

Journal of Defence and Security Industries: Strategy and Technology, 2026, 1(1)

Science & Technology Section

Development of Near Real Time Target Detection and Identification System for Ground Combat Vehicles via Artificial Intelligence

Reşat Ali Tütüncüoğlu [1], Selda Güney [2,*]

Abstract

Modern military intelligence systems are advancing rapidly, particularly in the classification of combat vehicles in battlefield environments. Accurately identifying the capabilities and vulnerabilities of these vehicles is crucial for developing effective tactics and operational strategies. The integration of artificial intelligence, specifically through image processing, pattern recognition, and deep learning techniques, has greatly enhanced the feasibility of military vehicle classification. This study employs the You Only Look Once (YOLO) algorithm, particularly the YOLOv8 model, which is optimized for mobile applications and has shown high performance in evaluations. Enhancements include the incorporation of a Squeeze and Excitation (SE) block, improving detection accuracy. The research emphasizes the importance of detecting detailed target characteristics using images collected from electro-optical systems and aims to bolster decision support processes in target management systems. The development of a deep learning-based Target Detection and Identification (TDI) system is outlined, encompassing specialized targeted data acquisition, pre-processing, image partitioning, feature extraction, classification, and recommendation generation through decision support matrices. This model significantly improves image processing and object detection capabilities. Notably, it facilitates passive identification of combat vehicles using existing electro-optical devices without the need for additional hardware, while estimating distances discreetly. The system delivers real-time predictions, achieving a mean Average Precision (mAP) of 88.38%, thereby facilitating informed decision-making and risk reduction in military operations.

Keywords: combat military vehicles, image processing, classification, detection, assessment, attention mechanism, decision support matrix.

Received:03.11.2025 Accepted: 20.12.2025 Research Article

[1] HAVELSAN Inc., Ankara Türkiye

[2] Department of Electrical-Electronics Engineering, Başkent University, Ankara, Türkiye

* Corresponding author.

✉ seldaguney@baskent.edu.tr

Cite this article as: Tütüncüoğlu, R. A. & Güney, S. (2026). Development of near real time target detection and identification system for ground combat vehicles via artificial intelligence. *Journal of Defence and Security Industry: Strategy and Technology 1*, 96-115.

1. Introduction

Combat vehicles are specialized military assets designed for operational effectiveness in armed conflicts. These vehicles exhibit a wide range of designs and dimensions and are classified according to their primary functions and characteristics. A thorough comprehension of the advantages and disadvantages of different combat vehicle types is critical for the development of effective military strategies and tactics. This understanding enables military leaders to leverage the advantages of each vehicle type while mitigating their inherent limitations, thereby enhancing the probability of favourable outcomes in combat scenarios.

The classification of enemy combat vehicles, which involves the identification and assessment of adversary capabilities on the battlefield, is essential for several reasons. Key considerations in this process include target prioritization, informed tactical decision-making, effective allocation of firepower, troop protection, intelligence gathering, reconnaissance missions, and the maintenance of situational awareness.

The integration of Artificial Intelligence (AI) models for the classification of enemy combat vehicles substantially enhances military operational capabilities. AI-driven classification systems provide rapid and accurate intelligence, which improves decision-making processes and reduces risks to personnel. These systems act as force multipliers, significantly impacting the efficacy of military operations in contemporary combat environments. By augmenting situational awareness and operational planning, AI technologies can profoundly influence the outcomes of military engagements.

Object classification represents a significant area of study within computer vision and machine learning, focused on categorizing objects found in images into distinct and meaningful groups (Szeliski, 2010). Convolutional Neural Networks (CNNs) can be used at the core of applications ranging from photo annotation to popular self-driving studies. They are working intensively behind the scenes in everything from agriculture to military security. There is an increasing demand of object detection and automatic vehicle type recognition systems in the last 10 years as a result of the development of the cheaper sensor and camera technologies (Berwo et al., 2023). Because human operators alone cannot efficiently analyse large volumes of visual data and this data has to be classified very fast and correlated to evaluation.

A disparity exists both object detection and classification algorithms in the field of computer vision. Object detection algorithms are designed to identify and delineate specific objects within an image by creating bounding boxes around the objects of interest. In this context, these algorithms are tasked with accurately positioning the objects within the image frame. Notably, object detection algorithms may generate multiple bounding boxes, each representing a distinct object within the image. It is crucial to highlight that the exact number of objects and, consequently, bounding boxes are unknown in advance, adding complexity to the detection process.

Addressing this type of issue involves extracting various regions of interest from the image and employing a Convolutional Neural Network (CNN) to determine the presence of objects within those regions. However, a significant challenge associated with this approach is that the objects of interest may be located at different spatial coordinates within the image and possess varying aspect ratios (Gandhi, 2025).

Several algorithm techniques have been suggested and investigated by different researchers to detect and classify vehicle types. There are one-stage and two-stage target detection algorithms. Two-stage CNN algorithms are Region-based CNN, Fast R-CNN and Faster R-CNN (Hu, 2014). The one-stage algorithm is the You Only Look Once (YOLO) algorithm. It has ability to calculate the classification and regression (Liu, 2017).

Except for YOLO algorithm, all previously described object detection algorithms use regions to localize the object in the image. The network does not analyse the entire image; rather, it focuses on regions of the image that exhibit a high probability of containing the object of interest. In the YOLO framework, a single convolutional network is responsible for predicting both the bounding boxes and the class probabilities associated with these boxes (Redmon et al., 2016). YOLO offers inherent advantages in terms of processing speed, superior intersection over union for bounding boxes, and enhanced prediction accuracy when compared to other real-time object detection systems.

YOLO is significantly faster than other object detection algorithms; however, it has a limitation in that it struggles to accurately detect small objects within the image (Redmon and Angelova, 2014). This is because of the algorithm's spatial limitations. YOLOv8 provides a variety of models tailored for specific tasks in computer vision. These models address a range of needs, including object detection and more complex tasks such as instance segmentation, pose and key point detection, oriented object detection, and classification (Jocher et al., 2023). Experimental results indicate that the optimized YOLOv8 model enhances the detection of small objects with greater accuracy (Huadong et al., 2024).

Challenging environmental conditions—variable vehicle sizes, heterogeneous backgrounds, and adverse weather—complicate the detection of ground combat vehicles, motivating continual improvements in deep learning methods. Building on the YOLOv8 framework, Wu and Dong (2023) propose YOLO-SE to address multi-scale and small-object detection: the architecture incorporates a lightweight convolutional module (SEConv) that reduces parameter count and accelerates inference, replaces the original detection head with a redesigned prediction head, and adds an auxiliary detection head specialized for different object scales, collectively yielding improved detection accuracy. Additionally, the advantages of deep learning-based object detection algorithms, particularly YOLOv8, in real-time applications should be considered. In the study by Gang Cheng and colleagues, a lightweight model named SGST-YOLOv8 was developed, achieving an accuracy rate of 88.6% in detecting pedestrians and vehicles in complex environments (Cheng et al., 2024). Such accuracy is critical for detecting ground combat vehicles, as rapid and precise detection can directly impact the success of military operations.

The quality of the datasets used for detecting ground combat vehicles is also crucial. Datasets that account for various types, sizes, and environmental conditions of vehicles serve a crucial function in training deep learning models. For instance, in a study by Xin Zhang and colleagues, the YOLOv8 algorithm was utilized for vehicle and pedestrian detection in complex traffic environments, integrating a Coordinate Attention (CA) module to enhance feature extraction (Zhang et al., 2024). Such innovations contribute to achieving higher success rates in detecting ground combat vehicles.

Cui et al. (2024) developed an optimized YOLOv7 algorithm that utilizes a hybrid convolutional fusion attention mechanism to tackle complex background challenges in optical remote sensing images. This algorithm effectively addresses issues such as the dense clustering of small targets, substantial variations in target scales, and intricate backgrounds. These improvements in target detection enable the integration of distance measurement algorithms, allowing for the development of more comprehensive systems.

Hu at al. (2018) proposed a new architectural unit called the Squeeze-and-Excitation (SE) block to enhance the representational power of networks. This block adaptively adjusts the responses of features across channels by explicitly modelling the relationships between them. Their research demonstrates that stacking these SE blocks can lead to the creation of SENet architectures that generalize exceptionally well on challenging datasets. Notably, it has been stated that SE blocks enhance the performance of existing deep architectures while incurring very little additional computational cost.

Jocher et al. (2022) conducted a study using the YOLOv5 algorithm to estimate the distance of certain objects. The system is based on their box ratios. This study aims to accurately estimate the distances of objects in the image based on their size and ratios using the object detection capabilities of YOLOv5.

Near real-time object distance estimation and measurement using deep learning Canny Edge Algorithm and OpenCV has been achieved for small objects and small distance (1m≤ X) (Basavaraj et al., 2023).

Lan et al. (2023) developed the YOLOv8 network model for distance measurement operations and parsed the optimized data, and incorporated it into the binocular distance system, proposing a fusion sensory distance model. In addition, the model provides high portability on executable embedded development boards by edge detection.

As a summary, over the past decade, research has shifted from two-stage region-proposal detectors (e.g., R-CNN variants) - which offer strong localization accuracy at the cost of throughput -toward single-stage, YOLO-type architectures that unify localization and classification for real-time operation (Liu, 2017; Redmon et al., 2016). To compensate for YOLO’s known small-object and multi-scale limitations, recent studies integrate lightweight attention and multi-scale modules: SE and Coordinate Attention modules improve channel and positional feature discrimination with minimal overhead (Hu et al., 2018; Zhang et al., 2024), and YOLO-SE augments YOLOv8 with SEConv plus an auxiliary detection head to boost small-object performance (Wu & Dong, 2023). Lightweight variants (e.g., SGST-YOLOv8) prioritize edge deployment and maintain high accuracy in complex scenes but often omit full latency and dataset details (Cheng et al., 2024), while hybrid convolutional-fusion designs target dense, scale-variant scenarios such as remote sensing (Cui et al., 2024). For metric ranging, monocular box-ratio methods are simple but depend on prior size models and have limited absolute accuracy (Jocher et al., 2022); edge-based geometry pipelines perform well at very short ranges (~1 m) (Basavaraj et al., 2023); and binocular/stereo fusion yields better metric estimates at the expense of hardware/calibration complexity (Lan et al., 2023). Key trade-offs across these works are accuracy versus latency, small-object sensitivity versus computational cost, and metric fidelity versus sensor/calibration requirements; remaining gaps include limited tactical datasets, underreported domain-shift evaluations, and sparse end-to-end embedded system validations.

In our study, we extract the features of objects using the improved by SE module added to YOLO algorithm. By employing the feature transfer learning method, the newly obtained features are utilized as input for distance calculations. This method utilizes the knowledge and experiences of models trained on large datasets to be applied in new tasks that work with less data. The trigonometric calculation method we employed enables us to achieve measurements that are both very simple and rapid. The need for this type of technology within this particular segment is to identify opposing force vehicles without revealing our presence. Moreover, a thorough review of the literature reveals that there are no studies of this kind specifically focused on the military tactical domain.

2. Methodology

This section describes the methodology used for the targeted system. It thoroughly investigates the architecture (Figure 1) and aims to identify the most effective approach to achieve the desired outcome.

Initially, detailed information about the targets is obtained using a single-stage detector algorithm powered by SE module. Subsequently, the target's distance is calculated using an algorithm that employs the features extracted through the feature transfer learning method and the prepared data tables. Following the estimation of the target distance, this information is interpreted in conjunction with the generated decision support matrices, which provide recommendations to the user. This approach allows the model to demonstrate a high level of generalization while requiring less data.

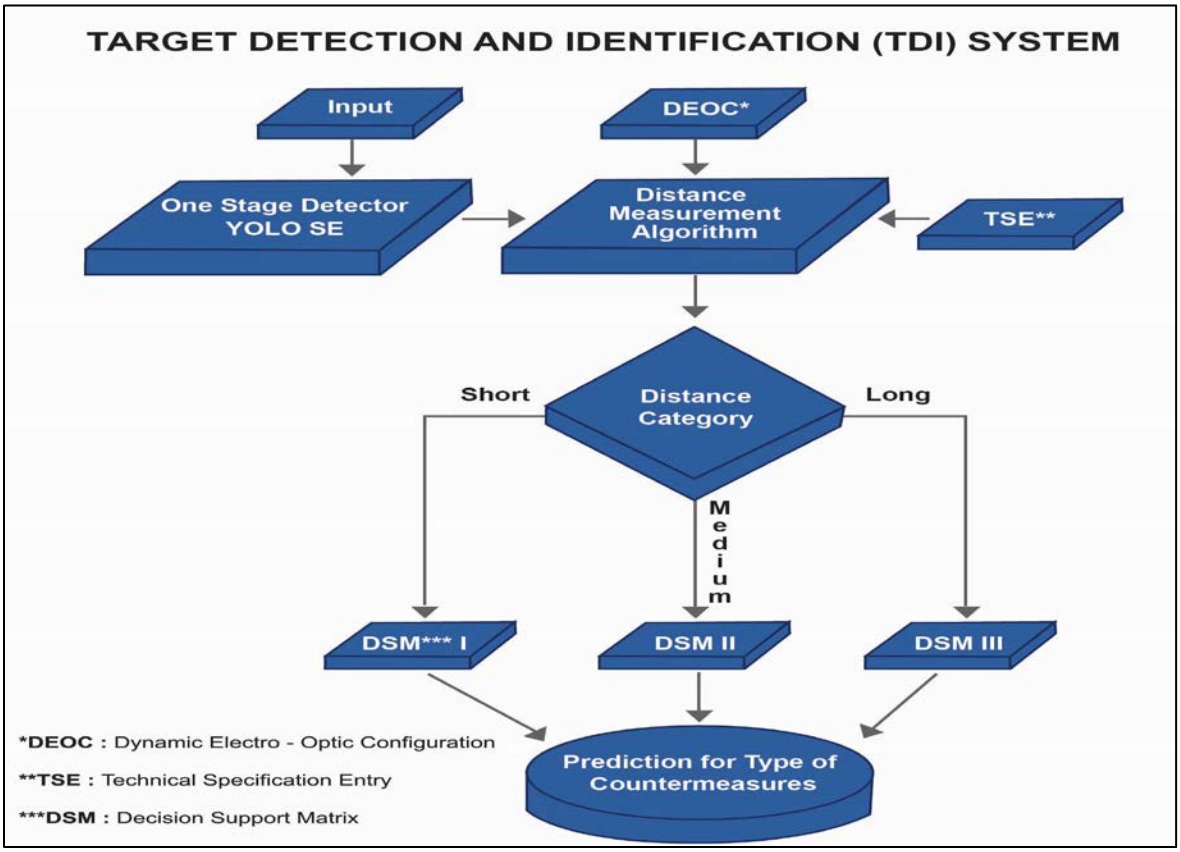

Figure 1. Main algorithm and steps.

2.1. Dataset

For the experimentations part, the dataset was prepared using Roboflow Universe (Roboflow, 2024). The initial dataset comprised 1,730 images and was first expanded through geometric augmentations (horizontal/vertical flips and image rotations); image rotations were applied in the range −20° to +20°, while associated bounding-box rotations were constrained to −15° to +15°, yielding 2,450 images. To maintain class balance, the set was then uniformly reduced to 2,400 images. Subsequently, a second augmentation stage introduced additional transformations - image rotation (−15° to +15°), shearing (analogous angular perturbations), random cropping, and grayscale conversion applied to 25% of the images (data augmentation techniques as seen at Figure 2) - producing a final augmented dataset of 6,000 images. These controlled augmentations were selected to emulate realistic viewpoint, scale, and illumination variations and thereby increase intra-class variability, with the explicit aim of improving model generalization and the robustness of detection and classification results.

(a) (b)

Figure 2. (a) Shows a sample light armoured wheeled vehicle, and (b) shows the same picture after applying rotate, shear, and grayscale augmentation techniques (MCV2).

By applying the rotation, bounding box rotation, shear, and grayscale, the new augmented data set consists of 6.000 images (see data split below Table 1).

Table 1. Data split.

Train Set	Valid Set	Test Set
%75	%15	%10
4,500	900	600

Average annotations per image is 1.2 per image, average image sizes are 0,41mp, median image ratios are 640x640). Also see for the training classes and number of samples that is used for training at Table 2.

Table 2. Train set data classes and number of samples.

Train Set Classes	Number of Samples
Medium and Heavy Armoured Wheeled (MHAW) Carriers	670
Medium and Heavy Armoured Tracked (MHAT) Carriers	652
Military Trucks (MT)	594
Heavy (Main Battle) Tanks (HT)	660
Light Armoured Wheeled (LAW) Carriers	653
Armoured Artillery (AA)	625
Mine Resistant Ambush Protected Vehicles (MRAP)	646

2.2. Operational Dataset Types

The classification of combat vehicles is a complex system that varies significantly across different countries and military organizations. Furthermore, advancements in technology can lead to the development of new categories or modifications to existing classifications. Combat vehicles are primarily categorized based on their mobility systems, which can be classified as either wheeled or tracked. Subsequently, military equipment is classified according to its weight category, specifically into heavy, medium, and light classifications (NATO, 2017).

In the context of surveillance reports, the type and number of combat vehicles present a critical aspect of data collection and analysis. True identification of combat vehicles is very essential for assessing the operational landscape and understanding potential engagements. Studies indicate that the effectiveness of certain combat vehicles against friendly forces on the battlefield significantly influences their classification and strategic deployment (U.S. Army, 2019) (U.S. Army, 2018).

Moreover, some vehicles are designed with versatility in mind, enabling them to adapt to various roles depending on mission requirements and configurations. This multipurpose capability further complicates the classification process but also enhances operational flexibility in diverse combat scenarios. Thus, the chosen classification framework not only reflects the physical characteristics of the vehicles but also their functional applications in different mission sets.

This data set consist of 7 (seven) types that are mostly used in the armies. These are Medium and Heavy Armoured Wheeled (MHAW) Carriers, Medium and Heavy Armoured Tracked (MHAT) Carriers, Military Trucks (MT), Heavy (Main Battle) Tanks (HT), Light Armoured Wheeled (LAW) Carriers, Armoured Artillery (AA), and Mine Resistant Ambush Protected Vehicles (MRAP). Also, the test data composed free from the trained datasets.

2.3. Main Algorithm

YOLOv8, specifically, is an improvement and refinement of the YOLO object detection algorithm (Jocher et al., 2022). A comparative analysis of the widely used YOLOv5 and YOLOv7 is carried out by Olorunshola et al. (2023) shows significant contribution compared to other works earlier mentioned in the literature review. The experiment demonstrates the effectiveness of the YOLOv5 model compared with YOLOv7. YOLOv8 is a computer vision model architecture developed by Ultralytics, the creators of YOLOv5.

2.3.1. Performance Comparison of YOLOv8

The results of the YOLOv8 to v5, v10 and v11 algorithms with the same dataset were obtained to check the performance of the model. For precision and inference speed, YOLOv8 outperforms the rest of the algorithms' results. YOLOv8 is offering cutting-edge performance in terms of accuracy and speed.

2.3.2. Advanced Features of YOLOv8

Building upon the advancements of previous YOLO versions, YOLOv8 introduces new features and optimizations. These new specifications make it an ideal choice for various object detection tasks as given below:

i. Upgraded backbone and neck architectures: YOLOv8 utilizes cutting-edge backbone and neck architectures, enhancing feature extraction and improving object detection performance.
ii. Anchor-Free split head: YOLOv8 features an anchor-free split head, which enhances accuracy and streamlines the detection process compared to traditional anchor-based methods.
iii. Optimized accuracy-speed trade-off: YOLOv8 maintains a balanced approach to accuracy and speed, making it suitable for real-time object detection across various applications.
iv. Variety of pre-trained models: YOLOv8 provides a selection of pre-trained models tailored to different tasks and performance needs, facilitating the selection of the appropriate model for specific applications.

2.4. Model Structure

The architecture is composed of three main components (Jocher et al., 2023):

i. Backbone: The backbone is the CNN that extracts features from the given image. YOLOv8 uses a custom CSPDarknet53 backbone, which utilizes cross-stage partial connections to enhance information flow between layers and improve accuracy.
ii. Neck: The neck combines feature maps from different stages of the backbone to capture information at various scales. Instead of the traditional Feature Pyramid Network (FPN), YOLOv8 utilizes a novel C2f module. This module integrates high-level semantic features with low-level spatial information, resulting in improved detection accuracy, particularly for small objects.
iii. Head: The head is responsible for generating predictions. YOLOv8 incorporates multiple detection modules that predict bounding boxes, objectness scores, and class probabilities for each grid cell in the feature map. These predictions are then combined to produce the final detection results.

2.5. The Squeeze-and-Excitation Module

The SE module is a structure developed to enhance channel attention and improve the representational power of models in deep learning. This module is effective specifically in CNNs. It is primarily used in object recognition and image classification.

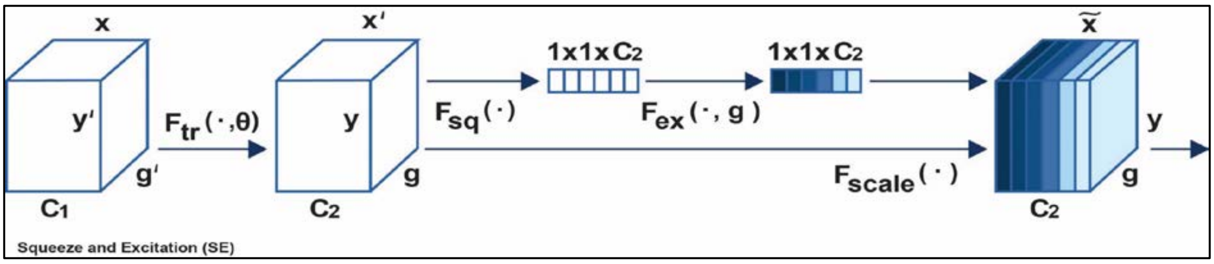

Figure 3. The SE module (Wu et al., 2023).

As shown in Figure 3, it has a simpler structure compared to other attention mechanisms. In the context of this design study, the (SE module has been integrated into each convolution (Conv) block, as indicated in Figure 4 and Figure 5. This allows the network to emphasize more critical channels, reduce the contribution of irrelevant channels, and acquire more distinctive features. It has been assessed that for military vehicles, which have similar subtypes, the inclusion of the SE layer positively influences the model's performance.

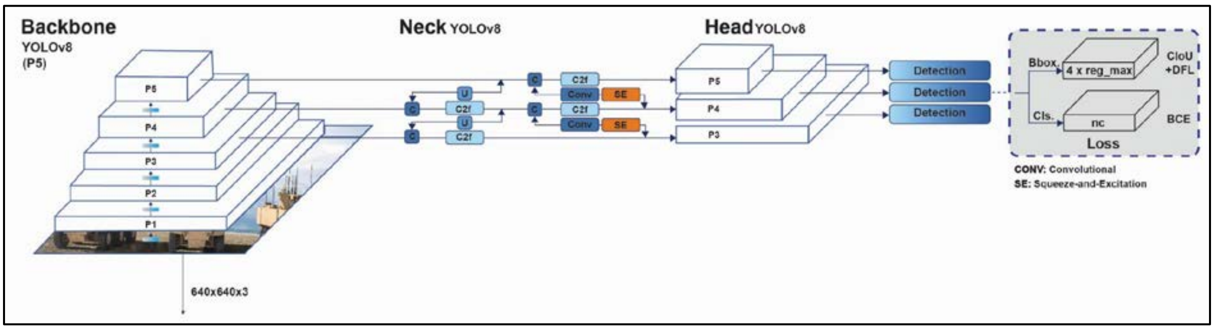

Figure 4. YOLOv8 SE algorithm.

Input Image → Backbone (CSP) →
↓
Conv → ReLU → SE (Squeeze) → Excitation → Multiply → Output Feature Map
↓
Conv → ReLU → SE (Squeeze) → Excitation → Multiply → Output Feature Map
↓
... (Other Conv Blocks)
↓
Feature Pyramid (FPN/ PAN) →
↓
Prediction Heads → Output (BBoxes & Class Probabilities)

Figure 5. Adding the SE module to the YOLOv8 algorithm.

The SE module learns the importance of each channel. Then it enables the re-scaling of these channels with weights. This process helps the model understand which features are important and create a more effective representation. Module consists of three phases:

i. Squeeze phase: The input feature map, which is a tensor with height, width, and channel count, undergoes global average pooling for each channel to create a "feature summary" representing the overall characteristics of each channel.
ii. Excitation phase: The squeezed feature vector is rescaled through connected (dense) two layers. The first layer uses the activation function of “ReLU”. The second layer uses the activation function of “Sigmoid”. At this stage, weights indicating the importance of each channel are calculated.

iii. Scaling phase: The original feature map to rescale it multiplies the computed channel importance weights. This process adjusts each channel according to its importance value.

The SE module enhances the model's ability to learn better and more meaningful features by emphasizing channels, thereby improving performance without incurring extra computational load. It generally performs well even in systems with limited resources. By utilizing the SE module, the generalization capability of networks is increased, resulting in better performance on more challenging datasets.

The SE module is an effective attention mechanism that can be used in deep learning architectures. By enhancing channel attention in convolutional neural networks, it significantly improves model performance. The applications of the SE module are extensive, making it a critical component in many modern deep learning models.

2.6. Additional Feature Extraction by Using Distance Measurement Algorithm

A picture can be used to localize the target in an image and associate it with the distance. Four numbers can be obtained in the bounding box. These are width and height variables. These variables are used in the formula for calculating the distance of object and describing the details of the detected object/objects. Depending on the distance of the object to the camera, width and height of the objects will change.

The values detected by the YOLOv8 algorithm and marked with a bounding box are used to estimate the distance based on the type of target detected, utilizing the calculation method described in Equation (1) and the logic of the calculation method can be understand from Figure 6. To determine the distance, revised formulas have been adapted to the algorithm (see distance measuring formulas in Equations (2) and (3). The focal length (f) depends on the specific type of electro-optic device used.

Using an empirical scale derived from a calibration target of known physical size (0.25 m) that subtends 1471.875 pixels in the image, we computed a linear conversion factor of 1471.875 / 0.25 = 5887.5 pixels per meter; consequently, any focal length given in meters can be converted to pixel units by multiplying by this factor.

$$f/d=r/R \tag{1}$$

$$f=d\times r/R \tag{2}$$

$$d=f\times R/r \tag{3}$$

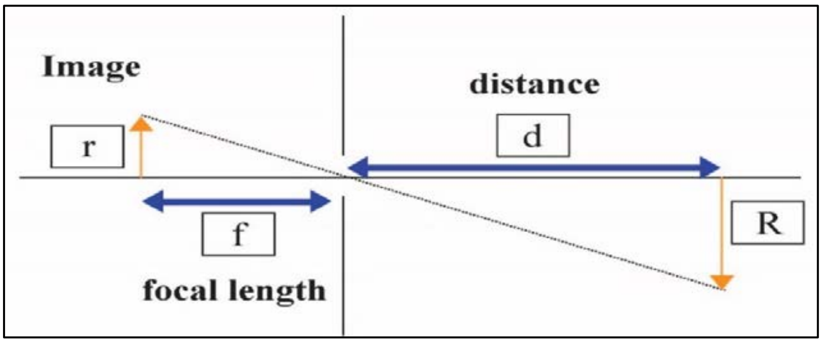

Figure 6. Trigonometric logic of distance measuring.

To achieve this, the width and height matrices (R) of the most commonly used vehicle types were created. When vehicle lengths are used, the false prediction rate due to the vehicle's stance position tends to increase. However, height generally remains consistent; therefore, average height values were adopted for different vehicle types (Tutuncuoglu and Guney, 2024). Additionally, when these values are adjusted according to the specific regions in which they will be applied, the estimation error rate decreases. The image height (r) of the identified vehicle is calculated by the YOLO algorithm.

2.7. Prediction by Using Decision Support Matrix (DSM)

After the combat vehicles are detected and identified, estimating their distance will force the decision maker to decide what precautions to take or what type of weapon system to use to neutralize the target.

The decision support matrix, which is created by examining the Land Combat Vehicles and the measures to be taken against these vehicles, makes recommendations (Table 3) to the user according to the information obtained from system.

Table 3. DSM I recommendation.

Type of Military Combat Vehicles	Minimum Ammunition /Weapon System Type
Short Distance (0-X00 m.)	Recommendation
Light Armoured Wheeled (LAW) Carriers	Medium Armour Piercing Ammunition, RPG
Medium and Heavy Armoured Wheeled (MHAW) Carriers	A/T Ammunition with Short Distance Weapon System
Medium and Heavy Armoured Tracked (MHAT) Carriers	A/T Ammunition with Short Distance Weapon System
Military Trucks (MT)	A/T Ammunition with Short Distance Weapon System
Heavy (Main Battle) Tanks (HT)	RPG
Armoured Artillery (AA)	RPG
Mine Resistant Ambush Protected Vehicles (MRAP)	RPG

3. Results and Discussion

3.1. Model Training Results

The YOLOv8 model was used for the training and test purpose. The YAML file was defined to configure the paths for the dataset and the number of classes to train. The model was trained for 241 epochs. A batch size of 32 was used for all epochs. The mean average precision is reached 83.6% mAP as seen Figure 7.

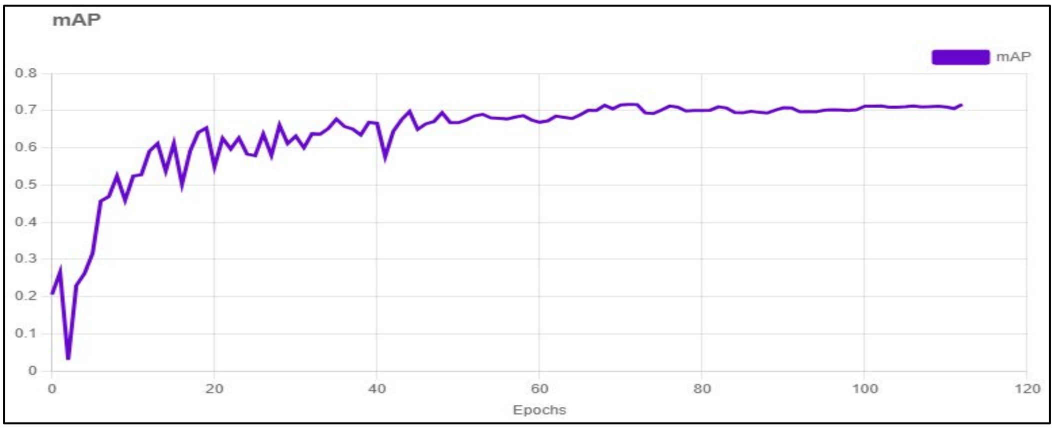

Figure 7. Data set mAP results.

For precision and inference speed, Table 4 also, provides the comparison of YOLO v10 and v11 results with YOLOv8. It can be seen that YOLOv8 outperforms the rest of the algorithms' results.

Table 4. YOLO v8 versus YOLO v10 and v11 at our dataset.

Class	Images	Mean Average Precision		
		YOLOv8	YOLOv10	YOLOv11
All	6,000	83.6%	68.7%	70.5%
Speed Of Inference		117 FPS	80 FPS	100 FPS

When the confusion matrix (Figure 8) is examined, it is observed that the lowest results are in MHAW, LAW and MT type classifications. It is considered that the similarity of LAW and MRAP type vehicles to civilian vehicles in some cases increases the error rates.

The detection and classification of a single observed combat vehicle is carried out very quickly by the YOLOv8 algorithm.

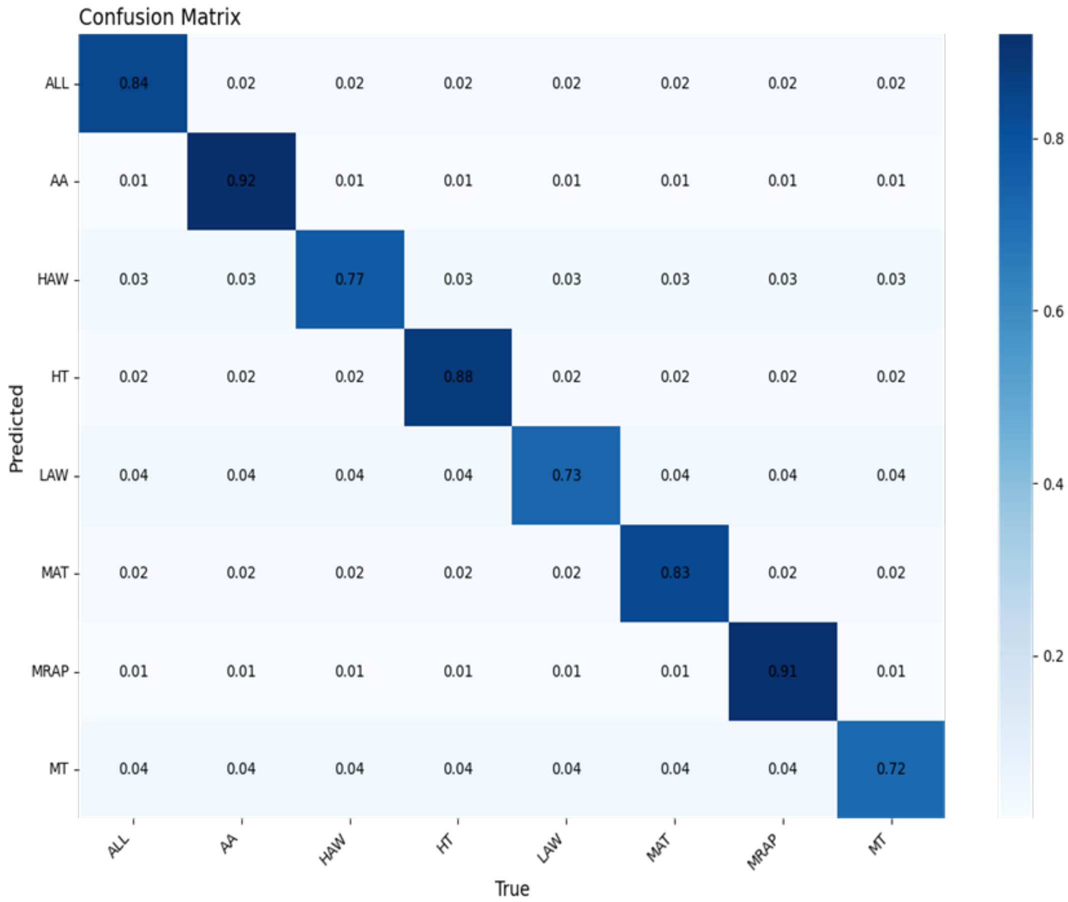

Figure 8. Confusion matrix.

3.2. Improved YOLOv8 by SE Module

A general evaluation of the application results of YOLOv8 SE has been conducted, along with a comparison to the classic YOLOv8 results Tütüncüoglu and Güney (2024). It has been determined that YOLOv8 SE, with the addition of SE modules, achieves mAP values exceeding 88.38% as seen at Table 5. This represents a significant improvement (approximately 5.7%), particularly for small objects and challenging scenes.

In our study, the addition of SE modules introduced no extra cost. The speed of YOLOv8 SE increase (approximately 17%) when we compare the classic YOLOv8.

Table 5. YOLOv8 and YOLOv8 SE test results comparison.

Class	Images	Mean Average Precision	
		YOLOv8	YOLOv8 SE
All	6,000	83.6%	88.38%
Speed of Inference		117 FPS	137 FPS

In addition, when we compared the lowest results of the YOLOv8 (LAW, MHAW and MT), YOLOv8 SE increased the performance of the lowest sub-types as seen at Table 6.

Table 6. Comparison of sub-types.

Lowest Classes Comparison	Mean Average Precision	
	YOLOv8	YOLOv8 SE
LAW	73%	82%
MHAW	77%	97%
MT	72%	86%

Following the main classification, the estimation of the distance using additional data obtained from the relevant tables, and the use of the appropriate decision support matrices, with the presentation of the results are calculated in milliseconds (Example for single target - Figure 9 and Table 7).

Figure 9. Single target detection.

Table 7. Single target detection and identification with recommendation.

Class	MAT (80.35%)
Detected Height (h)	490.35 px
Distance	74.98 meters
Recommendation	Medium Armour Piercing Ammunition, RPG

In cases where there are multiple targets, the required computation times are negligibly low (Example for multi target is given in Figure 10 and Table 8).

Table 8. Multi target identification with recommendation.

Class	LAW (92.89%)
Detected Height (h)	411.84 px
Distance	75.05 meters
Recommendation	Medium Armour Piercing Ammunition, RPG

Class	LAW (77.89%)
Detected Height (h)	83.87 px
Distance	368.54 meters
Recommendation	Medium Armour Piercing Ammunition, RPG

Figure 10. Multi target detection.

3.3. Operational Test Results and Discussion

The trained YOLOv8 SE model (algorithm, measuring distance and decision support matrix) is uploaded to the military type of computer (Panasonic Toughbook CF33). Next, field tests were conducted to evaluate the success of the TDI System utilizing both the tablet's camera and the vehicle's camera.

The type of the vehicles was MHAW type vehicles. The success of detection is 100% and classification precision 90%, the false precision is 10%. The false classification is only for 1 (one) LAW as seen at Table 9.

Table 9. Operational test results by YOLOv8 SE at field.

Class/T&F	MHAW
True	9
False	1 (LAW)

For validation, ten printed exemplars of each vehicle class were photographed with a tablet camera and processed by the YOLOv8-SE model deployed on the Panasonic Toughbook CF-33; the measured classification accuracy on these printed-image captures was approximately 6 percentage points lower than the accuracy observed during the controlled training test evaluation as seen at Table 10. This decline is consistent with a domain shift between the training distribution and the printed-image test distribution: printing and re-photographing alter image statistics, introduce halftone and paper-texture artifacts, and often reduce effective resolution and dynamic range; additionally, uncontrolled capture conditions (illumination, viewing angle, distance, tablet auto-exposure/white-balance, and lens distortions) and compression/noise from the tablet camera further diverge the test images from the original training data. Together, these factors reduce the discriminative cues the model learned, producing the observed performance drop.

Table 10. Printed picture test results by YOLOv8 SE.

Class/T&F	LAW	MHAW	MHAT	MT	HT	AA	MRAP
True	9	9	8	7	8	8	8
False	1	1	2	3	2	2	2

3.4. Operational Understanding of Training

MT, MHAW and MRAP type vehicle identification confusion results are investigated. It is observed that their sizes, heights from ground, and number of the wheels are different. Remember that the selected pictures are very distinctive examples (Figure 11).

(a) (b) (c)

Figure 11. (a) MT, (b) MHAW, and (c) MRAP examples (MCV2).

MHAT and HT type of vehicle identification confusion results are investigated. It is observed that their bases are almost same. Specifically, the towers are resembling each other. Only, the diameter of the tank barrels is bigger than the diameter of MHAT barrels (Figure 12).

(a) (b)

Figure 12. (a) MHAT, and (b) HT example (MCV2).

4. Conclusion

In this study, the YOLOv8 object detection model has been improved by SE and used to detect combat vehicles and to categorize their types efficiently. Also, the distances of the vehicles have been estimated by sub-algorithm, and a supporting decision matrix has been created with the obtained data to develop countermeasure recommendations. The model's detection and identification rates have been calculated as 88.38% in terms of mAP and 93% in terms of precision. When evaluating these results, it is evident that the model provides high accuracy and effectiveness in vehicle detection.

The ability to accurately identify the type and distance of the vehicle passively indicates that the model could be easily integrated with electro-optical systems or military vehicles in the future. These findings suggest that the model may offer a practical solution for military applications.

The results clearly highlight the potential of object recognition and distance estimation applications in the military domain. Future studies are recommended to additional improve the model's performance and test it under different operational scenarios. Suggestions for the development of the model can guide future research efforts. Due to the complex structure and dynamic variability of the real battlefield, there is a need to detect and to classify targets in this environment in near real time. This paper proposes an improved image recognition method. This method is formed by the combination of the image recognition algorithm, distance estimation algorithm (by additional feature extraction), and decision support matrices.

In conclusion, the enhancement of the capabilities of the developed model holds significant potential for supporting faster and more effective decision-making processes on the battlefield. Future studies may explore strategies to further improve the integration and performance of the model in this regard.

Author Contributions

The first author contributed to the study through research design, implementation, and manuscript development. The second author contributed significantly to the study by providing guidance and insights in areas of consultation and mentoring. Their expertise played a vital role in shaping the research direction and enhancing the overall quality of the work.

Data and Code Availability

The data and code used in this study are available upon reasonable request from the corresponding author. Access to the datasets and software will be provided to researchers who seek to replicate or build upon the findings of this work.

Supplementary Materials

The data utilized in this study are openly accessible in the Roboflow database. Researchers can freely access and download the datasets to facilitate further analysis and replication of the results.

References

Basavaraj, U., Raghuram, H., & Mohana. (2023). Real-time object distance and dimension measurement using deep learning and OpenCV. *Proceedings of the Third International Conference on Artificial Intelligence and Smart Energy (ICAIS)*, 929–932. https://doi.org/10.1109/ICAIS53537.2023.9762892

Berwo, M. A., Khan, A., Fang, Y., Fahim, H., Javaid, S., Mahmood, J., & Abideen, Z. U. (2023). Deep learning techniques for vehicle detection and classification from images/videos: A survey. *Sensors, 23*, 4832.

Cheng, G., Chao, P., Yang, J., & Ding, H. (2024). SGST-YOLOv8: An improved lightweight YOLOv8 for real-time target detection for campus surveillance. *Applied Sciences, 14*(12), 5341.

Cui, C., Wang, R., Wang, Y., Zhou, F., Bian, X., & Chen, J. (2024). Research on optical remote sensing image target detection technique based on DCH-YOLOv7 algorithm. *IEEE Transactions, 12*, 34741–34751.

Gandhi, R. (n.d.). *R-CNN, Fast R-CNN, Faster R-CNN, YOLO — Object detection algorithms*. Medium. https://medium.com/towards-data-science/r-cnn-fast-r-cnn-faster-r-cnn-yolo-object-detection-algorithms-36d53571365e

Hu, J. (2014). *Research on fast tracking algorithm of moving target based on optical flow method* (Master's thesis). Xidian University, Xi'an, China.

Hu, J., Shen, L., & Sun, G. (2018). Squeeze-and-excitation networks. In *Proceedings of the IEEE/CVF Conference on Computer Vision and Pattern Recognition* (pp. 713–722).

Huadong, H., Binyu, W., Jiannan, X., & Tianyu, Z. (2024). Improved small-object detection using YOLOv8: A comparative study. *Applied and Computational Engineering, 41*, 80–88.

Jocher, G., Chaurasia, A., & Qiu, J. (2023). *Ultralytics YOLOv8*. https://github.com/ultralytics/ultralytics

Jocher, G., Chaurasia, A., Stoken, A., Borovec, J., Kwon, Y., Michael, K., Fang, J., Yifu, Z., Wong, C., Montes, D., Wang, Z., Fati, C., Nadar, J., Sonck, V., Skalski, P., Hogan, A., Nair, D., Strobel, M., & Mrinal. (2022). *Ultralytics/yolov5: v7.0 – YOLOv5 SOTA realtime instance segmentation* [Data set]. Zenodo. https://doi.org/10.5281/zenodo.7035401

Lan, M., Wang, J., & Zhu, L. (2023). Perception and range measurement of sweeping machinery based on enhanced YOLOv8 and binocular vision. *IEEE Transactions, 11*, 126398–126408.

Liu, X. (2017). *End-to-end target detection and attribute analysis algorithm based on deep learning and its application* (Master's thesis). South China University of Technology, Guangzhou, China.

NATO. (2017). *Land symbols in APP-6 (D).* https://nisp.nw3.dk/standard/nato-app-06-ed.d-v1.html

Olorunshola, O., Irhebhude, M., & Evwiekpaefe, A. (2023). A comparative study of YOLOv5 and YOLOv7 object detection algorithms. *Journal of Computing and Social Informatics, 2*, 1–12. https://doi.org/10.33736/jcsi.5070.2023

Redmon, J., & Angelova, A. (2015). Real-time grasp detection using convolutional neural networks. In *Proceedings of the IEEE International Conference on Robotics and Automation (ICRA).*

Redmon, J., Divvala, S., Girshick, R., & Farhadi, A. (2016). You only look once: Unified, real-time object detection. In *Proceedings of the IEEE Conference on Computer Vision and Pattern Recognition (CVPR)* (pp. 779–788).

Roboflow. (n.d.). *Roboflow annotation tool.* https://roboflow.com/annotate and MCV2 Dataset; https://app.roboflow.com/baskent-univercity-5cybx/mcv2/browse?queryText =&page Size = 50&startingIndex=0&browseQuery=true

Szeliski, R. (2010). *Computer vision: Algorithms and applications* (1st ed.). Springer.

Tutuncuoglu, R. A., & Guney, S. (2024). Development of target detection and identification system for combat military vehicles via artificial intelligence and decision support matrix. *International Journal for Multidisciplinary Research, 6*(6).

U.S. Army. (2018). *ATP 3-21.10 Infantry rifle company: Appendix F—Armored, Stryker, and mounted employment*. U.S. Army Publishing Directorate.

U.S. Army. (2019). *ATP 2-01.3 Intelligence preparation of the battlefield: Chapter 5—Evaluate the threat*. U.S. Army Publishing Directorate.

Wu, T., & Dong, Y. (2023). YOLO-SE: Improved YOLOv8 for remote sensing object detection and recognition. *Applied Sciences, 13*(24), 12977.

Zhang, X., Huang, H., Yang, J., & Jiang, S. (2024). Research on deep learning-based vehicle and pedestrian object detection algorithms. *International Archives of the Photogrammetry, Remote Sensing and Spatial Information Sciences, XLVIII-4/W10-2024*, 213–220. https://doi.org/10.5194/isprs-archives-XLVIII

JOURNAL OF DEFENCE AND SECURITY INDUSTRY

Journal of Defence and Security Industries: Strategy and Technology, 2026, 1(1)

Science & Technology Section

A Novel Back Propagated Image Encryption Method with PGP Public Key and 1D Logical Map

Talha Çelik [1], Nurettin Doğan [1,*], Adem Alpaslan Altun [1,*]

Abstract

Encrypted communication plays a significant role in a wide range of areas today, both in protecting personal data and ensuring secure data exchange between governments. Encryption has been used for centuries to protect data generated by humans. In the past, data that needed to be encrypted has evolved from text-based writings to image and sound-based multimedia messages, depending on the development of technology. The high data density and abundance of similar data contained in multimedia messages have been seen to render the classic text-based encryption methods used to encrypt this data time-consuming and insecure in terms of encryption security. Therefore, this study examines recent work on encrypting multimedia messages and proposes a new hybrid encryption method. The proposed method consists of three stages. In the first stage, the rows and columns of the plain image are shifted using the classical Affine encryption algorithm. In this stage, the width and height values of the image are used to create the Affine key. In the second step, the recipient's Pretty Good Privacy (PGP) key is obtained. The resulting PGP key creates the key sequence K to be used in the encryption process. The values are used to obtain the μ value, which is the input parameter of the One-Dimensional (1D) logistic map, and the initial value x_0. In the last step, the XOR operation is applied to the image using the data obtained from the 1D logistic map, and all pixels of the plain image are encrypted. In the proposed work, experiments were conducted on greyscale and RGB images of different sizes. The NPCR value of 99.6078 and the UACI value of 33.5323 demonstrate the applicability of the proposed method.

Keywords: cryptography, chaos, logistic map, image encryption, public key.

Received: 26.10.2025 Accepted: 18.12.2025 Research Article

[1] Computer Engineering Department, Selçuk University, Konya, Türkiye

* Corresponding authors.

✉ nurettin.dogan@selcuk.edu.tr, altun@selcuk.edu.tr

Cite this article as: Çelik, T., Doğan, N., & Altun, A. A. (2026). A novel back propagated image encryption method with PGP public key and 1D logical map. *Journal of Defence and Security Industry: Strategy and Technology 1*, 116-139.

1. Introduction

While rapidly developing and expanding technology has brought convenience, it has also created new privacy issues. Sharing multimedia messages and sending data between individuals has become quite easy today. However, this leads to a violation of personal information privacy. Violation of information privacy can also lead to serious problems in interstate and military communications. Since Julius Seaser, many new methods have been developed for creating and transmitting encrypted messages. In this rapidly developing technological world, multimedia messages have begun to replace text-based messages. Multimedia messages can be both single-frame still images and multi-frame videos. The military devices transmitting these image sequences must encrypt the image during transmission and decrypt it only by the unit managing the military device. These situations are examples of today's information security and encryption needs.

Many new methods have been introduced for use in encryption processes. Some of these are symmetric encryption methods, while others are asymmetric (Althamir et al., 2023). DES, AES, and RSI algorithms are among the most commonly used symmetric encryption methods in today (Diffie, 2022). These methods are quite secure and fast for encrypting text-based messages. However, when used in image encryption, they are both slower than asymmetric encryption methods in terms of encryption speed and inadequate in ensuring the security of the encrypted data (Geetha et al., 2025). Using asymmetric encryption methods in their raw form for image encryption reduces the reliability of the encryption process, and the encrypted image can be decrypted with a number of decryption methods. Considering these circumstances, the need to develop new, more secure and faster methods for encrypting messages containing images or multimedia information has emerged.

RGB and grayscale image contains a high density of data. The similarity between this data and the large number of data to be encrypted are fundamental characteristics of an image. The similarity of the numerical values of two adjacent pixels in an image defines high similarity. The concept of data density and the large number of data to be encrypted describe the number of pixels in the image. An RGB image with 1024 horizontal and 768 vertical pixels requires a total of 2,359,296 data points to be encrypted. Due to these features of the image, encrypting an image with traditional text encryption methods causes both waste of time and reduces reliability because the encryption process takes longer than chaotic methods (Althamir et al., 2023).

Permutation and diffusion methods were developed to eliminate high pixel correlation in images (Karthik et al., 2025). These methods also utilized the randomness provided by the chaos architecture. Chaotic maps are frequently preferred in image encryption due to their unpredictability, sensitive variation depending on the initial condition, and ergodicity (Braverman & Nelson, 2025). Fridrich (1998) first proposed encrypting an NxN image using a two-dimensional (2D) Baker map. Also in that year, Baptista proposed a method for encrypting text using a one-dimensional (1D) logistic map using a chaos architecture.

In the following years, chaotic maps continued to be frequently used for image encryption. However, the initial values used in chaotic maps and the input parameters of the chaotic map were fixed at each encryption step. Consequently, when the chaotic values obtained from the chaotic map iterations are identical, decryption becomes considerably easier by estimating the initial value of the chaotic map. Several new methods have been proposed to eliminate this problem and to dynamically obtain the initial parameters of the chaotic map. Initial values and parameters for chaotic maps have been generated using data from biological generators such as electrocardiography (ECG), voice, iris, fingerprint, and similar data. This makes it difficult to predict the initial values and the result obtained for the first of the chaotic values to be used for encryption.

As an example of these methods for audio data, Lyle et al. (2022) applied the Discrete Fourier Transform (DFT) transform to recorded human voice. They generated the initial value of a 1D logistic map using the values obtained from the DFT analysis. They then encrypted the image by iterating the 1D logistic map 3000 times and applying a diffusion operation on each pixel using the data obtained starting from the 3001st value. The main purpose of advancing the 1D chaotic map 3000 steps after generating the initial chaotic value is to make it difficult to estimate the input parameter μ and the initial value x_0 of the 1D logistic map. In a similar study, Lyle et al. (2022) aimed to increase the initial value of the chaotic map and the unpredictability of its parameters by expanding the key space. They determined the initial values using a pseudo-random generator. They then examined the differences between the Zaslavsky Web Map and the New Adaptive Zaslavsky Web Map using a bifurcation diagram and key space analysis. The New Adaptive Zaslavsky Web Map was concluded to be more secure and usable. It was suggested that this chaotic map could be used in encryption operations (Lyle et al., 2022). This study proposed image encryption using a 1D logistic map for data obtained by digitally scanning the iris layer of the human eye, which allows sufficient light to enter the eye. Similar to other studies, data obtained from digitally scanning the iris layer was used to determine the initial values of the chaotic map (Archana et al., 2022). Archana et al. (2022) proposed encryption using digital data obtained from electrocardiography (ECG). The ECG values used in the encryption process were used to replace the input parameters α, β, and ν of the 3D logistic map. This study proposes to encrypt text-based data such as card numbers instead of image encryption. However, the methods and recommendations used, similar to other studies, were developed to ensure that the initial value and input parameters of the chaotic map are constantly changing (Eldesouky et al., 2022).

Based on the information obtained through literature review and research, this study proposes a new three-step image encryption method. This proposed method aims to eliminate the problem encountered in other studies, which requires constant generation of input parameters and initial values for chaotic maps. This aims to make the encryption process more secure and faster. Furthermore, the PGP public key is used to address the problem of sharing private keys, which is often the case in encryption methods.

In this study, the literature review examines studies on image encryption in the literature. The use of chaotic maps in image encryption was investigated, and the parameter and input value generation methods for chaotic maps were obtained. The back propagated image encryption process proposed in this study is explained in detail in three separate steps in the method section. In the performance analysis section, images encrypted with the proposed method are compared with other studies in the literature. The findings and results are detailed in tables. The final section outlines the contribution of the method developed in this study to the literature, along with its advantages and disadvantages. Considering its potential contribution to future studies, recommendations are made.

1.1. 1D Logistic Map

Chaotic systems are built on mathematical functions that depend on initial conditions and input parameters. Within the limits of the appropriate values used for the input parameter of the chaotic map to exhibit chaotic behaviour, the chaotic map function produces non-repetitive, unpredictable outputs. In this study, a 1D logistic map was used to encrypt RGB and grayscale images. The first use of a 1D logistic map began in 1998. Baptista used a 1D logistic map to encrypt a simple text. In his first study, he succeeded in encrypting and decrypting the word "hi." In the following years, 1D logistic maps were frequently used in image encryption due to their ease of use, reliability, and speed. The 1D logistic map is derived from Equation (3).

Figure 4 shows the Lyapunov exponent (a) and bifurcation graph (b) for a 1D logistic map. As can be seen from this graph, the values within the [3.47, 4.0] range represent the value range in which the 1D logistic map exhibits chaotic behaviour. In developing the algorithm proposed in this study, the range in which the 1D logistic map exhibits chaotic behaviour was taken as the reference for manipulating the input parameter μ of the 1D logistic map. Furthermore, the input parameter μ was generated using the PGP key belonging to the recipient of the encrypted message, making it unique to the recipient.

In this study, the 1024 characters corresponding to the first 2^{13} bits of the PGP public key were used to determine the input parameter μ and the initial value x_0 of the 1D logistic map at the beginning of the encryption process. The decimal values of these characters, found in the ASCII code table, were used for the numerical values. The 1D logistic map was iterated as many times as the number of pixels in the grayscale Lena image, and a key sequence equal to the total number of pixels was obtained. The resulting key sequence was then propagated by applying the XOR operation, with each element corresponding to each pixel in the grayscale Lena image.

1.2. Pretty Good Privacy Key (PGP)

RSA, one of the asymmetric encryption methods, was developed in 1977 at the Massachusetts Institute of Technology (MIT) laboratories (Susanti et al., 2025). In this method, each user has a private and a public key. The sender encrypts a file with the recipient's public key. The recipient decrypts the encrypted message with their private key. The term "key" in this method refers to the public and private key pair generated by the PGP software. The PGP software, developed by Philip Zimmermann in 1991, was developed by rearranging the public key and private key pair used in the RSA method for file and email encryption (Heinrich, 2025). In this study, the public key generated by the PGP software was generated using the function shown in Equation (4) as the input parameter μ of the chaotic map. The input parameter was generated to be between the values at which the 1D logistic map exhibits chaotic behaviour. The developed algorithms and methods are discussed in detail in the section titled generation of chaotic values. The obtained input parameter μ was used in the iterations of the 1D logistic map.

The keys in the public and private key pairs generated via the PGP software consist entirely of ASCII characters. These keys can be 512, 1024, and 2048 characters long (Heinrich, 2025). The lengths of these key pairs can be increased. However, a longer key does not necessarily imply increased security. While a 1024-character public key requires $3 * 10^{11}$ human years to be decrypted using brute force on modern computers, a 2048-character public key requires $4 * 10^{27}$human years. As can be seen from the obtained values, the time required for a brute-force attack to crack a password is quite long. Therefore, it is preferred due to its performance during both encryption and decryption. Furthermore, the use of 1024-character key pairs have become widespread due to its security against brute-force attacks (Saif, 2025). Studies have been conducted on the commonly used 1024-character PGP public key, taking into account both performance and security criteria. Therefore, in the proposed algorithm, 1024 characters corresponding to the first 2^3 bits of the public key were used in the algorithm used to generate the input parameter of the 1D logistic map.

For example, "mQINBGO133gBEADd" represents the first 16 characters of a public key. The μ parameter generated by the method specified in Equation (4) will be 3.62306202500612 based on the first 16 characters. All μ values obtained are in the range [3.47, 4.0], where the 1D logistic map exhibits chaotic behaviour. The number of digits after the decimal point in the generated values is kept constant at 15 in IEEE floating point standards (Boldo et al., 2023).

1.3. Affine Encryption

Affine encryption is a reversible encryption algorithm that uses modular arithmetic by establishing a relationship between numbers using the greatest common divisor. While it is generally used to manipulate values in text encryption, it is used to manipulate pixel positions in image encryption. Affine is a frequently used encryption method (Ihsan & Doğan, 2023). Unlike single-key encryption methods, Affine encryption uses two-key encryption (Ali et al., 2025). This aims to increase security, but using Affine alone in an encryption process is insecure. Therefore, other methods have been utilized in addition to Affine encryption.

$$E(x) = (ax + b) mod\, m, \quad a, b \in Z, \quad \gcd(a, m) = 1 \tag{1}$$

$$D(y) = a - 1(y - b) mod\, m, \quad a - 1a \equiv 1 (mod\, m) \tag{2}$$

$$x, y \in \{0,1,2, \dots, m - 1\}$$

The x value in Equation (1) and Equation (2) represents the value to be used in the encryption process. The $E(x)$ method represents the encryption process. M and N values are representing plain image sizes. In the Affine method, the values a and b are specified as two keys. To determine the value of a, the greatest common divisor must be determined, such that $(a, N) = 1$. No such requirement is required for the other Affine key used, but the value of b must be specified between 0 and $N - 1$.

2. Method

In this study, the method used to encrypt RGB and grayscale Lena images consists of three stages. In the first stage, the a and b values used in the Affine algorithm are determined by the width and height of the image. In this process, the a value of the Affine method is calculated by decreasing the image width from halfway up to $(a, W) = 1$. For example, for an image with a width of 1024 pixels, $N = 1024$ and $a = n/2 - step_n$. Based on this example, a value will be 511 and the b value will be 256. After finding the Affine keys, row and column shifting operations are applied to the Lena image. In the second stage, the first 1024 characters of the PGP public key are converted to numerical values to produce chaotic values in the 1D logistic map and processed with the normalization function in Equation (4). This normalization function normalizes the numerical values obtained from the PGP public key between the values $[3.47, 4.0]$, which is the region where the 1D logistic map will exhibit chaotic behaviour. Then, the appropriate input parameters and initial values for the 1D logistic map are obtained. The 1D logistic map is iterated as many times as the number of pixels in the image to be encrypted. Each chaotic value obtained at this stage is transferred to the key array K, which will be used in the diffusion process. In the third and final stage, a dynamic diffusion operation is applied using the XOR operator to each element in the key array K, each pixel in the gray-level Lena image (P_i), and the pixel value in the previous encrypted gray-level Lena image (C_i). Thus, the last encrypted pixel value establishes a close connection with the first pixel value in the image.

In the first step, the a and b values generated using the affine algorithm were used to perform the row and column shifting operation. The a and b values used in the Affine algorithm are explained in detail in the section affine encryption step.

In the second stage, the input parameter and initial value of the 1D logistic map are generated using the PGP public key. The input parameter and initial value generated using the PGP public key are within the region where the 1D logistic map exhibits chaotic behaviour. Therefore, the data obtained from the chaotic map is unpredictable. Next, a sequence of K keys, corresponding to the number of pixels in the Lena image, is generated using the 1D logistic map function Equation (3) and the K key generation function Equation (5). The K key sequence contains the chaotic outputs generated by the 1D logistic map. These values are stored for use in the next stage, the diffusion stage.

$$x_{n+1} = f(x_n) = b\, x_n(1 - x_n), [b = \mu]\ in\ [3.47,4] \quad (3)$$

In the third and final step, a dynamic XOR operation is applied between each element (K_i) of the key sequence K obtained from the iterations of the chaotic map and each pixel value (P_i) of the gray level Lena image. To increase the reliability of the encryption algorithm during the propagation phase and to obtain a stronger encryption method, the result of the previous XOR operation C_{i-1} is included in the next operation. This operation is shown in Equation (9). In this operation, because the result of the previous XOR value is obtained, the previous value is not generated in the first iteration. To eliminate this problem, the C_0 value in the first iteration is fixed to 1. The other C_i values are determined by the XOR operation and used in the next calculation. The diagram of the method developed within the scope of this study is shown in Figure 1.

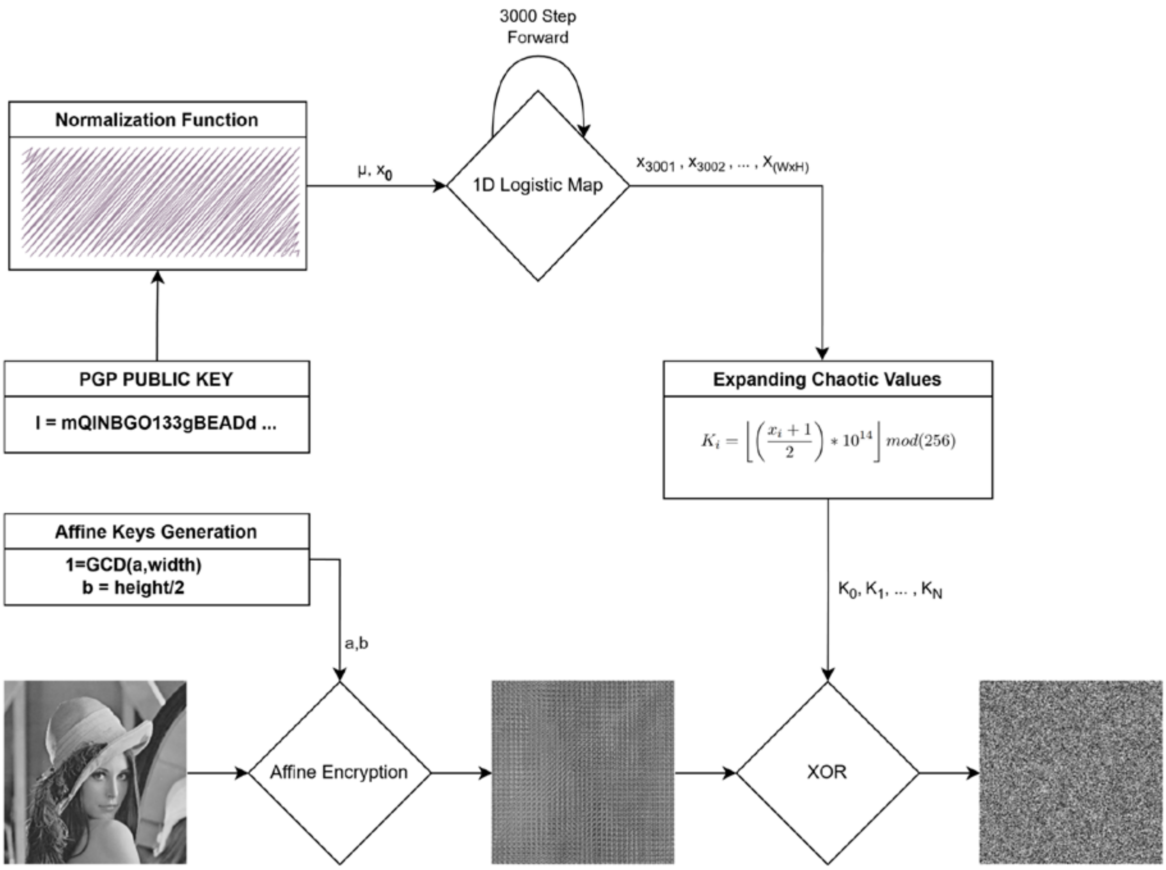

Figure 1. Diagram of the proposed method.

2.1. Affine Encryption Step

In the affine method, two keys are selected, a and b. These keys should be determined such that Greatest Common Divisor (GCD) $(a, N) = 1$ for a key space of length N. The Euclidean division algorithm is used to determine this key. This algorithm generates the value a by calculating $1 = \gcd(a, N)$. The other key, b, can be chosen to lie between the values $[0, N]$. In the proposed algorithm, the value b is set to $N/2$. $E(x)$ represents the encryption function, and $D(y)$ represents the decryption function, shown in the Equation (1) and Equation (2).

A 256x256 pixel grayscale Lena image, in which row and column shifting was applied using the Affine method, is shown in Figure 2. In this image, a = 511, b = 256 was set for the Affine encryption algorithm. As can be seen from the encrypted image (c), its pixels are not homogeneously spread. Therefore, the encrypted image obtained by using the Affine encryption algorithm alone can be easily decrypted using frequency analysis and similar methods. Therefore, in this study, in addition to the Affine method, a diffusion process was also used. A 1D chaotic map was utilized to ensure that the values used in the diffusion process were unpredictable. Thus, the reliability and encryption performance of the system were increased. As a result of the experiments, the encrypted images obtained with this method were examined under the reliability section. The Euclidean function used to determine the a and b parameters of the Affine method is shown in Algorithm 1. The K_a value obtained with the Euclidean function was used in the row and column shifting step.

Algorithm 1: An algorithm of Affine encryption method

Input: : $Image, Width, Height$

Output: : $PixelsShiftedImage\ (P)$

Step-1 : r ← $Width$ mod $Height$

Step-2 : **while** $r \neq 0$ **do**

a ← b

b ← r

r ← a mod b

Step-3 : **for** $i = 0$ to $Width$ **do**

$P_{[j]} \leftarrow (i * r + \frac{Width}{2}) \bmod Width$

Step-4 : **for** j= 0 to $Height$ **do**

$P_{[j]} \leftarrow (j * r + \frac{Height}{2}) \bmod Height$

Step-5 : return P

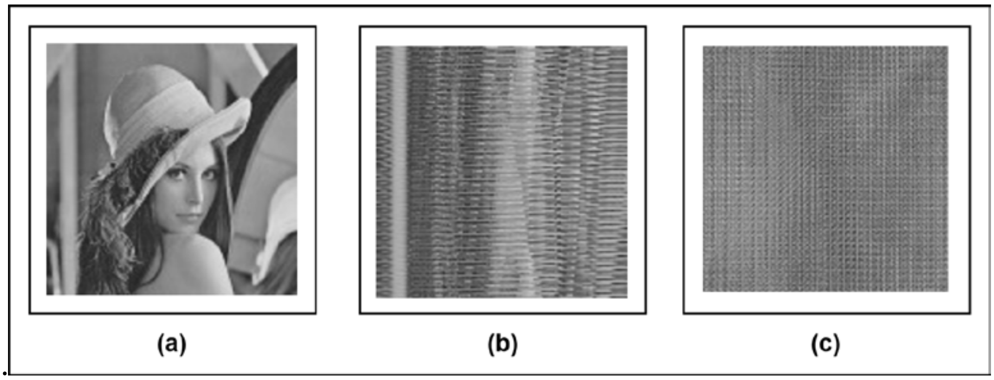

Figure 2. (a) Encryption of gray level Lena image using affine method. Original Lena image, (b) Row shifting with affine algorithm, and (c) Column shifting with affine algorithm.

2.2. Generation of Chaotic Values

This step explains how to generate the input parameter and initial value of the 1D logistic map used in the study using the PGP public key, and then how to prepare the chaotic outputs obtained from the 1D logistic map for use in the next diffusion phase.

First, the PGP public key of the recipient to whom the encrypted image will be sent is obtained. This public key, as described above, is published by the recipient in a publicly accessible format. The sender encrypts the message with the recipient's public key and sends it to the recipient. The recipient decrypts this encrypted message with the private key in their own public and private key pair. In this way, the sender encrypts and sends the message in a way that only the recipient can decipher. This method, used today especially for email and file encryption, eliminates the problem of key sharing. However, as explained in previous sections, this method, called asymmetric encryption, is quite successful in text and file encryption, but it fails in image encryption. However, it is quite successful in key generation and sharing. Thanks to this key sharing advantage, the encryption key, called the secret in image encryption, has become very efficient in generating the input parameters and initial values of the chaotic map.

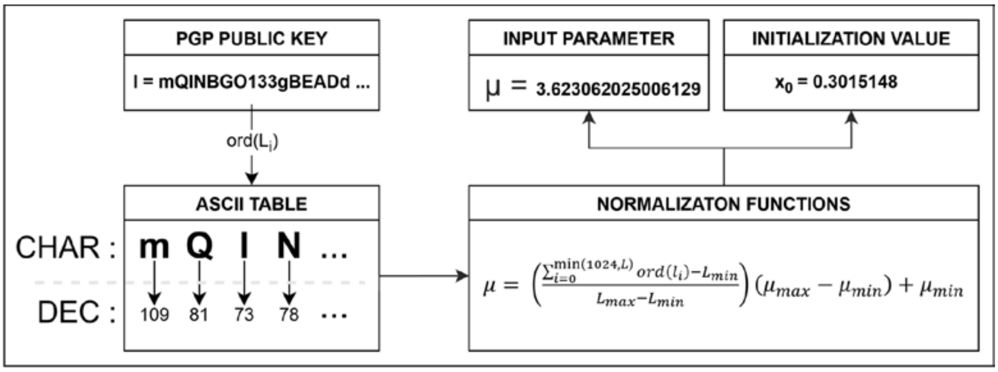

Figure 3. Explaining how to obtain from the PGP public key to 1D logistic map's the μ parameter and the x_0 initialization value.

In this study, the PGP public key of the person to whom the encrypted image will be sent is first obtained. This public key must be at least 1024 characters long. A PGP public key shorter than 1024 characters will reduce the sensitivity of the μ parameter and the initial value of x_0. This will make these values easier to estimate. Therefore, to ensure system security, it was concluded that the PGP public key must be at least 1024 characters long. The remaining characters in the PGP public key exceeding this value are not included in the calculation, as 1024 characters provide sufficient precision. The first 1024 characters of the PGP public key are expressed as decimal numbers using the ASCII code table. This provides numerical values that can be used in the normalization function. The Equation (4) generates the initial value of the μ parameter and x_0. The steps for generating the input parameter and initial value are shown in the diagram in Figure 3. The normalization function is specified in Equation (5) and Algorithm 2.

The value μ specified in the Equation (4) represents the input parameter of the 1D logistic map, the value L represents the character length of the PGP key, and the values L_{min}, L_{max} represent the minimum and maximum character lengths that the PGP key can hold. μ_{min}, μ_{max} represent the value range $[3.47, 4.0]$ in which the 1D logistic map exhibits chaotic behaviour. The $ord(l_i)$ function is used to convert the ASCII characters in the PGP key to decimal values. This function returns the decimal values of the characters specified in the ASCII character table.

After determining the input parameters and initial values of the 1D logistic map, the key array K to be used in the diffusion step was generated by generating the outputs x_i after the first 3000 iterations of the 1D logistic map, as specified in Equation (5). The element length of the key array K is equal to the number of pixels in the image to be encrypted. Thus, the XOR operation was applied such that each element K_i corresponds to the pixel value P_i in the image to be encrypted.

$$\mu = \left(\frac{\sum_{i=0}^{\min(1024,L)} ord(l_i) - L_{min}}{L_{max} - L_{min}}\right)(\mu_{max} - \mu_{min}) + \mu_{min} \tag{4}$$

$$K_i = \left\lfloor \left(\frac{x_i + 1}{2}\right) * 10^{14} \right\rfloor mod(256) \tag{5}$$

Figure 4 illustrates the parameter regions of the 1D logistic map, highlighting the interval in which chaotic dynamics emerge and providing the basis for selecting the control parameter μ in the proposed encryption scheme.

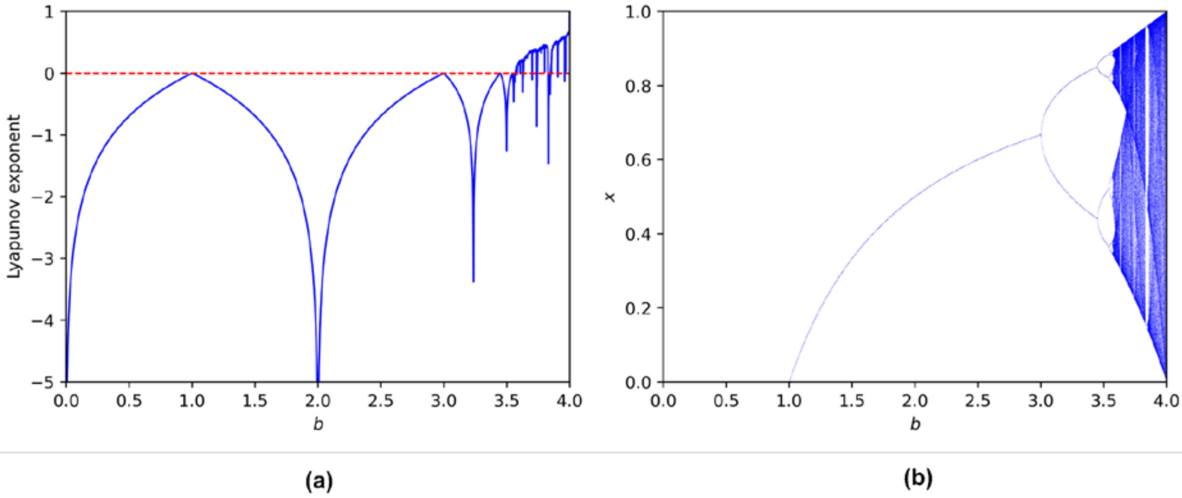

Figure 4. (a) The 1D logistic map Lyapunov exponent and (b) Bifurcation diagram.

2.3. Diffusion And Back Propagation Step

The XOR bit operator compares two bits. It is a logical operator that returns a value of one if the compared bits are different and a value of zero if they are the same. It is used in image encryption and similar tasks requiring bit operators (Gupta et al., 2023). The XOR operator is preferred in image encryption because it can produce unpredictable and random results when used with chaotic map data, making it difficult for unauthorized users to decipher the encrypted data. Furthermore, the XOR operation is computationally efficient and can be implemented on a variety of platforms. This property of the XOR bit operator has made it a popular choice for image encryption (Artuğer, 2025).

The use of the XOR operator in the diffusion and feedback step aims to increase encryption strength and processing speed. The NPCR and UACI values obtained from other studies on image encryption are compared in Tables 4 and 5. Within the scope of this study, it was observed that the proposed method resulted in an average increase of 0.01056 in the NPCR value on the Lena grey level image. Similarly, the results obtained for the UACI values indicated in Table 5 showed an average increase of 0.05385.

In this work, the XOR operator aims to encrypt the pixel values of the entire image one by one. To this end, the chaotic sequence of numbers generated by the 1D logistic map is converted into a K key array using the Equation (9). Each element of the resulting K key array is processed with each pixel on the RGB and grayscale Lena image using the XOR bit operator. This process creates a new encrypted image that can only be decrypted with the original K key array. Using the Equation (6) the two-dimensional matrix structure of dimension MxN in the two-dimensional image is converted into a 1D array for ease of processing and for matching with the 1D K key array. Here, P_i represents the two-dimensional image reduced to one dimension. The i and j values represent the row and column indices of the two-dimensional image, and the W value represents the width of the two-dimensional image.

$$P_i = iW + j, \quad i, j \in \mathbb{Z}, W \in \mathbb{R}, \tag{6}$$

$$C_i = P_i \oplus K_i \oplus C(i), \quad K_i \in \mathbb{Z}_2^n \tag{7}$$

$$C(i) = \begin{cases} i-1 & i > 0, \\ 1 & i \leq 0, \end{cases} \tag{8}$$

$$\Rightarrow C(i) = (iW + j) \oplus K_i \oplus \begin{cases} i-1 & i > 0, \\ 1 & i \leq 0, \end{cases} \tag{9}$$

Algorithm 2: Chaotic values generation and encryption process

Input: : $PGPKey, L_{min}, L_{max}, \mu_{min}, \mu_{max}, PixelsShiftedImage\ (P)$

Output: : $EncryptedImage$

Step-1 : **for** i ← 0 to $PGPKey$ **do**

$l = l + ord(PGPKey_i)$

Step-2 : $\mu \leftarrow \left[\frac{(l - L_{min}) * (\mu_{max} - \mu_{min})}{(L_{max} - L_{min}) + \mu_{min}}\right]$

Step-3 : **for** i ← 0 to 3000 **do**

$x_i \leftarrow \mu * x_0\ (1 - x_i)$

Step-4 : **for** i ← 1 to $Widht * Height + 1$ **do**

$x_{i-1} \leftarrow \mu * x_0\ (1 - x_{i-1})$

$K_{i-1} \leftarrow \left(\frac{x_{i-1} + 1}{2}\right) * 10^{14}\ mod\ 256$

$CipherImage_{i-1} \leftarrow P_i \oplus K_i \oplus P_{i-1}$

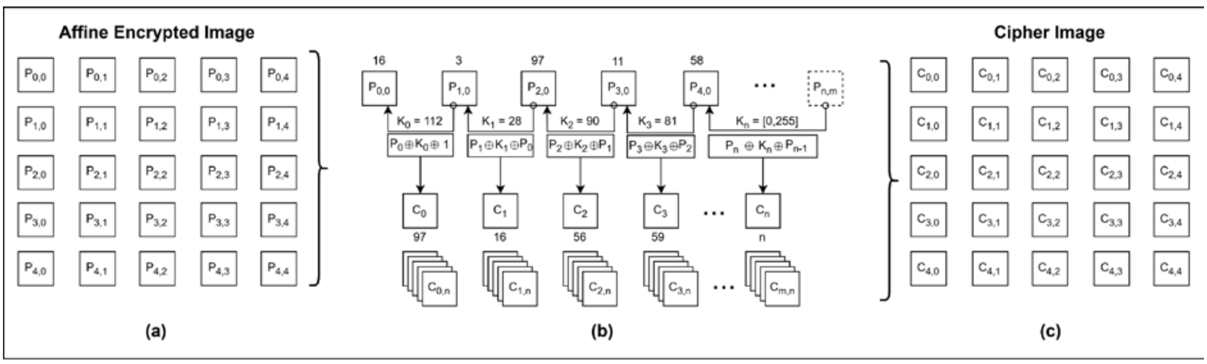

Figure 1. (a) Gray level Affine encrypted image pixels, (b) Application of the proposed method on pixel values, and (c) Cipher image pixels.

3. Results

In this study, the proposed algorithm was developed in the Python 3.8 programming language, and the performance results obtained from the experiments are reported for comparison with other studies. The images used in the experiments were taken from the SIPI database (California, 2024), and the width and height values of the images are shown in Table 1. This section presents the literature performance metrics that test the effectiveness of the proposed algorithm, including numerical results and comparisons. The test results and comparisons are explained in the tables and visual outputs in this section. The results obtained from the experiments conducted with the proposed algorithm demonstrate a high degree of accuracy compared to other studies. The results also demonstrate that the algorithm can accurately encode and decode images without compromising image quality.

Table 1. Images and attributes used in the study.

Filename	Image	Size	Colour
-	Lena	256x256	Gray
5.1.12	Clock	256x256	Gray
5.1.14	Chemical plant	256x256	Gray
boat.512	Boat	512x512	Gray
gray21.512	Gray	512x512	Gray
5.2.10	Stream and Bridge	512x512	Gray
7.1.03	Tank	512x512	Gray
5.3.01	Man	1024x1024	Gray
5.3.02	Airport	1024x1024	Gray
-	Lena	256x256	RGB
5.1.11	Plane	512x512	RGB
4.2.07	Peppers	512x512	RGB
house	Hause	512x512	RGB
4.2.03	Baboon	512x512	RGB

3.1. Histogram Analysis

An image histogram shows the pixel distribution in the image. The values on the horizontal axis in the graph represent the colour values in the image. The values on the vertical axis indicate the number of pixel values corresponding to the horizontal axis. When the pixel density distribution in the image reaches the same average number for each pixel value, the image histogram becomes equal. This makes it more difficult for attackers to decipher the encrypted image using statistical attack methods.

Attackers attempt to decrypt text or images using frequency analysis. In images where the pixel distribution is not homogeneous, attackers can decrypt image by performing frequency analysis and similar attacks. Figure 6 shows the histograms of the plain image and the encrypted image with the algorithm proposed in this paper. The results show that the proposed algorithm distributes the pixels of the image evenly.

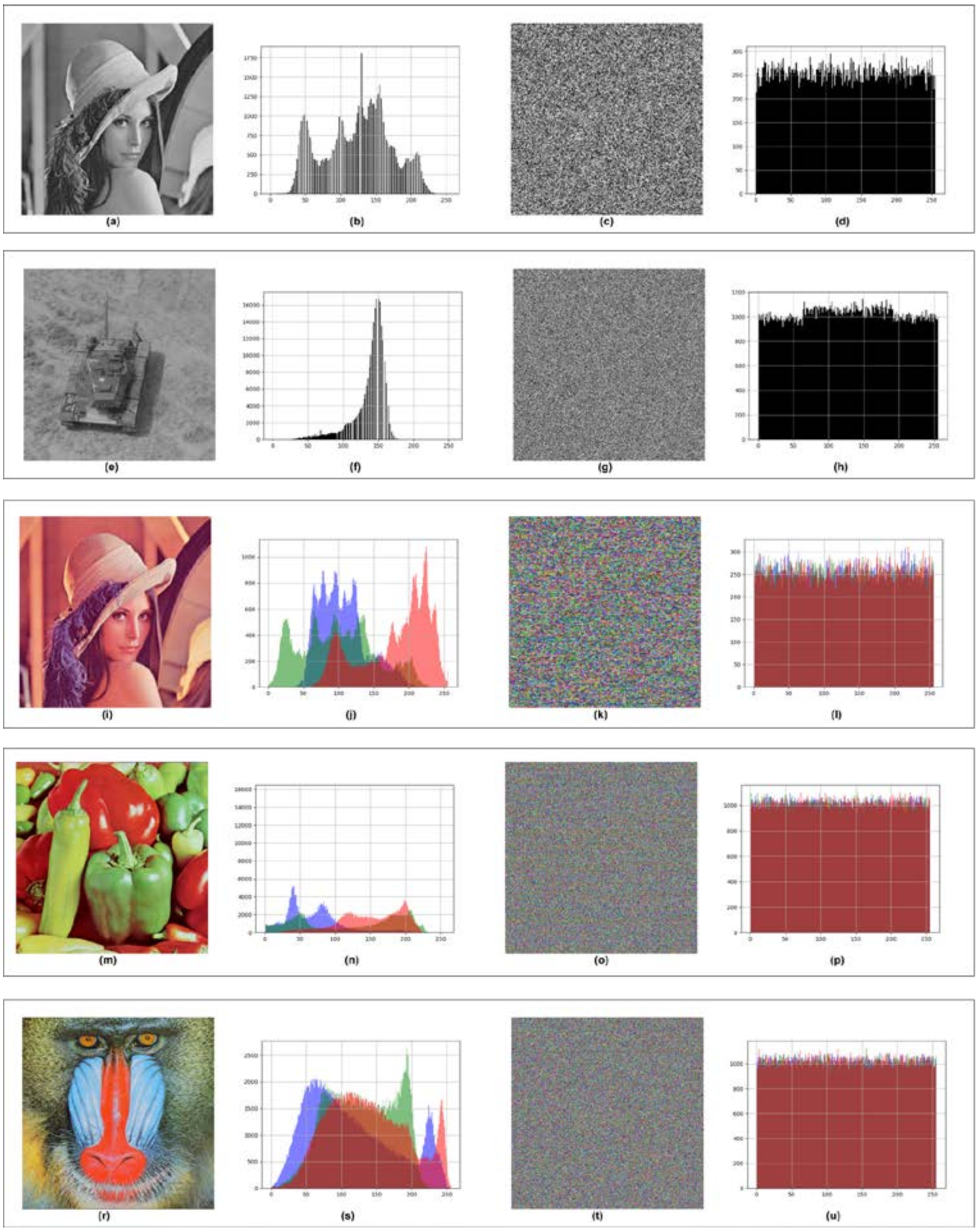

Figure 2. (a) Gray Lena image, (b) Gray Lena image histogram graph, (c) Encrypted Lena image with proposed method, (d) Encrypted gray Lena image with proposed method histogram graph, (e) Gray Tank image, (f) Gray Tank image histogram graph, (g) Encrypted Tank image with proposed method, (h) Encrypted gray Tank image with proposed method histogram graph, (i) RGB Lena image, (j) RGB Lena image histogram graph, (k) Encrypted Lena image with proposed method, (l) Encrypted RGB Lena image with proposed method histogram graph, (m) RGB Peppers image, (n) RGB Peppers image histogram graph, (o) Encrypted Peppers image with proposed method, (p) Encrypted RGB Peppers image with proposed method histogram graph, (r) RGB Baboon image, (s) RGB Baboon image histogram graph, (t) Encrypted Baboon image with proposed method, and (u) Encrypted RGB Baboon image with proposed method histogram graph.

3.2. Entropy Analysis

Entropy is used to measure the randomness of data in a dataset. The random distribution of pixel values in an image result in a high entropy value for the image. In the literature, the optimal entropy value for values consisting of 8 bits, i.e., 2^8 bits, is determined as 8. An entropy value smaller than this indicates that the randomness in the image is low. A low entropy value indicates that the encryption algorithm is not reliable. (Paramesha et al., 2025). In this study, the Shannon entropy calculation method was used, and the obtained data is shown in Table 2. They are compared with other studies in Table 2 According to this table, the obtained entropy values show better performance than other studies.

$$H(X) = -\sum_{i=0}^{L-1} p(x_i) \log_2 p\,(x_i) \tag{9}$$

Table 2. Comparison of the entropy values of the proposed method with other studies.

Studies	Lena	Boat	4.2.07
Proposed	7.9669	7.9675	7.9678
(Hanif et al., 2022)	7.9957	7.9955	-
(Zhou et al., 2022)	7.9977	-	-
(Taqi & Abdul-Haleem, 2023)	7.9920	-	-
(Ullah et al., 2022)	7.9960	-	7.9990
(Wang, 2024)	7.9960	-	-

3.3. Image Sensitivity Analysis

Differential attack analysis is used to determine changes in the encrypted image and the sensitivity of the algorithm. This method requires two images. The first image should be the original, and the second image should be a modified version of the original image's pixel values. Both images are encrypted with the proposed algorithm, and the difference between the resulting encrypted images indicates the algorithm's sensitivity. For these tests, the number of pixels change rate (NPCR) and unified average changing intensity (UACI) are used. The NPCR value should be as close to 100% as possible, and the UACI value should converge to 33.33. These analysis methods are calculated as follows Equation (10), Equation (11), and Equation (12).

$$NPCR(C, C') = \frac{1}{W * H} \sum_{i=0}^{W} \sum_{j=0}^{H} D\left(C_{ij}, C'_{ij}\right) \tag{10}$$

$$D\left(C_{ij}, C'_{ij}\right) = \begin{cases} 1 & if C_{ij} = C'_{ij} \\ 0 & if C_{ij} \neq C'_{ij} \end{cases} \tag{11}$$

$$UACI(C, C') = \frac{1}{W * H * F} \sum_{i=0}^{W} \sum_{j=0}^{H} | C_{ij} - C'_{ij} | \tag{12}$$

The C, C'values shown in the Equation (10), Equation (11), and Equation (12) represent the image encrypted with the proposed algorithm and the modified version of a pixel in the image. The W, H values represent the width and height of the image, and F represents the maximum possible pixel value.

The NPCR and UACI values obtained in experiments conducted with the proposed algorithm are shown in Table 2. Tables 3 and 4 compare the NPCR and UACI values of the proposed algorithm with those of other studies.

Table 3. NPCR and UACI results of the proposed algorithm.

Filename	Image	NPCR	UACI	Entropy
-	Lena	99.6078	33.4003	7.9669
5.1.12	Clock	99.6048	33.4563	7.9664
5.1.14	Chemical plant	99.6124	33.5052	7.9672
boat.512	Boat	99.6189	33.6229	7.9675
gray21.512	Gray	99.5872	33.4152	7.9661
5.2.10	Stream and Bridge	99.5895	33.4251	7.9663
7.1.03	Tank	99.6094	33.3137	7.9668
5.3.01	Man	99.6177	33.4804	7.9674
5.3.02	Airport	99.6044	33.4567	7.9666
-	Lena (RGB)	99.6158	33.4600	7.9679
5.1.11	Plane (RGB)	99.5952	33.4531	7.9676
4.2.07	Peppers (RGB)	99.6105	33.4582	7.9678
hause	Hause (RGB)	99.6082	33.4574	7.9677
4.2.03	Baboon (RGB)	99.6128	33.4590	7.9681

Table 4. Comparison of NPCR values.

Studies	Lena	Boat	5.1.14	7.1.03	5.3.01	4.2.07
Proposed	99.6078	99.6189	99.6124	99.6094	99.6177	99.6105
(Hanif et al., 2022)	99.5743	99.5987	-	-	-	-
(Li et al., 2023)	-	99.6040	99.6078	99.5972	-	-
(Feng et al., 2022)	-	99.6168	99.6075	99.6281	-	-
(Zhou et al., 2022)	99.6000	-	-	99.6300	99.6000	-
(Taqi & Abdul-Haleem, 2023)	99.6078	-	-	-	-	-
(Ullah et al., 2022)	-	-	-	-	-	99.6000
(Wang, 2024)	99.6050	-	-	-	-	-
(Zhang, 2024)	99.5991	-	-	-	-	-

Table 5. Comparison of UACI values.

Studies	Lena	Boat	5.1.14	7.1.03	5.3.01	4.2.07
Proposed	33.4003	33.6229	33.5052	33.3137	33.4804	33.4582
(Hanif et al., 2022)	33.0509	33.2262	-	-	-	-
(Li et al., 2023)	-	33.4814	33.4086	33.4773	-	-
(Feng et al., 2022)	-	33.4590	33.4667	33.5650	-	-
(Zhou et al., 2022)	33.4500	-	-	33.4200	33.4700	-
(Ullah et al., 2022)	-	-	-	-	-	33.3800
(Wang, 2024)	33.4820	-	-	-	-	-
(Zhang, 2024)	33.4029	-	-	-	-	-

3.4. Cropping and Noise Attack Analysis

Images can experience corruption along the transmission line as they are transmitted. These corruptions can stem from technical problems in the transmission line, and malicious attackers can manipulate the content of the message. This method employed by attackers is called man-in-the-middle (MITM) (Sivasankari & Kamalakkannan, 2022). In this attack, an attacker can intrude between the sender and receiver, view the message, and even manipulate the message content to mislead the recipient. In addition to the attackers themselves, technical problems in the transmission line can also cause corruption in the message. These corruptions typically manifest in the images in the form of salt and pepper noise, Gaussian noise, and changes in image size or pixel values (Yu, 2023).

This paper has conducted experiments using the proposed method. The results of the experiments are shown in Figure 7 and 8. As can be seen from the results, the encrypted image could be decrypted even in cases where more than 50% of the image is distorted.

3.5. Key Space Analysis

In an encryption process, the width of the key space indicates whether it is resistant to brute-force attacks. For the algorithm to be resistant to brute-force attacks, the key space is expected to be greater than 2^{100} (Abba et al., 2024). The algorithm proposed in this article uses the Affine encryption method in the first stage. The key space of this method consists of the values a and b. Each value a can take approximately 128 different values, while the value b can take 256 different values. Therefore, the key space width for the Affine encryption system will be 256*128 = 2^{15}.

In the diffusion step, the encryption process is manipulated with separate K keys for each pixel of the image. Therefore, for a $256x256$ image, the key space value will be 256! Consequently, since the key space width used in this algorithm will be $2^{100} * (2^{8})! > 2^{100}$, the proposed algorithm is resistant to brute force attacks.

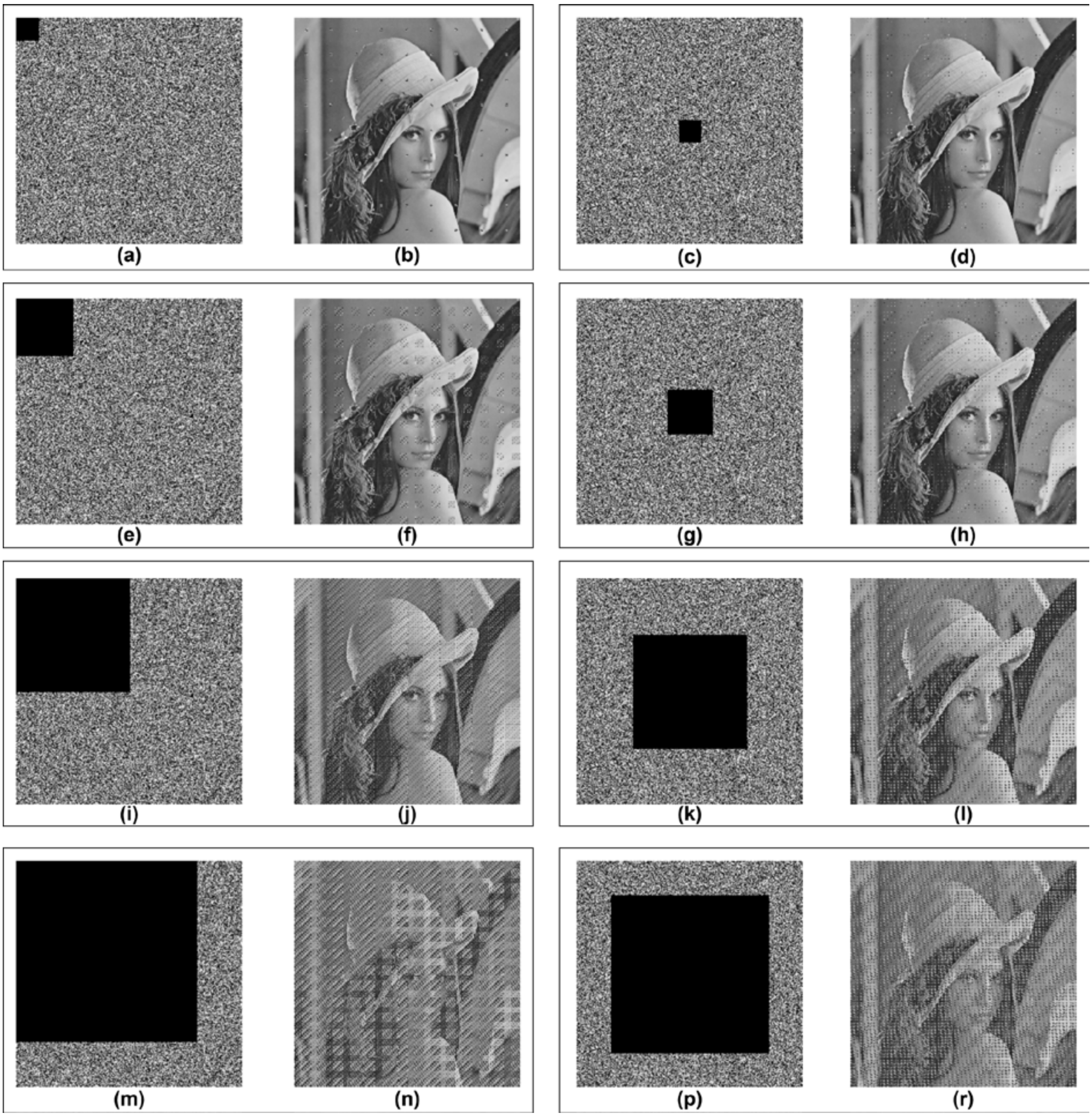

Figure 3. (a) 10% Cropped from left upside encrypted gray Lena image, (b) Decrypted image of the encrypted image with 10% cropped from the top left using the proposed method, (c) 10% Cropped from centre encrypted gray Lena image, (d) Decrypted image of the encrypted image with 10% cropped from the centre using the proposed method, (e) 20% Cropped from left upside encrypted gray Lena image, (f) Decrypted image of the encrypted image with 20% cropped from the top left using the proposed method, (g) 20% Cropped from centre encrypted gray Lena image, (h) Decrypted image of the encrypted image with 20% cropped from the centre using the proposed method, (i) 50% Cropped from left upside encrypted gray Lena image, (j) Decrypted image of the encrypted image with 50% cropped from the top left using the proposed method, (k) 50% Cropped from centre encrypted gray Lena image, (l) Decrypted image of the encrypted image with 50% cropped from the centre using the proposed method, (m) 70% Cropped from left upside encrypted gray Lena image, (n) Decrypted image of the

encrypted image with 70% cropped from the top left using the proposed method, (p) 70% Cropped from centre encrypted gray Lena image, and (r) Decrypted image of the encrypted image with 70% cropped from the centre using the proposed method.

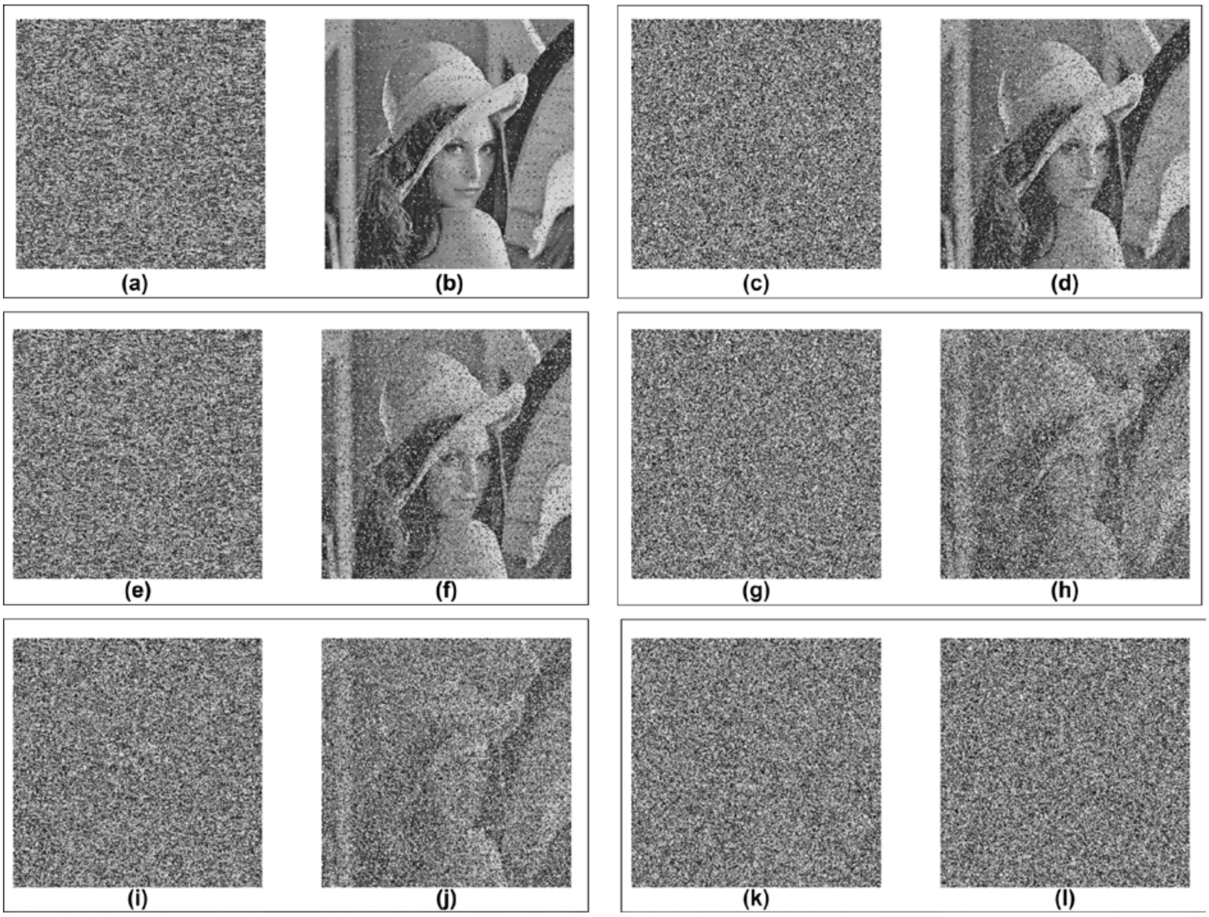

Figure 4. (a) 5% noise added image, (b) 5% noisily decrypted image, (c) 10% noise added image, (d) 10% noisily decrypted image, (e) 15% noise added image, (f) 15% noisily decrypted image, (g) 25% noise added image, (h) 25% noisily decrypted image, (i) 45% noise added image, (j) 45% noisily decrypted image, (k) 90% noise added image, and (l) 90% noisily decrypted image.

3.6. Time Consumption Results

An efficient algorithm should utilize the least number of resources. It is expected to complete the target operation in the shortest possible time, while also maximizing resource usage. Therefore, the developed algorithm is expected to be optimized for both resources and time. The system specifications for the proposed algorithm are as follows: i5-2400 CPU, 8GB 1333MHz RAM, Windows 10 operating system, and Python 3.8 programming language.

In this study, the time taken to encrypt and decrypt each image obtained from the SIPI database using the proposed method is specified in milliseconds in Table 6. The processing times obtained reflect the time consumption depending on the hardware resources of the system on which the method is executed. Additionally, it can be understood from the results obtained that the time consumption also varies depending on the dimensions and number of channels of the image to be encrypted.

Table 6. Time consumption for encryption of proposed method.

Image	Size	Colour	Encryption Time (ms)	Decryption Time (ms)
Lena	256x256	Gray	107	104
Clock	256x256	Gray	102	99
Chemical plant	256x256	Gray	103	100
Boat	512x512	Gray	406	400
Gray	512x512	Gray	407	403
Stream and Bridge	512x512	Gray	398	392
Tank	512x512	Gray	406	402
Man	1024x1024	Gray	1787	1740
Airport	1024x1024	Gray	1683	1638
Lena	256x256	RGB	1098	1076
Plane	512x512	RGB	1318	1295
Peppers	512x512	RGB	1227	1204
Hause	512x512	RGB	1217	1193
Baboon	512x512	RGB	1194	1170

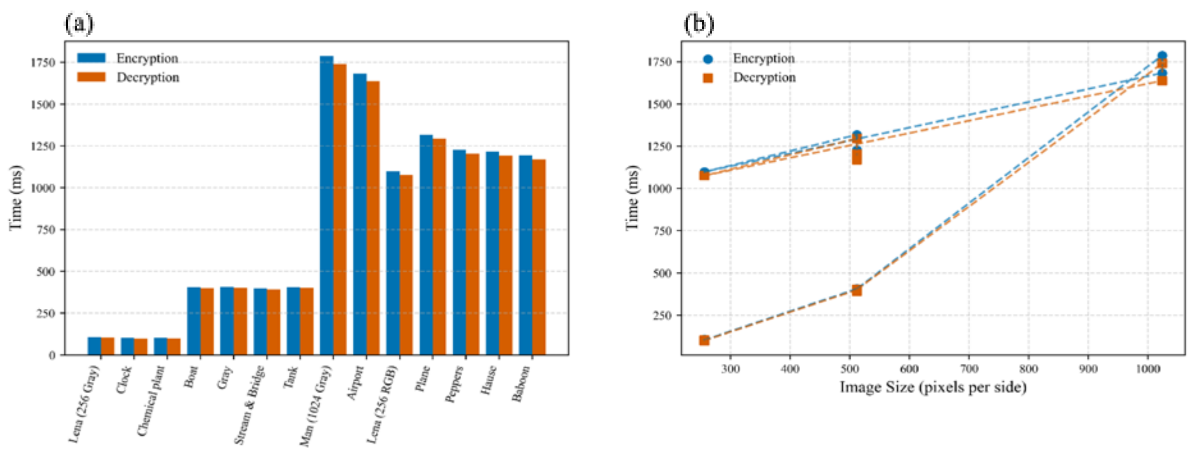

Figure 5. (a) Encryption and decryption time comparison of proposed method, and (b) Relation between image size and encryption - decryption times.

4. Discussion

In this study, a hybrid encryption method is proposed by addressing the problems of fixed initial conditions inherent in chaotic maps and the weakness of forward-only pixel encryption processes used in image encryption. A review of recent studies in the literature reveals that, due to the deterministic nature of chaotic maps, initial parameters are generated using pseudo-random mechanisms with fixed or limited variation (Zhou et al., 2022), from ECG signals (Eldesouky et al., 2022) or from data obtained through iris scanning (Archana et al., 2022) and assumes secret key sharing as an external assumption. In the proposed study, the key space obtained using the PGP public key is $2^{100} * (2^8)!$ while (Zhou et al., 2022) obtained a value of $2^{1096+8N}$ in their study. Similarly, in their work (Eldesouky et al., 2022), they stated that the key space would be the same as the chaotic map used and referred to the 1D logistic map's value of 2^{104}. Thus, it is observed that the PGP public key method used in generating the chaotic map's parameters is rich in terms of key space. The fundamental difference between the proposed method and similar studies in the literature is the use of an asymmetric encryption mechanism to dynamically generate the input parameters of the chaotic system and the encryption of the obtained values with the XOR operator using the back propagation pixel values. Whereas previous studies (Althamir et al., 2023; Heinrich, 2025; Schwenk, 2022) have generally addressed PGP or RSA-like methods for key transmission but in this study, the recipient's public key has been transformed into a recipient-specific source that determines the μ and $x_0$parameters of the 1D logical map. This approach initiates the encryption process using receiver-specific values by dynamically generating the input parameter and initial value of chaotic maps.

Following the dynamic generation of chaotic map parameters, studies utilizing diffusion methods and bit operators for image encryption were examined. It was concluded that there was an increase in performance in terms of encryption security metrics between the NPCR and UACI results obtained by using the XOR operator continuously to change forward-looking pixel values in methods where both methods were used combined, and the use of the feedback XOR operator proposed in this study. In the study using continuous forward XOR processing (Hanif et al., 2022), a performance increase of 0.0335 for the NPCR value and 0.3494 for the UACI value was observed in the grey-level Lena image. Similarly, in the study by (Feng et al., 2022) a performance increase of 0.0021 for NPCR and 0.1415 for UACI was achieved on the Boat image. Furthermore, a similar performance increase was observed on the multi-channel RGB 4.2.07 image file. However, the increase in pixel density resulting from the increase in image size revealed a disadvantage of the proposed method. In the image named 7.1.03, a performance loss of NPCR 0.2794 and UACI 0.1063 was observed according to the forward XOR operator method proposed by (Zhou et al., 2022).

5. Conclusion

In conclusion, it has been determined that the proposed dynamic chaotic map parameter generation and the use of the back propagated XOR method within the scope of this study are feasible in terms of encryption security but are open to improvement. Furthermore, it is anticipated that eliminating the fixed initial value and input parameter problem in chaotic maps and utilizing the XOR operator through backpropagation across the entire image will provide a new perspective to the literature. Future work is expected to improve the performance metrics of the encryption process by increasing the size of the chaotic map used in image encryption or by developing the backpropagation method of the XOR operator.

Acknowledgments

The authors gratefully acknowledge the support of "HAVELSAN Co. Inc." in this study.

Data and Code Availability

The source codes of all tests and analyses performed for the developed algorithm are shared at https://github.com/tlhcelik/a_novel_image_encryption_using_1d_logistic_map_and_pgp_key

References

Abba, A., Teh, J. S., & Alawida, M. (2024). Towards accurate keyspace analysis of chaos-based image ciphers. *Multimedia Tools and Applications*, *83*(33), 79047-79066. https://doi.org/10.1007/s11042-024-18628-8

Ali, N. H. M., Hoobi, M. M., & Hussien, S. A. S. (2025). Enhanced TEA Algorithm Performance using Affine Transformation and Chaotic Arnold Map. *Mesopotamian Journal of Computer Science*, *2025*, 341-354. https://doi.org/10.2139/ssrn.5681046

Althamir, M., Alabdulhay, A., & Yasin, M. M. (2023). A systematic literature review on symmetric and asymmetric encryption comparison key size. *2023 3rd International Conference on Smart Data Intelligence (ICSMDI)*, 110-117. https://doi.org/10.1109/icsmdi57622.2023.00027

Archana, K., Kumar, S. S., Gokak, P. P., Pragna, M., & Shruthi, M. (2022). IRIS Image Encryption and Decryption Based Application Using Chaos System and Confusion Technique. In *Modeling, Simulation and Optimization: Proceedings of CoMSO 2021* (pp. 155-175). Springer. https://doi.org/10.1007/978-981-19-0836-1_13

Artuğer, F. (2025). Innovative image encryption approach based on bitwise XOR high nonlinear S-boxes and random permutation. *Soft Computing*, *29*(6), 2891-2903. https://doi.org/10.1155/2017/6969312

Boldo, S., Jeannerod, C.-P., Melquiond, G., & Muller, J.-M. (2023). Floating-point arithmetic. *Acta Numerica*, *32*, 203-290. https://doi.org/10.1017/S0962492922000101

Braverman, L., & Nelson, D. R. (2025). Transition to chaos with conical billiards. *arXiv preprint arXiv:2508.02786*. https://doi.org/doi.org/10.1103/18f7-sqhz

California, U. o. S. (2024). *SIPI database of University of Southern California*. Retrieved 16 March from https://sipi.usc.edu/database/database.php?volume=misc

Diffie, W., & Hellman, M. E. (2022). New directions in cryptography. In Democratizing cryptography: the work of Whitfield Diffie and Martin Hellman (pp. 365-390)

Eldesouky, S., El-Shafai, W., Ahmed, H. E. d. H., & El-Samie, F. E. A. (2022). Cancelable electrocardiogram biometric system based on chaotic encryption using three-dimensional logistic map for biometric-based cloud services. *Security and Privacy*, *5*(2), e198. https://doi.org/10.1002/spy2.198

Feng, W., Zhao, X., Zhang, J., Qin, Z., Zhang, J., & He, Y. (2022). Image encryption algorithm based on plane-level image filtering and discrete logarithmic transform. *Mathematics*, *10*(15), 2751. https://doi.org/10.3390/math10152751

Geetha, M., Ranjithkannan, T., Yogeshwaran, R., & Nishanth, S. (2025). Next-Gen Multimedia Encryption by Combining Symmetric and Asymmetric Cryptographic Techniques. *2025 5th International Conference on Expert Clouds and Applications (ICOECA)*, 49-53. https://doi.org/10.1109/icoeca66273.2025.00020

Gupta, L., Jaiswal, P., Lather, I., Agarwal, R., & Thakur, A. (2023). Image Encryption using Chaotic maps: State of the art. *2023 3rd International Conference on Intelligent Technologies (CONIT),* 1-8. https://doi.org/10.1109/CONIT59222.2023.10205829

Hanif, M., Iqbal, N., Ur Rahman, F., Khan, M. A., Ghazal, T. M., Abbas, S., Ahmad, M., Al Hamadi, H., & Yeun, C. Y. (2022). A novel grayscale image encryption scheme based on the block-level swapping of pixels and the chaotic system. *Sensors*, *22*(16), 6243. https://doi.org/10.3390/s22166243

Heinrich, C. (2025). Pretty good privacy (PGP). In *Encyclopedia of Cryptography, Security and Privacy* (pp. 1863-1868). Springer. https://doi.org/10.1007/978-3-030-71522-9_215

Ihsan, A., & Doğan, N. (2023). Improved affine encryption algorithm for color images using LFSR and XOR encryption. *Multimedia Tools and Applications*, *82*(5), 7621-7637. https://doi.org/10.1007/s11042-022-13727-w

Karthik, G., Suresh, P., Ganesh, V., Kumar, H., & Amirtharajan, R. (2025). Elliptical Curve Cryptography for Images Using Mandelbrot Fractal and Zaslavskii Map Based Multiple Key with DNA Encoding. *2025 11th International Conference on Communication and Signal Processing (ICCSP)*, 960-964. https://doi.org/10.1109/iccsp64183.2025.11088650

Li, H., Yu, S., Feng, W., Chen, Y., Zhang, J., Qin, Z., Zhu, Z., & Wozniak, M. (2023). Exploiting dynamic vector-level operations and a 2D-enhanced logistic modular map for efficient chaotic image encryption. *Entropy*, *25*(8), 1147. https://doi.org/10.3390/e25081147

Lyle, M., Sarosh, P., & Parah, S. A. (2022). Adaptive image encryption based on twin chaotic maps. *Multimedia Tools and Applications*, *81*(6), 8179-8198. https://doi.org/10.1007/s11042-022-11917-0

Paramesha, K., Karthik, V., Prashanth, M., Sathisha, M., Bhargav, H., HS, R. K., Raju, K., & Puttegowda, K. (2025). A novel image cryptosystem for biomedical images and secured storage by randomized chaotic encryption scheme. *Journal of Integrated Science and Technology*, *13*(5), 1103-1103. https://doi.org/10.62110/sciencein.jist.2025.v13.1103

Saif, A. (2025). *Data Security on cloud using Hybrid Cryptography a PGP based encryption methodology* Dublin, National College of Ireland].

Schwenk, J. (2022). File Encryption: PGP. In *Guide to Internet Cryptography: Security Protocols and Real-World Attack Implications* (pp. 377-399). Springer. https://doi.org/10.1007/978-3-031-19439-9_16

Sivasankari, N., & Kamalakkannan, S. (2022). Detection and prevention of man-in-the-middle attack in iot network using regression modeling. *Advances in Engineering software*, *169*, 103126. https://doi.org/10.1016/j.advengsoft.2022.103126

Susanti, B. H., Sumule, A. S. L., & Ardyani, M. W. (2025). Security Analysis of Modified ESRKGS-RSA Using Lenstra's Elliptic Curve Method. *CAUCHY: Jurnal Matematika Murni dan Aplikasi*, *10*(2), 805-820. https://doi.org/0.18860/cauchy.v10i2.32189

Taqi, I. A., & Abdul-Haleem, M. G. (2023). An Efficient Cryptosystem for Image Using 1D and 2D Logistic Chaotic Maps. *International Journal of Intelligent Engineering & Systems*, *16*(4). https://doi.org/10.22266/ijies2023.0831.11

Ullah, A., Shah, A. A., Khan, J. S., Sajjad, M., Boulila, W., Akgul, A., Masood, J., Ghaleb, F. A., Shah, S. A., & Ahmad, J. (2022). An efficient lightweight image encryption scheme using multichaos. *Security and Communication Networks*, *2022*(1), 5680357. https://doi.org/10.1155/2022/5680357

Wang, G. (2024). *Remote sensing image encryption algorithm based on novel spatiotemporal chaotic system* (Patent No. CN119814936). U. S. T. LIAONING. https://patentscope.wipo.int/search/en/detail.jsf?docId=CN454494386

Yu, J. (2023). Based on Gaussian filter to improve the effect of the images in Gaussian noise and pepper noise. *Journal of Physics: Conference Series*, *2580*(1), 012062. https://doi.org/10.1088/1742-6596/2580/1/012062

Zhang, Y. T. Y. (2024). *Image encryption and decryption method and system based on SM2 and DNA* (Patent No. CN118018659A). E. U. O. T. C. P. S. A. P. FORCE. https://patentscope.wipo.int/search/en/detail.jsf?docId=CN429414066

Zhou, S., Wang, X., Zhang, Y., Ge, B., Wang, M., & Gao, S. (2022). A novel image encryption cryptosystem based on true random numbers and chaotic systems. *Multimedia Systems*, *28*(1), 95-112. https://doi.org/10.1007/s00530-021-00803-8

JOURNAL OF DEFENCE AND SECURITY INDUSTRY

Journal of Defence and Security Industries: Strategy and Technology, 2026, 1(1)

Science & Technology Section

Comprehensive Investigation of Static and Fatigue Performance of Fiber Bragg Grating, Digital Image Correlation and Strain Gages

Şahin Gören [1], Salim Çalışkan [1,*]

Abstract

In contemporary practice, a significant application of strain gauges lies in the experimental stress analysis of structural components, particularly within the aerospace sector. However, over the last two decades, fiber optic sensors, particularly Fiber Bragg Grating (FBG) sensors, have been successfully utilized for strain measurements, gaining recognition for their dependable performance. These sensors deliver strain measurement precision that rivals traditional methods such as strain gauges and extensometers. A major advantage of FBG sensors over electrical strain gauges lies in their long-term stability. Additionally, FBG sensors support multiplexing, meaning several sensors can be placed on a single fiber, enabling the collection of multiple simultaneous measurements including the detection of strain, pressure, temperature, and vibration signals. Nevertheless, FBG and conventional techniques also exhibit similar features: they provide localized, directional measurements, require temperature compensation, and are often applied by bonding them to the surface of structures. Digital Image Correlation (DIC), on the other hand, is a non-contact optical method that measures full-field surface geometry, displacement, and strain using digital cameras. DIC is especially useful for monitoring structures by taking periodic images and determining strain and displacement over time or under various operating conditions. While traditional tools such as resistive strain gauges are frequently used in testing composite materials, they come with certain challenges. These include bonding and surface preparation difficulties, the need for direct surface contact and providing only single-point data. While DIC provides a broader measurement capability, its precision depends heavily on the quality of the calibration process and the testing conditions. This study investigates the experimental assessment of strain through the application of traditional strain gauges, FBG sensors, and DIC methodologies on glass fiber reinforced composite (GFRC) laminate coupon specimens subjected to quasi-static and constant amplitude fatigue loading. The work aims to comparatively investigate the sensitivity of optical fiber sensors, strain gauges and DIC.

Keywords: Fiber Bragg Grating, strain gage, digital image correlation, mechanical testing, composite.

Received: 14.11.2025 Accepted: 24.12.2025 Research Article

[1] Turkish Aerospace Industries Inc., Ankara, Türkiye
* Corresponding author.
✉ salim.caliskan@tai.com.tr

Cite this article as: Gören, S., & Çalışkan, S. (2026). Comprehensive investigation of static and fatigue performance of Fiber Bragg Grating, digital image correlation and strain gages. *Journal of Defence and Security Industry: Strategy and Technology 1*, 140-153.

1. Introduction

Although Digital Image Correlation (DIC), Fiber Bragg Grating (FBG) sensors, and strain gauges are widely utilized in experimental mechanics, most existing studies primarily emphasize their individual strengths and weaknesses, often neglecting a holistic comparison under diverse and complex loading scenarios. This study seeks to address this shortcoming by conducting a systematic evaluation of these techniques, focusing on their performance, comparative error assessment, and practical utility. By doing so, it provides valuable insights to inform the selection of the most suitable measurement methods for various engineering applications. Ultimately, this research aims to advance the precision and dependability of deformation measurements within experimental mechanics.

Accurate strain measurement techniques are essential for understanding material behaviour under various loading conditions. Among these, DIC has gained significant attention as a non-contact optical method capable of measuring full-field displacements and strains with high spatial resolution. Recent advancements have focused on improving its accuracy by addressing issues related to calibration, noise reduction, and uncertainty quantification (Pan et al., 2009; Schreier et al., 2009). However, despite its advantages, DIC faces challenges under dynamic conditions and with non-uniform strain fields. On the other hand, FBG sensors, known for their high sensitivity, multiplexing capabilities, and ability to withstand harsh conditions, have demonstrated effectiveness in monitoring localized strain and temperature changes, making them invaluable for applications in structural health monitoring (Campanella et al., 2018). Strain gauges pose a significant challenge to measure mechanical movements at the micro level. Accurate measurement of small resistance changes is critical in the case of strain gauges. Several attempts have been made and are still being made to improve the measurement quality using the Wheatstone bridge because of its very high potential in the field of precision measurement (Kalita et al., 2016). While individual studies have explored the uncertainties and performance of these methods, a comprehensive comparison of their capabilities, particularly under extreme or complex loading scenarios, remains limited. This study aims to fill this gap by conducting a systematic evaluation of these techniques, with a focus on comparative error assessment, dynamic performance, and practical applicability in experimental mechanics. Such an analysis is crucial to advancing measurement reliability and guiding the selection of appropriate techniques for diverse engineering applications.

The principle of strain gauge measurement has been identified as a means to quantify various parameters, including displacement, force, pressure, and acceleration. The strain gauge principle represents about half of all sensor measurement methods (Bethe, 1989). A strain gauge is a device specifically engineered to measure the deformation that a material undergoes when subjected to external forces. It operates on the principle that as the material deforms in response to stress, the strain gauge attached to its surface also experiences deformation, leading to a measurable alteration in its electrical resistance. This relationship between deformation and resistance is defined by the gauge factor, which quantifies the sensitivity of the strain gauge (Hoffmann, 1989). Strain gauges are widely utilized in mechanical testing, structural assessment, and materials science. For instance, they play a crucial role in experimental stress analysis, providing an indirect and reliable measurement of stress distribution across different materials (Dally et al., 1978). Furthermore, resistance strain gauges have been a predominant method for measuring strain, largely attributed to their operational simplicity, cost efficiency, and presumed precision. While generally regarded as accurate instruments, improper application and the neglect of potential error sources remain prevalent issues. Given the impossibility of completely eradicating measurement error, it is imperative to systematically quantify and mitigate such uncertainties to a level that is acceptable for the specific measurement objectives (Montero et al., 2011). While every measurement involves a degree of error and uncertainty, it is impossible to entirely eliminate these inaccuracies; thus, the focus must be on reducing them to an acceptable threshold. Accurately determining measurement uncertainty requires a thorough identification and quantification of the primary error sources. From a practical standpoint, measurement errors and uncertainties should be recognized as integral aspects of the process, often surpassing the significance of the measurement results themselves (Dokoupil, 2017).

FBG sensors consist of periodic changes in the refractive index along an optical fiber, which are produced by exposing the fiber core to a high-intensity optical interference pattern (Hill et al., 1978). Hill and colleagues first introduced this concept in 1978, demonstrating the creation of permanent gratings in germania-doped silica fibers using Argon-ion laser light (Kawasaki et al., 1978). This process led to the reflection of almost all incident light, a phenomenon that came to be known as Hill gratings. Further research found that ultraviolet light, especially at a wavelength of 244 nm, induces photosensitivity more effectively through a two-photon process, resulting in more efficient grating formation. Initially a subject of scientific interest, FBG have since become critical components in optical communication and sensing systems (Hill & Meltz, 1997). Fibers are composed of a core with a diameter ranging from 4 to 9 µm, surrounded by an outer cladding made of pure silica (SiO_2) with a diameter of 125 µm. The core exhibits a higher refractive index due to significant doping with germanium. To enhance protection against environmental factors such as water and hydrogen, which can lead to crack propagation and diminish mechanical stability (with the breaking point potentially decreasing from over 30,000 µm/m to as low as 1,000 µm/m), the glass fiber is coated with materials such as acrylate, polyimide, or ORMOCER (modified ceramic) (Kreuzer, 2006).

The fundamental operational principle employed in an FBG sensor system involves observing the variation in the wavelength of the reflected Bragg signal in response to alterations in the measurand, such as strain or temperature. The Bragg wavelength (λ_B), which represents the resonance condition of the grating, can be described by the following Equation (1) where Λ represents the grating period, while n denotes the effective index of the core (Kersey et al., 1997).

$$\lambda_B = 2n\Lambda \tag{1}$$

Mechanical axial strain changes the grating period. It also alters refractive index via the photo-elastic effect. Effective photo-elastic constant (p_e) is a function of axial strain. Hereby, tensile strain results in decreasing the refractive index through the photo-elastic effect. So, strain (ε) under constant temperature can be calculated by following Equation (2);

$$\varepsilon = \frac{\Delta\lambda_B}{\lambda_B\,(1-p_e)} \tag{2}$$

FBG sensors, acknowledged for their superior photosensitivity and optical performance, have emerged as key instruments in structural assessments. Research has extensively evaluated their utility in this domain. For instance, FBG sensors were integrated onto the shear web of a wind turbine blade and employed strain gauges at corresponding locations for comparison (Choi et al., 2012). The findings indicated that the average measurement discrepancies between the FBG sensors and strain gauges were within 2.25%, thereby affirming the FBG sensors' effectiveness for blade evaluation. Similarly, FBG sensors were positioned at the junction of the shear web and beam cap of a blade and performed static testing (Kim et al., 2013). Their results showed minimal variation between FBG sensor measurements, strain gauges, and finite element analysis (FEA), further corroborating the sensors' reliability. Additionally, a distributed FBG sensor system on a prototype blade was utilized to gather data on natural frequencies and strain, which informed improvements in the blade's structural design (Arsenault et al., 2023). The comparative analysis of the original and revised blade designs confirmed the substantial contribution of the sensor data to the enhancement of blade performance (Liu et al., 2020).

DIC, on the other hand, first introduced by researchers from the University of South Carolina in the 1980s, has been systematically refined and extensively utilized across various disciplines over the past thirty years (Peters & Ranson, 1982). The technique is distinguished by its straightforward experimental setup, ease of implementation, and robustness against environmental vibrations and variations in illumination since advanced post-processing algorithms can correct artefacts caused by vibrations. Additionally, high contrast and robust speckle pattern on the surface can enhance capturing image under non-ideal lighting condition to maximize the accuracy of the measurement results. Its adaptability in terms of temporal and spatial resolutions has rendered DIC a highly versatile and effective tool for measuring shape, motion, and deformation in a wide array of materials and structures, across diverse experimental conditions and scales (Dong & Pan, 2017; Isah & Mohamad, 2021; Mata-Falcón et al., 2020). DIC is recognized as a sophisticated and adaptable optical metrology technique for deformation measurement in experimental mechanics. This method entails analysing grayscale digital images of a specimen's surface captured prior to and following deformation to obtain comprehensive deformation data. DIC analysis typically utilizes algorithms based on either subset-based Cross-Correlation (CC) or Sum-Squared Difference (SSD) criteria (Tong, 2005). The precision of DIC measurements is contingent upon several factors, including the implementation of sub-pixel optimization algorithms, the selection of subset shape functions, subset dimensions, sub-pixel intensity interpolation methods, image noise, and lens distortion. Extensive studies have examined the influence of these factors on measurement accuracy (Pan et al., 2008). Experimental studies on small-scale specimens have been utilized to evaluate tensile behaviour, adhesion to substrates, and durability. In contrast, tests on medium- and large-scale specimens, as well as field trials, have provided valuable data on the performance of reinforced structures and have informed the optimization of reinforcement strategies. These studies highlight the critical need to accurately determine mechanical properties essential for effective strengthening design, such as tensile ultimate strength, strain, stiffness, crack spacing, and shear bond strength and displacement. However, traditional measurement devices—such as potentiometers, LVDTs, laser transducers, extensometers, and strain gauges—often face limitations in accurately capturing displacements and strains, particularly in mortar-based composites. Challenges such as cracking, sliding at gripping points, or uneven load distribution may not be adequately detected by these sensors. Furthermore, the reliability of strain and stiffness measurements can be compromised if cracks occur outside the gauge length or if local measurements do not accurately reflect global behaviour. Additionally, traditional sensors may complicate setup preparation, involve high costs, or suffer from damage, which can affect their practicality and reliability (Tekieli et al., 2017).

2. Materials and Experimental Setup

The material utilized in this experiment was CYCOM 5575-3. CYCOM 5575 is predominantly favoured for applications within the defence sector. The GFRC material is a modified cyanate ester resin which was subjected to 4 hours curing at 177°C with a cooling rate of 1.8±0.5°C plus 2 hours final curing at 227°C according to ASTM D7028 (ASTM International, 2015). The autoclave pressure was set to 6.9±0.3 bar. The prepregs associated with CYCOM 5575 are available in two primary flow variations, specifically CYCOM 5575-2 and CYCOM 5575-3, and they offer reinforcement options utilizing either quartz or glass fabric (Syensqo, n.d.). The geometry of the specimen as shown Figure 1 and the orientation of the plies were established in accordance with the EN 2747 Type-3 standard (NABau im DIN, 1998).

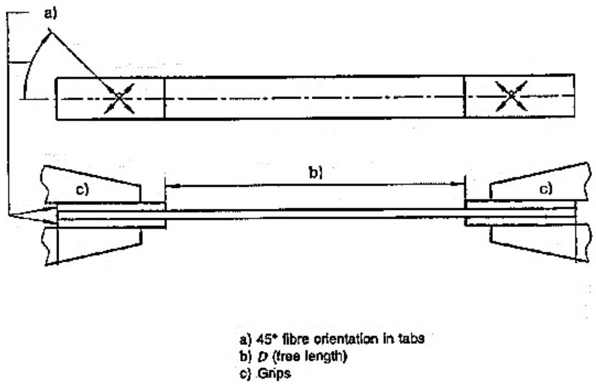

Figure 1. Specimen geometry (NABau im DIN, 1998).

EN 2747 Type-3 standard delineates a methodology for evaluating the tensile properties of GFRC designed for aerospace applications. Detailed specifications of the specimen dimensions are provided in Table 1.

Table 1. Test specimen dimensions.

Test Specimen						Tab (tapered)		
Length (mm)	Width (mm)	Thickness (mm)	# of Plies	Ply Orientation	Material	Length (mm)	Thickness (mm)	Ply Orientation
250±0.5	25±0.5	2.5±0.5	9	00	CYCOM 5575-3	50	6.75±0.5	±450

Linear gage measures uniaxial strain along with the applied load. Because of its high accuracy, cost-effective and straightforward instrumentation, strain gages are ideal for basic strain measurements. The strain gauge in a 3-wire configuration, or in other words 1/4 Wheatstone bridge, with a 2V supply voltage chosen for the strain measurement was the CEA-00-125UNA-350 model from Micro-Measurements to gather data from the strain gauge, the MTS FlexDAC 20 (B24 Type) data acquisition system was employed. This system facilitated shunt calibration for the strain gauges, ensuring their proper functionality.

The study employed FBGs FSG-A01-PP0 (Figure 2a), characterized by an effective grating length of 4 mm and a diameter of 155 µm. The initial wavelength recorded was 1558 nm. This sensor utilized a uniform apodised grating modulation, with a 1 mm length Bragg grating inscribed on a single-mode optical fiber. To gather and monitor FBG data during the measurements, the Luna Micron Optics HYPERION si255 (Figure 2b) industrial grade fanless optical sensing interrogator, known for its 1 pm resolution and accuracy, was employed. The FBG sensor was connected to one end of the fiber optic cable via a fixed connection angled physical contact (FC/APC) fiber connector.

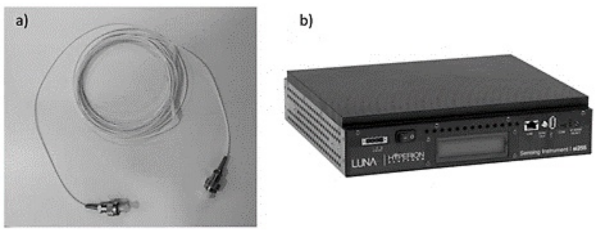

Figure 2. (a) FBGs FSG-A01- PP0 sensor and (b) Luna's Micron Optics HYPERION si255 interrogator.

In the DIC system (Dantec Dynamics GmbH), measurements were taken with high-resolution cameras, each capable of capturing images with a resolution of 4096 (H) x 3000 (V) pixels at Bayer 8-bit depth. The camera sensors feature square pixels with a pixel aspect ratio of 1:1. The tilt of the cameras allowed for the focal planes of both cameras to rotate and overlap within the same region of interest. Illumination was provided by an LED white light source. Camera calibration prior to the test was conducted utilizing a 3D calibration plate that features a defined rectangular dot pattern, characterized by known dot dimensions and spacing at least two different surface elevations. Following the recording of data, image correlation processing was conducted to assess the physical strain derived from the acquired image data. Based on this approach, the facet size was set to 19 pixels and the grid spacing to 3 pixels in order to obtain the best strain values during post-processing of data. In this study, the grid spacing factor and smoothing factor were set to 0.5 and 2.5.

3. Static and Fatigue Tests

The specimens were subjected to testing at ambient temperature (23±2°C) and in a controlled laboratory environment with regulated humidity. The test specimens were mounted to an Instron 8801 servo-hydraulic testing machine, which has a load capacity of 100 kN, and were subjected to both static and fatigue loading conditions. The testing was carried out in load-control mode for both types of tests. Prior to the initiation of the tests, one surface of each specimen was prepared for DIC measurement, while the opposite side was instrumented with an FBG sensor and a strain gauge. The FBG sensor was strategically placed at the midpoint of the specimen, with the strain gauge positioned directly above it, aligned along the same axis. KYOWA CC-33A Strain Gauge Adhesive was used for the instrumentation of both strain gage and FBG sensor. Before conducting the static and fatigue tests, a Proportional-Integral-Derivative (PID) settings were established under 1.5 kN alternating loading based on stiffness-based tuning, resulting in a strain of 1000 με on the specimen. At this strain level, all parameters for the strain gauges, FBG sensor, and DIC measurement were fixed. Prior to initiating the testing phase, the camera brightness settings were conducted to enhance illumination, followed by a calibration process aimed at achieving minimal global residuum values. Before calibration process, the camera positions were secured, and all measurements were carried out under the same configuration to isolate any extrinsic parameters that may significantly affect the DIC measurements (Caliskan & Akyuz, 2024). Two images were captured within one second during both static and fatigue loading conditions.

In the static testing phase, the specimen was subjected to a load of 12 kN, implemented in eight distinct steps. Static test was performed with a 20-second ramp time and holding a 20-second to stabilize the sensor output. Following the completion of the static test, a constant amplitude fatigue loading was introduced to the specimen with 0.2 Hz test frequency. This fatigue specimen loading was similarly executed in eight steps, with variations in both the mean and amplitude loads at each stage. The fatigue testing was conducted for 50 cycles at each specified load level. The profiles for both static and fatigue loading are illustrated in Figure 3.

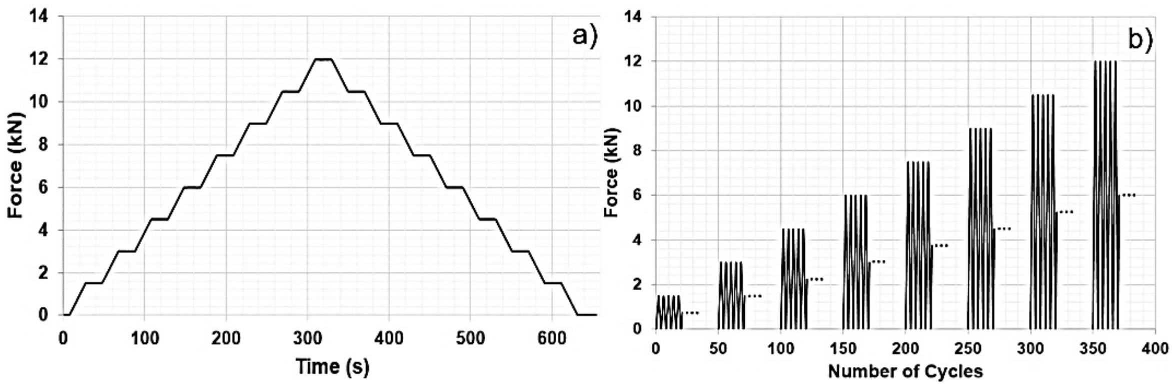

Figure 3. (a) Static loading profile and (b) Fatigue loading profile.

Figure 4 depicts the configuration of the experimental apparatus. Strain measurements were obtained from three distinct systems: DIC, FBG sensors, and strain gauges. The strain gauge and DIC were measured at a sampling rate of 2 Hz, while the FBG was at 50 Hz in the static test. On the other hand, the sampling rate for the strain gauge and FBG was 50 Hz, while the sampling rate for the DIC was 2 Hz under fatigue loading at a test frequency of 0.2 Hz. It is important to note that these systems were not synchronized. Nevertheless, efforts were made to initiate recordings from all three systems as concurrently as possible. nCode software was used to generate synchronized data points via down-sampling.

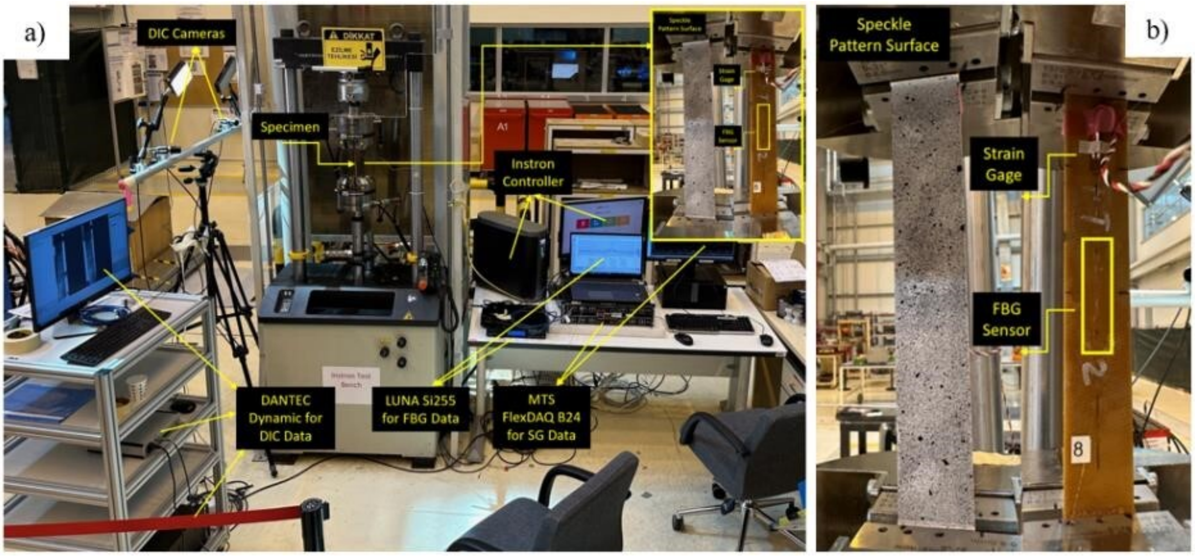

Figure 4. (a) Experimental setup and (b) Specimen with sensors.

4. Results and Discussion

Strain gage and FBG sensors provide effective real-time monitoring of strain during both static and fatigue testing. In contrast, the images obtained through DIC necessitate post-test analysis. In terms of DIC correlation parameters, the literature indicates no significant correlation between grid spacing and strain values, as these values are derived from the deformation gradient at each data point. Grid spacing decreases below around half of the facet size the facets cease to be independent of each other. Expanding grid spacing decreases data density, which may result in the loss of critical information and the introduction of artificial errors, particularly in regions with high strain variation. Additionally, larger facet sizes tend to distort the accuracy of the strain evaluation due to the inherent smoothing effect. Moreover, the use of larger grid reduction and smoothing factors can lead to over-smoothing in both high and low strain regions, with the smoothing factor exerting a more pronounced effect than the grid reduction factor. The correlation parameters enabled the results to converge to the theoretical strain values. Figure 5 illustrates the graphs depicting strain in relation to time for the results of the static test.

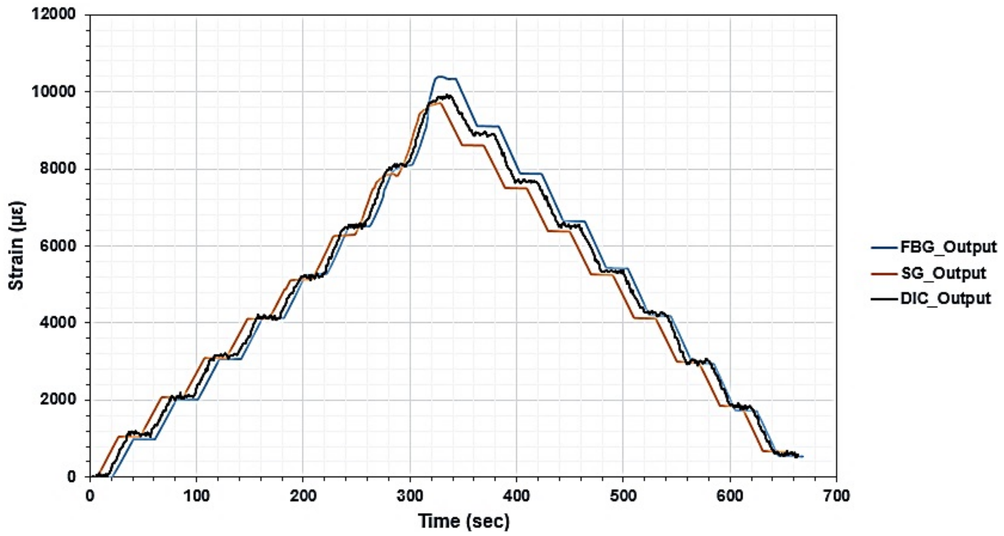

Figure 5. Strain vs time graph for static test.

Even though the calibration was performed at 1000 με for all systems, the sensitivity of each measurement system may differ slightly, resulting in variations in response. In addition, factors such as temperature or mechanical noise during calibration may cause small deviations between systems. The static test results demonstrate that DIC having more noise in the measurements. This issue can possibly be resolved by utilizing higher resolution cameras. In order to interpret the result in detail, measured strain values were compared with expected theoretical strain values that is presented in Table 2. The outputs from the three strain measurement techniques reveal comparable results under static loading conditions. The difference between measured strain values for all techniques and theoretical values is maximum 10% until end of Step-6. This difference starts to increase more for last two steps that may be explained by failure of the specimen because the linearity of the measured strain values starts to deviate and nonlinear strain behaviour can be discerned following the fifth loading step. There is a difference of 13% for Step-1 in DIC measurement which could be attributed to post-processing errors.

Table 2. Measured strain difference between three different techniques under static load.

Loading Steps	Step-1	Step-2	Step-3	Step-4	Step-5	Step-6	Step-7	Step-8
Expected Strain (Theoretical, μm/m)	1,000	2,000	3,000	4,000	5,000	6,000	7,000	8,000
Strain Gage (SG) Output (μm/m)	1,054	2,076	3,093	4,116	5,130	6,289	7,855	9,586
FBG Strain Output (μm/m)	983	2,014	3,064	4,132	5,268	6,496	8,015	10,320
DIC Strain Output (μm/m)	1,128	2,088	3,143	4,149	5,202	6,501	8,036	9,784
% Difference (SG vs Expected Strain)	5	4	3	3	3	5	12	20
% Difference (FBG vs Expected Strain)	2	1	2	3	5	8	15	29
% Difference (DIC vs Expected Strain)	13	4	5	4	4	8	15	22

In literature, conducted research comparing strain gauge, FBG, and DIC for strain measurements under fatigue loading, especially at high strain levels, has been relatively scarce. Given the variation in sample rates between the DIC measurements and other techniques, it was essential to resample the outputs from the strain gauge and FBG sensor to correspond with the sampling rate established by the DIC. Following this, the strain versus time graphs were generated using the resampled results derived from of strain gage and FBG. The results of the fatigue tests are illustrated in Figure 6.

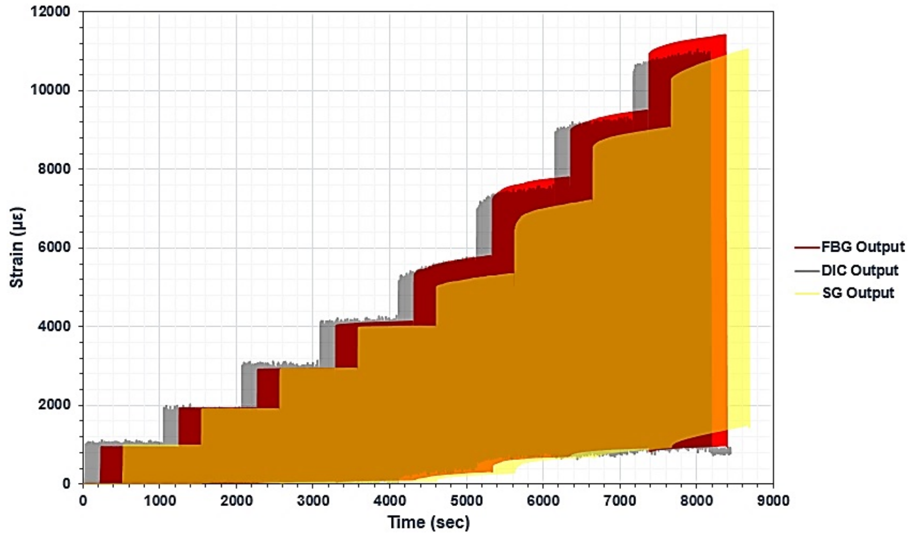

Figure 6. Strain vs time graph for fatigue test.

The results of the fatigue test indicate that noise in the DIC measurements persists under fatigue loading, potentially attributable to the resolution of the cameras used. Furthermore, it can be observed that the linearity of the measured strain values begins to diverge following the fourth loading step. It can also be stated that the three strain measurement techniques yield comparable results in fatigue testing up to the point of maximum fatigue loading. At Step-4, the observed strain values exhibit a close proximity to each other as well as to the theoretical value. The measured strain values from strain gauges, FBG, and DIC exhibit a greater deviation from theoretical values under fatigue loading compared to the discrepancies noted during static testing, particularly in the last three steps of the assessment. The comparison of the measured strain values against the theoretical values is thoroughly outlined in Table 3.

Table 3. Measured strain difference between three different techniques under fatigue load.

Loading Steps	Step-1	Step-2	Step-3	Step-4	Step-5	Step-6	Step-7	Step-8
Expected Delta-Strain (Theoretical, μm/m)	1,000	2,000	3,000	4,000	5,000	6,000	7,000	8,000
Strain Gage (SG) Delta-Output (μm/m)	982	1,908	2,917	3,981	5,178	6,834	8,826	10,666
FBG Delta-Strain Output (μm/m)	940	1,930	2,909	4,013	5,557	7,509	9,236	11,176
DIC Delta-Strain Output (μm/m)	1,022	1,893	2,936	4,079	5,448	7,225	9,088	10,743
% Difference (SG vs Expected Strain)	2	5	3	0	4	14	26	33
% Difference (FBG vs Expected Strain)	6	4	3	0	11	25	32	40
% Difference (DIC vs Expected Strain)	2	5	2	2	9	20	30	34

Adhesives used in strain gauges usually begin to degrade when subjected to strain levels between 3,000 and 5,000 µm/m, because the mechanical stress can exceed their bonding and elastic limits. This degradation can lead to a weakening of the bond between the strain gauge and the specimen surface, causing inaccuracies and variability in strain readings. Furthermore, over time - especially under cyclic loading or in extreme environmental conditions such as high temperatures and humidity - the performance of the adhesive can degrade significantly, ultimately leading to complete bond failure. According to the results of the study, specimen deterioration such as starting fiber breakage and adhesive slippage was observed after a strain value of 4,000 µm/m under alternating loading while the variation in data is consistent for all measurements. However, since the results of the non-contact measurement method DIC show the same trend in terms of specimen degradation as the FBG and strain gauge results, it can be evaluated that specimen degradation is a more dominant effect compared to adhesive degradation.

5. Conclusion

This study attempts to address the shortcomings by conducting a systematic evaluation of FBG, DIC and strain gage measurement techniques, focusing on their performance, comparative error assessment, and practical usability. In doing so, it provides valuable information to guide the selection of the most appropriate measurement methods for different engineering applications. Ultimately, this research is aimed at improving the accuracy and reliability of strain measurements in experimental mechanics. The following conclusions can be reached from this study. The same types of adhesives are applicable for the mounting of both strain gauges and FBG sensors. The DIC measurement exhibit higher level of fluctuation compared to strain gage and FBG sensor under static and fatigue loading. This research indicates that strain gauges, FBG sensors, and DIC show a maximum ten 10% variation in strain values from theoretical estimates, applicable for strains reaching up to 6,000 µm/m under static loading. The results of strain measurement utilizing strain gages, FBG, and DIC techniques exhibit a high degree of comparability when subjected to fatigue loading, specifically up to 4,000 µm/m.

Conflict of Interest

The corresponding author confirms on behalf of all authors that there have been no involvements that might raise the question of bias in the work.

Author Contributions

The corresponding author contributed to the FBG section, and the secondary author contributed to the DIC section.

Funding

This research received no specific grant from any funding agency in the public, commercial, or not-for-profit sectors.

Acknowledgments

Authors acknowledge Turkish Aerospace Industries.

Ethical Statements

The corresponding author testify on behalf of all co-authors that our article submitted followed ethical principles in publishing.

Data and Code Availability

The authors confirm that the data supporting the findings of this study are available within the article.

Supplementary Materials

The authors confirm that the data supporting the findings of this study are available within the article and its supplementary materials.

References

Arsenault, T. J., Achuthan, A., Marzocca, P., Grappasonni, C., & Coppotelli, G. (2013). Development of a FBG-based distributed strain sensor system for wind turbine structural health monitoring. *Smart Materials and Structures*, *22*(7), 075027. https://doi.org/10.1088/0964-1726/22/7/075027

ASTM International. (2015). *ASTM D7028-07: Standard test method for glass transition temperature (DMA Tg) of polymer matrix composites by dynamic mechanical analysis (DMA).* ASTM International.

Bethe, K. (1989). The scope of the strain gage principle. In *Proceedings of COMPEURO 89: VLSI and computer peripherals.* COMPEURO 89 (pp. 3–31). IEEE.

Caliskan, S., & Akyuz, H. (2024). Investigation of the speckle pattern effect for displacement assessments by DIC. *Journal of Intelligent Manufacturing and Special Equipment*.

Campanella, C. E., Cuccovillo, A., Campanella, C., Yurt, A., & Passaro, V. M. (2018). Fibre Bragg grating based strain sensors: Review of technology and applications. *Sensors, 18*(9), 3115. https://doi.org/10.3390/s18093115

Choi, K. S., Huh, Y. H., Kwon, I. B., & Yoon, D. J. (2012). A tip deflection calculation method for a wind turbine blade using temperature compensated FBG sensors. *Smart Materials and Structures, 21*(2), 025008. https://doi.org/10.1088/0964-1726/21/2/025008

Cycom 5575. (n.d.). *Syensqo*. https://www.syensqo.com/en/product/cycom-5575-0

Dally, J. W., Riley, W. F., & Kobayashi, A. S. (1978). *Experimental stress analysis*. McGraw-Hill.

DIN Deutsches Institut für Normung. (1998). *DIN EN 2747: Glass fiber-reinforced plastics – Tensile test*. DIN.

Dokoupil, P. (2017). *Determination of measurement uncertainty of strain and stress using strain gages. Sborník vědeckých prací Vysoké školy báňské - Technické univerzity Ostrava. 63*(1), 9-23, https://doi.org/10.22223/tr.2017-1/2023

Dong, Y. L., & Pan, B. (2017). A review of speckle pattern fabrication and assessment for digital image correlation. *Experimental Mechanics, 57,* 1161–1181. https://doi.org/10.1007/s11340-017-0283-1

Hill, K. O., & Meltz, G. (1997). Fiber Bragg grating technology fundamentals and overview. *Journal of Lightwave Technology, 15*(8), 1263–1276. https://doi.org/10.1109/50.618320

Hill, K. O., Fujii, Y., Johnson, D. C., & Kawasaki, B. S. (1978). Photosensitivity in optical fiber waveguides: Application to reflection filter fabrication. *Applied Physics Letters, 32*(10), 647–649. https://doi.org/10.1063/1.89881

Hoffmann, K. (1989). *An introduction to measurements using strain gages*. Hottinger Baldwin Messtechnik.

Isah, B. W., & Mohamad, H. (2021). Surface-mounted bare and packaged fiber Bragg grating sensors for measuring rock strain in uniaxial testing. *Sensors, 21*(9), 2926. https://doi.org/10.3390/s21092926

Kalita, K., Das, N., Boruah, P. K., & Sarma, U. (2016). Design and uncertainty evaluation of a strain measurement system. *MAPAN, 31*, 17–24. https://doi.org/10.1007/s12647-015-0155-z

Kawasaki, B. S., Hill, K. O., Johnson, D. C., & Fujii, Y. (1978). Narrow-band Bragg reflectors in optical fibers. *Optics Letters, 3*(2), 66–68. https://doi.org/10.1364/OL.3.000066

Kersey, A. D., Davis, M. A., Patrick, H. J., LeBlanc, M., Koo, K. P., Askins, C. G., … Friebele, E. J. (1997). Fiber grating sensors. *Journal of Lightwave Technology, 15*(8), 1442–1463. https://doi.org/10.1109/50.618377

Kim, S., Kang, W., Jeong, M., Lee, I., & Kwon, I. (2013). Deflection estimation of a wind turbine blade using FBG sensors embedded in the blade bonding line. *Smart Materials and Structures, 22*(12), 125004. https://doi.org/10.1088/0964-1726/22/12/125004

Kreuzer, M. (2006). *Strain measurement with fiber Bragg grating sensors*. HBM.

Liu, Z., Liu, X., Zhu, S. P., Zhu, P., Liu, W., Correia, J. A., & De Jesus, A. M. (2020). Reliability assessment of measurement accuracy for FBG sensors used in structural tests of wind turbine blades based on strain transfer laws. *Engineering Failure Analysis, 112,* 104506. https://doi.org/10.1016/j.engfailanal.2020.104506

Mata-Falcón, J., Haefliger, S., Lee, M., Galkovski, T., & Gehri, N. (2020). Combined application of distributed fibre optical and digital image correlation measurements to structural concrete experiments. *Engineering Structures, 225*, 111309. https://doi.org/10.1016/j.engstruct.2020.111309

Montero, W., Farag, R., Diaz, V., Ramirez, M., & Boada, B. L. (2011). Uncertainties associated with strain-measuring systems using resistance strain gauges. *Journal of Strain Analysis for Engineering Design*, *46*(1), 1–13. https://doi.org/10.1243/03093247JSA661

Pan, B., Qian, K., Xie, H., & Asundi, A. (2009). Two-dimensional digital image correlation for in-plane displacement and strain measurement: A review. *Measurement Science and Technology, 20*(6), 062001. https://doi.org/10.1088/0957-0233/20/6/062001

Pan, B., Xie, H., Wang, Z., Qian, K., & Wang, Z. (2008). Study on subset size selection in digital image correlation for speckle patterns. *Optics Express, 16*(10), 7037–7048. https://doi.org/10.1364/OE.16.007037

Peters, W. H., & Ranson, W. F. (1982). Digital imaging techniques in experimental stress analysis. *Optical Engineering, 21*(3), 427–431. https://doi.org/10.1117/12.7972925

Schreier, H., Orteu, J. J., & Sutton, M. A. (2009). *Image correlation for shape, motion and deformation measurements: Basic concepts, theory and applications*. Springer. https://doi.org/10.1007/978-0-387-78747-3

Tekieli, M., De Santis, S., de Felice, G., Kwiecień, A., & Roscini, F. (2017). Application of digital image correlation to composite reinforcements testing. *Composite Structures, 160*, 670–688. https://doi.org/10.1016/j.compstruct.2016.10.096

Tong, W. (2005). An evaluation of digital image correlation criteria for strain mapping applications. *Strain, 41*(4), 167–175. https://doi.org/10.1111/j.1475-1305.2005.00227.x

Comparison of Powder Mixing Methods for Metal Matrix Composite Powders Used in Laser Powder Bed Fusion

Gökhan Dursun [1,*], Dilara Çelik [1], Yağmur Can Gündoğan [1], İrem Bal [1]

Abstract

Metal Matrix Composites (MMCs) reinforced with ceramic particles provide enhanced mechanical properties for high-performance applications. Accordingly, Laser Powder Bed Fusion (LPBF) enables the fabrication of complex and lightweight structures from these materials. However, achieving a homogeneous particle distribution within metal matrix remains a key challenge while maintaining powder processability. In this work, we investigated different powder mixing techniques: acoustic, tumbler, and ball milling for dispersing TiC ceramic particles into Inconel 625 powders. Micro- and nano-sized particles were systematically studied to examine the effect of particle size on the reinforcement distribution within the matrix during powder preparation. The objective was to achieve homogeneous dispersion of reinforcement particles within the Inconel 625 while preserving the spherical morphology of matrix powders. Powder characteristics such as flowability, apparent density, and tap density with respect to particle size, content and mixing parameters for each method were analysed. Results revealed that the acoustic mixing achieved uniform dispersion of TiC particles with minimal agglomeration and maintained the spherical shape of the matrix powders. In comparison, ball milling resulted in surface deformation and particle clustering in mixed powders, whereas tumbler mixing caused significant agglomeration of the reinforcements. The addition of TiC particles and applied mixing methods led to slight decrease in flowability of the composite powders due to increased surface roughness. Among all methods, powders prepared with acoustic system showed superior flow behaviour and the lowest Hausner ratio. Furthermore, fully dense samples were successfully produced using the powders processed via acoustic mixer, confirming their suitability for LPBF processing. This study demonstrated the potential use of acoustic mixing as an efficient and scalable method to produce high-quality MMC powders with improved dispersion while fulfilling the requirements of LPBF process.

Keywords: metal matrix composites, laser powder bed fusion, additive manufacturing, powder mixing.

Received: 13.11.2025 Accepted: 24.12.2025 Research Article

[1] TUSAS Engine Industries Inc., Eskişehir, Türkiye
* Corresponding author.
✉ gokhan.dursun@tei.com.tr

Cite this article as: Dursun, G., Celik, D., Gundogan, Y.C., & Bal, İ. (2025). Comparison of powder mixing methods for metal matrix composite powders used in laser powder bed fusion. *Journal of Defence and Security Industry: Strategy and Technology 1*, 154-174.

1. Introduction

The Metal Matrix Composites (MMCs) belong to a class of advanced materials with improved mechanical and physical properties, derived from the integration of reinforcements with distinctive individual properties. These include enhanced strength, stiffness, reduced density, improved hardness, and superior wear resistance (Tjong, 2007). Ductile alloys are commonly used as matrix materials to combine with reinforcements, which typically exhibit low thermal expansion and advanced toughness (Parsons & Shaik, 2022). Although MMCs present noticeable advantages in thermomechanical properties compared to their pure alloy forms, they still have gained limited acceptance in industry. Thus, MMCs have significant potential for wide range of application within various sectors.

The fabrication methods for MMCs include stir casting, powder metallurgy, and additive manufacturing. However, most traditional techniques result in high cost and mostly limits the geometrical complexity. Therefore, Additive Manufacturing (AM) in MMCs fabrication presents outstanding capability for complicated parts and will gradually involve the adoption of MMCs in industry thanks to the advantages offered by AM technologies. Among the AM techniques, Laser Powder Bed Fusion (LPBF) has emerged as the leading technology for fabricating MMCs. The operation principle for is LPBF based on layer-by-layer processing. A thin layer of powder is spread uniformly onto a substrate and then is partially fused by a high-energy input, usually either a laser or electron beam.

It is well known that characteristics and composition of feedstock powders have a major effect on material properties of final parts produced by LPBF (Murray, et al., 2019). Apparent density, flowability, morphology, and particle size basically control the powder behaviour during processing. From this perspective, there are various studies that investigate the powder quality and its effects on material properties of components. Liu, et al. (2011) demonstrated that an increase in the fraction of fine particles in 316L stainless steel powders allows higher density of parts in addition to enhancing the surface quality. Similarly, Baitimerov, et al. (2018) investigated different batches of gas atomized powders from different manufacturers and found that powder flowability and apparent density have an effect on the processability and eventually lead variation in microstructure and porosity in specimens. It has also been determined that powder flowability is enhanced with spherical particles which ultimately ensures the quality of LPBF parts (Niu & Chang, 1999).

In MMCs, material properties of the fabricated components strongly depend on parameters related to the size, type and concentration of reinforcement, in addition to powder mixing methods (Baitimerov et al., 2018). In addition, inappropriate powder properties might lead to undesirable defects such as increased porosity or void formation within manufactured parts, thus compromising their structural integrity.

Ball milling is one of the methods that allows wet or dry grinding of materials, mechanical alloying and homogeneous mixing using impact force. This process is carried out as a result of the interaction between chamber and balls. In this process, mixing is carried out by providing centrifugal movement within the determined parameters such as rotation speed, time, number of repetitions. Gu et al. (2009) applied high-energy mechanical alloying to Ti-Al-graphite powder mixtures and achieved morphological evolution from flattened to coarsened spherical shapes with increasing milling time. In another study, conducted by Zhuang et al. (2020), nanocomposite powders prepared using planetary ball milling was investigated and found that prolonged milling time causes undesirable clustering of reinforcement particles. Meanwhile, Yang et al. (2022) investigated the ball milling technique under different conditions, including dry, wet, and hollow ball milling. They concluded that powder sphericity is damaged with the long dry ball milling time while wet ball milling cannot ensure the particles to be welded. These studies further highlight the complexities involved in achieving optimal dispersion of reinforcements through ball milling.

Tumbler mixing is another widely used method in composite powder preparation. The three-dimensional rotational motion in the tumbler mixing offers minimizing the mechanical deformation of metallic powders and allows powder mixing without agglomeration. The composite powder preparation of 316L stainless steel reinforced with Y_2O_3 nanoparticles was carried out using tumbler mixing. It was observed that tumbler mixing can result in rough particle surfaces, which ultimately lead to reduced powder flowability during the LPBF process (Zhai, et al., 2020). Similarly, this technique was also employed for preparing Inconel 718 powder reinforced with TiC nanoparticles and revealed that constituents are dispersed uniformly within the matrix (Yao, et al., 2017). However, this method typically requires a long processing time to prepare the composite powder, which is considered a significant drawback for industrial applications (Dadbakhsh et al., 2020).

Even though different powder mixing methods are available in industrial applications, resonant acoustic mixing (RAM) has emerged as an innovative technique by offering uniform dispersion, minimizing agglomeration, and maintaining powder flow properties. RAM is known for its ability to achieve rapid and uniform mixing via of low-frequency energy. It generates acoustic interaction and unique material movement inside the chamber. Specifically, RAM mixers control vertical motion to induce vibration and movement of the resonator plate, thereby transferring energy to the contents within the mixing vessel. Compared to traditional mechanical mixers, RAM technology combines low-frequency, high-intensity motion with the acoustic energy. Smith et al. (2020) demonstrated that efficient mixing of Y_2O_3-coated NiCoCr composite powders can be achieved using RAM technology. Similarly, in another study, RAM was used to mix carbon nanotubes (CNTs) with AlSi10Mg in order to attain uniform particle dispersion (Thompson et al., 2019).

This research conducts a systematic study for comparison of composite powder preparation techniques, namely, high-energy ball milling, tumbler mixing, and resonant acoustic mixing. A detailed and systematic analysis of powder morphology, apparent density, and flowability was conducted for Inconel 625 alloy reinforced with micro- and nano-sized TiC particles. The objective was to determine an optimal composite powder preparation strategy for LPBF technology that ensures both homogeneity and processability across different reinforcement particle sizes.

2. Methodology

Gas-atomized Inconel 625 powder, with an average particle size of 35 µm, was employed as the matrix alloy in this study (Figure 1). TiC reinforcements were introduced at a fixed content of 2 wt% in two size ranges: nano-sized particles (35–55 nm) and micro-sized particles (1–10 µm). The composite powders were mixed using three different techniques: acoustic mixing, high-energy ball milling, and a tumbler system. The process parameters for each mixing method were investigated and optimized to achieve a uniform distribution of TiC particles within the matrix. LPBF process parameters were adopted from literature optimized for Inconel alloy as shown in Table 1 (Poyraz & Kushan, 2019).

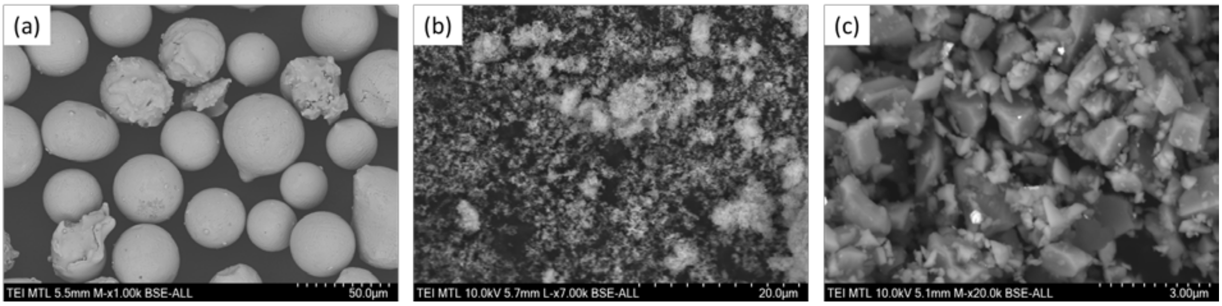

Figure 1. SEM images of (a) Virgin Inconel 625 particles (matrix), (b) Nano-sized TiC particles, and (c) Micro-sized TiC particles.

Table 1. LPBF process parameters (Poyraz & Kushan, 2019).

Laser power (W)	285
Laser scanning speed (mm/s)	960
Hatch distance (mm)	0.11
Layer thickness (mm)	0.040

2.1. Preparation of Powder Mixtures

2.1.1. Ball Mill Mixing

Planetary Mono Mill Pulverisette 6 classic line device was used for ball milling process. Dry mixing was performed in a ZrO_2 chamber with ZrO_2 grinding balls, maintaining a ball-to-powder mass ratio of 1:1. The mixing parameters are summarized in Table 2. To prevent excessive heating, 10 min cooling period was applied after every 15 min of milling. These parameters were independently applied to mix both micro-sized and nano-sized TiC particles with the Inconel 625 matrix powder.

Table 2. The parameters of the mixture experiments for ball milling.

Time (min)	Rotation speed (rpm)
60	150 300
120	150 300
180	150 300

2.1.2. Tumbler Mixing

The tumbler mixing process was carried out using a Turbula T2F device. The rotational speed was adjusted by changing the position of the drive belts on the five-stage pulley system, enabling a velocity range of 23–101 rpm. The experimental setup employed 2 wt% micro- and nano-sized TiC particles as reinforcements. TiC/Inconel 625 composite powders were mixed for durations of 4, 8, and 12 h at a constant rotational speed of 101 rpm. A 2000 mL cylindrical plastic vessel was used with a fill level of 50%. The complete set of experimental parameters is summarized in Table 3.

Table 3. Tumbler mixing parameters for tumbler mixing.

	2 wt% micro-sized TiC	2 wt% nano-sized TiC
Mixing time (h)	4, 8, 12	4, 8, 12
Fill level (%)	50%	50%
Rotational Speed (RPM)	101	101

2.1.3. Resonant Acoustic Mixing (RAM)

The Resodyn LabRAM II device was used for the RAM method. The vertical movement of the resonator plate and the attached vessel holder generate acoustic energy, which induces dispersion of reinforcement within matrix. To maintain the desired outcomes and ensure a safe mixing environment, powders were added to the system in accordance with specific weight limits. The container was periodically cooled during the mixing process to prevent powder agglomeration due to the risk of the excessive heating. The RAM device has 1 kg mixing capacity and can deliver up to 100 g acceleration for effective processing. In the experimental procedure, 2 wt% micro-sized TiC was first introduced into the container and mixed at 90 g for 1 min. Following this, the matrix powder was added and mixed at 80 g for durations ranging from 1 to 4 min. A similar procedure was applied for 2 wt% nano-sized TiC particles, with mixing times ranging from 1 to 6 min. The experimental setup for the acoustic mixer is shown in Table 4.

Table 4. Experimental parameters for resonant acoustic mixing.

	Micro-sized TiC	Nano-sized TiC
Mixing time (min)	1-4	1-6
Fill ratio (%)	80	80
G-force	80	80

2.2. Characterization

Morphology, particle size, shape, and distribution of the composite powders were characterized using Hitachi SU5000 scanning electron microscope (SEM) equipped with an energy-dispersive spectroscopy (EDS) system. Flow rate measurements of the composite powders were carried out using the PowderFlow Measurement Kit in accordance with ASTM B213 and ASTM B964. Hall flow tests were conducted with 50.0 g of powder, while Carney flow tests used 150.0 g in accordance with ASTM B213 and ASTM B964 standards. Apparent density was determined using 25 cm^3 of powder via the PowderFlow Measurement Kit, following ASTM B212 and ASTM B417 standards. Tapped density measurements were performed with 100.0 g of powder using a Torontech Tap Density Tester in accordance with ASTM B527. Flow properties were evaluated by calculating the Hausner ratio from the apparent and tapped density results. SEM was also used to analyse the microstructure of the bulk samples. The specimens were sectioned along the XY-plane using electrical discharge machining (EDM), mounted within a polymer (Bakelite) holder, and subsequently ground, polished, and etched using a glycaemia solution.

3. Results

The Inconel 625 matrix alloy was analysed using SEM, as shown in Figure1a, revealing that the matrix powders mainly had a spherical morphology, with minor irregularities. EDS analysis confirmed the presence of the expected elements in the Inconel 625. Figure 1b presents SEM images of the nano-sized TiC particles, which exhibited slight agglomeration due to their nanoscale size. Figure 1c presents SEM images of the micro-sized TiC particles, which exhibit an irregular and non-spherical shape form. The matrix powder (as shown in Table 5) exhibited an apparent density of 4.616 g/cm^3 and a tapped density of 5.264 g/cm^3. The resulting Hausner ratio was 1.14, while the Hall flow rate was measured as 17.106 s, both of which indicate good powder flowability. Distribution of reinforcement in Inconel 625 powder

Figure 2 presents SEM images of the composite powder reinforced with 2 wt% micro-sized TiC, prepared by the ball milling method. The results reveal that TiC particles caused noticeable deterioration in the surface texture and morphology of Inconel 625 particles, attributed to mechanical impact from the ceramic particles during milling. Similarly, Figure 3 illustrates the morphology of the 2 wt.% nano-sized TiC particles-reinforced powder, which exhibited comparable surface damage and a higher degree of particle adhesion. A homogeneous distribution of TiC particles was not achieved; instead, both nano- and micro-sized TiC reinforcements formed localized agglomerates, indicating limited dispersion. Furthermore, increasing the milling time and rotational speed did not effectively suppress agglomeration. Among all tested parameters, the most favourable results for the ball milling technique were obtained at 150 rpm for 180 min for both nano- and micro-sized powders.

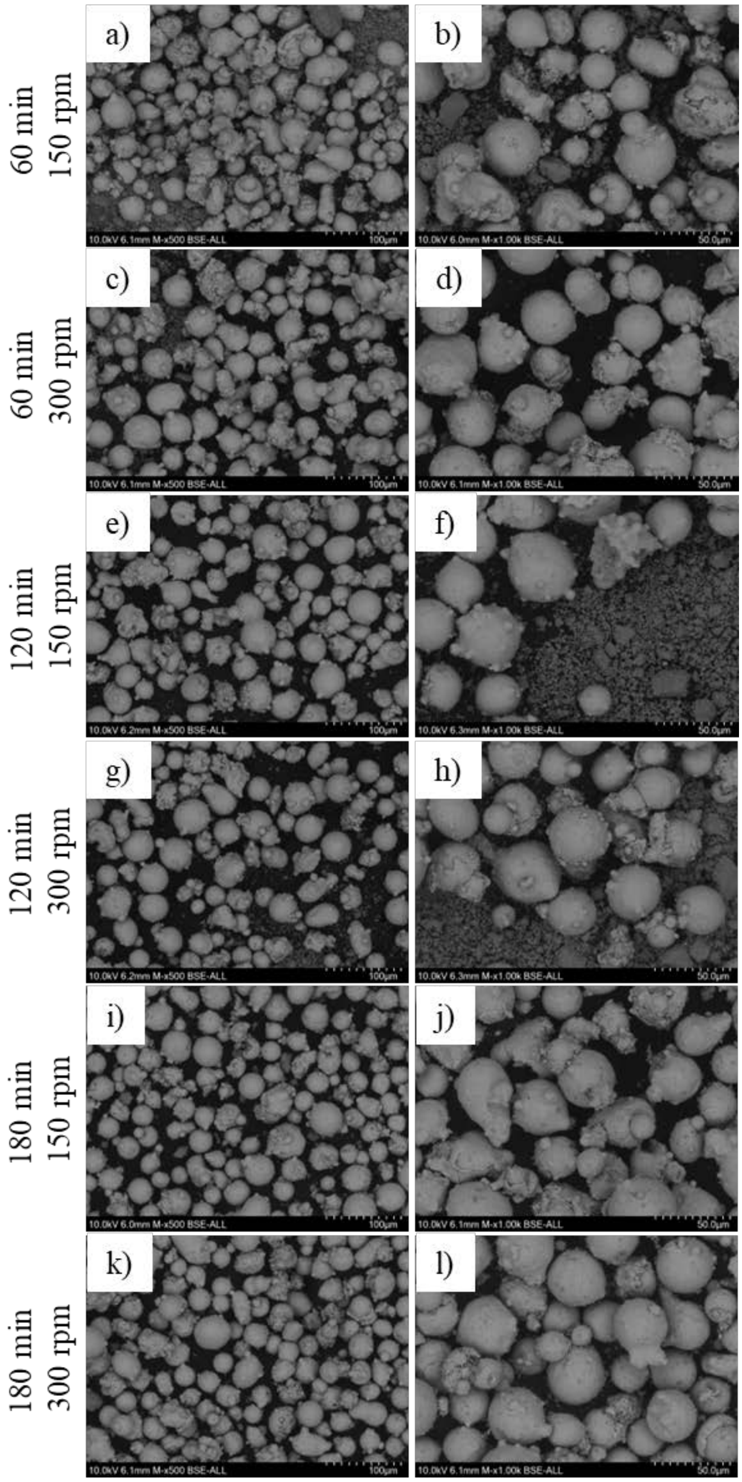

Figure 2. SEM micrographs of the 2 wt% micro-size TiC particles-reinforced Inconel 625 composite powders processed via ball milling at different magnifications with (a), (b) for 60 min 150 rpm; (c), (d) for 60 min 300 rpm; (e), (f) for 120 min 150 rpm; (g), (h) for 120 min 300 rpm; (i), (j) for 180 min 150 rpm; (k), (l) for 180 min and 300 rpm.

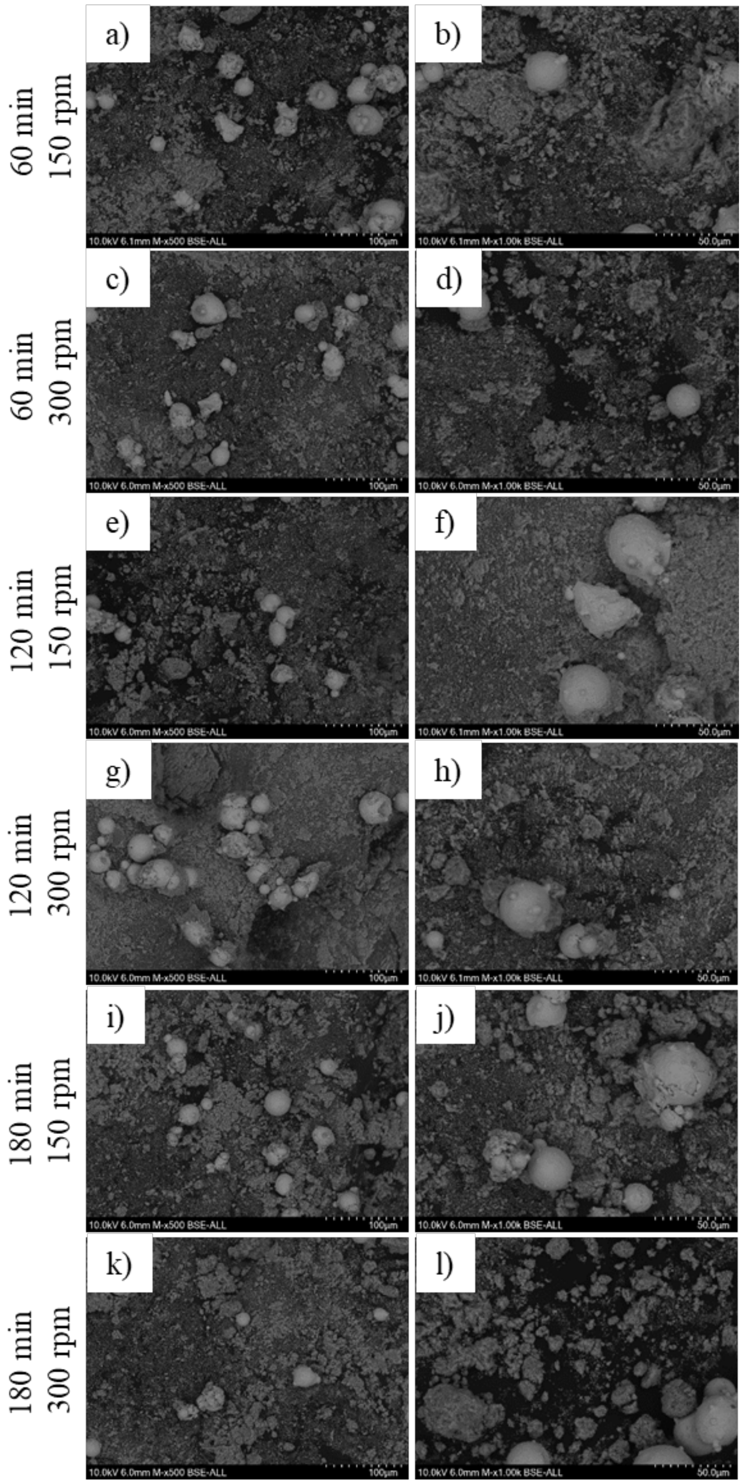

Figure 3. SEM micrographs of the 2 wt% nano-sized TiC particles-reinforced Inconel 625 composite powders processed via ball milling at different magnifications with (a), (b) for 60 min 150 rpm; (c), (d) for 60 min 300 rpm; (e), (f) for 120 min 150 rpm; (g), (h) for 120 min 300 rpm; (i), (j) for 180 min 150 rpm; (k), (l) for 180 min and 300 rpm.

In Figure 4, SEM images of the powder mixture composed of nano-sized TiC reinforcement particles prepared using a tumbler mixer are presented. As shown in Figure 4, majority of the nano-sized particles did not adhere to the matrix powders, and a significant agglomeration was observed. This indicates that a 4 h mixing duration is insufficient to achieve effective dispersion of the reinforcement particles. Although some matrix particles were partially coated with reinforcement particles, remaining powders exhibited minimal adhesion, resulting in an inconsistent and non-uniform mixture. To further evaluate the effect of mixing time, SEM images were analysed after 8 and 12 h of mixing. However, no significant improvement in the homogeneity of the nano-sized particles was observed, even with extended mixing durations.

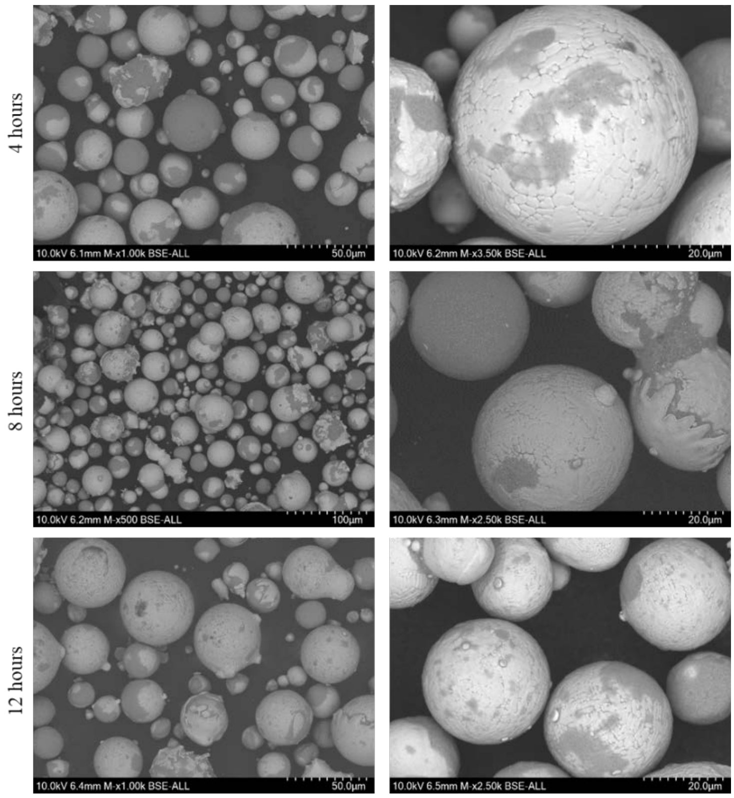

Figure 4. SEM images of 2 wt% nano-sized TiC/Inconel 625 composite powder from the different mixing time and magnification (Turbula system).

In the case of micro-sized TiC particles, Inconel 625 processed using the tumbler mixer, SEM images in Figure 5 reveals that poor dispersion of the reinforcement particles after 4 h of mixing, with visible clusters and agglomerates. The surfaces of the Inconel 625 powders remained largely uncoated, as the relatively larger micro-sized TiC particles tended to remain embedded within the matrix. However, a significant improvement in particle distribution and interfacial adhesion was observed with extended mixing times. After 8 h, particle clustering was noticeably reduced, and a more uniform distribution across the matrix was achieved, indicating an improvement in mixture homogeneity due to prolonged mechanical interaction. Further enhancement was observed after 12 h of mixing, where clustering was minimized and a more consistent, homogeneous dispersion was achieved. These findings highlight the critical influence of both particle size and mixing duration on the homogeneity of composite powders.

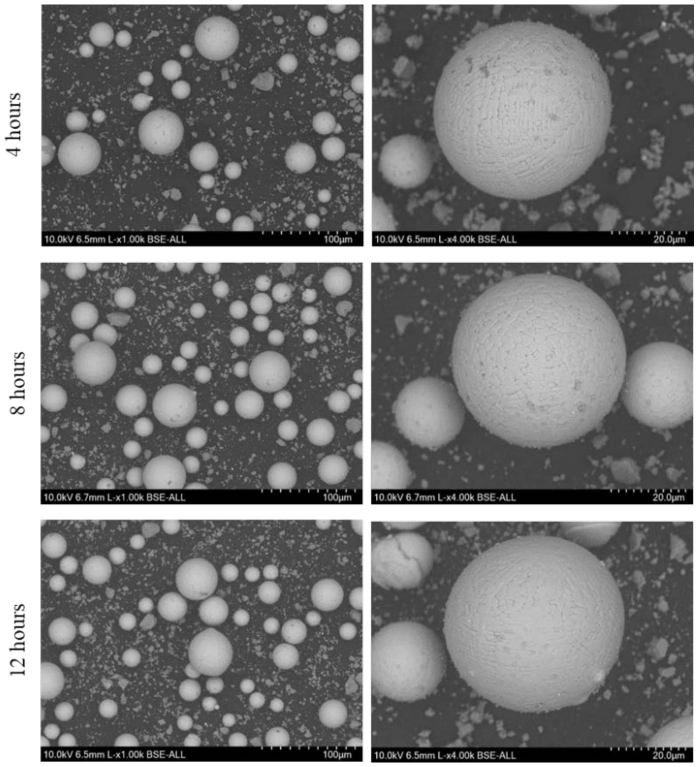

Figure 5. SEM images of 2 wt% micro-sized TiC/Inconel 625 composite powder from the different mixing time and magnification (Turbula system).

Figure 6 shows the morphology and particle shape of 2 wt% nano-sized TiC/Inconel 625 composite powders processed via resonant acoustic under varying mixing times at constant g-force. The results indicate that nano-sized TiC particles were uniformly distributed throughout the matrix without any agglomeration. The spherical morphology of the matrix particles was preserved since there was no mechanical impact during the process. During the initial mixing periods of 3, 4, and 5 min, partial surface attachment of TiC particles to the Inconel 625 matrix was observed; however, some regions remained insufficiently coated. After 6 min of mixing, a significant improvement in adhesion between TiC particles and Inconel 625 matrix was observed as shown in Figure 7. This suggests that 6 min of processing represents the optimal mixing time for achieving uniform dispersion and effective coating of the reinforcement particles.

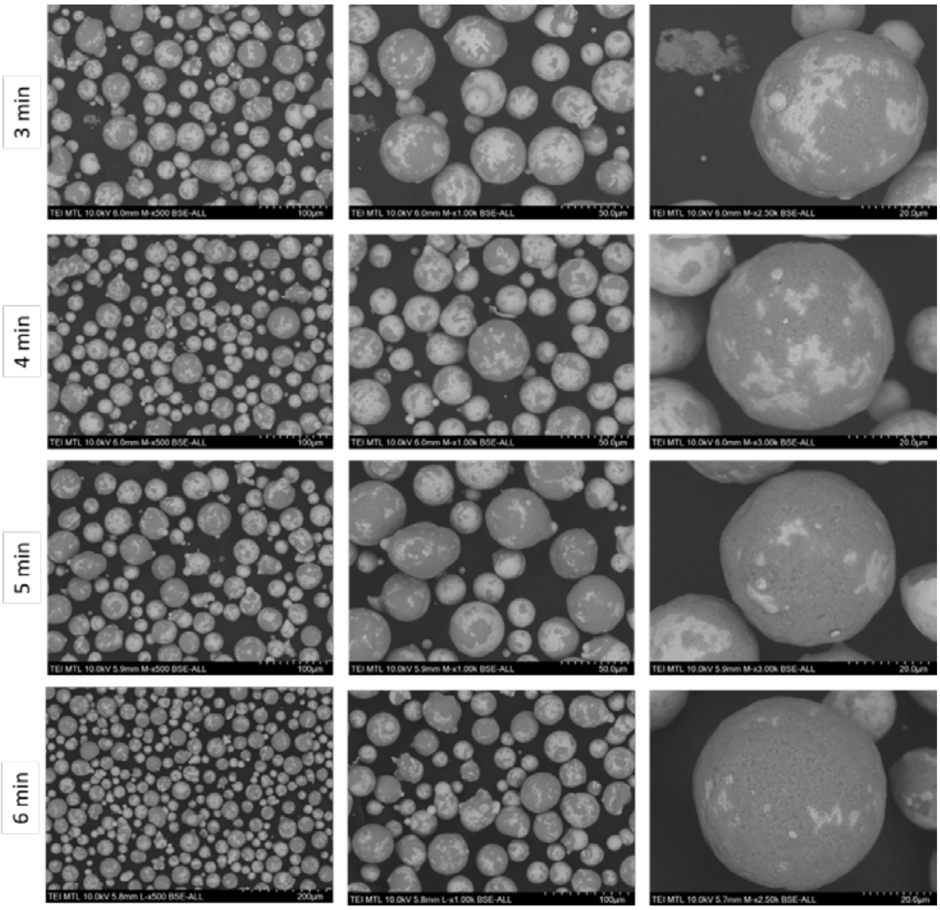

Figure 6. SEM images of 2 wt% nano-sized TiC/Inconel 625 composite powder (RAM) prepared at different mixing time.

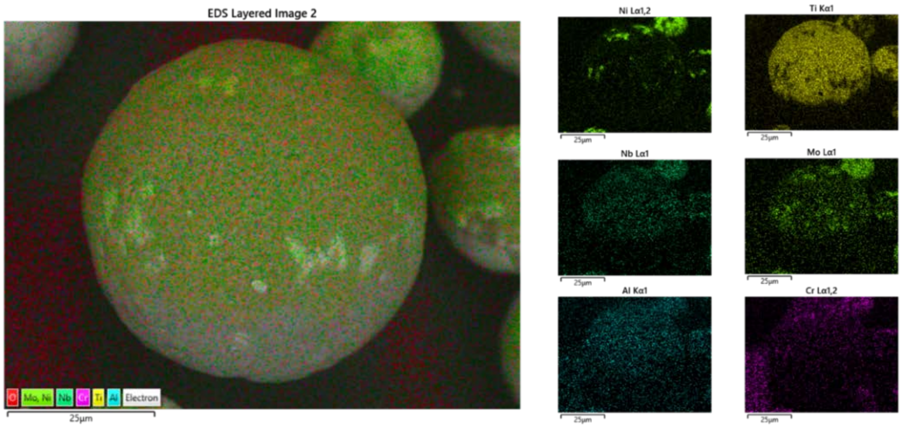

Figure 7. EDS mapping images of 2 wt% nano-sized TiC/ Inconel 625 composite powder prepared (RAM) at 6 min mixing time.

As anticipated, micro-sized TiC particles exhibited, different mixing behaviour compared to their nano-sized counterparts. Owing to their irregular morphology and interparticle van der Waals interactions, micro-sized TiC particles showed a pronounced tendency to agglomerate.

As shown in Figure 8, after 1 min of mixing, although some reinforcement particles were observed on the matrix surface, a significant fraction had already formed agglomerates on the carbon band. However, with extended mixing time, the distribution of micro-sized TiC particles became more uniform, and greater adherence to the matrix particle surfaces was achieved. In contrast to nano-sized TiC particles, the primary challenge for micro-sized TiC reinforcements was minimizing interparticle agglomeration rather than achieving complete surface coverage of the matrix. This observation suggests that mixing strategies for micron-sized reinforcements should prioritize dispersion stability over surface coating efficiency.

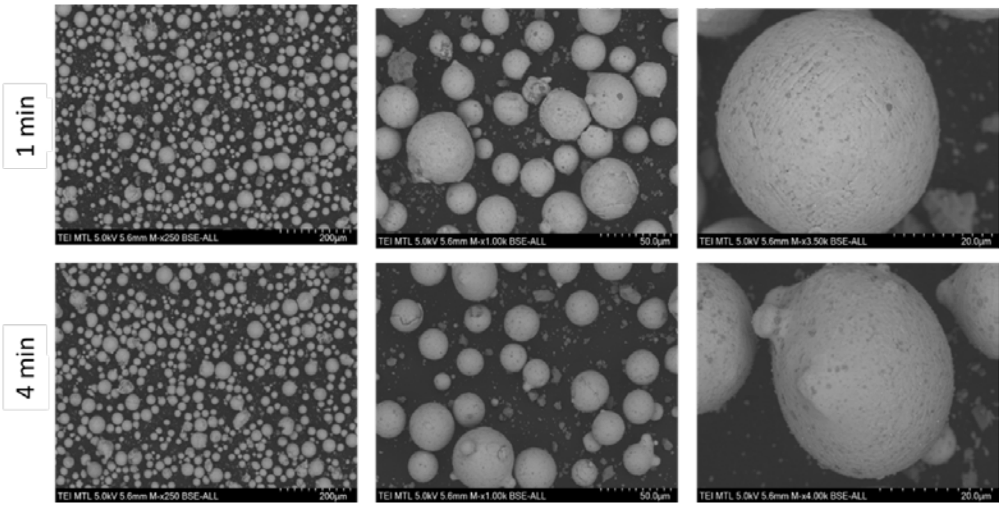

Figure 8. SEM images of 2 wt% micro-sized TiC/Inconel 625 composite powder prepared (RAM) at different mixing.

The apparent density, tapped density, Hausner ratio, and Hall flow rate of TiC-reinforced composite powders processed via RAM and ball milling, along with the matrix powder, are presented in Table 5. No flow measurements were obtained for the powder mixed via tumbler mixer, as the powder failed to flow through the funnel during the test, indicating poor flowability. The matrix powder exhibited an apparent density of 4.616 g/cm³ and a tapped density of 5.264 g/cm³, resulting in a Hausner ratio of 1.14. The Hall flow rate was measured at 17.106 s, both of which indicate good powder flow characteristics.

As shown in Table 5, the flow behaviour of TiC-reinforced composite powders prepared by ball milling is slower compared to the matrix powder, with flow rate decreasing as the reinforcement particle size decreases. The nano-sized TiC/Inconel 625 composite powder exhibited an apparent density of 3.5 g/cm³ and a tapped density of 4.1 g/cm³. The corresponding Hausner ratio was 1.17, and the Hall flow rate was measured as 25.2 s, indicating fair flowability. In contrast, the micro-sized TiC/Inconel 625 composite powder showed higher apparent and tapped densities of 4.2 g/cm³ and 5.0 g/cm³, respectively, with a Hausner ratio of 1.19 and a Hall flow rate of 24.1 s, showing fair flowability. These results indicate that even though both composite powders show reasonable flow properties, the nano-sized TiC/Inconel 625 composite powder indicates slightly poor flow characteristics, likely due to increased interparticle cohesion and surface area.

On the other hand, 2 wt% micro-sized TiC/Inconel 625 composite powder prepared via RAM exhibited an apparent density of 4.508 g/cm^3 and tap density of 5.449 g/ml. The calculated Hausner ratio was 1.208, and the Hall flow rate was measured as 25.014 s, indicating fair flowability. Analysis of the tap density values reveals that the micro-sized TiC particles exhibited the highest tap density, followed by the Inconel 625 matrix powder, while the nano-sized TiC particles showed the lowest value. This behaviour for micro-sized TiC partciles can be attributed to the insufficient adhesion to the matrix. In contrast, the strong adhesion of nano-sized TiC particles to the matrix prevents such separation, resulting in more efficient particle packing. The flowability of the composite powder consisting of an Inconel 625 matrix and nano-sized TiC particles was found to be favourable, whereas the composite powder containing micro-sized TiC particles exhibited slightly reduced flowability but remained within acceptable limits. These results suggest that the insufficient adhesion of micro-sized TiC particles adversely affects the flow behaviour of the composite powder, whereas the nano-sized TiC particles exhibits no detrimental impact on flow properties.

Table 5. Density and flow characteristics of powders (values correspond to composite powder mixtures prepared using optimized mixing parameters).

Mixing method	Sample	Apparent Density (g/cc)	Tap Density (g/ml)	Hausner Ratio	Flow Character	Hall Flow Rate (50g/s)
-	Inconel 625	4.616	5.264	1.14	Good	17.106
Acoustic	µm-TiC composite	4.508	5.449	1.208	Fair	25.014
Acoustic	nm-TiC composite	4.334	4.965	1.145	Good	16.606
Ball Mill	µm-TiC composite	4.2	5	1.19	Fair	24.1
Ball Mill	nm-TiC composite	3.5	4.1	1.17	Good	25.2
Tumbler	nm-TiC composite	Test could not be performed				
Tumbler	µm-TiC composite	Test could not be performed				

Figure 9 shows that the apparent density of Inconel 625 decreases upon reinforcement with TiC particles This can be attributed to the influence of reinforcement particles on powder packing characteristics. However, the RAM method provides higher apparent density compared to both ball milling and tumbler mixing. This improvement is attributed to more uniform dispersion and enhanced interfacial interaction between the matrix and reinforcement particles.

As shown in Figure 10, Hall flow rates for the Inconel 625 matrix and nano-sized TiC/Inconel 625 composite powders processed via RAM are higher than those for micro-sized TiC/Inconel 625 composite powders, while powders prepared by ball milling and tumbler mixing exhibit significantly slower flow rates. This difference is primarily due to uniform particle dispersion and preserved spherical morphology achieved through RAM. In contrast, ball milling induces surface deformation and particle flattening, which negatively affect the flowability.

Figure 11 presents the tapped density results, which follow a trend similar to the apparent density trend observed in Figure 9. The nano-sized TiC/Inconel 625 composite powder processed via RAM exhibits the highest tapped density, indicating improved particle packing efficiency. This is due to minimized agglomeration and improved interfacial contact between the reinforcement and matrix, resulting in more efficient particle arrangement.

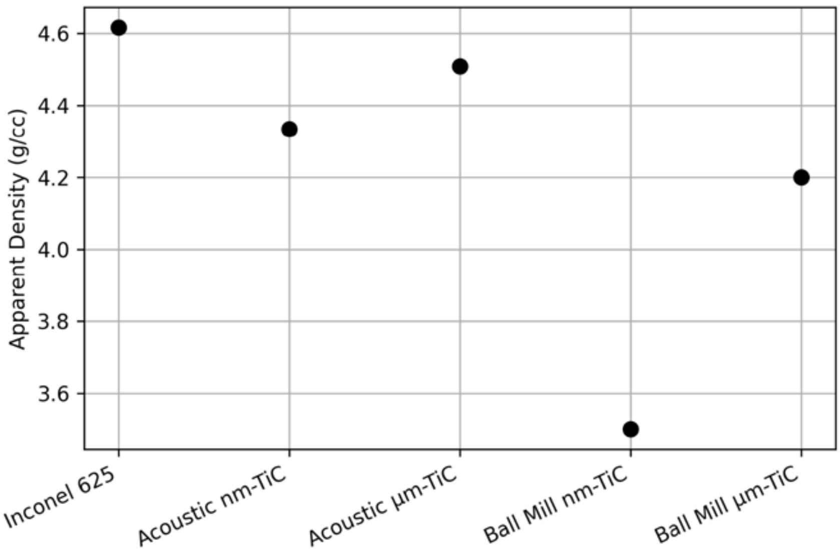

Figure 9. Apparent density of samples by mixing methods.

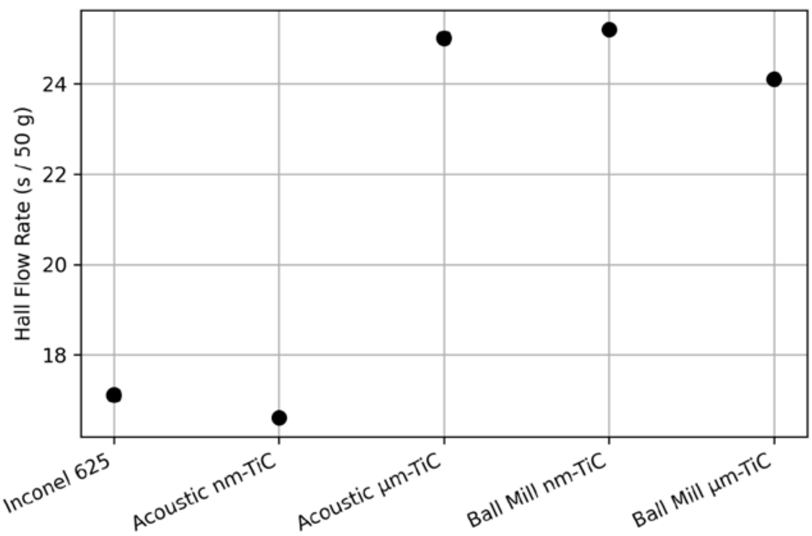

Figure 10. Hall Flow Rates density of samples by mixing methods.

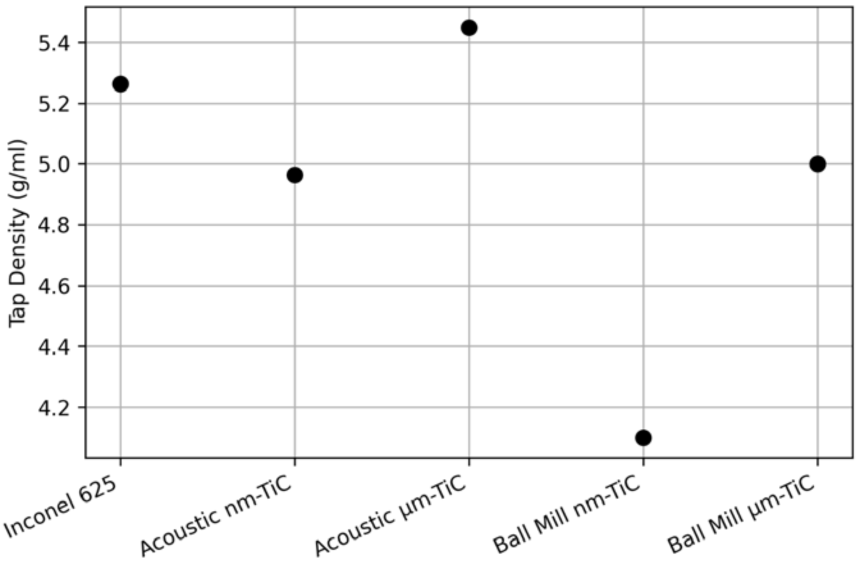

Figure 11. Tap density of samples by mixing methods.

In summary, Table 6 compares different mixing methods for MMC powders and demonstrates that RAM provides enhanced particle dispersion in shorter processing times, along with improved powder flow properties.

Table 6. Comparative chart of mixing methods for MMC powders.

Parameter	Resonant Acoustic Mixing	Ball Milling	Tumbler Mixing
Mixing time	1-6 min	1-3 h	4-12 h
Homogeneity	Minimal agglomeration	Partial dispersion	Visible clustering
Agglomeration	Minimal	Moderate	High
Particle morphology	Preserved	Deformation observed	Preserved
Flow properties (Hausner ratio)	Good (1.145-1.208)	Fair (1.17-1.19)	Fair (1.208)

Figure 12 shows the microstructure of the bulk Inconel 625 matrix sample, revealing distinct melt pools with dendritic features exhibiting a cellular morphology that are generally distributed in a homogeneous manner. Variations in local cooling rates during the additive manufacturing process resulted in dendritic structures aligned parallel to the solidification direction in some regions, while exhibiting a more perpendicular orientation in others. No gas porosity was observed within the microstructure. EDS analysis confirmed the chemical composition of the material, with no detectable signs of contamination.

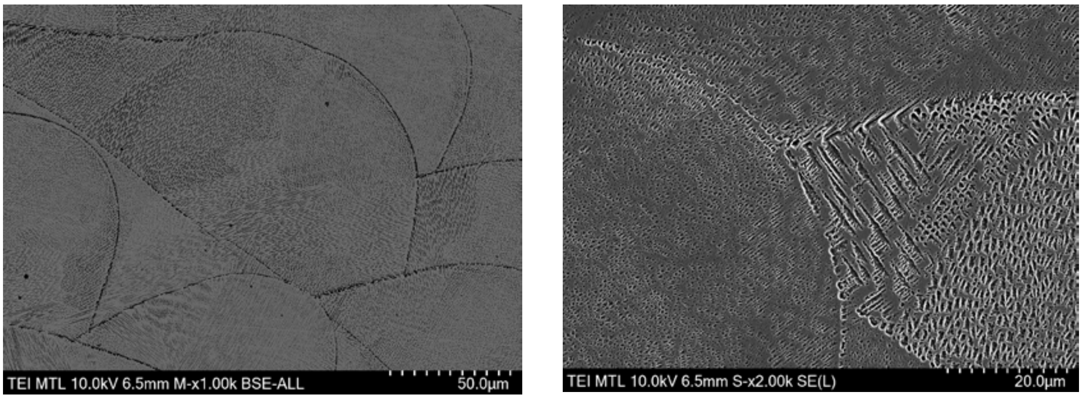

Figure 12. SEM images of the bulk Inconel 625 matrix.

Figure 13 shows that, similar to the Inconel 625 matrix, distinct melt pools were observed in the bulk nano-sized TiC/Inconel 625 composite sample. The nano-sized TiC particles acted as effective nucleation sites, promoting the formation of equiaxed grains instead of the typical columnar dendritic structures. This grain refinement is consistent with established literature, where ceramic reinforcements such as TiC are known to enhance nucleation and suppress columnar growth (Al Mangour et al., 2007). However, EDS analysis revealed localized agglomeration of nano-sized TiC particles within the microstructure, suggesting incomplete dispersion despite their role in grain refinement.

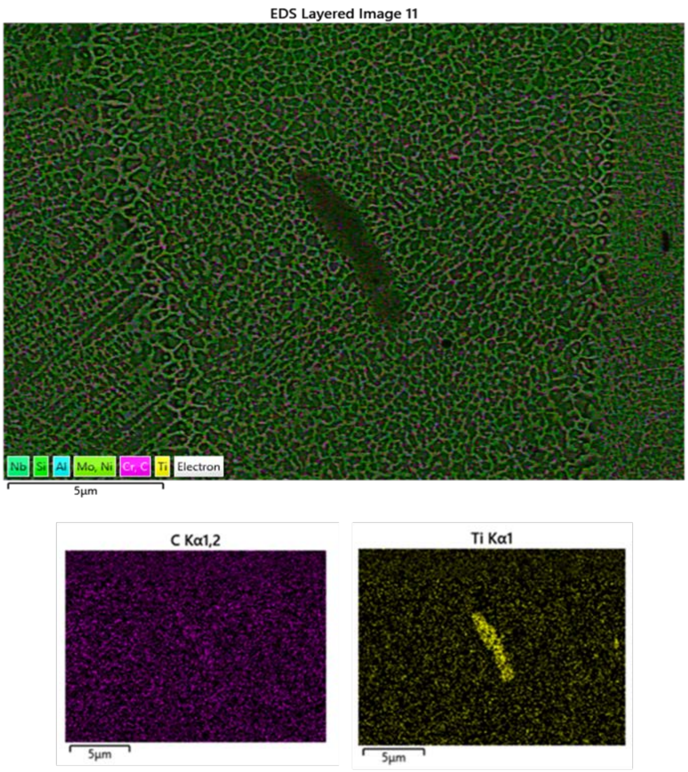

Figure 13. SEM-EDS images of the bulk nano-sized TiC/Inconel 625 sample.

Figure 14 shows distinct melt pools within the microstructure of micron-sized TiC/Inconel 625 bulk sample, with EDS analysis revealing the presence of agglomerations. These agglomerations are significantly higher compared to the nano-sized TiC/Inconel 625 bulk sample and distributed throughout the matrix and primarily attributed to their larger particle size. Moreover, it can be seen that unmelted or partially melted micron-sized particles were located near the melt pool boundaries during processing, where they accumulate and form agglomerates.

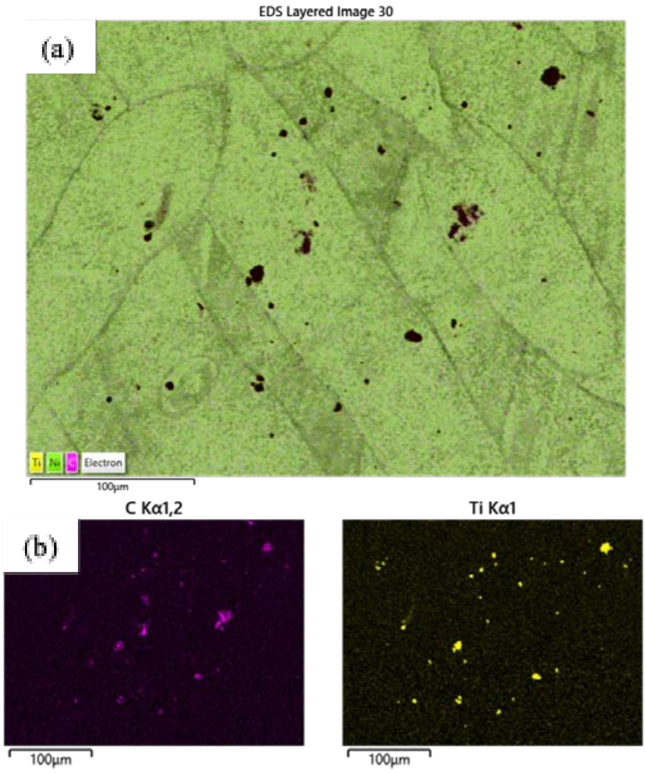

Figure 14. (a) SEM images and (b) EDS analysis of the bulk micro-sized TiC/Inconel 625 sample.

As shown in Table 7, the Inconel 625 matrix exhibited average hardness values of 24 HRC in the Z-direction and 23 HRC in the XY-direction. Both bulk TiC particles-reinforced composite samples achieved higher average hardness values compared to the unreinforced matrix, indicating a substantial improvement in mechanical resistance. This enhancement is primarily attributed to effective load transfer from the ductile Inconel 625 matrix to the hard, rigid TiC particles, as well as contributions from grain refinement and dispersion strengthening mechanisms.

Table 7. Comparative macro-hardness chart.

Material	Z-direction	XY-direction
Inconel 625 matrix	24	23
2 wt% micro-sized TiC/Inconel 625	35	35
2 wt% nano-sized TiC/Inconel 625	33	34

4. Discussion

These findings show that composite powder flow properties may substantially depend on mixing method regardless of the reinforcement particles (nano- or micro-scale size). Meanwhile, achieving strong adhesion between the reinforcement particles and the matrix powder is critical for maintaining powder integrity during LPBF, where optimal flowability and consistent powder deposition are essential for quality of final part. The results showed that mixing methods such as ball milling and tumbler mixing produced composite powders with poor flow characteristics, while RAM provided improved flowability due to the ability to homogeneously disperse TiC particles in the Inconel 625 matrix without compromising spherical powder morphology.

In the case of nano-sized TiC/Inconel 625 composite powders, tumbler mixing resulted in pronounced agglomeration, with no significant improvement observed even after extended mixing durations. Similarly, ball milling was unable to achieve fully homogeneous mixing despite variations in rotational speed and mixing time. In contrast, RAM proved to be highly efficient, achieving homogeneous particle dispersion and strong adhesion to the matrix within only 3 min, with no evidence of agglomeration.

Considering micro-sized TiC/Inconel 625 composite powders, while the mixtures exhibited slight changes in uniformity, tumbler mixing had limited effectiveness since even at longer mixing duration. However, the ball milling method managed improved homogeneity than tumbler mixing, where higher rotational speed and longer duration enhanced the mixing quality. Nevertheless, RAM accomplished more uniform distribution compared to both alternatives, and longer mixing duration further improved dispersion quality. Among the methods tested, RAM provided the most effective and homogeneous mixing for micro-sized TiC particles.

The addition of TiC particles promotes the alteration in microstructure from columnar to equiaxed grain structures. Although agglomeration is observed in bulk samples with both nano- and micro-sized TiC particles, it is more noticeable in specimens reinforced with micro-sized particles. TiC usually does not melt during processing owing to its high melting point. Due to its high melting point, TiC typically does not melt during processing; however, partial dissolution may occur when particle size is reduced to the nanoscale, combined with low TiC content. In nano-sized TiC particles-reinforced specimens, agglomeration is primarily driven by the relatively low density of TiC particles, which promotes their flotation within the melt pool. During rapid solidification, these floating particles tend to segregate toward melt pool boundaries, where they accumulate and form agglomerates. In contrast, agglomeration in micro-sized TiC particles-reinforced specimens is mainly attributed to the larger particle size, the inability of the particles to melt, and insufficient interfacial bonding with the matrix.

Among the powder mixing techniques investigated, RAM has emerged as a promising method for achieving rapid and uniform particle dispersion. Compared to ball milling, which may deform the powder morphology, or tumbler mixing, which often requires extended processing times, acoustic mixing offers a balance between processing efficiency and powder quality. This method is particularly effective for nano-sized reinforcements, as it minimizes agglomeration while preserving the original morphology of the particles.

5. Conclusion

This study aimed to uniformly disperse 2 wt% TiC particles with different sizes in Inconel 625 matrix powders using the various mixing techniques. Among the methods tested, RAM achieved homogeneity in short time, maintaining the spherical morphology of the matrix particles. The flow properties of the RAM-prepared powders remained at optimal levels, as a result of low Hausner ratio (1.145) and Hall flow rate (16.6 g/s). These characteristics ensures that composite powders suitable for LPBF. Ball milling resulted in partial improvement in reinforcement dispersion but introduced surface deformation and agglomeration. These effects decreased the powder flowability apparent and tap and density. Tumbler mixing preserved particle morphology but failed to disperse agglomeration, even with extended mixing times (4-12 hours). Additionally, the TiC particles showed poor adhesion to the matrix. The samples produced with LPBF using the powders created with RAM showed low level of porosity. Due to the small size of the TiC nano-sized particles, they acted as nucleation sites for the equiaxed grain growth. On the other hand, the micro-sized TiC particles agglomerated due to their shape and size. The reinforcement of 2 wt% TiC into Inconel 625 matrix significantly enhanced hardness around 47%. The RAM mixing technique was found to be the most effective method in this study since it produced high-quality composite powders within the shortest time possible. RAM has proved its effectiveness as an ideal method for producing MMC powders, which can be used in LPBF technology.

Conflict of Interest

The authors declare no conflict of interest

Author Contributions

Dursun, G. devised the project and main conceptual. Celik, D., Gundogan, Y.C., and Bal, İ carried out the experiments. Dursun, G., Celik, D., Gundogan, Y.C., and Bal, İ. wrote the article.

Funding

This research was supported by Secretariat of Defence Industries (SSB).

Acknowledgments

Authors would like to express sincere gratitude to Secretariat of Defence Industries (SSB) and Tusas Engine Industries (TEI) for all supports throughout the current study.

References

AlMangour, B., Grzesiak, D. & Yang, J. (2007). Scanning strategies for texture and anisotropy tailoring during selective laser melting of TiC/316L stainless steel nanocomposites. *Journal of Alloys and Compounds, 728*, 424-435, https://doi.org/10.1016/j.jallcom.2017.08.022.

Baitimerov, R., Lykov, P., Zherebtsov, D., Radionova, L., Shultc, A., & Prashanth, K. G. (2018). Influence of Powder Characteristics on Processability of AlSi12 Alloy Fabricated by Selective Laser Melting. *Materials*, *11*(5), 742. https://doi.org/10.3390/ma11050742.

Dadbakhsh, S., Mertens, R., Vanmeensel, K., Ji, G., & Kruth, J. P. (2020). In situ transformations during SLM of an ultra-strong TiC reinforced Ti composite. *Scientific Reports, 10*, https://doi.org/10.1038/s41598-020-67434-3.

Gorji, N. E., O'Connor, R., Mussatto, A., Snelgrove, M., González, P. M., & Brabazon, D. (2019). Recyclability of stainless steel (316 L) powder within the additive manufacturing process. *Materialia, 8,* https://doi.org/10.1016/j.mtla.2019.100489.

Gu, D., Wang, Z., Shen, Y., Li, Q., & Li, Y. (2009). In-situ TiC particle reinforced Ti–Al matrix composites: Powder preparation by mechanical alloying and Selective Laser Melting behavior. *Applied Surface Science, 255*(22), 9230–9240. https://doi.org/10.1016/j.apsusc.2009.07.008.

Liu, B., Wildman, R., Tuck, C., Ashcroft, I., & Hague, R. (2011). Investigation the effect of particle size distribution on processing parameters optimisation in selective laser melting process. *Additive manufacturing research group, Loughborough University*, 227-238.

Murray, J. W., Simonelli, M., Speidel, A., Grant, D. M., & Clare, A. T. (2019). Spheroidisation of metal powder by pulsed electron beam irradiation. *Powder Technology*, *350*, 100–106. https://doi.org/10.1016/j.powtec.2019.03.041.

Niu, H. & Chang, I. (1999). Selective laser sintering of gas and water atomized high speed steel powders. *Scripta Materialia, 41*(1), 25-30. https://doi.org/10.1016/s1359-6462(99)00089-5.

Parsons, E. M. & Shaik, . S. Z. (2022). Additive manufacturing of aluminum metal matrix composites: Mechanical alloying of composite powders and single track consolidation with laser powder bed fusion, *Additive Manufacturing, 50,* https://doi.org/10.1016/j.addma.2021.102450.

Poyraz, O. & Kushan, M. (2019). Residual Stress-induced Distortions in Laser Powder Bed Additive Manufacturing of Nickel-based Superalloys. *Journal of Mechanical Engineering, 65*(6), 343-350. http://dx.doi.org/10.5545/sv-jme.2019.6004.

Smith, T. M., Thompson, A. C., Gabb, T. P., Bowman, C. L., & Kantzos, C. A. (2020). Efficient production of a high-performance dispersion strengthened, multi-principal element alloy. *Scientific Reports, 10*(1), https://doi.org/10.1038/s41598-020-66436-5.

Thompson, P., Poveda, R., Bezsonov, I., Rossini, M., Orthner, D., Cobb, K., ... & Iqbal, Z. (2019). *AlSi10Mg Nanocomposites Prepared by DMLS Using In-Situ CVD Growth of CNTs: Process Effects and Mechanical Characterization.* , Orthner, D., Cobb, K., Leng, B., Iqbal, Z., (pp. 41-46). Cham: Springer International Publishing.

Tjong, S. C., 2007. Novel Nanoparticle-Reinforced Metal Matrix Composites with Enhanced Mechanical Properties. *Advanced Engineering Materials,* 9(8), 639–652. https://doi.org/10.1002/adem.200700106.

Yang, G., Xie, Y., Zhao, S., Ren, Y., & Wang, C. (2022). Methods and Mechanism of Powder Mixing for Selective Laser Melting. *Manufacturing Technology,* 22(1), 102–110. https://doi.org/10.21062/mft.2022.006.

Yao, X., Moon, S. K., Lee, B. Y. & Bi, G. (2017). Effects of heat treatment on microstructures and tensile properties of IN718/TiC nanocomposite fabricated by selective laser melting. *Int. J. Precis. Eng. Manuf, 18,*1693–1701. https://doi.org/10.1007/s12541-017-0197-y.

Zhai, W., Zhou, W., Nai, S. M. L. & Wei, J. (2020). Characterization of nanoparticle mixed 316 L powder for additive manufacturing. *Journal of Material Science and Technology,* Volume 47, 162–168. https://doi.org/10.1016/j.jmst.2020.02.019.

Zhuang, J., Gu, D., Xi, L., Lin, K., Fang, Y., & Wang, R. (2020). Preparation method and underlying mechanism of MWCNTs/Ti6Al4V nanocomposite powder for selective laser melting additive manufacturing. *Powder Technology, 368,* 59-69. https://doi.org/10.1016/j.powtec.2020.04.041.